The Asphericity of the Earth from Free Oscillations

A thesis presented

by

Xiang-Dong Li

to

The Department of Earth and Planetary Sciences

in partial fulfillment of the requirements

for the degree of

Doctor of Philosophy

in the subject of

Geophysics

Harvard University

Cambridge, Massachusetts

March, 1990

Abstract

Spectra of the Earth's free oscillations, which depart significantly from those predicted for spherically symmetric earth models, contain important information on the Earth's large-scale aspherical structure. The studies contained in this thesis represent the initial attempt to use such data and the theory of spectral "splitting" to constrain the Earth's large-scale three-dimensional structure.

An important theoretical result is that for an isolated free-oscillation mode, and for known earthquake sources, a single function on the sphere, termed the *splitting function* of the mode, is sufficient to determine the spectra of the mode for all sources and receivers. This makes it possible to pose the nonlinear inverse problem in which many spectra are used to determine the comparatively few parameters which define the splitting function of the mode. Using long-period accelerograms of large events recorded by the IDA network, splitting functions of 34 multiplets are retrieved.

The splitting functions, which provide linear constraints on the Earth's aspherical structure, are used to investigate the compatibility of the modal data set with preexisting mantle models based upon other types of data. This kind of investigation provides fairly strong constraints on the value of $d\ln v_P/d\ln v_S$ in the lower mantle, which is shown to lie in the interval (0.21, 0.51) with 90% confidence, strongly discriminating against the value (0.8) that is often supposed.

Assuming proportionality among the relative perturbations in v_P, v_S and ρ, the splitting functions are inverted for heterogeneous mantle structure, without reference to preexisting models based upon other kinds of seismic data. The models so generated are found to be remarkably similar to previous models, demonstrating that the heterogeneity in seismic velocities is, at most, weakly dependent on frequency.

A second approach to the problem of inferring three-dimensional structure is also developed, in which we directly solve the inverse problem in which the data are observed modal spectra and the unknowns are the structural parameters. This approach has advantages in the case that there are insufficient data to obtain stable results for the splitting functions of some modes. The models generated in this way

are similar to those obtained by the inversion of splitting functions.

Some modes penetrating deep into the core are found to have a strong zonal pattern in their splitting functions which is attributed to zonal anisotropy of the inner core. Although the data set does not adequately constrain all of the parameters upon which such anisotropy can depend, we derive a simple example of an anisotropic inner-core model which can explain the splitting of the core modes and does not violate the constraints provided by *PKIKP* travel-time data.

Contents

1 Introduction 1

1.1 Seismological Studies of the Earth's Interior 1

1.2 Study of Earth Structure from Splitting of Normal Modes 3

1.3 Scope and Structure of the Thesis 6

2 Theoretical Formalism 11

2.1 Theory of Splitting of Free Oscillations 12

2.2 The Splitting Function 14

2.3 Differential Kernels 18

2.3.1 Kernel coefficients for undulations of discontinuities 18

2.3.2 Kernels for heterogeneity 19

2.3.3 Kernels for anisotropy 20

2.4 Aspects on Heterogeneity in Fluid Regions 23

2.4.1 Response of a fluid to density anomalies in solid regions 24

2.4.2 Splitting effects due to heterogeneity in fluid regions of the Earth 29

2.5 Expansion of an Inner-Core Anisotropic Tensor Field 34

2.5.1 Expansion in generalized spherical harmonics of a constant tensor field 35

2.5.2 Expansion of analytic tensor fields 50

2.5.3 Basis tensors which contribute to splitting 58

3 Inverse Theory 59

3.1 Stochastic Solution of the Inverse Problem 60

3.2 Error and Resolution Estimates 61

4 Data Selection and Processing **64**

4.1 Data Selection 65

4.2 Editing and Filtering of Seismic Traces 69

4.3 Noise 74

5 Inversion for the Splitting Functions **75**

5.1 Modeling Considerations 75

5.2 Results 77

5.2.1 Splitting functions 78

5.2.2 Error maps 86

5.2.3 Resolution matrices 91

5.2.4 Size of the splitting functions 91

5.2.5 Aliasing 92

5.2.6 Central frequency 94

5.2.7 Splitting width 96

5.2.8 Attenuation 97

5.3 Discussion 98

6 Forward Modeling of Splitting Functions Using Existing Mantle Models **107**

6.1 The Relative Amplitudes of Lower-Mantle Heterogeneity in P and S Velocities 108

6.1.1 Experiment 1a: Value of α^{TT}/β^{MD} 111

6.1.2 Experiment 1b: Correction for α^{MD}/α^{TT} 115

6.1.3 Experiment 2a: Value of α^{MD}/β^{SW} 118

6.1.4 Experiment 2b: Correction for β^{MD}/β^{SW} 119

6.1.5 Estimate of $d\ln\alpha/d\ln\beta$ in the lower mantle 119

6.1.6 Implications of physical dispersion 122

6.2 Relationship between Heterogeneities in Density and in Velocities . . 125

6.3 Prediction of Splitting Functions from Existing Mantle Models 127

7 Inversion for Earth Models **132**

7.1 Introduction 132

7.2 Modeling Parameters 134

7.2.1 Parameterizing heterogeneity in the mantle 134

7.2.2 Boundary undulations 136

7.2.3 Anisotropy in the inner core 137

7.2.4 Attenuation structure in the mantle 144

7.3 Models to Fit Splitting Functions 145

7.3.1 Aspherical model of the mantle 145

7.3.2 Modeling inner-core anisotropy 147

7.4 Models to Fit Split Spectra Directly 152

7.5 Discussion 160

7.5.1 Heterogeneity in the mantle 160

7.5.2 Core-mantle boundary 168

7.5.3 Spherical corrections in the mantle 170

7.5.4 Core modes and inner-core anisotropy 171

8 Conclusions **176**

References **178**

To my Mother and Father

Acknowledgements

I sincerely thank my thesis advisor, John Woodhouse, who has introduced me to low-frequency seismology. I have had the fortune of working closely with him during the course of this research and have benefited very much from his scientific insight and experience. I have also enjoyed the experience of working together with Domenico Giardini in the early stage of this research. The publication in *Journal of Geophysical Research* by Domenico, myself, and John provides the foundation for Chapters 4 and 5 of this thesis. Many of my computer codes were developed by modifying Domenico's and John's programs.

Adam Dziewonski and Richard O'Connell, who are members of my thesis committee, have provided valuable advice and have been invariably willing to be of assistance during this research and my whole graduate education.

I would like to give very special thanks to Alessandro Forte, who has very kindly spent his time reading carefully the manuscript of this thesis and pointing out grammatical and stylistic errors.

I am also grateful to Brian Farrell, a member of my thesis committee, for his reading of the manuscript and asking stimulating questions.

It is a pleasure to express my thanks to Philip England for his encouragement during the first two years of my graduate study at Harvard.

I am grateful to the many people who have influenced this work and have enriched my life over the years, particularly to my collaborators and classmates. Among them are (alphabetically) Göran Ekström, Carl Gable, Hua-Jian Gao, Andrea Morelli, Mike Ritzwoller, Wei-Jia Su, Winston Tao, and Yun Wong.

Most importantly and with greatest joy, I would like to sincerely thank my wife, Yu-Hong, who has continually offered me moral support. Her encouragement, understanding, and tolerance were essential.

I acknowledge the digital data provided by Jon Berger, Duncan Agnew, and staff of the IDA project. I also thank Andrea Morelli and Adam Dziewonski for allowing me to make use of their unpublished model V.3, and John Woodhouse and Adam

Dziewonski for their unpublished lower-mantle S-velocity model. This research was supported by the grants EAR85-11400, EAR86-18829, EAR87-08622 from the National Science Foundation.

Chapter 1

Introduction

1.1 Seismological Studies of the Earth's Interior

Understanding the Earth, the planet on which we live, has been one of the major goals in the course of science. Until the beginning of this century our knowledge of the Earth was, however, largely limited to understanding near-surface phenomena which were used to infer some very shallow structures just beneath the surface. It is only in this century that seismology has begun to yield a series of revolutionary discoveries on the Earth's deep interior. Studies of seismic waves, which can penetrate deep into the Earth, have led to most of our current knowledge about the interior. Among all the disciplines of the Earth sciences, seismology continues to play the most important role in detection of the spatial distribution of physical properties within the Earth.

After several decades of effort seismologists have determined the radial distributions of the Earth's elastic parameters and the density at all depths, with fair precision which is comparable to the lateral variations in these quantities. In recent years, the accumulation of data from global seismological networks and the availability of computers have enabled seismologists to begin the study of the lateral variations of physical properties in the Earth. Although these variations are much smaller, approximately by two orders of magnitude, than the radial variations, they play an

extremely important role in keeping the Earth dynamically active – without them we would have a tectonically dead Earth. Within the past few years independent results of modeling the three-dimensional Earth have been obtained from different kinds of data and by different techniques. These seismic tomographic inferences have already benefited other disciplines of the earth sciences. Geophysicists, for example, have employed these tomographic results to model the mantle convection, the plate motions, the undulation of the core-mantle boundary, and the geoid [e.g., *Hager et al.*, 1985; *Forte and Peltier*, 1987, 1989].

Seismological studies of the large-scale three-dimensional structure of the Earth, in recent years, may be broadly classified in terms of the data sets upon which they are based. These are (1) large collections of P (and PKP, $PKIKP$) travel times, [e.g., *Dziewonski et al.*, 1977; *Poupinet et al.*, 1983; *Clayton and Comer*, 1983; *Dziewonski*, 1984; *Creager and Jordan*, 1986; *Morelli et al.*, 1986; *Morelli and Dziewonski*, 1987a, 1987b; *Shearer et al.*, 1988]; (2) measurements of the locations of spectral peaks of fundamental modes, interpreted asymptotically, and measurements of phase and group velocities of fundamental mode surface waves, [e.g., *Masters et al.*, 1982; *Nakanishi and Anderson*, 1983, 1984; *Woodhouse and Wong*, 1986; *Nataf et al.*, 1986; *Davis*, 1987; *Park*, 1987; *Wong*, 1989]; (3) complete waveforms of mantle waves, used as data in a least-squares inversion, [e.g., *Lerner-Lam and Jordan*, 1983; *Woodhouse and Dziewonski*, 1984; *Tanimoto*, 1985, 1986, 1987, 1988]; (4) complete waveforms of long-period body waves, [e.g., *Woodhouse and Dziewonski*, 1986]; and (5) complete spectra of split multiplets in the free-oscillation spectrum, [e.g., *Masters and Gilbert*, 1981; *Woodhouse and Giardini*, 1985; *Woodhouse et al.*, 1986; *Ritzwoller et al.*, 1986, 1988; *Giardini et al.*, 1987, 1988]. For recent reviews and more references to the literature, see *Lay* [1987], *Dziewonski and Woodhouse* [1987], and *Woodhouse and Dziewonski* [1989].

The subject of this thesis is to study large-scale three-dimensional Earth structure from data of class (5), i.e., spectra of split multiplets in the free-oscillation spectrum.

1.2 Study of Earth Structure from Splitting of Normal Modes

The observed free oscillations of the Earth after a large earthquake were first reported approximately 30 years ago [*Benioff et al.*, 1961; *Ness et al.*, 1961; *Alsop et al.*, 1961; *Bogert*, 1961]. Since then, central frequencies of more than a thousand modes have been measured. These frequencies, together with other seismic data, have been used to develop the widely used spherical earth models, e.g., Preliminary Reference Earth Model of *Dziewonski and Anderson* [1981]. In these analyses, it has been assumed that the Earth is a spherically symmetric body, for which the $2l + 1$ eigenfunctions (singlets) belonging to the same multiplet of angular order l will have a single degenerate frequency. For the real Earth, however, sphericity is an approximation and is not always valid. When certain aspherical structure of the Earth is considered, the degeneracy of the singlets breaks down and the so-called "splitting" occurs. This is a phenomenon analogous to, for instance, the Zeeman effect in atomic physics. Although theoretical analyses on the effects of aspherical structure on the Earth's free oscillations have a relatively long history (among important contributions are by *Dahlen* [1968], *Dahlen* [1969], *Woodhouse and Dahlen* [1978], *Woodhouse* [1980], and *Woodhouse and Girnius* [1982]), high-quality low-frequency digital recordings have become available only in the last ten years or so. The fine structure of the spectra of these recordings carries valuable information on the interior structure of the Earth and provides the data on which the studies in this thesis are based.

Very low frequency seismic signals, having wavelengths comparable to the Earth's radius, constitute valuable information on the Earth's three-dimensional structure. In studies of the lower mantle using travel-time anomalies [*Clayton and Comer*, 1983; *Dziewonski*, 1984; *Morelli and Dziewonski*, 1987b] the individual data are sensitive to very short wavelength features of the Earth, since typical wavelengths of 1-Hz signals are less than 10 km. In order to determine the long wavelength heterogeneity, which undoubtedly is of fundamental geodynamic significance, one has to rely upon an

inversion algorithm to correctly evaluate the appropriate averages. Because of the distribution of events and stations, sampling is poor in some regions. Therefore, although every precaution may be taken to avoid systematic errors, and although a convincing case can be made that such errors have not seriously affected the results, the suspicion might remain, for example, that features in travel-time models bearing a relation to subduction zones may be artifacts of the high density of sources at convergent plate boundaries.

Although it is not to be expected that free oscillations will yield high-resolution images of the Earth, their physical nature is such that they are sensitive only to very large-scale heterogeneity, and they provide therefore a natural data set for constraining such structure. Moreover, free oscillations of low angular degree constitute the only kind of data for which source and receiver bias can be essentially ruled out as a source of systematic error. It will be shown later in this thesis that despite the fact that only 10 events and a sparse array of stations have been used, formal model errors are rather uniform over the globe.

In addition to these spatial averaging properties, many free oscillation multiplets are particularly sensitive to S-velocity structure which it has not yet proved possible to model using S-wave travel times. Thus the study of the splitting of normal modes [*Giardini et al.*, 1987], together with the study by *Woodhouse and Dziewonski* [1986] in which long-period body waveforms are employed, are the first to constrain the lower-mantle S-velocity heterogeneity.

Although it is not possible to obtain an independent reliable image of the three-dimensional distribution of the density from the current data, the study of the splitting and the coupling of the free oscillations will presumably provide solutions to this geophysically very important problem as more data become available.

Masters and Gilbert [1981] showed that the mode ${}_{10}S_2$ is split by an amount more than double that predicted by virtue of the Earth's rotation and ellipticity. *Ritzwoller et al.* [1986], *Woodhouse et al.* [1986], *Giardini et al.* [1987], and the current study confirm this phenomenon for a number of other multiplets which have in common the property of being sensitive to heterogeneity deep in the core. This

large and unexpected effect, requiring an exotic phenomenon in the core, has been another primary motivation for the work reported here. In an earlier stage of our study [*Woodhouse et al.*, 1986; *Giardini et al.*, 1987], we have tested the hypothesis that the anomalous splitting of the core modes is caused by heterogeneity in the core and by the deviations of the core-mantle boundary (CMB) and the inner-core boundary (ICB) from their hydrostatic shapes. We have found that the inclusion of outer-core heterogeneity leads to models inconsistent with some modes. Under the assumption that the outer core is homogeneous, our experiments required large zonal structures at the CMB ($\sim$ 8 km undulation) and the ICB ($\sim$ 25 km undulation) and in the inner core ($\sim$ 5% lateral heterogeneity). These results conflict with measurements of the Earth's nutation periods [*Gwinn et al.*, 1986] and with evidence from core-phase travel times [*Morelli et al.*, 1986; *Morelli and Dziewonski*, 1987a; *Shearer et al.*, 1988; *Souriau and Souriau*, 1989]. An anisotropic inner-core model has, therefore, been proposed [*Woodhouse et al.*, 1986] to properly explain the the behavior of the anomalously split modes. Evidence for the inner-core anisotropy has been also obtained from studies of *PKIKP* travel times [*Morelli et al.*, 1986; *Shearer et al.*, 1988]. In order to provide a physical rationale for inner-core anisotropy, *Jeanloz and Wenk* [1988] have shown that the convection in the inner core, suggested by the high Rayleigh number of this region, can cause dynamic recrystallization of inner-core material. The original seismological studies in which inner-core anisotropy was proposed considered the model of transverse isotropy in the plane of the equator, but they showed that while this model was fairly effective in separately modeling the modal observations and the travel-time observations, it was not possible to obtain a model of this kind which simultaneously explained both types of data. It was pointed out that both kinds of data favor, to a first approximation, a cylindrically symmetric distribution of anisotropy, in which the symmetry axis coincides with the Earth's rotation axis. In this thesis we present a relatively simple model of such kind which can explain the modal data without violating the constraints provided by *PKIKP* travel-time data.

One shortcoming of the analysis to be presented here is the assumption that mul-

tiplets are "isolated"; that is to say that coupling among multiplets [*Dahlen*, 1969; *Luh*, 1973; *Woodhouse*, 1980] is neglected. As a consequence of this assumption the theoretical spectra depend only upon heterogeneity of even harmonic degrees, and thus it is only even degrees which are determinable by this approach. This assumption also limits us to using only a small portion of the available data. Coupling among multiplets is strongest, in general, for modes which are closely spaced in frequency; some pairs of multiplets to be discussed below have singlets which are interspersed, but nevertheless we neglect coupling and treat the data as if they were simply the superposition of the spectra for isolated modes. Tests of the expected strength of coupling have convinced us that the error made in this procedure is not large for the multiplets studied here. Undoubtedly it is an important effect for many other sets of multiplets, however, and the correct treatment of coupled modes is a priority for future work.

1.3 Scope and Structure of the Thesis

A very important concept, which may also serve as an intermediate step in the inversion for earth structure, is the so-called "splitting function" of a multiplet [*Woodhouse and Giardini*, 1985]. If the sources are known, the spectra of a given multiplet for many sources and many receivers depend only upon the splitting function $\eta(\theta, \phi)$ of the multiplet. This function is similar to the function $\delta\omega_{\text{local}}(\theta, \phi)$ introduced by *Jordan* [1978] which, in turn, is similar to a phase velocity distribution for a surface wave of a given frequency. In fact $\eta(\theta, \phi)$ is equivalent to $\delta\omega_{\text{local}}(\theta, \phi)$ in the limit that the horizontal wavelength of the mode is much smaller than the wavelength of the heterogeneity; the analysis in terms of $\eta(\theta, \phi)$, however, does not require any asymptotic approximations to be made, and thus it is equally applicable to modes of high and low angular order.

One of our approaches to invert for three-dimensional earth models is to use the splitting functions as an intermediate step in the inversions. We may first retrieve the splitting functions mode by mode. For each mode we invert for the harmonic

coefficients of the splitting function from many spectra in a least-squares iterative procedure. The resulting splitting functions (or their spherical harmonic coefficients) constitute linear constraints on the Earth's aspherical structure. These constraints are, moreover, essentially model independent. We can then use these splitting functions as data in an invert for the earth structure. The inversion carried out in this second step is linear, and quantities of different spherical harmonic degree s and order t are decoupled.

An alternative inversion procedure is to bypass the intermediate step. Namely, we may invert for earth models directly from the seismic spectra by a least-squares iterative procedure. In this thesis the results using both schemes are presented and compared with each other.

With the current data set we elect to ignore the higher-degree coefficients of the splitting functions and the earth structure, rather than solve a very underconstrained nonlinear problem. We are going to be concerned with spherical harmonics only up to degree $s = 4$. Under this constraint some splitting coefficients are well resolved, whereas others must be considered marginal. The earth models retrieved are fairly satisfying in terms of our knowledge about the Earth from other independent data and techniques. With a greater number of very-long-period seismic stations and a sufficient period of operation for many large events to be recorded, the splitting functions of many multiplets could be determined with higher precision, enabling tighter constraints to be placed on the Earth's very-large-scale, three-dimensional structure.

The multiplets used in this study, 34 in total, have very long periods, ranging from 193 s to 2134 s, and are thus sensitive to the very-large-scale structures of the Earth. These modes can be naturally divided into two groups: those whose splitting behavior can be well explained by aspherical structure in the mantle; and those whose splitting functions are dominated by zonal patterns which cannot be accommodated in the mantle.

The splitting of the mantle modes depends upon aspherical perturbations in P-velocity (α), S-velocity (β), and density (ρ) simultaneously. Unfortunately the data

involved in this study are insufficient to constrain all three quantities independently. As a first approximation, the relative perturbations in these quantities may be assumed proportional to one another. The splitting of our modes as a whole depends much more upon the structures of the seismic velocities than upon the structure of the density; therefore the value of the ratio $d\ln\alpha/d\ln\beta$ has great importance in this study. The evidence that this ratio as constrained by seismic data is much lower, for the lower mantle, than the value based on laboratory experiments [*Anderson et al.*, 1968] has been reported in *Giardini et al.* [1987]. *Ritzwoller et al.* [1988] have, however, argued that this result can be debated if a proper model of the core-mantle boundary (CMB) topography is introduced. In this thesis we will give a more careful treatment on this issue. First we shall try to eliminate the CMB contamination by combining the modal data so that the sensitivities of the combined data to the CMB structure are canceled out. We will also treat the ratio $d\ln\alpha/d\ln\beta$ as a statistical variable and hence estimate its distribution. Together with some existing models of the mantle, we find that the modal data do indeed constraint the value of this ratio and that a significantly lower value than that of *Anderson et al.* [1968] is required for the lower mantle by seismic data.

In order to model the anomalous splitting of the core modes, we derive, as a theoretical result, a general form of the inner-core anisotropic tensor field which causes splitting effects possessing cylindrical symmetry. With only 8 core modes available in this study, we do not expect to uniquely determine the parameters, even for lower degrees, upon which the tensor field can depend. However we are able to present examples of relatively simple anisotropic inner-core models which reconcile the modal and the travel-time data.

In an independent study, *Ritzwoller et al.* [1986 and 1988] have also studied the splitting of normal modes by using similar techniques. In order to interpret their interaction coefficients (essentially equivalent to our splitting functions), they modeled the aspherical structure (of degree $s = 2$ only) of the mantle. They adopted in the inversion the value of $d\ln\alpha/d\ln\beta$ from the laboratory experiments, which is challenged in this study. Since they also included as data the results of *Smith et*

al. [1987] for many fundamental surface-wave equivalent modes, much attention was paid to the structure in the upper mantle. Although they realized that the source of the zonal structure in the splitting functions of the anomalously split modes is located beneath the core-mantle boundary, *Ritzwoller et al.* [1988] did not model it.

In Chapter 2 of this thesis we present the theoretical results of this study. It contains three major independent subjects: (1) The concept of splitting functions and their relationship with observed seismograms and with earth structure (including heterogeneity, anisotropy, and the undulations of discontinuities) are discussed. (2) Considering that the fluid regions of the Earth are in hydrostatic equilibrium, the lateral heterogeneity in these regions due to density anomalies located in solid regions is calculated in a gravitationally consistent way; the significance of the secondary splitting effect of such heterogeneity in the fluid regions is checked. (3) As a theoretical preparation for modeling inner-core anisotropy, a set of orthonormal tensor bases is developed to expand analytic tensor fields in the unit sphere.

In Chapter 3 we set up the framework of the inverse theory relevant to this study. Stochastic solutions to nonlinear inverse problems are formally approached by iteration. Formal analysis of resolution and errors is discussed for the linear neighborhood of the model to which the iteration converges. In all analyses the case is considered that additional constraints may be imposed on the basic equation.

The data used in this study are long-period accelerograms recorded by the International Deployment of Accelerometers (IDA) network. The selection and processing of these data are described in Chapter 4.

The inversion procedure and our inferences of the splitting functions are presented in Chapter 5. The inferred splitting functions possess a series of well-defined patterns which can be directly linked to specific regions of the Earth's interior by examining the corresponding modal differential kernels. The close correspondence between the inferred splitting functions of multiplets possessing similar differential kernels provides evidence (which is more compelling, we believe, than the formal error estimates) that the splitting functions have been accurately retrieved and that they do, indeed, reflect the Earth's three-dimensional structure.

Forward modeling of splitting functions using some preexisting earth models is performed in Chapter 6. Such an investigation provides a fairly strong constraint on the value of $d\ln\alpha/d\ln\beta$ in the lower mantle, which is shown to lie in the interval (0.21, 0.51) with 90% confidence, strongly discriminating against the value (0.8) that is often supposed. The synthetic splitting functions calculated from preexisting earth models are essentially consistent with the retrieved splitting functions for most of the multiplets we study.

In Chapter 7, large-scale three-dimensional earth models are developed by two approaches: first by inverting the splitting functions which have been retrieved from split seismic spectra, and second by inverting the split spectra directly. The mantle models resulting from these two approaches are essentially identical, indicating that the splitting functions can serve as a very useful intermediate stage for the study of earth structure using split normal modes. Both models are remarkably similar to preexisting models based upon studies of travel-time residuals and SH waveforms, demonstrating that the heterogeneity in seismic velocities is, at most, weakly dependent on frequency. The anomalous splitting of core modes is attributed to zonal anisotropy in the inner core. Although the data set does not adequately constrain all of the parameters upon which such anisotropy can depend, we do derive a simple example of an anisotropic inner-core model which can explain the splitting of the core modes without violating the constraints provided by $PKIKP$ travel-time data.

Chapter 2

Theoretical Formalism

We shall start this chapter with a brief summary of the theory of the splitting of the Earth's free oscillations. Assuming that we have already determined the eigenfunctions and associated eigenfrequencies of free oscillations for a spherically symmetric, non-rotating, elastic isotropic (SNREI) earth model and that the earthquake source parameters and receiver responses are known, in order to calculate the seismogram contribution from a particular isolated multiplet for a slightly aspherically perturbed earth model we need only know the splitting matrix of this multiplet.

As an inverse problem, we may seek to retrieve from observed seismograms the elements of splitting matrices, which contain information on the structure of the Earth's interior. However, the connections between the elements of a splitting matrix and the structure of the Earth are not transparent. In Section 2.2 we introduce the concept of *splitting functions* [*Woodhouse and Giardini*, 1985], which are equivalent to splitting matrices in terms of the information they contain. The splitting function is defined on the surface of a sphere and represents the radially integrated heterogeneity and anisotropy of the Earth's interior. In order to formulate the linearized inverse problem for the spherical harmonic coefficients of the splitting function, we also derive the partial derivatives of the seismogram with respect to these coefficients.

In the following section, we turn our attention to the relationship between the splitting function and the Earth's three-dimensional structure. The differential ker-

nels, as functions of depth, of lateral heterogeneity, anisotropy, and the undulations of internal discontinuities will be given.

If we consider the fluid regions of the Earth to be in hydrostatic equilibrium, the lateral variation in these regions may not be specified independently. In Section 2.4 we give the formulation to calculate, in a gravitationally consistent way, the the lateral heterogeneity in the fluid regions as the response to the density anomalies located in the solid regions. We may attribute the splitting effects of such responses directly to their origins – the density anomalies in the solid regions. In order to check the significance of these secondary effects, we compare them to the splitting effects caused directly by the heterogeneity in the solid regions for an ad hoc mantle model, which is based upon some existing models.

As a theoretical preparation for modeling inner-core anisotropy, we present in Section 2.5 a technique for expanding an inner-core anisotropic tensor field. We demonstrate there that a general elastic tensor field which is analytic in the unit sphere can be expanded in a series of orthogonal basis tensor fields and that these bases partition into two categories: (1) those which span a splitting-sensitive subspace and (2) those which span a null-subspace for splitting.

2.1 Theory of Splitting of Free Oscillations

At times after the source of an earthquake has ceased to act, the low-frequency elastic displacement field may be regarded as the superposition of many standing waves. For a SNREI earth model, the displacement field may be written [*Gilbert*, 1971a; *Gilbert and Dziewonski*, 1975]

$$\mathbf{u}(\mathbf{x},t) = \sum_k \sum_{m=-l}^{l} a_m^{(k)} \mathbf{u}_m^{(k)}(\mathbf{x}) \exp(i\omega_k t) \tag{2.1}$$

where the real part is understood, $a_m^{(k)}$ are coefficients determined by the source, $\mathbf{u}_m^{(k)}$ are the eigenfunctions and ω_k are the eigenfrequencies of the free oscillations of the Earth. Eigenfunctions with the same k and different m have the same degenerate eigenfrequency ω_k. Together, they constitute a mode, or more precisely a multiplet,

of free oscillation; each of them with different m is termed a singlet. The multiplet index k, incorporates the angular order (l), the overtone number (n), and the type (spheroidal or toroidal) of the mode.

For a multiplet of angular order l, the eigenfunctions $\mathbf{u}_m^{(k)}$ may be expressed in terms of complex spherical harmonics $Y_l^m(\theta, \phi)$

$$\mathbf{u}_m^{(k)} = U^{(k)} Y_l^m \hat{\mathbf{r}} + V^{(k)} \nabla_1 Y_l^m + W^{(k)} (-\hat{\mathbf{r}} \times \nabla_1 Y_l^m) \tag{2.2}$$

where $U^{(k)}$, $V^{(k)}$, and $W^{(k)}$ are functions of radius r and characterize the mode ($U^{(k)}$ and $V^{(k)}$ vanish for a toroidal mode; $W^{(k)}$ vanishes for a spheroidal mode); $\nabla_1 \equiv \hat{\theta}\partial_\theta + \csc\theta\, \hat{\phi}\partial_\phi$; and $\hat{\mathbf{r}}$, $\hat{\theta}$, $\hat{\phi}$ are unit vectors in the spherical-coordinate directions. In this thesis we normalize the eigenfunctions $\mathbf{u}_m^{(k)}$ according to *Woodhouse and Dahlen* [1978]

$$\int \rho\, \mathbf{u}_m^{(k)*} \cdot \mathbf{u}_{m'}^{(k')} dV = \delta_{kk'} \delta_{mm'} \tag{2.3}$$

where ρ is the density distribution of the Earth, '$*$' denotes complex conjugation, and $\delta_{kk'}$ are Kronecker deltas.

Throughout this thesis it is assumed that we can separate an isolated multiplet from the other modes, i.e., we neglect coupling between multiplets [*Dahlen*, 1969; *Luh*, 1973, 1974; *Woodhouse*, 1980]. Thus we are able to treat one mode at a time, and accordingly we shall often omit the multiplet index k from our notations for simplicity.

When certain aspherical structure of the Earth is considered, the degeneracy of the singlets breaks down and so-called "splitting" occurs. A result of first-order splitting theory [*Dahlen*, 1968, 1974; *Woodhouse and Dahlen*, 1978] is that for a slightly asphericallly perturbed earth model, the eigenfunctions and eigenfrequencies of the singlets of a mode can be derived from the splitting matrix $\mathbf{H}$ of that mode, which is obtainable from the unperturbed spherical reference model. If $\mathbf{U}$ is the matrix whose columns are the eigenvectors of $\mathbf{H}$ we have

$$\mathbf{HU} = \mathbf{U}\Omega \tag{2.4}$$

where $\mathbf{\Omega}$ is the diagonal matrix of eigenvalues, with each diagonal element Ω_{jj} being the perturbation in frequency of the jth singlet. The associated perturbed eigenfunction of the jth singlet can be expressed (to zeroth order) as

$$\mathbf{u}'_j = \sum_{m=-l}^{l} U_{mj}\mathbf{u}_m(\mathbf{x}) \tag{2.5}$$

Woodhouse and Girnius [1982] have shown that the contribution of a particular isolated multiplet to an observed seismogram (the convolution of ground displacement with the instrumental response) can be written

$$u(t) = \mathrm{Re}[\exp(i\omega t)\ \mathbf{r}\cdot\exp(i\mathbf{H}t)\cdot\mathbf{s}] \tag{2.6}$$

where $\mathbf{r}$ is the "receiver vector", $\mathbf{s}$ is the "source vector", and ω is the complex reference frequency of the multiplet; these are evaluated for the unperturbed spherical reference model. The vectors $\mathbf{r}$, $\mathbf{s}$ have $2l+1$ complex elements, labeled by azimuthal order m ($-l \le m \le l$), and given, in the notation of *Woodhouse and Girnius* [1982], by

$$s_m = S_k^m(\theta_s,\phi_s) \qquad r_m = R_k^m(\theta_r,\phi_r) \tag{2.7}$$

where k is the multiplet index and $\theta_s, \phi_s, \theta_r, \phi_r$ are the source and receiver co-latitude and longitude. The vector $\mathbf{s}$ depends (linearly) upon the source moment tensor, and the vector $\mathbf{r}$ depends upon instrument orientation and incorporates the instrumental response.

2.2 The Splitting Function

The splitting matrix $\mathbf{H}$ is a $(2l+1)\times(2l+1)$ complex matrix [*Dahlen*, 1968; *Woodhouse and Dahlen*, 1978], which can be written

$$H_{mm'} = m\Omega\bar{\beta}\delta_{mm'} + \omega_0 \sum_{\substack{s=0 \\ \text{s even}}}^{2l} \sum_{t=-s}^{s} \gamma_{ls}^{mm't}\ c_{st} \tag{2.8}$$

with $\omega_0 \equiv \mathrm{Re}(\omega)$ and

$$\gamma_{ls}^{mm't} \equiv \int_0^{2\pi}\int_0^{\pi} Y_l^{m*}(\theta,\phi)\ Y_s^t(\theta,\phi)\ Y_l^{m'}(\theta,\phi)\sin\theta\, d\theta\, d\phi \tag{2.9}$$

where $Y_l^m(\theta,\phi)$ are completely normalized spherical harmonics, and symbol $*$ denotes complex conjugation; we use the convention of *Edmonds* [1960]. We may also write

$$\gamma_{ls}^{mm't} = f_{ls}(-1)^m \begin{pmatrix} l & l & s \\ -m & m' & t \end{pmatrix} \tag{2.10}$$

where the Wigner 3-j symbol has been employed and where

$$f_{ls} \equiv (2l+1)\left(\frac{2s+1}{4\pi}\right)^{\frac{1}{2}} \begin{pmatrix} l & l & s \\ 0 & 0 & 0 \end{pmatrix} \tag{2.11}$$

The first term on the right side of (2.8) is the contribution arising from Coriolis forces; Ω is the Earth's rotational angular velocity, and $\bar{\beta}$ is the Coriolis splitting parameter of the multiplet [*Dahlen*, 1968] (a bar is put over β in this thesis to distinguish the usage of β which is reserved for S velocity). The coefficients c_{st} in (2.8) depend linearly upon the Earth's internal heterogeneity of harmonic degree s and order t, through expressions of the form

$$\begin{aligned} c_{st} &= \delta_{s2}\delta_{t0}c^{ell} + \sum_d H_s^d \delta h_{st}^d + \int_0^a \mathbf{M}_s(r)\cdot\delta\mathbf{m}_{st}(r)dr \\ &\quad + \int_0^a \bar{\mathbf{M}}_s(r)\cdot\delta\bar{\mathbf{m}}_{st}(r)dr \end{aligned} \tag{2.12}$$

where the first term on the right side is the known, theoretical contribution from the Earth's hydrostatic ellipticity of figure [*Dahlen*, 1968, 1976; *Woodhouse and Dahlen*, 1978]. In terms of the ellipticity splitting parameter $\bar{\alpha}\varepsilon_h' \equiv \bar{\alpha}\varepsilon_h + \alpha'\Omega^2/\omega^2$ (see *Woodhouse and Dahlen*, 1978, equation A14; α is overbarred in this thesis to distinguish the usage of α which is reserved for P velocity) we have

$$c^{ell} = \left(\frac{4\pi}{5}\right)^{\frac{1}{2}} \frac{(2l+3)(2l-1)}{l(l+1)}\bar{\alpha}\varepsilon_h' \tag{2.13}$$

Quantities δh_{st}^d, $\delta\mathbf{m}_{st}$, and $\delta\bar{\mathbf{m}}_{st}$ in (2.12) represent spherical harmonic coefficients of the undulation of the d'th boundary, heterogeneity, and anisotropy of the Earth, respectively. The corresponding differential kernels H_s^d, $\mathbf{M}_s$, and $\bar{\mathbf{M}}_s$ can be calculated from the spherical reference earth model.

The motivation for this study is to determine aspects of the Earth's internal aspherical structure by analyzing seismic spectra; i.e., our aim is to use a collection

of seismograms $u(t)$, together with (2.6), (2.8), (2.12) to infer δh^d_{st}, $\delta \mathrm{m}_{st}(r)$, and $\delta \bar{\mathrm{m}}_{st}(r)$. Because f_{ls} vanishes for odd s, we are necessarily restricted to even degrees s. Equations (2.6) and (2.8), however, provide a useful intermediate stage in the analysis, since they demonstrate that when the source and receiver parameters are known, all spectra for a given multiplet depend only upon the relatively few parameters represented by c_{st}. Let us suppose that the maximum (even) degree of heterogeneity which we wish to consider is $s_{max} \leq 2l$. Then the number of unknown coefficients c_{st} is

$$\sum_{\substack{s=0 \\ \text{s even}}}^{s_{max}} (2l+1) = \frac{1}{2}\,(s_{max}+1)(s_{max}+2) \tag{2.14}$$

For a mode of degree 2, for example, for which the largest possible value of s_{max} is 4, there are only 15 coefficients c_{st}; these should enable all spectra for the mode to be modeled. Once these coefficients are determined, (2.12) then represents a set of linear constraints on the model parameters δh^d_{st}, $\delta \mathrm{m}_{st}$, and $\delta \bar{\mathrm{m}}_{st}$.

A useful visual representation of the splitting coefficients c_{st} is given by the *splitting function* [*Woodhouse and Giardini*, 1985] which is defined to be

$$\eta(\theta,\phi) = \sum_{\substack{s=0 \\ \text{s even}}}^{2l} \sum_{t=-s}^{s} c_{st}\, Y^t_s(\theta,\phi) \tag{2.15}$$

In the asymptotic limit, $l \gg s_{max}$, the splitting function $\eta(\theta,\phi)$ is equal to the even degree expansion of the relative local eigenfrequency perturbation $\delta\omega_{\text{local}}/\omega_0$ defined by *Jordan* [1978]. Equation (2.8) shows that the splitting matrix is completely determined by the splitting coefficients c_{st}, together with the Coriolis parameter $\Omega\bar{\beta}$. It is of interest to show that the converse is also true, namely, that $\Omega\bar{\beta}$ and c_{st} are uniquely determined by the splitting matrix. Using an orthogonality property of the Wigner 3-j symbols [*Edmonds*, 1960, equation 3.7.8], it may be shown that (2.8) has the explicit inverse

$$\begin{aligned} \Omega\bar{\beta} &= \tfrac{3}{l(l+1)(2l+1)} \textstyle\sum_m m H_{mm} \\ c_{st} &= \tfrac{2s+1}{\omega_0 f_{ls}} \textstyle\sum_{mm'} (-1)^m \begin{pmatrix} l & l & s \\ -m & m' & t \end{pmatrix} H_{mm'} \end{aligned} \tag{2.16}$$

which demonstrates the stated result.

It may be noted that setting $s = 0$, $t = 0$ in (2.16), we find

$$(4\pi)^{-\frac{1}{2}}\omega_0 c_{00} = \frac{1}{2l+1}\ \mathrm{tr}\ \mathbf{H} \tag{2.17}$$

which is equivalent to the diagonal sum rule of *Gilbert* [1971b]; the right side is the mean of the singlet eigenfrequency perturbations, and the left side is the spherical part of $\omega_0\eta(\theta,\phi)$, which depends only upon the deviation of the "terrestrial monopole" from the reference model. Thus (2.16) may be regarded as a generalization of the diagonal sum rule.

In order to formulate the linearized, iterative inverse problem for c_{st} we require partial derivatives of the seismogram $u(t)$ with respect to these coefficients.

Let us first evaluate:

$$\frac{\partial}{\partial H_{mm'}} \exp(i\mathbf{H}t) \tag{2.18}$$

We note that $\mathbf{P}(t) = \exp(i\mathbf{H}t)$ is the solution of the initial value problem

$$\frac{d\mathbf{P}}{dt} = i\mathbf{H}\mathbf{P} \qquad \mathbf{P}(0) = \mathbf{I} \tag{2.19}$$

where $\mathbf{I}$ is the unit matrix. Perturbing this equation, we find that

$$\frac{d}{dt}\delta\mathbf{P} \ = \ i\delta\mathbf{H}\ \mathbf{P} + i\mathbf{H}\ \delta\mathbf{P} \qquad \delta\mathbf{P}(0) = \mathbf{0} \tag{2.20}$$

which has the (unique) solution

$$\delta\mathbf{P}(t) = \int_0^t \mathbf{P}(t-t')i\ \delta\mathbf{H}\ \mathbf{P}(t')dt' \tag{2.21}$$

Introducing the matrix $\mathbf{U}$ whose columns are the eigenvectors of $\mathbf{H}$, we have

$$\begin{aligned} &\mathbf{H}\mathbf{U} = \mathbf{U}\boldsymbol{\Omega} \\ &\mathbf{P}(t) = \exp(i\mathbf{H}t) = \mathbf{U}\exp(i\boldsymbol{\Omega}t)\ \mathbf{U}^{-1} \end{aligned} \tag{2.22}$$

where $\boldsymbol{\Omega}$ is the diagonal matrix of eigenvalues. Equation (2.21) can then be written

$$\delta P_{ij}(t) = \sum_{pqmm'} \int_0^t iU_{ip}e^{i\Omega_{pp}(t-t')}U^{-1}_{pm}\delta H_{mm'}U_{m'q}e^{i\Omega_{qq}t'}U^{-1}_{qj}dt' \tag{2.23}$$

Thus performing the integrations, we find that

$$\frac{\partial \exp(i\mathbf{H}t)_{ij}}{\partial H_{mm'}} = \sum_{pq} U_{ip} U^{-1}_{pm} U_{m'q} U^{-1}_{qj} \frac{e^{i\Omega_{qq}t} - e^{i\Omega_{pp}t}}{\Omega_{qq} - \Omega_{pp}} \tag{2.24}$$

where the term for p equal to q is obtained by taking the limit $\Omega_{pp} \rightarrow \Omega_{qq}$. Using (2.8), we find the following linearized form of (2.6):

$$\delta u(t) = \mathrm{Re}\left(\sum_{pqst} \omega_0 e^{i\omega t} r'_p s'_q \gamma'_{pqst} \frac{e^{i\Omega_{qq}t} - e^{i\Omega_{pp}t}}{\Omega_{qq} - \Omega_{pp}} \delta c_{st} \right) \tag{2.25}$$

where

$$\begin{aligned} r'_p &= \sum_{p'} U_{p'p} r_{p'} \\ s'_q &= \sum_{q'} U^{-1}_{qq'} s_{q'} \\ \gamma'_{pqst} &= \sum_{mm'} U^{-1}_{pm} U_{m'q} \gamma^{mm't}_{ls} \end{aligned} \tag{2.26}$$

Equation (2.25) may also be written

$$\begin{aligned} \delta u(t) = \mathrm{Re}\Bigg[& \omega_0 e^{i\omega t} \sum_{st} \delta c_{st} \sum_{q} e^{i\Omega_{qq}t} \\ & \times \left(\sum_{p \neq q} \frac{r'_p s'_q \gamma'_{pqst} + r'_q s'_p \gamma'_{qpst}}{\Omega_{qq} - \Omega_{pp}} + i t r'_q s'_q \gamma'_{qqst} \right) \Bigg] \end{aligned} \tag{2.27}$$

which yields a relatively efficient procedure for the evaluation of $\partial u(t)/\partial c_{st}$.

2.3 Differential Kernels

2.3.1 Kernel coefficients for undulations of discontinuities

If we choose normalized undulation (divided by the radius, r, of the discontinuity) as our parameter δh in (2.12), the corresponding kernel can be obtained from equations (97) and (110) of *Woodhouse and Dahlen* [1978]

$$\begin{aligned} \omega_0 H_s &= r^3 [\rho(\alpha^2 - \frac{4}{3}\beta^2)\tilde{K}_s + \rho\beta^2 \tilde{M}_s + \rho R^{(2)}_s]^+_- \\ &= r^3 [\kappa \tilde{K}_s + \mu \tilde{M}_s + \rho R^{(2)}_s]^+_- \end{aligned} \tag{2.28}$$

where the notation $[\,\cdot\,]^+_-$ denotes the jump discontinuity of the enclosed quantity across the boundary, with the positive contribution arising from that side of the boundary toward which $\hat{\mathbf{r}}$ is directed; and kernels $\tilde{K}_s$, $\tilde{M}_s$, and $R^{(2)}_s$ are given in equations (101),(103), and (110) of *Woodhouse and Dahlen* [1978], respectively.

2.3.2 Kernels for heterogeneity

The heterogeneity can be characterized by different sets of parameters. In this thesis we choose the relative perturbations in compressional velocity α, shear velocity β and density ρ to describe the heterogeneity, i.e., we set $\delta\mathbf{m}_{st}$ in (2.12) as

$$\delta\mathbf{m}_{st}(r) = (\delta\alpha_{st}/\alpha, \delta\beta_{st}/\beta, \delta\rho_{st}/\rho) \tag{2.29}$$

where the denominators are evaluated at the spherical reference model and the numerators are the spherical harmonic components of degree s and order t of the perturbations. $\delta\alpha_{st}$ and $\delta\beta_{st}$ could be complex to incorporate attenuation effects. The kernel $\mathbf{M}_s(r)$ corresponding to this specification of heterogeneity can be written

$$\mathbf{M}_s(r) = (A_s(r), B_s(r), R_s(r)) \tag{2.30}$$

The expressions for $A_s(r), B_s(r)$ and $R_s(r)$ in terms of the eigenfunctions of the multiplet in the reference model may be calculated by using equations (97) and (110)–(112) of *Woodhouse and Dahlen* [1978]. After some straightforward algebra, we obtain

$$\begin{aligned} \omega_0 A_s(r) &= 2r^2\alpha^2\rho K_s \\ &= 2r^2(\kappa + \frac{4}{3}\mu)K_s \end{aligned} \tag{2.31}$$

$$\begin{aligned} \omega_0 B_s(r) &= 2r^2\beta^2\rho(M_s - \frac{4}{3}K_s) \\ &= 2r^2\mu(M_s - \frac{4}{3}K_s) \end{aligned} \tag{2.32}$$

and

$$\begin{aligned} \omega_0 R_s(r) &= r^2\rho[(\alpha^2 - \frac{4}{3}\beta^2)K_s + \beta^2 M_s + R_s^{(2)}] \\ &= r^2(\kappa K_s + \mu M_s + \rho R_s^{(2)}) \end{aligned} \tag{2.33}$$

where kernels K_s, M_s and $R_s^{(2)}$ are given in equations (100), (102) and (110) of *Woodhouse and Dahlen* [1978], respectively; and κ is the bulk modulus and μ is the shear modulus of the reference model.

2.3.3 Kernels for anisotropy

Mochizuki [1986] has given explicit expressions for the coupling effects of anisotropy in terms of spherical harmonic coefficients of 21 independent contravariant components of an elastic tensor field. Here we show, however, that only 13 independent combinations of these contribute in the case of splitting (i.e., self-coupling). It is convenient, therefore, to decompose the elastic tensor perturbations into two parts: one belonging to the subspace which does not contribute to splitting and the other belonging to the orthogonal subspace.

The splitting matrix elements of a particular mode due to a general perturbation in the elastic tensor $\mathbf{L}$ can be written [*Woodhouse and Dahlen*, 1978]

$$H_{mm'} = \frac{1}{2\omega_0} \int [\nabla \mathbf{u}_{m'} : \mathbf{L} : \nabla \mathbf{u}_m^*] dV \tag{2.34}$$

where $\mathbf{u}_m (m = -l, \ldots, 0, \ldots, l)$ are the displacement eigenfunctions given in (2.2) and (2.3) with the multiplet index k omitted

The general elastic tensor $\mathbf{L}$, a fourth rank tensor, can be expanded in terms of generalized spherical harmonics

$$\mathbf{L} = \sum_{\alpha\beta\gamma\delta} \sum_{s=0}^{\infty} \sum_{t=-s}^{s} L_{st}^{\alpha\beta\gamma\delta}(r) \hat{Y}_s^{Nt}(\theta, \phi) \mathbf{e}_\alpha \mathbf{e}_\beta \mathbf{e}_\gamma \mathbf{e}_\delta \tag{2.35}$$

where $L_{st}^{\alpha\beta\gamma\delta}$ ($\alpha, \beta, \gamma, \delta$ each take values -1, 0, 1) are the coefficients characterizing tensor $\mathbf{L}$, $\mathbf{e}_\alpha$ are complex basis vectors as defined by equation (1.4) of *Phinney and Burridge* [1973], $\hat{Y}_s^{Nt}$ (with $N = \alpha+\beta+\gamma+\delta$) are the generalized spherical harmonics normalized so that

$$\int \hat{Y}_s^{Nt} (\hat{Y}_{s'}^{Nt'})^* \sin\theta d\theta d\phi = \delta_{ss'} \delta_{tt'} \tag{2.36}$$

where the integration is taken over the surface of the unit sphere. The generalized spherical harmonics used here are related to Y_s^{Nt} defined by *Phinney and Burridge* [1973] through

$$\hat{Y}_s^{Nt}(\theta, \phi) = \left(\frac{2s+1}{4\pi} \right)^{\frac{1}{2}} Y_s^{Nt}(\theta, \phi) \tag{2.37}$$

The expansion of $\mathbf{L}$ in terms of generalized spherical harmonics enables us to rewrite (2.34)

$$H_{mm'} = \frac{1}{2\omega_0} \sum_{\substack{s=0 \\ s \text{ even}}}^{2l} \sum_{t=-s}^{s} \gamma_{sl}^{mm't} \int_0^a \sum_{\alpha\beta\gamma\delta} L_{st}^{\alpha\beta\gamma\delta}(r) \varepsilon^{-\alpha-\beta} \varepsilon^{-\gamma-\delta} \xi_{sl}^{\alpha+\beta\,\gamma+\delta} r^2 dr \tag{2.38}$$

where the integration is taken from the center ($r = 0$) to the surface ($r = a$) of the Earth; indices α, β, γ, δ take values -1, 0, 1; $\varepsilon^{\alpha\beta}$ are symmetric variables (i.e., $\varepsilon^{\alpha\beta} = \varepsilon^{\beta\alpha}$) and are given by

$$\varepsilon^{\pm 1 \pm 1} = \Omega_0^l \Omega_2^l r^{-1} (V \pm iW) \tag{2.39}$$

$$\varepsilon^{00} = \dot{U} \tag{2.40}$$

$$\varepsilon^{+1-1} = -\frac{1}{2} r^{-1} [2U - l(l+1)V] \tag{2.41}$$

$$\varepsilon^{0\pm 1} = \frac{1}{2} \Omega_0^l [\dot{V} + r^{-1}(U - V) \pm i(\dot{W} - r^{-1} W)] \tag{2.42}$$

with $\Omega_N^l \equiv [(l+N)(l-N+1)/2]^{\frac{1}{2}}$, and "$\cdot$" denotes differentiation with respect to r. Finally the coefficients $\xi_s^{\alpha+\beta\,\gamma+\delta}$ in (2.38) are dimensionless constants defined, for even s, as

$$\xi_{s\ell}^{N'N''} = (-1)^{N'+N''} \begin{pmatrix} l & l & s \\ -N'' & -N' & N'+N'' \end{pmatrix} \Big/ \begin{pmatrix} l & l & s \\ 0 & 0 & 0 \end{pmatrix} \tag{2.43}$$

Equation (2.38) indicates that $L_{st}^{\alpha\beta\gamma\delta}$ with s odd do not contribute to splitting. This can be verified by using the symmetry property $L_{st}^{\alpha\beta\gamma\delta} = L_{st}^{\gamma\delta\alpha\beta}$, along with the properties of the Wigner 3-j symbols.

A comparison between (2.8) and (2.38) leads to the result:

$$c_{st} = \frac{1}{2\omega_0^2} \int_0^a \sum_{\alpha\beta\gamma\delta} L_{st}^{\alpha\beta\gamma\delta} g_s^{\alpha\beta\gamma\delta} r^2 dr \tag{2.44}$$

for the contribution of anisotropy to the splitting functions, where

$$g_s^{\alpha\beta\gamma\delta} = \varepsilon^{-\alpha-\beta} \varepsilon^{-\gamma-\delta} \xi_s^{\alpha+\beta\,\gamma+\delta} \tag{2.45}$$

It is easy to check that

$$g_s^{\alpha\beta\gamma\delta} = g_s^{-\alpha-\beta-\gamma-\delta} \tag{2.46}$$

for both spheroidal and toroidal modes, where it is assumed that s is even (see (2.38)). Therefore (2.44) may be written in the form

$$c_{st} = \frac{1}{2\omega_0^2}\int_0^a \sum_{\alpha\beta\gamma\delta}\frac{1}{2}(L_{st}^{\alpha\beta\gamma\delta} + L_{st}^{-\alpha-\beta-\gamma-\delta})g_s^{\alpha\beta\gamma\delta}r^2 dr \tag{2.47}$$

For any tensor $L^{\alpha\beta\gamma\delta}$, we may decompose it into two parts

$$L^{\alpha\beta\gamma\delta} = \Lambda^{\alpha\beta\gamma\delta} + \bar{\Lambda}^{\alpha\beta\gamma\delta} \tag{2.48}$$

such that

$$\Lambda^{\alpha\beta\gamma\delta} = \sum_{s,t}\frac{1}{2}(L_{st}^{\alpha\beta\gamma\delta} + L_{st}^{-\alpha-\beta-\gamma-\delta})\widehat{Y}_s^{Nt} \tag{2.49}$$

and

$$\bar{\Lambda}^{\alpha\beta\gamma\delta} = \sum_{s,t}\frac{1}{2}(L_{st}^{\alpha\beta\gamma\delta} - L_{st}^{-\alpha-\beta-\gamma-\delta})\widehat{Y}_s^{Nt} \tag{2.50}$$

where $N = \alpha+\beta+\gamma+\delta$. With the above decomposition of $\mathbf{L}$, (2.47) becomes

$$c_{st} = \frac{1}{2\omega_0^2}\int_0^a \sum_{\alpha\beta\gamma\delta}\Lambda_{st}^{\alpha\beta\gamma\delta}g_s^{\alpha\beta\gamma\delta}r^2 dr \tag{2.51}$$

And the tensor $\bar{\mathbf{\Lambda}}$ does not contribute to splitting. The symmetry properties of $\mathbf{\Lambda}$ can be summarized as

$$\Lambda_{st}^{\alpha\beta\gamma\delta} = \Lambda_{st}^{\beta\alpha\gamma\delta} = \Lambda_{st}^{\gamma\delta\alpha\beta} = \Lambda_{st}^{-\alpha-\beta-\gamma-\delta} \tag{2.52}$$

This implies that for each degree s and order t, $\Lambda_{st}^{\alpha\beta\gamma\delta}$ has only 13 independent components. And for $s = (0,2)$ this number is further reduced to $(5,11)$ since $\Lambda_{st}^{\alpha\beta\gamma\delta}$ are not defined for $|\alpha+\beta+\gamma+\delta| > s$ ($\widehat{Y}_s^{Nt} \equiv 0$ if $|N| > s$).

Based on the symmetries (2.52), $\delta\tilde{\mathbf{m}}_{st}$ in (2.12) may be put into the form

$$\delta\tilde{\mathbf{m}}_{st} = (q_{st}^{(1)}, q_{st}^{(2)}, \ldots, q_{st}^{(n)}) \tag{2.53}$$

where $n = 13$ for $s \geq 4$, and $n = (11,5)$ for $s = (2,0)$; and the independent parameters $\{q_{st}^{(i)}, i = 1,2,\ldots,n\}$ are defined by

$$q_{st}^{(i)} = w_i\Lambda_{st}^{\alpha_i\beta_i\gamma_i\delta_i}/C(r) \tag{2.54}$$

with w_i being weighting coefficients and $C = \kappa(r) + \frac{4}{3}\mu(r)$ being an elastic constant evaluated at the reference model. We choose the weighting coefficients w_i in such a way that the parameter set $\{q_{st}^{(i)}, i = 1,2,\ldots,n\}$ is normalized, i.e.,

$$\delta\varphi^{(S)} + \delta\varphi^{(F)} = \sum_{s,t}[\delta\varphi_{st}^{(S)}(r) + \delta\varphi_{st}^{(F)}(r)]Y_s^t(\theta,\phi) \tag{2.62}$$

where $\delta\varphi^{(S)}$ is the effect "directly" due to the specified anomaly $\delta\rho'$ and $\delta h'$, as if the fluid regions did not respond to the density loading ($\delta\rho'' = \delta h'' = 0$); and $\delta\varphi^{(F)}$ is due to the effect of $\delta\rho''$ and $\delta h''$ alone.

Poisson's equation and the associated boundary conditions for the perturbed system then take the form of

$$\nabla^2(\varphi + \delta\varphi^{(S)} + \delta\varphi^{(F)}) = 4\pi G(\rho + \delta\rho' + \delta\rho'') \tag{2.63}$$

$$[\varphi + \delta\varphi^{(S)} + \delta\varphi^{(F)}]_-^+ = 0 \qquad \text{at } r = r_d(1 + \delta h) \tag{2.64}$$

$$[\hat{\mathbf{n}} \cdot \boldsymbol{\nabla}(\varphi + \delta\varphi^{(S)} + \delta\varphi^{(F)})]_-^+ = 0 \qquad \text{at } r = r_d(1 + \delta h) \tag{2.65}$$

where $\hat{\mathbf{n}}$ denotes the unit outward normal to the boundary; the notation $[\,\cdot\,]_-^+$ denotes the jump discontinuity of the enclosed quantity across boundary, with the positive contribution arising from that side of the boundary toward which $\hat{\mathbf{n}}$ is directed; and δh represents either $\delta h'$ at Σ' or $\delta h''$ at Σ''. Note that in (2.63) $\delta\rho'$ vanishes in the fluid regions, $\delta\rho''$ vanishes in the solid regions, and both vanish in the space outside of the Earth. The boundary conditions (2.64) and (2.65) are specified at the perturbed boundaries $r = r_d(1 + \delta h)$; it is convenient to continue them to the unperturbed boundaries $r = r_d$. To the first order, these two conditions may be specified at $r = r_d$ as

$$[\varphi + gr_d\delta h + \delta\varphi^{(S)} + \delta\varphi^{(F)}]_-^+ = 0 \qquad \text{at } r = r_d \tag{2.66}$$

$$[\partial_r(\varphi + gr_d\delta h + \delta\varphi^{(S)} + \delta\varphi^{(F)})]_-^+ = 0 \qquad \text{at } r = r_d \tag{2.67}$$

where $g = d\varphi/dr$ is the gravitational acceleration and $\hat{\mathbf{r}}$ is the unit outward normal to the unperturbed boundary.

Since for the unperturbed Earth we have

$$\nabla^2\varphi = 4\pi G\rho \tag{2.68}$$

$$[\varphi]_-^+ = 0 \qquad \text{at } r = r_d \tag{2.69}$$

$$[\partial_r \varphi]^+_- = 0 \qquad \text{at } r = r_d \tag{2.70}$$

(2.63), (2.66) and (2.67) then reduce to

$$\nabla^2(\delta\varphi^{(S)} + \delta\varphi^{(F)}) = 4\pi G(\delta\rho' + \delta\rho'') \tag{2.71}$$

$$[\delta\varphi^{(S)} + \delta\varphi^{(F)}]^+_- = -[g r_d \delta h]^+_- = 0 \tag{2.72}$$

$$[\partial_r(\delta\varphi^{(S)} + \delta\varphi^{(F)})]^+_- = -[r_d \frac{d^2\varphi}{dr^2}\delta h]^+_- = -4\pi G[\rho]^+_- r_d \delta h \tag{2.73}$$

or for each spherical harmonic component

$$(\frac{d^2}{dr^2} + \frac{2}{r}\frac{d}{dr} - \frac{s(s+1)}{r^2})(\delta\varphi^{(S)}_{st} + \delta\varphi^{(F)}_{st}) = 4\pi G(\delta\rho'_{st} + \delta\rho''_{st}) \tag{2.74}$$

$$[(\delta\varphi^{(S)}_{st} + \delta\varphi^{(F)}_{st})]^+_- = 0 \tag{2.75}$$

$$[\frac{d}{dr}(\delta\varphi^{(S)}_{st} + \delta\varphi^{(F)}_{st})]^+_- = -4\pi G[\rho]^+_- r_d \delta h_{st} \tag{2.76}$$

where δh_{st} are the spherical harmonic expansion coefficients of δh.

By the definition of $\delta\varphi^{(S)}$ and $\delta\varphi^{(F)}$, the boundary-value problem (2.74)–(2.76) may be decoupled into two parts

$$(\frac{d^2}{dr^2} + \frac{2}{r}\frac{d}{dr} - \frac{s(s+1)}{r^2})\delta\varphi^{(S)}_{st} = 4\pi G\delta\rho'_{st} \tag{2.77}$$

$$[\delta\varphi^{(S)}_{st}]^+_- = 0 \qquad \text{at both } \Sigma' \text{ and } \Sigma'' \tag{2.78}$$

$$[\frac{d}{dr}\delta\varphi^{(S)}_{st}]^+_- = \begin{cases} -4\pi G[\rho]^+_- r_d \delta h'_{st} & \text{at } \Sigma' \\ 0 & \text{at } \Sigma'' \end{cases} \tag{2.79}$$

and

$$(\frac{d^2}{dr^2} + \frac{2}{r}\frac{d}{dr} - \frac{s(s+1)}{r^2})\delta\varphi^{(F)}_{st} = 4\pi G\delta\rho''_{st} \tag{2.80}$$

$$[\delta\varphi^{(F)}_{st}]^+_- = 0 \qquad \text{at both } \Sigma' \text{ and } \Sigma'' \tag{2.81}$$

$$[\frac{d}{dr}\delta\varphi^{(F)}_{st}]^+_- = \begin{cases} 0 & \text{at } \Sigma' \\ -4\pi G[\rho]^+_- r_d \delta h''_{st} & \text{at } \Sigma'' \end{cases} \tag{2.82}$$

Since $\delta\rho'_{st}$ and $\delta h'_{st}$ are given, $\delta\varphi^{(S)}_{st}$ can be readily solved from (2.77)–(2.79) together with the condition at infinity.

In order to solve the problem (2.80)–(2.82), we have to use the requirement that the fluid regions are in hydrostatic equilibrium:

$$(\rho + \delta\rho'')\nabla(\varphi + \delta\varphi^{(S)} + \delta\varphi^{(F)}) = -\nabla[p(r) + \delta p(r,\theta,\phi)] \tag{2.83}$$

where p is the hydrostatic pressure of the unperturbed reference model, and δp is the perturbations in pressure in the fluid regions. Collecting the first order terms in (2.83), we obtain

$$\delta\rho''\nabla\varphi + \rho\nabla(\delta\varphi^{(S)} + \delta\varphi^{(F)}) = -\nabla\delta p \tag{2.84}$$

or

$$[g\delta\rho'' - (\delta\varphi^{(S)} + \delta\varphi^{(F)})\frac{d\rho}{dr}]\hat{\mathbf{r}} = -\nabla[\delta p + \rho(\delta\varphi^{(S)} + \delta\varphi^{(F)})] \tag{2.85}$$

Expanding all perturbations in (2.85) in spherical harmonics and separating the radial and tangential components yield

$$\frac{d}{dr}\delta p_{00} = -g\delta\rho''_{00} - \rho\frac{d}{dr}(\delta\varphi^{(S)}_{00} + \delta\varphi^{(F)}_{00}) \tag{2.86}$$

$$\delta p_{st} = -\rho(\delta\varphi^{(S)}_{st} + \delta\varphi^{(F)}_{st}) \qquad \text{for } s \neq 0 \tag{2.87}$$

$$\delta\rho''_{st} = g^{-1}(\delta\varphi^{(S)}_{st} + \delta\varphi^{(F)}_{st})\frac{d\rho}{dr} \qquad \text{for } s \neq 0 \tag{2.88}$$

where δp_{st} are the the spherical harmonic coefficients of δp.

The relation (2.88) may be easily modified to relate the topography, $\delta h''_{st}$, to the gravitational potential $\delta\varphi^{(S)}_{st} + \delta\varphi^{(F)}_{st}$. At a fluid-fluid boundary, Σ'', where the radius is r_d, we have the relations

$$\frac{d\rho}{dr} = [\rho]^{+}_{-}\delta(r - r_d) \tag{2.89}$$

$$\delta\rho''_{st} = -[\rho]^{+}_{-}r_d\delta h''_{st}\delta(r - r_d) \tag{2.90}$$

where $\delta(r)$ is the Dirac delta function. Substituting (2.89) and (2.90) into (2.88), we obtain simply

$$r_d \delta h''_{st} = -g^{-1}(\delta\varphi^{(S)}_{st} + \delta\varphi^{(F)}_{st}) \qquad \text{at } \Sigma'', \text{ for } s \neq 0 \tag{2.91}$$

Now we turn our attention back to the problem (2.80)–(2.82), which becomes by virtue of (2.88) and (2.91)

$$[\frac{d^2}{dr^2} + \frac{2}{r}\frac{d}{dr} - (\frac{s(s+1)}{r^2} + 4\pi\varphi G g^{-1}\frac{d\rho^*}{dr})]\delta\varphi^{(F)}_{st} = 4\pi G g^{-1}\frac{d\rho^*}{dr}\delta\varphi^{(S)}_{st} \tag{2.92}$$

$$[\delta\varphi^{(F)}_{st}]^+_- = 0 \qquad \text{for all } \Sigma' \text{ and } \Sigma'' \tag{2.93}$$

$$[\frac{d\delta\varphi^{(F)}_{st}}{dr}]^+_- = 0 \qquad \text{for } \Sigma' \tag{2.94}$$

$$[\frac{d\delta\varphi^{(F)}_{st}}{dr} - 4\pi G g^{-1}\rho\delta\varphi^{(F)}_{st}]^+_- = 4\pi G g^{-1}[\rho]^+_-\delta\varphi^{(S)}_{st} \qquad \text{for } \Sigma'' \tag{2.95}$$

where ρ^* is defined as

$$\rho^* = \begin{cases} \rho & \text{in fluid regions} \\ 0 & \text{in solid regions} \end{cases} \tag{2.96}$$

Once $\delta\varphi^{(S)}_{st}$ have been determined from (2.77)–(2.79), the boundary-value problem for $\delta\varphi^{(F)}_{st}$, (2.92)–(2.95), can be readily be solved for $s \neq 0$. (Note that these equations are valid only for $s \neq 0$). Equations (2.88) and (2.91) then give the result for $\delta\rho''_{st}$ and $\delta h''_{st}$.

For the spherical component ($s = 0$) $\delta\rho''_{00}$ and $\delta h''_{00}$ are simply zero, and thus so is $\delta\varphi^{(F)}_{00}$.

Finally, we may also wish to consider the perturbations in other physical quantities in fluid regions due to the loading of the density anomaly $\delta\rho'$ and $\delta h'$. We take the perturbation in α (P velocity) in fluid regions

$$\delta\alpha'' = \sum_{s,t} \delta\alpha''(r)_{st} Y^t_s(\theta, \phi) \tag{2.97}$$

as an example, but the argument is applicable to other quantities. For the spherical component ($s = 0$), the change in α results from the perturbation in the pressure, and we need to know more about the physical properties of the fluid to determine $\delta\alpha''_{00}$.

For the purely aspherical case ($s \neq 0$), we may define a quantity $\Delta r_{st}(r)$ in the fluid regions by virtue of (2.87) and (2.88)

$$\Delta r_{st} \equiv -\delta p_{st}(\frac{dp}{dr})^{-1} = -\delta\varphi_{st}(\frac{d\varphi}{dr})^{-1} = -\delta\rho''_{st}(\frac{d\rho}{dr})^{-1} \tag{2.98}$$

where $\delta\varphi_{st} = \delta\varphi^{(S)}_{st} + \delta\varphi^{(F)}_{st}$ are the total perturbation in the gravitational potential. An implication of (2.98) is that the thermodynamic state, which is characterized by the pressure and the density, of the perturbed system at r is the same as that of the unperturbed system at $r - \Delta r_{st}$, where Δr_{st} are the spherical-harmonic coefficients of the geoid in the perturbed system. This immediately leads to

$$\delta\alpha''_{st} = -\frac{d\alpha}{dr}\Delta r_{st} \qquad \text{for } s \neq 0 \tag{2.99}$$

2.4.2 Splitting effects due to heterogeneity in fluid regions of the Earth

We have in the previous subsection developed a formulation which enables us to calculate the response, $\delta\rho''$ and $\delta\alpha''$, of the fluid regions to a given density anomaly $\delta\rho$ specified in a solid region. This response will also contribute to the splitting of normal modes.

Since the spherical perturbation can be specified in fluid regions independently, we shall assume, without loss of generality (the linearity of the problem guarantees this), that a density anomaly $\delta\rho_{st}(r)$ with $s \neq 0$ is specified in a solid region. The total splitting effect of $\delta\rho_{st}$ can be written

$$c_{st} = \int R_s(r)(\delta\rho_{st}/\rho)dr + c''_{st} \tag{2.100}$$

where the first term of the right side is the "direct" contribution of $\delta\rho_{st}$ with the differential kernel R_s being defined in (2.33), and c''_{st} represents the secondary effect due to the response of the fluid regions to this density loading $\delta\rho_{st}$. The response is completely described by the density and P-velocity redistributions ($\delta\rho''_{st}$ and $\delta\alpha''_{st}$, respectively) in the fluid regions and by the deformations ($\delta h^{d''}_{st}$) of the sea surface and other fluid-fluid interfaces (if any). Since these perturbations are obtainable by using the formulae presented in the previous subsection, the secondary splitting effect is easy to calculate:

$$c''_{st} = \int_F [A_s(r)(\delta\alpha''_{st}/\alpha) + R_s(r)(\delta\rho''_{st}/\rho)]dr + \sum_{d''} H_s^{d''}\delta h_{st}^{d''} \tag{2.101}$$

where the integration is over all the fluid regions and the summation is over all the fluid-fluid boundaries d'' (including the sea surface); kernels $A_s(r)$, $R_s(r)$, and H_s^d are given in (2.31), (2.33) and (2.28).

Equation (2.101) may be rewritten by virtue of (2.91), (2.98), and (2.99)

$$c''_{st} = \int_F [\sum_{d''} \frac{1}{r_{d''}} H_s^{d''}\delta(r - r_{d''}) - \frac{1}{\alpha}A_s(r)\frac{d\alpha}{dr} - \frac{1}{\rho}R_s(r)\frac{d\rho}{dr}]\Delta r_{st}(r)dr \tag{2.102}$$

If we regard the geoid perturbation Δr_{st} as a functional of the specified density distribution $\delta\rho_{st}(\bar{r})$

$$\Delta r_{st}(r) = \Delta r_{st}\,(r; \delta\rho_{st}(\bar{r})) \tag{2.103}$$

a Green's function may be defined[1] by

$$G_s(r, \tilde{r}) \equiv \Delta r_{st}\,(r; \delta(\bar{r} - \tilde{r})) \tag{2.104}$$

Then the geoid perturbation may be expressed by

$$\Delta r_{st}(r) = \int G_s(r, \bar{r})\delta\rho_{st}(\bar{r})d\bar{r} \tag{2.105}$$

Substituting (2.105) into (2.102), we obtain

$$c''_{st} = \int (\delta\rho_{st}/\rho)R''_s(r)dr \tag{2.106}$$

where the differential kernel R''_s is given by

$$\begin{aligned} R''_s(r) \;=\; & \rho(r)\left[\sum_{d''} \frac{H_s^{d''}}{r_{d''}} G_s(r_{d''}, r)\right. \\ & \left. - \int_F G_s(\bar{r}, r)\left(\frac{A_s(\bar{r})}{\alpha(\bar{r})}\frac{d\alpha(\bar{r})}{dr} + \frac{R_s(\bar{r})}{\rho(\bar{r})}\frac{d\rho(\bar{r})}{dr}\right)d\bar{r}\right] \end{aligned} \tag{2.107}$$

Defining

$$\bar{R}_s(r) \equiv R_s(r) + R''_s(r) \qquad s \neq 0 \tag{2.108}$$

the total splitting effect due to the purely aspherical density anomaly $\delta\rho_{st}$ specified in the solid regions can be obtained from (2.100), (2.107), and (2.108)

[1]It is easy to show that the form of this Green's function is independent of spherical harmonic order t

Table 2.2: Geoid for the ad hoc earth model

	A_2^0	A_2^1	B_2^1	A_2^2	B_2^2	A_4^0	A_4^1	B_4^1	A_4^2	B_4^2	A_4^3	B_4^3	A_4^4	B_4^4
sea surface	-32	-80	-105	82	-196	12	18	11	-9	12	-31	12	-1	32
CMB	72	68	-257	16	-111	-16	28	56	-47	-1	-90	2	-30	-88
ICB	24	22	-83	5	-36	-1	1	2	-2	0	-3	0	-1	-3

The geoid is expressed in meters as $\Delta r = \sum_s \sum_{t=0}^{s} (A_s^t \cos t\phi + B_s^t \sin t\phi) p_s^t(\theta)$ (see *Stacey* [1977]).

$$c_{st} = \int \bar{R}_s (\delta\rho_{st}/\rho) dr \tag{2.109}$$

where the integration needs to be taken only over the solid regions in which the density anomaly is specified.

The above analysis is readily modified for specified undulations of solid-solid and solid-fluid boundaries. Since (2.90) is also valid for a general boundary undulation δh_{st}, the geoid perturbation due to the undulation δh_{st}^d of the d'th boundary can be obtained from (2.105):

$$\Delta r_{st}(r) = -G_s(r_d, r)[\rho]_-^+ r_d \delta h_{st}^d \tag{2.110}$$

which enables us to calculate the total splitting effect due to the specified undulation δh_{st}^d of the d'th boundary:

$$c_{st} = H_s^d \delta h_{st}^d + c_{st}'' = \bar{H}_s^d \delta h_{st}^d \tag{2.111}$$

where

$$\begin{aligned} \bar{H}_{st}^d &= H_s^d + r_d [\rho]_-^+ \left[\int_F G_s(\bar{r}, r_d) \left(\frac{A_s(\bar{r})}{\alpha(\bar{r})} \frac{d\alpha(\bar{r})}{dr} + \frac{R_s(\bar{r})}{\rho(\bar{r})} \frac{d\rho(\bar{r})}{dr} \right) d\bar{r} \right. \\ &\quad \left. - \sum_{d''} \frac{H_s^{d''}}{r_{d''}} G_s(r_{d''}, r_d) \right] \end{aligned} \tag{2.112}$$

with H_s^d being given by (2.28).

In this model, the density anomaly is specified in the mantle and the undulation is specified at the CMB. These specified features will cause a perturbation in the gravity field. In Table 2.2 the coefficients of the spherical harmonics of the geoid are listed for the sea surface, the core-mantle boundary, and the inner-core boundary. As a result of these gravitational perturbations, the distributions of density and elastic

Table 2.3: Significance of splitting effects due to undulation of sea surface

Mode	$s=2$					$s=4$								
	$t=0$	$t=1$		$t=2$		$t=0$	$t=1$		$t=2$		$t=3$		$t=4$	
	Re	Re	Im	Re	Im	Re	Re	Im	Re	Im	Re	Im	Re	Im
${}_0S_3$	-3	-1	-281	-37	-2	-2	0	1	0	0	0	0	0	1
${}_0S_4$	1	0	2	1	-1	-1	-1	4	0	0	-1	-4	0	-1
${}_0S_5$	0	0	1	0	-1	-1	3	-4	0	1	-34	0	0	0
${}_1S_3$	-3	0	-6	1	0	1	0	1	0	0	1	-2	0	7
${}_3S_1$	1	-1	1	1	-23									
${}_0S_6$	0	0	2	0	-1	0	1	-1	0	0	5	0	0	0
${}_3S_2$	0	0	1	0	-1	0	0	1	0	0	0	0	0	0
${}_1S_4$	-1	-1	-4	7	-1	1	5	1	0	1	3	-2	0	22
${}_0S_7$	0	0	4	0	-2	0	1	-1	0	0	21	0	0	0
${}_2S_3$	0	0	2	0	0	-1	0	0	0	0	0	0	0	0
${}_1S_5$	7	-1	-8	2	-2	1	5	1	0	1	6	-1	0	15
${}_2S_4$	0	0	-6	0	0	-3	0	0	0	0	1	0	0	0
${}_2S_5$	0	0	0	0	0	0	0	0	0	0	0	0	0	0
${}_1S_6$	1	-2	-13	1	-3	2	2	2	0	1	6	-1	0	7
${}_0S_9$	2	-1	-5	2	-3	-1	-9	-3	0	-6	-2	0	0	-1
${}_1S_7$	0	-1	-239	0	-3	3	1	3	0	0	4	-1	0	-58
${}_2S_6$	0	0	0	0	0	0	0	0	0	0	0	0	0	0
${}_1S_8$	0	-1	5	0	-2	-129	1	9	0	0	1	0	0	-2
${}_4S_3$	-2	-2	-172	12	-2	2	-13	1	1	25	7	14	-1	6
${}_2S_8$	0	0	-1	0	0	-3	0	-4	0	0	0	0	0	0
${}_5S_3$	0	0	-2	-7	0	0	8	0	0	1	0	0	0	-1
${}_4S_4$	0	0	-6	2	0	0	-1	0	0	0	2	0	0	-5
${}_5S_4$	-2	-2	29	30	-2	1	-4	1	1	5	5	25	0	16
${}_5S_5$	-2	-2	25	47	-2	1	-4	1	1	3	4	36	0	161
${}_3S_8$	0	0	-1	-10	0	0	0	0	0	0	0	0	0	0
${}_6S_3$	0	0	2	32	-1	1	1	0	0	1	1	-17	0	-2
${}_5S_6$	-2	-2	47	215	-3	1	-5	1	1	3	4	51	0	43
${}_9S_3$	-3	-3	7	17	-3	2	-46	1	1	1	3	202	0	-11
${}_6S_{10}$	-1	-1	12	-9	-2	0	6	2	4	5	-7	6	0	7
${}_{11}S_4$	-3	-2	8	8	-3	1	3	1	2	6	4	8	0	14
${}_{13}S_2$	-2	-3	7	34	-4	1	4	1	3	8	6	-18	0	4
${}_{11}S_5$	-3	-2	9	5	-3	1	2	1	1	19	8	26	0	10
${}_{13}S_3$	-3	-3	6	7	-4	1	2	1	1	3	6	-11	0	5

Ratios c'_{st}/c_{st} are listed as percentages, where c_{st} are the coefficients of the synthetic splitting function calculated from the ad hoc model under the assumption that the fluid regions of the Earth are still spherically symmetric; c'_{st} are the effects due to the undulation of the sea surface which is caused by the aspherical geoid of the ad hoc model.

Table 2.4: Significance of splitting effects due to perturbations in the outer core

Mode	$s=2$					$s=4$								
	$t=0$	$t=1$		$t=2$		$t=0$	$t=1$		$t=2$		$t=3$		$t=4$	
	Re	Re	Im	Re	Im	Re	Re	Im	Re	Im	Re	Im	Re	Im
${}_0S_3$	0	0	-89	0	0	0	0	0	0	0	0	0	0	0
${}_0S_4$	0	0	1	0	0	0	0	3	0	0	0	0	5	0
${}_0S_5$	0	0	1	0	0	0	1	-5	0	0	-24	0	0	0
${}_1S_3$	0	0	0	0	0	0	0	0	0	0	0	0	0	1
${}_3S_1$	11	-5	-11	-1	45									
${}_0S_6$	0	0	1	0	0	0	0	-2	0	0	3	0	0	0
${}_3S_2$	2	-2	-9	0	3	-1	-1	-18	-1	0	-2	0	-2	-1
${}_1S_4$	0	0	0	0	0	0	0	0	0	0	0	0	0	0
${}_0S_7$	0	0	2	0	0	0	0	-1	0	0	9	0	0	0
${}_2S_3$	1	0	-10	0	1	-4	-1	12	-1	0	-3	0	-2	-2
${}_1S_5$	0	0	0	0	0	0	0	0	0	0	0	0	0	0
${}_2S_4$	0	0	13	0	0	-6	-1	2	0	0	-6	0	-2	-1
${}_2S_5$	0	0	0	0	0	0	0	0	-1	0	0	0	2	0
${}_1S_6$	0	0	-4	0	0	0	0	0	0	0	1	0	0	-1
${}_0S_9$	0	0	0	0	0	0	0	0	0	0	0	0	0	0
${}_1S_7$	0	0	-149	0	0	0	0	3	0	0	2	0	0	28
${}_2S_6$	0	0	0	0	0	0	0	0	0	0	0	0	0	0
${}_1S_8$	0	0	5	0	0	53	0	15	0	0	1	0	0	1
${}_4S_3$	-1	0	89	0	0	0	4	-1	-1	0	-4	0	9	3
${}_2S_8$	0	0	0	0	0	0	0	0	0	0	0	0	0	0
${}_5S_3$	-2	-1	18	3	0	2	-30	-3	-1	0	-6	0	-2	-9
${}_4S_4$	-4	0	50	-1	0	0	5	-5	-1	0	-19	0	-4	-38
${}_5S_4$	0	0	-8	0	0	0	0	0	0	0	-1	0	1	4
${}_5S_5$	0	0	-3	0	0	0	0	0	0	0	0	0	0	20
${}_3S_8$	1	0	3	2	0	-1	0	1	0	0	1	0	0	0
${}_6S_3$	-4	-2	-21	-21	2	3	-4	-8	-7	0	-8	7	-5	-18
${}_5S_6$	0	0	-4	-1	0	0	0	0	0	0	0	0	0	4
${}_9S_3$	-5	-1	-13	-2	1	1	31	-4	-2	0	-4	-15	9	-12
${}_6S_{10}$	0	0	-1	0	0	0	0	0	-1	0	1	0	0	1
${}_{11}S_4$	-8	-2	-25	-1	2	1	-4	-5	-9	0	-12	-1	-4	34
${}_{13}S_2$	-4	-2	-16	-5	2	0	-4	-4	-12	0	-12	2	-3	8
${}_{11}S_5$	-11	-2	-31	-1	2	1	-3	-6	-7	1	-23	-4	-2	28
${}_{13}S_3$	-6	-2	-13	-1	2	0	-2	-4	-3	0	-10	1	-1	8

Ratios c'_{st}/c_{st} are listed as percentages, where c_{st} are the coefficients of the synthetic splitting function calculated from the ad hoc model under the assumption that the fluid regions of the Earth are still spherically symmetric; c'_{st} are the effects due to the perturbations in the outer core which is caused by the aspherical gravity field of the ad hoc model.

property in the fluid regions are deformed from their original spherically symmetric state. The splitting effects due to these perturbations in the fluid regions have been calculated. The effects due to the undulation of the sea surface are listed in Table 2.3, and Table 2.4 tabulates the effects due to the perturbations in the outer core.

In order to check how significant the secondary effects (c''_{st}) are, we have performed some synthetic experiments. We construct an ad hoc earth model which contains only perturbations of spherical harmonic degree $s = 2$ and 4, using model M84A of *Woodhouse and Dziewonski* [1984] for the upper-mantle heterogeneity, model V.3 of *Morelli and Dziewonski* [1987b] for the lower-mantle heterogeneity, and model X222 of *Morelli and Dziewonski* [1987a] for the topography for the core-mantle boundary. We assume that heterogeneity in α, β, and ρ are related by

$$\delta \ln \beta = 2\delta \ln \alpha = 4\delta \ln \rho \tag{2.113}$$

where β is the S velocity, α is the P velocity, and ρ is the density.

Typically these secondary effects c''_{st} are a few percent of the total effect c_{st}. However in certain anomalous circumstances, where the contributions from the solid regions themselves are very small due to cancellation, the contribution from the fluid regions could dominate. We believe that this is an unstable phenomenon, i.e., a small variation of the ad hoc model would eliminate those anomalies (but it would lead new anomalies meanwhile).

2.5 Expansion of an Inner-Core Anisotropic Tensor Field

The seismological evidence that the inner core of the Earth is anisotropic has been reported [e.g., *Woodhouse et al.*, 1986; *Morelli et al.*, 1986; *Shearer et al.*, 1988]. In those studies the anisotropic tensor field is assumed to take some very special forms. These assumption, of course, do not necessarily represent reality. Indeed the modal data and travel-time data cannot be explained simultaneously if the anisotropy is assumed, as in studies mentioned above, to be transversely isotropic in the plane of

the equator *Woodhouse et al.*, 1986]. Therefore it is interesting and safe to approach the problem in a natural, general way: expanding the inner-core anisotropy in terms of a set of complete basis tensors. Here we derive a suitable basis of orthonormal tensor fields in the unit sphere. The fields are required to be analytic at the origin, which makes the task of constructing the basis not entirely straightforward.

In order to achieve our desired result in 2.5.2, we need first accomplish some preparatory work in 2.5.1, where we shall discuss how to expand a constant tensor field in generalized spherical harmonics. Finally in 2.5.3 we partition the basis tensors into two subspaces: those which contribute to the splitting of normal modes and those who do not.

2.5.1 Expansion in generalized spherical harmonics of a constant tensor field

Consider a constant tensor field $\mathbf{t}$ of rank n having Cartesian components $t_{i_1 i_2 \ldots i_n}$. A rotation of the co-ordinate frame leads to a new set of components $t'_{i_1 i_2 \ldots i_n}$ which are related to the original components by a certain linear transformation. Such linear transformations, for a tensor of given rank, constitute a representation of the rotation group which, in general, is reducible. Here we show that the problem of expanding a constant tensor field in terms of generalized spherical harmonics [*Phinney and Burridge*, 1973] is equivalent to that of decomposing this representation into canonical irreducible representations.

It is well known that the irreducible representations of the rotation group are of dimension $2j + 1$ where j is an integer (the requirements that physical quantities be single valued rules out the half-odd integral spin representations which occur in quantum mechanical applications). We shall refer to j as the *degree* of the representation. Let $D(\alpha, \beta, \gamma)$ represent a rotation operator corresponding to a rotation of the coordinate frame by Euler angles α, β, γ [see *Edmonds*, 1960)]. Any irreducible representation of degree j is isomorphic with the group of rotation matrices having elements

$$\mathcal{D}^{(j)}_{mm'}(\alpha,\beta,\gamma) = e^{im\gamma} d^{(j)}_{mm'}(\beta) e^{im'\alpha} \tag{2.114}$$

where the notation is that of *Edmonds* [1960]. We shall refer to this as the canonical representation of degree j. The generalized spherical harmonics of *Phinney and Burridge* [1973] are a special case of the rotation matrix elements

$$Y_j^{mm'}(\theta,\phi) = \mathcal{D}^{(j)}_{mm'}(\phi,\theta,0) = d^{(j)}_{mm'}(\theta) e^{im'\phi} \tag{2.115}$$

Let us suppose that we have determined that the representation generated by certain tensor transformations can be resolved into R irreducible representations of degrees $j_1, j_2, \ldots, j_R$ (i.e., of dimension $2j_1+1, 2j_2+1, \ldots, 2j_R+1$); i.e., let us assume that we can define quantities T_{km} ($k=1,2,\ldots,R$; $m=-j_k, -j_k+1, \cdots, j_k$) which are known linear combinations of the components of $\mathbf{t}$, which transform under rotations according to the canonical irreducible representations of the rotation group of degree j_R. If the coordinate frame is rotated by Euler angles α, β, γ the transformed values are therefore given by

$$T'_{km} = \sum_{m'} \mathcal{D}^{(j_k)}_{mm'}(\alpha,\beta,\gamma) T_{km'} \tag{2.116}$$

In order that T_{km} represent a complete decomposition into irreducible representations, the number of them must be the same as the number of independent elements, M, say, in the original tensor. i.e.,

$$\sum_{k=1}^{R} (2j_k + 1) = M \tag{2.117}$$

If $\mathbf{t}$ is taken to be a completely general tensor of given rank, n, then $M = 3^n$; however, if we restrict attention to tensors possessing certain symmetries, then M will have some smaller value. We shall refer to T_{km} as a set of *canonical components* of the tensor $\mathbf{t}$. In what follows we shall outline a general method for determining such canonical components of a given tensor.

In this study we require such a decomposition for fourth rank tensors possessing the symmetries of the elastic tensor:

$$t_{ijkl} = t_{jikl} = t_{ijlk} = t_{klij} \tag{2.118}$$

In this case it is well known that there are 21 independent elements, and it will be shown below that these transform according to a representation which reduces to 5 representations of degrees $j_1 = 4$, $j_2 = 2$, $j_3 = 2$, $j_4 = 0$, $j_5 = 0$ – a result previously obtained by *Backus* [1970]. In this case, therefore, equation (2.117) becomes

$$9 + 5 + 5 + 1 + 1 = 21 \tag{2.119}$$

A decomposition of this kind has also recently been obtained by *Mochizuki* [1988]. In addition to the case of an elastic tensor, we shall require such a decomposition for tensors of arbitrary rank, n, which are completely symmetric under permutations of their indices. The number of independent elements of such tensors is equal to the number of different combinations of n indices, each taking values 1, 2 or 3. The number of such combinations is given by the number of different ordered pairs of non-negative integers (the number of 1's and 2's for example among the indices of $t_{i_1 i_2 \ldots i_n}$) having a sum not greater than n. This gives $M = \frac{1}{2}(n+1)(n+2)$.

It will be shown that, in this case, the transformations of the elements of t lead to irreducible representations of degrees $j_1 = n$, $j_2 = n-2$, ..., $j_R = n-2(R-1)$, where R is the largest integer for which j_R is nonnegative, i.e., $R = 1+n/2$ for even n and $R = (n+1)/2$ for odd n. In this case (2.117) becomes

$$(2n+1) + (2n-3) + \cdots + (1 \text{ or } 3) = \frac{1}{2}(n+1)(n+2) \tag{2.120}$$

In a right handed co-ordinate frame (x, y, z), let ϵ_x, ϵ_y, ϵ_z be the unit vectors parallel to the co-ordinate axes. We shall regard these as constant vector fields defined everywhere in space. Let us now consider a rotation of the co-ordinate frame by an infinitesimal angle γ about the z-axis, and let ϵ'_x, ϵ'_y, ϵ'_z represent the unit vectors of the rotated frame. Then, to first order,

$$\begin{aligned} \epsilon_x &= \epsilon'_x - \gamma\epsilon'_y \\ \epsilon_y &= \epsilon'_y + \gamma\epsilon'_x \\ \epsilon_z &= \epsilon'_z \end{aligned} \tag{2.121}$$

Following the conventions of *Edmonds* [1960] we define the infinitesimal rotation

operator J_z, such that, to first order:

$$\begin{aligned}(1+i\gamma J_z)\epsilon_x &= \epsilon_x - \gamma\epsilon_y \\ (1+i\gamma J_z)\epsilon_y &= \epsilon_y + \gamma\epsilon_x \\ (1+i\gamma J_z)\epsilon_z &= \epsilon_z\end{aligned} \tag{2.122}$$

Thus

$$\begin{aligned}J_z\epsilon_x &= i\epsilon_y \\ J_z\epsilon_y &= -i\epsilon_x \\ J_z\epsilon_z &= 0\end{aligned} \tag{2.123}$$

Similarly we define operator J_x, J_y such that:

$$\begin{aligned}&J_x\epsilon_x = 0 \qquad && J_y\epsilon_x = -i\epsilon_z \\ &J_x\epsilon_y = i\epsilon_z && J_y\epsilon_y = 0 \\ &J_x\epsilon_z = -i\epsilon_y && J_y\epsilon_z = i\epsilon_x\end{aligned} \tag{2.124}$$

and operators $J_\pm = J_x \pm iJ_y$ satisfying

$$\begin{aligned}J_\pm\epsilon_x &= \pm\epsilon_z \\ J_\pm\epsilon_y &= i\epsilon_z \\ J_\pm\epsilon_z &= \mp\epsilon_x - i\epsilon_y\end{aligned} \tag{2.125}$$

The vector fields $\epsilon_x, \epsilon_y, \epsilon_z$ form a basis for the description of constant vector fields. A general procedure for finding combinations of these vectors which transform according to the canonical irreducible representations, which will later be applied to tensors of higher rank, is as follows (see *Edmonds* [1960]).

Among all constant tensor fields of some given rank n and satisfying a given set of symmetries, first identify all eigenfunctions of J_z which are annihilated by J_+. The eigenvalues of J_z are necessarily integers, j_k, say and the eigenfunctions annihilated by J_+ will also be eigenfunctions of $J^2 \equiv J_x^2 + J_y^2 + J_z^2 = J_-J_+ + J_z(J_z+1)$ belonging to eigenvalue $j_k(j_k+1)$. Successive operations of J_- yields a sequence of functions which simultaneously are eigenfunctions of J^2 belonging to the same eigenvalue and eigenfunctions of J_z belonging to eigenvalues $j_k-1, j_k-2, \ldots, -j_k$.

Using the notation commonly employed in quantum mechanics, we shall write j_k and $|j_k\ j_k\ k)$ for the k'th solution of the equations

$$J_z|j_k\ j_k\ k) = j_k|j_k\ j_k\ k) \tag{2.126}$$

$$J_+|j_k\ j_k\ k) = 0 \tag{2.127}$$

The number, R, of linearly independent solutions determines the number of irreducible representations. The simultaneous eigenfunctions of the k'th representation are then given by the recurrence

$$\begin{aligned} |j_k\ m{-}1\ k) \ &= \ [(j_k+m)(j_k-m+1)]^{-\frac{1}{2}} \times \\ &\qquad J_-|j_k\ m\ k) \qquad (m = j_k, j_k{-}1, \ldots, -j_k{+}1) \end{aligned} \tag{2.128}$$

where m is the eigenvalue of J_z. The multiplying factor on the right side of (2.128) ensures that all member of the sequence have the same norm. Since, in our case, $|j_k\ m\ k)$ will represent constant vector or tensor fields we normalize according to

$$\sum_{i_1,i_2,\ldots,i_n} t^*_{i_1 i_2 \ldots i_n} t_{i_1 i_2 \cdots i_n} = 1 \tag{2.129}$$

where $*$ denotes complex conjugation. It is readily shown that solutions of (2.126) and (2.127) having different values of j_k are orthogonal. If there is more than one solution for a given value of j_k (e.g., $j_1 = j_2$) the eigenfunctions may be orthogonalized, since any linear combinations of them also satisfy (2.126) and (2.127). It may be shown that the recurrence (2.128) preserves orthogonality and, furthermore, eigenfunctions of different m are orthogonal. Thus we have

$$(j_{k'}\ m'\ k'|j_k\ m\ k) = \delta_{kk'}\delta_{mm'} \tag{2.130}$$

where the left side represents a scalar product of tensors of the form (2.129). We shall term the set of constant tensor fields $|j_k\ m'\ k)$ $(k{=}1,2,\ldots,R; m{=}-j_k, -j_k+1,\ldots,j_k)$ a *canonical basis* for tensors of given rank and satisfying given symmetries. Such tensors may be expanded in the form

$$\mathrm{t} = \sum_{k\,m} T_{km}|j_k\ m\ k) \tag{2.131}$$

where, by virtue of orthogonality (2.130)

$$T_{km} = (j_k\ m\ k| \cdot \mathbf{t} \equiv |j_k\ m\ k)^* \cdot \mathbf{t} \tag{2.132}$$

Because of the manner of construction of the basis tensors $|j_k\ m\ k)$, T_{km} transform under rotations according to (2.116).

Let us now apply this procedure to the case of constant vector fields. It is easily seen that among linear combinations of $\boldsymbol{\epsilon}_x$, $\boldsymbol{\epsilon}_y$, $\boldsymbol{\epsilon}_z$ only the vector

$$|1\ 1\ 1) = \boldsymbol{\epsilon}_{+1} \equiv \frac{1}{\sqrt{2}}(-\boldsymbol{\epsilon}_x - i\boldsymbol{\epsilon}_y) \qquad (j_1 = 1) \tag{2.133}$$

satisfies (2.126) and (2.127), where the phase is arbitrary and the multiplying factor ensures $|\boldsymbol{\epsilon}_+|^2 = \boldsymbol{\epsilon}_+^* \cdot \boldsymbol{\epsilon}_+ = 1$ (cf. (2.129)). Employing (2.128) we find

$$\begin{aligned} |1\quad 1\quad 1) &= \quad \boldsymbol{\epsilon}_{+1} \quad \equiv \quad \tfrac{1}{\sqrt{2}}(-\boldsymbol{\epsilon}_x - i\boldsymbol{\epsilon}_y) \\ |1\quad 0\quad 1) &= \quad \boldsymbol{\epsilon}_0 \quad \equiv \quad \boldsymbol{\epsilon}_z \\ |1\quad -1\quad 1) &= \quad \boldsymbol{\epsilon}_{-1} \quad \equiv \quad \tfrac{1}{\sqrt{2}}(\boldsymbol{\epsilon}_x - i\boldsymbol{\epsilon}_y) \end{aligned} \tag{2.134}$$

Note, therefore, that

$$J_+ \boldsymbol{\epsilon}_m = \sqrt{2}\boldsymbol{\epsilon}_{m+1} \tag{2.135}$$

where $\boldsymbol{\epsilon}_m \equiv 0$ for $|m| > 1$.

Thus the canonical components of a constant vector field $\mathbf{v}$ are (cf. (2.131), (2.132))

$$V_{1m} = V^m \equiv \boldsymbol{\epsilon}^* \cdot \mathbf{v} \qquad (m = -1, 0, 1) \tag{2.136}$$

From (2.134) we find that V^m are given by

$$V^m = \sum_{i=1}^{3} C^\dagger_{mi} v_i \tag{2.137}$$

where $C^\dagger_{mi}$ are the elements of the matrix

$$\mathbf{C}^\dagger = \begin{array}{c} \begin{matrix} i=1 & i=2 & i=3 \end{matrix} \\ \begin{bmatrix} -2^{-\frac{1}{2}} & 2^{-\frac{1}{2}}i & 0 \\ 0 & 0 & 1 \\ 2^{-\frac{1}{2}} & 2^{-\frac{1}{2}}i & 0 \end{bmatrix} \end{array} \begin{matrix} (m=1) \\ (m=0) \\ (m=-1) \end{matrix} \tag{2.138}$$

we shall also refer to the quantities V^m $(m=-1,0,1)$ as the *Cartesian contravariant components* of $\mathbf{v}$.

Let us define spherical polar co-ordinates (r, θ, ϕ) through the relations

$$\begin{aligned} x &= r\sin\theta\cos\phi \\ y &= r\sin\theta\sin\phi \\ z &= r\cos\theta \end{aligned} \tag{2.139}$$

Under a rotation $\alpha=\phi$, $\beta=\theta$, $\gamma=0$ the vectors ϵ'_x, ϵ'_y, ϵ'_z of the rotated frame are parallel to the unit vectors in the co-ordinate directions: $\hat{\theta}$, $\hat{\phi}$, $\hat{\mathbf{r}}$ at the point (θ,ϕ), and thus

$$\epsilon'_m = \mathbf{e}_m(\theta,\phi) \equiv \begin{cases} \frac{1}{\sqrt{2}}(-\hat{\theta} - i\hat{\phi}) & (m=1) \\ \hat{\mathbf{r}} & (m=0) \\ \frac{1}{\sqrt{2}}(\hat{\theta} - i\hat{\phi}) & (m=-1) \end{cases} \tag{2.140}$$

These are the covariant spherical basis vectors introduced by *Phinney and Burridge* [1973]. A constant vector field $\mathbf{v}$ may be written:

$$\mathbf{v} = \sum_{m=-1}^{1} V'^m \mathbf{e}_m \tag{2.141}$$

where, from (2.116) ← before rotation

$$V'^m = \sum_{m'} \mathcal{D}^{(1)}_{mm'}(\phi,\theta,0) V^{m'} \tag{2.142}$$

It is clear from (2.141) that V'^m coincide with the *spherical contravariant components*, v^m of $\mathbf{v}$, in the sense of *Phinney and Burridge* [1973], at the point (θ,ϕ). Using (2.142) and (2.115) we have

$$v^m = v^m(\theta,\phi) = \sum_{m'=-1}^{1} Y_1^{mm'}(\theta,\phi) V^{m'} \tag{2.143}$$

This gives the expansion of $\mathbf{v}$ in generalized spherical harmonics.

In the preceding analysis we have defined Cartesian contravariant components

$$V^m = \sum_{i=1}^{3} C^{\dagger}_{mi} v_i \tag{2.144}$$

where v_i are the Cartesian components of $\mathbf{v}$, and spherical contravariant components, which are given by

$$v^m = \sum_{i=1}^{3} C^{\dagger}_{mi} \tilde{v}_i \tag{2.145}$$

where $\tilde{v}_i$ are the spherical components of $\mathbf{v}$ (v_θ, v_ϕ, v_r). These definitions may be generalized to tensors of arbitrary rank; we shall write

$$T^{m_1 m_2 \ldots m_n} = \sum_{i_1 i_2 \ldots i_n} C^{\dagger}_{m_1 i_1} C^{\dagger}_{m_2 i_2} \cdots C^{\dagger}_{m_n i_n} t_{i_1 i_2 \ldots i_n} \tag{2.146}$$

$$t^{m_1 m_2 \ldots m_n} = \sum_{i_1 i_2 \ldots i_n} C^{\dagger}_{m_1 i_1} C^{\dagger}_{m_2 i_2} \cdots C^{\dagger}_{m_n i_n} \tilde{t}_{i_1 i_2 \ldots i_n} \tag{2.147}$$

We have also shown (equation 2.143) that

$$v^m = \sum_{m'-1}^{1} Y_1^{mm'}(\theta, \phi) V^{m'} \tag{2.148}$$

and thus we find

$$t^{m_1 m_2 \ldots m_n} = \sum_{\mu's} Y_1^{m_1 \mu_1}(\theta, \phi) Y_1^{m_2 \mu_2}(\theta, \phi) \cdots Y_1^{m_n \mu_n}(\theta, \phi) T^{\mu_1 \mu_2 \ldots \mu_n} \tag{2.149}$$

The problem of expanding $t^{m_1 m_2 \ldots m_n}$ in terms of generalized spherical harmonics:

$$t^{m_1 m_2 \ldots m_n} = \sum_{j\, m} Y_j^{Nm}(\theta, \phi) t^{m_1 m_2 \ldots m_n}_{jm} \qquad (N = m_1 + m_2 + \cdots + m_n) \tag{2.150}$$

is that of expressing products of generalized spherical harmonics, such as those appearing in (2.149), as linear combinations of other generalized spherical harmonics. This may be accomplished by repeated application of the formula (*Edmonds* [1960], equation 4.3.2)

$$\begin{aligned} Y_{j_1}^{m_1 \mu_1}(\theta, \phi) Y_{j_1}^{m_2 \mu_2}(\theta, \phi) \;=\; & \sum_{j\, m\, \mu} (-1)^{m-\mu} (2j+1) \begin{pmatrix} j_1 & j_2 & j \\ m_1 & m_2 & -m \end{pmatrix} \\ & \times \begin{pmatrix} j_1 & j_2 & j \\ \mu_1 & \mu_2 & -\mu \end{pmatrix} Y_j^{m\mu}(\theta, \phi) \end{aligned} \tag{2.151}$$

However, it is very laborious to obtain concrete results in this way. It is much more straightforward to first derive the canonical components T_{km} of $\mathbf{t}$ and then to obtain the generalized harmonic expansion of $\mathbf{t}$ by an argument similar to that leading to (2.143). Here we carry out his procedure for fourth rank tensors satisfying the elastic tensor symmetries, and then for completely symmetric tensors of arbitrary rank.

First we note that the 3^n dyadic products $\epsilon_{m_1}\epsilon_{m_2}\cdots\epsilon_{m_n}$, where each m_i takes values $-1, 0, 1$, form a complete orthonormal basis for the representation of constant tensor fields of rank n. Furthermore, applying the "chain rule" we have

$$J_z\epsilon_{m_1}\epsilon_{m_2}\cdots\epsilon_{m_n} = (m_1+m_2+\cdots+m_n)\epsilon_{m_1}\epsilon_{m_2}\cdots\epsilon_{m_n} \tag{2.152}$$

Thus each element of the basis is an eigenfunction of J_z belonging to eigenvalue $N = m_1+m_2+\cdots+m_n$. It follows that in seeking to construct irreducible representations by solving (2.126) and (2.127) we need consider only linear combinations of basis tensors of uniform, nonnegative N. The result of $J_\pm$ operating upon an element of the basis is also given by the chain rule; using (2.135)

$$\begin{aligned} J_\pm\epsilon_{m_1}\epsilon_{m_2}\cdots\epsilon_{m_n} = \sqrt{2}\ \big(\ & \epsilon_{m_1\pm1}\epsilon_{m_2}\cdots\epsilon_{m_n} + \epsilon_{m_1}\epsilon_{m_2\pm1}\cdots\epsilon_{m_n} \\ & + \cdots\cdots + \epsilon_{m_1}\epsilon_{m_2}\cdots\epsilon_{m_n\pm1}\big) \end{aligned} \tag{2.153}$$

where, as previously, it is understood that ϵ_m vanishes for $|m| > 1$. It may also be noted that J_+ operating upon elements of a given N, yields combinations of elements the sum of whose indices is $N+1$. The ability to immediately rank the basis vectors according to their J_z eigenvalues makes it very simple to determine the degrees of the irreducible representations involved in a given tensor transformation. Let us suppose that there are p_N independent basis elements having $\sum_{i=1}^n m_i = N$. If the most general tensor of rank n is being considered, p_N is the number of different ordered n-tuples of the numbers $-1, 0, 1$ having the sum N [1]; however if only tensors possessing certain symmetries are considered (e.g., (2.118)) p_N will have some smaller values. It is clear that $-n \le N \le n$. The eigenfunctions $|j_k\ m\ k)$ will be linear combinations of the p_N independent basis tensors having $N = m$. In the space spanned by these basis tensors, there will be a subspace (S_{0N}, say, possibly null) annihilated by J_+ and a complementary subspace (S_{1N}, say) mapped onto the space of dimension p_{N+1} spanned by basis tensor having indices summing to $N+1$. Thus the dimension of S_{1N} is equal to p_{N+1} and therefore the dimension of S_{0N} is $p_N - p_{N+1}$ $(N \ge 0)$. Each element of an orthonormal basis of S_{0N} will solve (2.126) and (2.127) with $j_k = N$,

[1] These p_N are obtainable from the generating function $(x^{-1}+1+x)^n = \sum_N x^N p_N$

and thus will generate, through (2.128), an irreducible representation of degree N. Therefore the number of representations of degree N (≥ 0) is $p_N - p_{N+1}$ (this is valid for $N = n$ provided that we define $p_N \equiv 0$ for $|N| > n$) and the total number of representations is p_0. In order to apply this procedure to fourth rank tensors possessing the elastic tensor symmetries (2.118) we first identify, by enumerating them, the number of independent elements corresponding to each value of N, and thus determine p_N:

$N = 4$	$p_4 = 1$	T^{++++}				
$N = 3$	$p_3 = 1$	T^{+++0}				
$N = 2$	$p_2 = 3$	T^{++00},	T^{+0+0},	T^{+++-}		
$N = 1$	$p_1 = 3$	T^{+000},	T^{++-0},	T^{+-+0}		
$N = 0$	$p_0 = 5$	T^{0000},	T^{-+00},	T^{-0+0},	T^{--++},	T^{-+-+}
$N = -1$	$p_{-1} = 3$	T^{-000},	T^{--+0},	T^{-+-0}		
$N = -2$	$p_{-2} = 3$	T^{--00},	T^{-0-0},	T^{---+}		
$N = -3$	$p_{-3} = 1$	T^{---0}				
$N = -4$	$p_{-4} = 1$	T^{----}				

(2.154)

Thus there is 1 ($= p_4 - p_5$) representation of degree 4 ($j_1 = 4$), 2 ($= p_2 - p_3$) representations of degree 2 ($j_2 = 2,\ j_3 = 2$), and 2 ($= p_0 - p_1$) representations of degree 0 ($j_4 = 0,\ j_5 = 0$). Appropriate orthonormal basis tensor fields are $|N\ i)$ ($N = -4, -3, \ldots, 4;\ i = 1, 3, \ldots, p_N$) given by

$$|\ 4\ \ 1) = \epsilon_{++++}$$

$$|\ 3\ \ 1) = 4^{-\frac{1}{2}}(\epsilon_{+++0} + \epsilon_{++0+} + \epsilon_{+0++} + \epsilon_{0+++})$$

$$|\ 2\ \ 1) = 2^{-\frac{1}{2}}(\epsilon_{++00} + \epsilon_{00++})$$

$$|\ 2\ \ 2) = 4^{-\frac{1}{2}}(\epsilon_{+0+0} + \epsilon_{0++0} + \epsilon_{+00+} + \epsilon_{0+0+})$$

$$|\ 2\ \ 3) = 4^{-\frac{1}{2}}(\epsilon_{+++-} + \epsilon_{++-+} + \epsilon_{+-++} + \epsilon_{-+++})$$

$$|\ 1\ \ 1) = 4^{-\frac{1}{2}}(\epsilon_{+000} + \epsilon_{0+00} + \epsilon_{00+0} + \epsilon_{000+})$$

$$|\ 1\ \ 2) = 4^{-\frac{1}{2}}(\epsilon_{++-0} + \epsilon_{++0-} + \epsilon_{-0++} + \epsilon_{0-++})$$

$$|\ 1\ \ 3) = 8^{-\frac{1}{2}}(\epsilon_{+-+0} + \epsilon_{-++0} + \epsilon_{+-0+} + \epsilon_{-+0+} + \epsilon_{+0+-} + \epsilon_{+0-+} + \epsilon_{0++-} + \epsilon_{0+-+})$$

$$
\begin{aligned}
|\ 0\ \ 1) &= \epsilon_{0000} \\
|\ 0\ \ 2) &= 4^{-\frac{1}{2}}(\epsilon_{-+00}+\epsilon_{+-00}+\epsilon_{00-+}+\epsilon_{00+-}) \\
|\ 0\ \ 3) &= 8^{-\frac{1}{2}}(\epsilon_{-0+0}+\epsilon_{0-+0}+\epsilon_{-00+}+\epsilon_{0-0+}+\epsilon_{+0-0}+\epsilon_{+00-}+\epsilon_{0+-0}+\epsilon_{0+0-}) \\
|\ 0\ \ 4) &= 2^{-\frac{1}{2}}(\epsilon_{--++}+\epsilon_{++--}) \\
|\ 0\ \ 5) &= 4^{-\frac{1}{2}}(\epsilon_{-+-+}+\epsilon_{+--+}+\epsilon_{-++-}+\epsilon_{+-+-}) \\
|-1\ 1) &= 4^{-\frac{1}{2}}(\epsilon_{-000}+\epsilon_{0-00}+\epsilon_{00-0}+\epsilon_{000-}) \\
|-1\ 2) &= 4^{-\frac{1}{2}}(\epsilon_{--+0}+\epsilon_{--0+}+\epsilon_{+0--}+\epsilon_{0+--}) \\
|-1\ 3) &= 8^{-\frac{1}{2}}(\epsilon_{-+-0}+\epsilon_{+--0}+\epsilon_{-+0-}+\epsilon_{+-0-}+\epsilon_{-0-+}+\epsilon_{-0+-}+\epsilon_{0---}+\epsilon_{0-+-}) \\
|-2\ 1) &= 2^{-\frac{1}{2}}(\epsilon_{--00}+\epsilon_{00--}) \\
|-2\ 2) &= 4^{-\frac{1}{2}}(\epsilon_{-0-0}+\epsilon_{0--0}+\epsilon_{-00-}+\epsilon_{0-0-}) \\
|-2\ 3) &= 4^{-\frac{1}{2}}(\epsilon_{---+}+\epsilon_{--+-}+\epsilon_{-+--}+\epsilon_{+---}) \\
|-3\ 1) &= 4^{-\frac{1}{2}}(\epsilon_{---0}+\epsilon_{--0-}+\epsilon_{-0--}+\epsilon_{0---}) \\
|-4\ 1) &= \epsilon_{----}
\end{aligned}
\tag{2.155}
$$

where we have used the notation $\epsilon_{+-00} = \epsilon_{\ 1}\epsilon_{-1}\epsilon_{\ 0}\epsilon_{\ 0}$ etc. We may also write $|m\ i) = w_{mi}(\epsilon_{\mu_1\mu_2\mu_3\mu_4} + \cdots)$ where w_{mi}, μ_1, μ_2, μ_3, μ_4 are those given in Table 2.5, and where the ellipsis indicates a sum over all *different* permutations of the indices related to the first element by symmetries of the form (2.118). There are 21 ($= \sum p_N$) basis tensors in all, corresponding to the 21 independent elements of t_{ijkl}.

Solutions of (2.126) and (2.127) may now be sought in the form

$$
|j_k\ j_k\ k) = \sum_i |j_k\ i)(j_k\ i|j_k\ j_k\ k) \tag{2.156}
$$

employing the relation

$$
J_+|N\ i) = \sum_j |N{+}1\ j)(N{+}1\ j|J_+|N\ i) \tag{2.157}
$$

whence (2.127) becomes

$$
\sum_i (j_k{+}1\ j|J_+|j_k\ i)(j_k\ i|j_k\ j_k\ k) = 0 \tag{2.158}
$$

Table 2.5: Coefficients $\alpha_{km}^{\mu_1\mu_2\mu_3\mu_4}$

							matrix elements $(m\ i\|j_k\ m\ k)$				
		μ_1	μ_2	μ_3	μ_4	w_{mi}	$k=1\ \ j_k=4$	$k=2\ \ j_k=2$	$k=3\ \ j_k=2$	$k=4\ \ j_k=0$	$k=5\ \ j_k=0$
$m=4$	$i=1$	+	+	+	+	1	1				
$m=3$	$i=1$	+	+	+	0	$\sqrt{1/4}$	1				
	$i=1$	+	+	0	0	$\sqrt{1/2}$	$\sqrt{2/7}$	$-\sqrt{1/21}$	$\sqrt{2/3}$		
$m=2$	$i=2$	+	0	+	0	$\sqrt{1/4}$	$\sqrt{4/7}$	$-\sqrt{2/21}$	$-\sqrt{1/3}$		
	$i=3$	+	+	+	−	$\sqrt{1/4}$	$\sqrt{1/7}$	$\sqrt{18/21}$	0		
	$i=1$	+	0	0	0	$\sqrt{1/4}$	$\sqrt{4/7}$	$-\sqrt{9/21}$	0		
$m=1$	$i=2$	+	+	−	0	$\sqrt{1/4}$	$\sqrt{1/7}$	$\sqrt{4/21}$	$\sqrt{2/3}$		
	$i=3$	+	−	+	0	$\sqrt{1/8}$	$\sqrt{2/7}$	$\sqrt{8/21}$	$-\sqrt{1/3}$		
	$i=1$	0	0	0	0	$\sqrt{1/1}$	$\sqrt{8/35}$	$-\sqrt{36/63}$	0	$\sqrt{9/45}$	0
	$i=2$	−	+	0	0	$\sqrt{1/4}$	$\sqrt{8/35}$	$\sqrt{1/63}$	$-\sqrt{2/9}$	$-\sqrt{4/45}$	$-\sqrt{4/9}$
$m=0$	$i=3$	−	0	+	0	$\sqrt{1/8}$	$\sqrt{16/35}$	$\sqrt{2/63}$	$\sqrt{1/9}$	$-\sqrt{8/45}$	$\sqrt{2/9}$
	$i=4$	−	−	+	+	$\sqrt{1/2}$	$\sqrt{1/35}$	$\sqrt{8/63}$	$\sqrt{4/9}$	$\sqrt{8/45}$	$-\sqrt{2/9}$
	$i=5$	−	+	−	+	$\sqrt{1/4}$	$\sqrt{2/35}$	$\sqrt{16/63}$	$-\sqrt{2/9}$	$\sqrt{16/45}$	$\sqrt{1/9}$
	$i=1$	−	0	0	0	$\sqrt{1/4}$	$\sqrt{4/7}$	$-\sqrt{9/21}$	0		
$m=-1$	$i=2$	−	−	+	0	$\sqrt{1/4}$	$\sqrt{1/7}$	$\sqrt{4/21}$	$\sqrt{2/3}$		
	$i=3$	−	+	−	0	$\sqrt{1/8}$	$\sqrt{2/7}$	$\sqrt{8/21}$	$-\sqrt{1/3}$		
	$i=1$	−	−	0	0	$\sqrt{1/2}$	$\sqrt{2/7}$	$-\sqrt{1/21}$	$\sqrt{2/3}$		
$m=-2$	$i=2$	−	0	−	0	$\sqrt{1/4}$	$\sqrt{4/7}$	$-\sqrt{2/21}$	$-\sqrt{1/3}$		
	$i=3$	−	−	−	+	$\sqrt{1/4}$	$\sqrt{1/7}$	$\sqrt{18/21}$	0		
$m=-3$	$i=1$	−	−	−	0	$\sqrt{1/4}$	1				
$m=-4$	$i=1$	−	−	−	−	1	1				

Coefficients $\alpha_{km}^{\mu_1\mu_2\mu_3\mu_4}$ are given by $\alpha_{km}^{\mu_1\mu_2\mu_3\mu_4} = w_{mi}(m\ i|j_k\ m\ k)$. Combinations of indices not listed are obtained using symmetries of the form (2.118) under permutations of μ_i.

The matrix elements $(N{+}1\ j|J_+|N\ i)$ may be found by operating with J_+ on the basis tensors $|N\ i)$, using (2.153). The complete set of matrix elements relevant to this problem are found to be

$$\begin{aligned}(N{+}1\ j|J_+|N\ i) &= (-N\ i|J_+|-N{-}1\ j) = (N\ i|J_-|N{+}1\ j) \\ &= (-N{-}1\ j|J_-|-N\ i) \\ &= \begin{cases} 2\sqrt{2} & (N=3) \\ \begin{bmatrix} 2 \\ 2\sqrt{2} \\ \sqrt{2} \end{bmatrix} & (N=2) \\ \begin{bmatrix} 2 & 2\sqrt{2} & 0 \\ 2 & 0 & \sqrt{2} \\ 0 & 2 & 2 \end{bmatrix} & (N=1) \\ \begin{bmatrix} 2\sqrt{2} & 0 & 0 \\ \sqrt{2} & 0 & 2 \\ 2 & 2 & \sqrt{2} \\ 0 & 2 & 0 \\ 0 & 0 & 2 \end{bmatrix} & (N=0) \end{cases}\end{aligned} \tag{2.159}$$

where on the right side $i = 1, 2, \ldots, p_N$ is a row index and $j = 1, 2, \ldots, p_{N+1}$ is a column index.

Having found the appropriate number $(p_{j_k}{-}p_{j_k+1})$ of orthonormal solutions $(j_k\ i|j_k\ j_k\ k)$ of (2.158) and constructed $|j_k\ j_k\ k)$ using (2.156), other elements $|j_k\ m\ k)$ may be constructed using (2.128), giving tensors of the form

$$|j_k\ m\ k) = \sum_i |m\ i)(m\ i|j_k\ m\ k) \tag{2.160}$$

In practice it is somewhat simpler to calculate $(j_k\ i|j_k\ j_k\ k)$ using the fact that $|j_k\ j_k\ k)$ is orthogonal to $|j_{k'}\ j_{k'}\ k')$ for $j_{k'} \neq j_k$, which leads to the requirement

$$\sum_i (j_{k'}\ j_{k'}\ k'|j_k\ i)(j_k\ i|j_k\ j_k\ k) = 0 \qquad (j_{k'} > j_k) \tag{2.161}$$

Table 2.5 gives values of $(m\ i|j_k\ m\ k)$ calculated in this way. Note that the first column $(k = 1)$ is generated by applying (2.128) repeatedly to ϵ_{++++}. Then the two

3-vectors heading columns $k=2$, $k=3$ are chosen to be orthogonal to one another and to the corresponding 3-vector of the first column. Then the remainder of column $k=2$, $k=3$ are generated by application of (2.128). Similarly the two 5-vectors heading column $k=4$, $k=5$ are chosen to be orthogonal to each other and to the corresponding 5-vectors of all columns to the left. For each m the nonvanishing vectors form a $p_m \times p_m$ unitary matrix. It is clear that there is a degree of arbitrariness in the choice of columns 2 and 3 and columns 4 and 5. In this example it has been resolved by choosing columns 2 and 4 to represent completely symmetric tensors. Of necessity, column 1 also represents completely symmetric tensors. This decomposition into completely symmetric tensors of degrees 4,2,0 and orthogonal tensors of degrees 2,0 is the same as that obtained by *Backus* [1970]. An alternative decomposition into "compressional" and "shear" components, suggested by *Mochizuki* [1988], may be obtained by taking the following orthonormal combinations of the columns of Table 2.5:

$$\begin{aligned}
\text{compressional, degree 2}: &\quad -\sqrt{\tfrac{7}{9}} \times [k=2] + \sqrt{\tfrac{2}{9}} \times [k=3] \\
\text{shear, degree 2}: &\quad \sqrt{\tfrac{2}{9}} \times [k=2] + \sqrt{\tfrac{7}{9}} \times [k=3] \\
\text{compressional, degree 0}: &\quad \sqrt{\tfrac{4}{9}} \times [k=4] + \sqrt{\tfrac{5}{9}} \times [k=5] \\
\text{shear, degree 0}: &\quad \sqrt{\tfrac{5}{9}} \times [k=4] - \sqrt{\tfrac{4}{9}} \times [k=5]
\end{aligned}$$

The expansion in generalized spherical harmonics of fourth rank constant tensor fields satisfying (2.118) can be obtained by an argument similar to that leading to (2.143). Let $\mathbf{t}$ represent such a tensor field; $\mathbf{t}$ may be expanded in terms of the canonical basis tensors

$$\mathbf{t} = \sum_{km} T_{km} |j_k \; m \; k) \tag{2.162}$$

The basis tensors given by (2.160) may be written

$$|j_k \; m \; k) = \sum_{\mu's} \alpha_{km}^{\mu_1\mu_2\mu_3\mu_4} \epsilon_{\mu_1\mu_2\mu_3\mu_4} \tag{2.163}$$

where the coefficients $\alpha_{km}^{\mu_1\mu_2\mu_3\mu_4}$ satisfy the selection rule

$$\alpha_{km}^{\mu_1\mu_2\mu_3\mu_4} = 0 \qquad \text{if } m \neq \mu_1+\mu_2+\mu_3+\mu_4 \tag{2.164}$$

The values of these coefficients are obtainable from Table 2.5. Making use of the orthonormality of the basis tensors

$$(j_{k'}\ m'\ k'|j_k\ m\ k) = \delta_{kk'}\delta_{mm'} \tag{2.165}$$

and the relation

$$\epsilon^*_{\mu'} \cdot \epsilon_\mu = \delta_{\mu\mu'} \tag{2.166}$$

(2.163) can be used to obtain the unitarity condition

$$\sum_{\mu's} \alpha^{\mu_1\mu_2\mu_3\mu_4}_{k'm'} \alpha^{\mu_1\mu_2\mu_3\mu_4}_{km} = \delta_{kk'}\delta_{mm'} \tag{2.167}$$

From (2.162), (2.163) we find that the Cartesian contravariant components of $\mathbf{t}$ are

$$T^{\mu_1\mu_2\mu_3\mu_4} = \sum_{km} T_{km}\alpha^{\mu_1\mu_2\mu_3\mu_4}_{km} \tag{2.168}$$

and using (2.167)

$$T_{km} = \sum_{\mu's} \alpha^{\mu_1\mu_2\mu_3\mu_4}_{km} T^{\mu_1\mu_2\mu_3\mu_4} \tag{2.169}$$

As previously, we now employ the known transformation properties of T_{km} (see, (2.116)) to write the spherical contravariant components of $\mathbf{t}$ in the form (cf. (2.142) and (2.143))

$$t^{\mu_1\mu_2\mu_3\mu_4} = \sum_{k\,m\,m'} \mathcal{D}_{mm'}(\phi,\theta,0) T_{km'} \alpha^{\mu_1\mu_2\mu_3\mu_4}_{km} \tag{2.170}$$

Hence, using (2.115) and (2.164), the expansion of $\mathbf{t}$ in generalized spherical harmonics is given by

$$t^{\mu_1\mu_2\mu_3\mu_4} = \sum_{jm} t^{\mu_1\mu_2\mu_3\mu_4}_{jm} Y^{Nm}_j(\theta,\phi) \tag{2.171}$$

with

$$t^{\mu_1\mu_2\mu_3\mu_4}_{jm} = \sum_{\substack{k \\ j_k=j}} T_{km}\alpha^{\mu_1\mu_2\mu_3\mu_4}_{kN} \tag{2.172}$$

where $N = \mu_1 + \mu_2 + \mu_3 + \mu_4$. Equations (2.171), (2.172), (2.169) give the generalized spherical harmonic expansion of t.

In what follows we shall require a similar decomposition for completely symmetric constant tensors of rank, n. A basis for such tensor may be formed from dyadic products $\epsilon_{m_1}\epsilon_{m_2}\cdots\epsilon_{m_n}$, completely symmetrized over their indices. Such symmetric products are completely characterized by specifying the number of 1's, the number of 0's, and the number of -1's among the indices $m_1, m_2, \ldots, m_n$. Denoting these by $n_+ \geq 0$, $n_0 \geq 0$, $n_- \geq 0$, we have

$$n_+ + n_0 + n_- = n \tag{2.173}$$

and the corresponding basis tensor will be an eigenfunction of J_z belonging to eigenvalue

$$N = n_+ - n_- \tag{2.174}$$

The number of independent basis tensors corresponding to a given value of N is equal to the number of different triplets of non-negative integers (n_-, n_0, n_+) satisfying (2.173), (2.174); i.e., $p_N = 1 + \text{ent}\,\frac{1}{2}(n - |N|)$. As previously, the number of representations of degree $j_k = N$ is

$$p_N - p_{N+1} = \begin{cases} 1 & \text{if } n-N \text{ is even} \\ 0 & \text{if } n-N \text{ is odd} \end{cases} \tag{2.175}$$

Thus we have a total number p_0 of representations, having degrees $j_1 = n$, $j_2 = n-2, \ldots$, $j_{p_0} = 1$ or 0. Since the degrees are all different, the canonical basis $|j_k\ m\ k)$ is essentially unique. In the forthcoming application of this result it will prove to be unnecessary to know the precise form of the canonical basis tensors, although it is straightforward to find them. In order to indicate the rank of tensors which comprise these bases we shall use the notation $|j_{qn}\ m\ q\ n)$, where $j_{qn} \equiv n - 2q$.

2.5.2 Expansion of analytic tensor fields

Let $t_{i_1 i_2 i_3 i_4}$ represent the Cartesian components of a tensor field satisfying (2.118) which is analytic in the unit sphere centered at the origin. Thus is has a convergent

Taylor series in $0 \leq r < 1$:

$$t_{i_1 i_2 i_3 i_4} = t^{(0)}_{i_1 i_2 i_3 i_4} + \sum_{i_5} x_{i_5} t^{(1)}_{i_1 i_2 i_3 i_4, i_5} + \frac{1}{2} \sum_{i_5 i_6} x_{i_5} x_{i_6} t^{(2)}_{i_1 i_2 i_3 i_4, i_5 i_6} + \cdots \tag{2.176}$$

where the constant tensor fields $\mathbf{t}^{(n)}$ are the n'th derivatives of $\mathbf{t}$ at the origin. In spherical contravariant form we have

$$t^{\mu_1 \mu_2 \mu_3 \mu_4} = \sum_{n=0}^{\infty} \frac{r^n}{n!} t^{(n) \mu_1 \mu_2 \mu_3 \mu_4, 00 \ldots 0} \tag{2.177}$$

where there are n vanishing indices of $\mathbf{t}^{(n)}$. The constant tensor fields $\mathbf{t}^{(n)}$ possess the symmetries (2.118) with respect to their first four indices and are completely symmetric with respect to permutations of their last n indices. A basis for the expansion of such fields is provided by all products of the form $|j_k \; m \; k)|j_{qn} \; m' \; q \; n)$ where the first factor is a fourth rank tensor from the canonical basis appropriate for tensors having symmetries (2.118) and where the second factor is a member of the canonical basis for symmetric tensors of rank n. Thus from the analysis of the preceding subsection j_k takes the values 4,2,2,0,0 ($k = 1, 2, 3, 4, 5$) and j_{qn} takes the values $n - 2q$ ($q = 0, 1, \ldots, \text{ent}\, \frac{n}{2}$) (see above). The problem of finding a canonical basis appropriate to the symmetries of $\mathbf{t}^{(n)}$ is that of recombining these products of basis tensors into a new canonical basis. That is: we seek the decomposition of the Cartesian product of irreducible representations of degrees j_k, j_{qn} into other irreducible representations; this is equivalent to the problem of coupling of angular momentum in quantum mechanics [*Edmonds*, 1960] and the solution is well known. The product representation reduces to a set of representations of all degrees, j, satisfying the triangle inequality:

$$|j_k - j_{qn}| \leq j \leq j_k + j_{qn} \tag{2.178}$$

The canonical bases of these representations are given by

$$|j \; m \; k \; q \; n) = \sum_{m' m''} |j_k \; m' \; k)|j_{qn} \; m'' \; q \; n)(j_k \; m' \; j_{qn} \; m''|j_k \; j_{qn} \; j \; m) \tag{2.179}$$

where $(j_k\ m'\ j_{qn}\ m''|j_k\ j_{qn}\ j\ m)$ are the vector-coupling coefficients [*Edmonds*, 1960]. The tensor fields of rank $n+4$ represented by (2.179) form a canonical basis for the expansion of $\mathrm{t}^{(n)}$. A representation of specified degree, j, will be generated by coupling each representation of degree j_k with a representation of degree $j_{qn} = n-2q$ for all k and q (≥ 0) satisfying

$$|j - j_k| \leq n - 2q \leq j + j_k \tag{2.180}$$

Equation (2.179) may also be written

$$\begin{aligned} |j\ m\ k\ q\ n) \ &= \ \sum_{m'm''} |j_k\ m'\ k)|j_{qn}\ m''\ q\ n) \times \\ &(-1)^{j_k - n + m}(2j+1)^{\frac{1}{2}} \begin{pmatrix} j_k & n-2q & j \\ m' & m'' & -m \end{pmatrix} \end{aligned} \tag{2.181}$$

where the vector-coupling coefficients have been replaced by their representations in terms of Wigner symbols.

Corresponding to (2.163), let us now define coefficients $\alpha_{km'}^{\mu_1\mu_2\mu_3\mu_4}$, $\beta_{qnm''}^{\nu_1\nu_2\cdots\nu_n}$, and $\gamma_{kqnjm}^{\mu_1\mu_2\mu_3\mu_4\nu_1\nu_2\cdots\nu_n}$ through

$$|j_k\ m'\ k) = \sum_{\mu's} \alpha_{km'}^{\mu_1\mu_2\mu_3\mu_4} \epsilon_{\mu_1\mu_2\mu_3\mu_4} \tag{2.182}$$

$$|j_{qn}\ m''\ q\ n) = \sum_{\nu's} \beta_{qnm''}^{\nu_1\nu_2\cdots\nu_n} \epsilon_{\nu_1\nu_2\cdots\nu_n} \tag{2.183}$$

$$|j\ m\ k\ q\ n) = \sum_{\mu's\nu's} \gamma_{kqnjm}^{\mu_1\mu_2\mu_3\mu_4\nu_1\nu_2\cdots\nu_n} \epsilon_{\mu_1\mu_2\mu_3\mu_4\nu_1\nu_2\cdots\nu_n} \tag{2.184}$$

From (2.181) we have

$$\begin{aligned} \gamma_{kqnjm}^{\mu_1\mu_2\mu_3\mu_4\nu_1\nu_2\cdots\nu_n} \ &= \ \sum_{m'm''} \alpha_{km'}^{\mu_1\mu_2\mu_3\mu_4} \beta_{qnm''}^{\nu_1\nu_2\cdots\nu_n} \times \\ &(-1)^{j_k - n + m}(2j+1)^{\frac{1}{2}} \begin{pmatrix} j_k & n-2q & j \\ m' & m'' & -m \end{pmatrix} \end{aligned} \tag{2.185}$$

As in (2.171), we may use the coefficients γ to expand the terms of (2.177) in generalized spherical harmonics:

$$t^{(n)\mu_1\mu_2\mu_3\mu_4 00\cdots 0} = \sum_{kqjm} T_{kqjm}^{(n)} \gamma_{kqnjN}^{\mu_1\mu_2\mu_3\mu_4 00\ldots 0} Y_j^{Nm}(\theta,\phi) \tag{2.186}$$

for some coefficients $T^{(n)}_{kqjm}$, where $N = \mu_1+\mu_2+\mu_3+\mu_4$. Thus, using (2.185)

$$\begin{aligned} t^{(n)\mu_1\mu_2\mu_3\mu_4 00\ldots 0} &= \sum_{kqjm} T^{(n)}_{kqjm}\alpha^{\mu_1\mu_2\mu_3\mu_4}_{kN}\beta^{00\cdots 0}_{qn0}(-1)^{j_k-n+N}(2j+1)^{\frac{1}{2}} \times \\ &\quad \begin{pmatrix} j_k & n-2q & j \\ N & 0 & -N \end{pmatrix} Y^{Nm}_j(\theta,\phi) \\ &= \sum_{kqjm} \overline{T}^{(n)}_{kqjm}\alpha^{\mu_1\mu_2\mu_3\mu_4}_{kN}(2n-4q+1)^{\frac{1}{2}} \times \\ &\quad (-1)^N \begin{pmatrix} j & n-2q & j_k \\ -N & 0 & N \end{pmatrix} \widehat{Y}^{Nm}_j(\theta,\phi) \end{aligned} \tag{2.187}$$

where we have employed the symmetries of the Wigner symbols, and defined [1]

$$\overline{T}^{(n)}_{kqjm} = T^{(n)}_{kqjm}\beta^{00\cdots 0}_{qn0}(-1)^{j_k-n}(4\pi)^{\frac{1}{2}}(2n-4q+1)^{-\frac{1}{2}} \tag{2.188}$$

and where we have used completely normalized generalized spherical harmonics which are defined in (2.37) and satisfy

$$\int \widehat{Y}^{Nm*}_j(\theta,\phi)\widehat{Y}^{Nm'}_{j'}(\theta,\phi)\,\sin\theta\,d\theta d\phi = \delta_{jj'}\delta_{mm'} \tag{2.189}$$

In (2.189) integration is over the surface of the unit sphere. Using the unitarity condition (2.167), together with the relation

$$\sum_N \begin{pmatrix} j & n-2q & j_k \\ -N & 0 & N \end{pmatrix}\begin{pmatrix} j & n-2q' & j_k \\ -N & 0 & N \end{pmatrix} = (2n-4q+1)^{-1}\delta_{qq'} \tag{2.190}$$

(equation 3.7.8 of *Edmonds* [1960]), it may be shown that (2.187) represents a sum over tensor fields which are orthonormal on the unit sphere, i.e., representing the left side of (2.187) as the components of a fourth rank tensor $\mathbf{t}^{(n)0}$,

$$\int |\mathbf{t}^{(n)0}|^2\,\sin\theta d\theta d\phi = \sum_{kqjm} |\overline{T}^{(n)}_{kqjm}|^2 \tag{2.191}$$

We may also write (2.187) in the form

$$\mathbf{t}^{(n)0} = \sum_{kqjm} \overline{T}^{(n)}_{kqjm}\boldsymbol{\tau}^{(n-2q)}_{kjm}(\theta,\phi) \tag{2.192}$$

[1] If $\beta^{00\cdots 0}_{qn0}$ vanishes the number of independent coefficients $\overline{T}$ may differ from the number of coefficients T. It may be shown, however, that for all q, n $(0 \le 2q \le n)$ $\beta^{00\cdots 0}_{qn} \neq 0$. We omit the demonstration of this.

where tensor fields $\boldsymbol{\tau}^{(n)}_{kjm}(\theta,\phi)$ have spherical contravariant components

$$\tau^{(n)\mu_1\mu_2\mu_3\mu_4}_{kjm} = \alpha^{\mu_1\mu_2\mu_3\mu_4}_{kN}(2n+1)^{\frac{1}{2}}(-1)^N \begin{pmatrix} j_k & n & j \\ -N & 0 & N \end{pmatrix} \hat{Y}^{Nm}_j(\theta,\phi) \qquad (2.193)$$

Substituting into (2.177) we obtain the expansion

$$\begin{aligned} t^{\mu_1\mu_2\mu_3\mu_4} &= \sum_{jm}\sum_{kqn} \frac{r^n}{n!}\overline{T}^{(n)}_{kqjm}\boldsymbol{\tau}^{(n-2q)}_{kjm}(\theta,\phi) \\ &= \sum_{jm}\sum_{k}\sum_{n} \boldsymbol{\tau}^{(n)}_{kjm}(\theta,\phi)\sum_q \frac{r^{n+2q}}{(n+2q)!}\overline{T}^{(n+2q)}_{kqjm} \end{aligned} \qquad (2.194)$$

In (2.194) the summation indices are subject to the selection rules

$$q \geq 0 \qquad |j-j_k| \leq n \leq j+j_k \qquad 1 \leq k \leq 5 \qquad (2.195)$$

For different values of j,k,m,n, the orthonormality of $\boldsymbol{\tau}^{(n)}_{kjm}$ guarantees that the corresponding terms in (2.194) are orthogonal. We now seek to orthogonalize the functions r^{n+2q} $(q=0,1,2,\ldots)$ respect to radial integration; i.e., we seek polynomials R^n_q of degree q such that

$$\int_0^1 r^n R^n_q(r^2) r^n R^n_{q'}(r^2) r^2 dr = \delta_{qq'} \qquad (2.196)$$

Writing $\varrho = r^2$, we require

$$\int_0^1 \frac{1}{2}\varrho^{n+\frac{1}{2}} R^n_q(\varrho)\, R^n_{q'}(\varrho) d\varrho = \delta_{qq'} \qquad (2.197)$$

This is the defining relation of the Jacobi polynomials $G_q(n+3/2, n+3/2, \varrho)$ on the interval $\varrho \in [0,1]$ [*Abramowitz and Stegun*, 1965] subject to the appropriate normalization. G_q satisfy

$$\int_0^1 \varrho^{p-1} G_q(p,p,\varrho) G_{q'}(p,p,\varrho) d\varrho = \delta_{qq'} \frac{\Gamma^2(q+1)\Gamma^2(q+p)}{(2q+p)\Gamma^2(2q+p)} \qquad (2.198)$$

Thus we write $p = n+3/2$ and define

$$R^n_q(\varrho) = \frac{(4q+2n+3)^{\frac{1}{2}}\Gamma(2q+n+3/2)}{\Gamma(q+1)\Gamma(q+n+3/2)} G_q(n+3/2,\, n+3/2,\, \varrho) \qquad (2.199)$$

Using the relation between G_q and the Jacobi polynomials $P_q^{(u,v)}(2\varrho-1)$ [*Abramowitz and Stegun*, 1965], we may also write

$$\begin{aligned} R_q^n(r^2) &= (4q+2n+3)^{\frac{1}{2}} P_q^{(0,n+\frac{1}{2})}(2r^2-1) \\ &= \frac{(4q+2n+3)^{\frac{1}{2}}}{\Gamma(q+1)} \sum_{m=0}^{q} (-1)^{q-m} \binom{q}{m} \frac{\Gamma(n+q+m+3/2)}{\Gamma(n+m+3/2)} r^{2m} \end{aligned} \tag{2.200}$$

where $\binom{q}{m}$ is the binomial coefficient. Equation (2.194) becomes

$$t^{\mu_1\mu_2\mu_3\mu_4} = \sum_{jm} \sum_{k} \sum_{n} \sum_{q} \tau_{kjm}^{(nq)}(r,\theta,\phi)\, \tilde{T}_{kjm}^{(nq)} \tag{2.201}$$

for some coefficients $\tilde{T}_{kjm}^{(nq)}$, where $\tau_{kjm}^{(nq)}(r,\theta,\phi)$ are tensor fields having spherical contravariant components

$$\tau_{kjm}^{(nq)\mu_1\mu_2\mu_3\mu_4} = C_{knqj}^{\mu_1\mu_2\mu_3\mu_4}(r)\hat{Y}_j^{Nm}(\theta,\phi) \tag{2.202}$$

with

$$\begin{aligned} C_{knqj}^{\mu_1\mu_2\mu_3\mu_4}(r) &= \alpha_{kN}^{\mu_1\mu_2\mu_3\mu_4}(2n+1)^{\frac{1}{2}}(-1)^N \begin{pmatrix} j_k & n & j \\ -N & 0 & N \end{pmatrix} \times \\ &\quad r^n(4q+2n+3)^{\frac{1}{2}} P_q^{(0,n+\frac{1}{2})}(2r^2-1) \end{aligned} \tag{2.203}$$

and satisfying the orthonormality relation

$$\int \tau_{kjm}^{(nq)*} \cdot \tau_{k'j'm'}^{(n'q')} dv = \delta_{kk'}\delta_{jj'}\delta_{mm'}\delta_{nn'}\delta_{qq'} \tag{2.204}$$

where the volume integration is over the unit sphere and where "$\cdot$" signifies contraction over all tensor indices. In (2.202) $N \equiv \mu_1+\mu_2+\mu_3+\mu_4$.

The indices n, q, k, j, m which specify a particular tensor field $\tau_{kjm}^{(nq)}$ satisfy selection rules

$$\begin{aligned} &1 \le k \le 5 \qquad (j_k = 4,2,2,0,0) \\ &|j_k - j| \le n \le j_k + j \\ &q \ge 0 \\ &j \ge 0 \\ &-j \le m \le j \end{aligned} \tag{2.205}$$

For a given spherical harmonic component (j,m) it is of interest to determine the number of independent basis tensor fields containing a given power of r, r^ν, say, and lower powers. This is given by the number of different triplets (k,n,q) satisfying (2.205) and also satisfying

$$n + 2q = \nu \tag{2.206}$$

For low values of ν and j the allowed triplets are shown in Table 2.6. Table 2.7 gives the total numbers, $n_{j\nu}$, of such triplets for a larger range of ν and j.

In general, it may be shown that $n_{j\nu}$ satisfy the recurrence

$$n_{j\nu} = n_{j\,\nu-2} + p_{\nu-j} - p_{\nu+j+1} \tag{2.207}$$

where p_N are those given in (2.154) (p_N is defined to be zero for $|N| > 4$). Equation (2.207) may be used to generate all $n_{j\nu}$ using starting values $n_{j\,-1} = n_{j\,-2} = 0$. It may also be shown that, for sufficiently large ν, $n_{j\nu}$ reach limiting values, for odd and even ν, as follows

$$\begin{aligned}
j = 0 \qquad n_{j\nu} &= \begin{cases} 5 & j-\nu \text{ even} \quad \nu \geq 4 \\ 0 & j-\nu \text{ odd} \quad \nu \geq 1 \end{cases} \\
j = 1 \qquad n_{j\nu} &= \begin{cases} 8 & j-\nu \text{ even} \quad \nu \geq 5 \\ 3 & j-\nu \text{ odd} \quad \nu \geq 4 \end{cases} \\
j = 2 \qquad n_{j\nu} &= \begin{cases} 11 & j-\nu \text{ even} \quad \nu \geq 6 \\ 6 & j-\nu \text{ odd} \quad \nu \geq 5 \end{cases} \\
j = 3 \qquad n_{j\nu} &= \begin{cases} 12 & j-\nu \text{ even} \quad \nu \geq 7 \\ 7 & j-\nu \text{ odd} \quad \nu \geq 6 \end{cases} \\
j \geq 4 \qquad n_{j\nu} &= \begin{cases} 13 & j-\nu \text{ even} \quad \nu \geq j+4 \\ 8 & j-\nu \text{ odd} \quad \nu \geq j+3 \end{cases}
\end{aligned} \tag{2.208}$$

Thus for large j and ν ($\nu \geq j+4$), the condition of analyticity at the origin requires that the 21 degrees of freedom for each j,m be "shared" between even and odd powers of r. For small j,ν the condition of analyticity reduces the number of degree of freedom substantially with respect to these limiting values (see Table 2.7).

Table 2.6: Allowed Triplets (k, n, q) for Some ν and j

	$j=0$	$j=1$	$j=2$	$j=3$	$j=4$	$j=5$	$j=6$
$\nu=0$	4,0,0 5,0,0		2,0,0 3,0,0		1,0,0		
$\nu=1$		2,1,0 3,1,0 4,1,0 5,1,0	2,1,0 3,1,0	1,1,0 2,1,0 3,1,0	1,1,0	1,1,0	
$\nu=2$	4,0,1 5,0,1 2,2,0 3,2,0	2,2,0 3,2,0	2,0,1 3,0,1 1,2,0 2,2,0 3,2,0 4,2,0 5,2,0	1,2,0 2,2,0 3,2,0	1,0,1 1,2,0 2,2,0 3,2,0	1,2,0	1,2,0

Table 2.7: The Total Numbers, $n_{j\nu}$, of Allowed Triplets (k, n, q)

	$j=0$	$j=1$	$j=2$	$j=3$	$j=4$	$j=5$	$j=6$	$j=7$	$j=8$
$\nu=0$	2	0	2	0	1				
$\nu=1$	0	4	2	3	1	1			
$\nu=2$	4	2	7	3	4	1	1		
$\nu=3$	0	7	5	8	4	4	1	1	
$\nu=4$	5	3	10	6	9	4	4	1	1
$\nu=5$	0	8	6	11	7	9	4	4	4
$\nu=6$	5	3	11	7	12	7	9	4	4
$\nu=7$	0	8	6	12	8	12	7	9	4
$\nu=8$	5	3	11	7	13	8	12	7	9

2.5.3 Basis tensors which contribute to splitting

It has been shown in (2.201) that a general analytic elastic tensor field may be expressed in terms of the basis tensors $\boldsymbol{\tau}_{kst}^{(nq)}$. However not all of these bases can cause the splitting of normal modes. First of all, it is easy to verify that $\boldsymbol{\tau}_{kst}^{(nq)}$ with s odd give no contribution to splitting. In addition we have shown in 2.3.3 that any tensor $\bar{\mathbf{\Lambda}}$ whose components satisfy

$$\bar{\Lambda}_{st}^{\alpha\beta\gamma\delta} = -\bar{\Lambda}_{st}^{-\alpha-\beta-\gamma-\delta} \tag{2.209}$$

contributes nothing to splitting. Here we show that all basis tensors for which $n+s$ is odd satisfy (2.209) and thus do not contribute to splitting. From Table 2.5, we find that $\alpha_{kn}^{\mu_1\mu_2\mu_3\mu_4}$ in (2.203) have the symmetry property

$$\alpha_{kN}^{\mu_1\mu_2\mu_3\mu_4} = \alpha_{k-N}^{-\mu_1-\mu_2-\mu_3-\mu_4} \tag{2.210}$$

where $N \equiv \mu_1+\mu_2+\mu_3+\mu_4$. Thus from the definition (2.203), we obtain

$$C_{knqs}^{\mu_1\mu_2\mu_3\mu_4} = (-1)^{n+s} C_{knqs}^{-\mu_1-\mu_2-\mu_3-\mu_4} \tag{2.211}$$

where we have employed the fact that j_k are always even and a property of the 3-j symbols (see equation (3.6.7) of *Edmonds* [1960]), i.e.

$$\begin{pmatrix} j_1 & j_2 & j_3 \\ m_1 & m_2 & m_3 \end{pmatrix} = (-1)^{j_1+j_2+j_3} \begin{pmatrix} j_1 & j_2 & j_3 \\ -m_1 & -m_2 & -m_3 \end{pmatrix} \tag{2.212}$$

Equation (2.211) shows that the basis tensors $\boldsymbol{\tau}_{kst}^{(nq)}$ with $n+s$ odd satisfy the condition (2.209). This implies that the basis tensors $\boldsymbol{\tau}_{kst}^{(nq)}$ may be partitioned into two categories: those with both s and n even span the subspace in which any non-zero tensor has effects on the splitting of normal modes; the remaining basis tensors span the subspace in which no tensor contributes to splitting.

Since in this thesis we limit attention to low-degree (spherical harmonic degree $s \leq 4$, radial expansion up to degree $\nu = 2$) elastic tensor fields, it is only the 20 triplets at the intersections of the columns $j = 0, 2, 4$ and the rows $\nu = 0, 2$ in Table 2.6 which are needed in the inversions performed here; when the spherical perturbations are ignored the number of unknowns reduces further, from 20 to 14.

20 - 6 = 14

Chapter 3

Inverse Theory

In this thesis inverse problems are encountered in several contexts. For example, we invert for the splitting function coefficients, c_{st}, from a collection of observed seismograms, $u(t)$, by virtue of relations (2.6) and (2.8). This is a nonlinear, discrete inverse problem. Another inverse problem is defined by (2.12): retrieving the three-dimensional structure of the Earth, $\delta \mathbf{m}_{st}(r)$, δh^d_{st}, and $\delta \bar{\mathbf{m}}_{st}(r)$, from the splitting function coefficients c_{st} of many multiplets. Clearly this is a linear continuous inverse problem. Using a finite collection of data, one is limited to solutions of finite resolution which are smoothed or filtered versions of reality, namely one can only invert for a discrete set of parameters which approximate the continuous functions $\delta \mathbf{m}_{st}(r)$ and $\delta \bar{\mathbf{m}}_{st}(r)$.

Without loss of generality, the inverse problems arising in this thesis may be stated as follows: we seek a discrete set of parameters, represented by model vector $\mathbf{x}$, satisfying

$$\begin{cases} \mathbf{d} = \mathbf{f}(\mathbf{x}) + \mathbf{e} \\ \mathbf{B}\mathbf{x} = \mathbf{g} \end{cases} \tag{3.1}$$

where the first equation is the basic equation and the second one imposes an additional constraint, which could be trivial. In (3.1) vector $\mathbf{d}$ is a collection of data of dimension N, the function $\mathbf{f}$ could be either linear or nonlinear, the vector $\mathbf{x}$ has finite dimension M, vector $\mathbf{e}$ represents stochastic errors associated with $\mathbf{d}$, matrix

$\mathbf{B}$ has dimension of $N' \times M$ with $0 \leq N' < M$, and $\mathbf{g}$ is a known vector of dimension N'. For $N' = 0$, the constraint $\mathbf{Bx} = \mathbf{g}$ is trivial.

3.1 Stochastic Solution of the Inverse Problem

One general way to solve the inverse problem (3.1) is to employ a stochastic formulation [*Jackson*, 1979; *Tarantola and Valette*, 1982; *Gubbins and Bloxham*, 1985]. We assume in what follows that the errors $\mathbf{e}$ are independent samples from a normal distribution having zero mean and variance σ_e^2. The data covariance matrix $\mathbf{C}_e$ therefore is the diagonal matrix having all diagonal entries equal to σ_e^2. We also assume that when the constraint $\mathbf{Bx} = \mathbf{g}$ is ignored the model parameters $\mathbf{x}$ are Gaussian variables and have a priori mean value $\mathbf{x}_0$ with a certain convariance matrix $\mathbf{C}_x$. Under these assumptions, the posteriori probability distribution of model vector $\mathbf{x}$ is given by

$$\begin{aligned} P(\mathbf{x}) \propto \exp\{-\tfrac{1}{2}(\mathbf{f}(\mathbf{x}) - \mathbf{d})^T \mathbf{C}_e^{-1}(\mathbf{f}(\mathbf{x}) - \mathbf{d})\} \times \\ \exp\{-\tfrac{1}{2}(\mathbf{x} - \mathbf{x}_0)^T \mathbf{C}_x^{-1}(\mathbf{x} - \mathbf{x}_0)\} \end{aligned} \tag{3.2}$$

This relation indicates that the maximum likelihood solution to $\mathbf{d} = \mathbf{f}(\mathbf{x}) + \mathbf{e}$ is obtainable by minimizing the objective function

$$\Phi(\mathbf{x}) = (\mathbf{f}(\mathbf{x}) - \mathbf{d})^T \mathbf{C}_e^{-1}(\mathbf{f}(\mathbf{x}) - \mathbf{d}) + (\mathbf{x} - \mathbf{x}_0)^T \mathbf{C}_x^{-1}(\mathbf{x} - \mathbf{x}_0) \tag{3.3}$$

The minimum of $\Phi(\mathbf{x})$ subject to the constraint $\mathbf{Bx} = \mathbf{g}$ is found by the iterative application of the recursion

$$\begin{aligned} \begin{bmatrix} \mathbf{x}_{i+1} \\ \boldsymbol{\lambda} \end{bmatrix} = \begin{bmatrix} \mathbf{x}_i \\ \mathbf{0} \end{bmatrix} + \begin{bmatrix} \mathbf{A}_i^T \mathbf{C}_e^{-1} \mathbf{A}_i + \mathbf{C}_x^{-1} & \mathbf{B}^T \\ \mathbf{B} & \mathbf{0} \end{bmatrix}^{-1} \times \\ \begin{bmatrix} \mathbf{A}_i^T \mathbf{C}_e^{-1}(\mathbf{d} - \mathbf{f}(\mathbf{x}_i)) - \mathbf{C}_x^{-1}(\mathbf{x}_i - \mathbf{x}_0) \\ \mathbf{g} - \mathbf{B}\mathbf{x}_i \end{bmatrix} \end{aligned} \tag{3.4}$$

where $\boldsymbol{\lambda}$ is a vector Lagrange multiplier of dimension N', and $\mathbf{A}_i$ is the $N \times M$ matrix of partial derivatives

$$\mathbf{A}_i = \left[\frac{\partial \mathbf{f}(\mathbf{x})}{\partial \mathbf{x}}\right]_{\mathbf{x}=\mathbf{x}_i} \tag{3.5}$$

In this study the a priori model $\mathbf{x}_0$ is always taken to be zero. Namely we are always seeking the solutions which are small perturbations from a known spherical reference model. Correspondingly the model covariance matrix $\mathbf{C}_x$ quantifies the strength of our desire for smallness of the model $\mathbf{x}$. And matrix $\mathbf{C}_x$ can always be diagonalized provided $\mathbf{x}$ is chosen to be associated with orthogonal bases. Thus (3.4) becomes

$$\begin{bmatrix} \mathbf{x}_{i+1} \\ \boldsymbol{\lambda} \end{bmatrix} = \begin{bmatrix} \mathbf{x}_i \\ \mathbf{0} \end{bmatrix} + \begin{bmatrix} \mathbf{A}_i^T \mathbf{C}_e^{-1} \mathbf{A}_i + \varsigma \mathbf{C}_x^{-1} & \mathbf{B}^T \\ \mathbf{B} & \mathbf{0} \end{bmatrix}^{-1} \times \begin{bmatrix} \mathbf{A}_i^T \mathbf{C}_e^{-1} (\mathbf{d} - \mathbf{f}(\mathbf{x}_i)) - \varsigma \mathbf{C}_x^{-1} \mathbf{x}_i \\ \mathbf{g} - \mathbf{B}\mathbf{x}_i \end{bmatrix} \tag{3.6}$$

where ς is the parameter which quantifies the overall strength of the desire for the smallness of the model, and $\mathbf{C}_x$ is now diagonalized and has diagonal entries equal to σ_i^2 $(i = 1, 2, \ldots, M)$; σ_i specify the relative strength of each model parameter x_i.

For the linear case, $\mathbf{f}(\mathbf{x}) = \mathbf{A}\mathbf{x}$, if we assume that the strength of the desire for smallness of the different components, x_i, are the same (i.e., set $\sigma_i = 1$ for all i's) and if the constraint $\mathbf{B}\mathbf{x} = \mathbf{g}$ is removed (i.e., set $N' = 0$), (3.6) may be simplified by setting $\mathbf{x}_i = \mathbf{0}$

$$\mathbf{x} = \mathbf{x}_{i+1} = [\mathbf{A}^T \mathbf{A} + \varsigma \mathbf{I}]^{-1} \mathbf{A}^T \mathbf{d} \tag{3.7}$$

which is the well-known damped least-squares solution with ς being the damping parameter.

3.2 Error and Resolution Estimates

Since the concept of resolution does not easily extend to nonlinear problems, we analyze resolution only for the linearized problem in the neighborhood of the model, $\mathbf{x}_\infty$, to which (3.6) converges.

Let us suppose that we have obtained a solution $\mathbf{x}_i$ in the neighborhood of $\mathbf{x}_\infty$. We may introduce a variation of the model, $\delta\mathbf{x}$, which would cause the variations of data $\mathbf{d}$ and $\mathbf{g}$ by $\delta\mathbf{d} = \mathbf{A}\delta\mathbf{x}$ and $\delta\mathbf{g} = \mathbf{B}\delta\mathbf{x}$ with $\mathbf{A} \equiv \mathbf{A}_\infty$. Thus the variation of our solution $\mathbf{x}_{i+1}$ is, according to (3.6), given by

$$\delta \mathbf{x}_{i+1} = (\mathbf{G}^{(1)}\mathbf{A}^T\mathbf{C}_e^{-1}\mathbf{A} + \mathbf{G}^{(2)}\mathbf{B})\delta\mathbf{x} \tag{3.8}$$

where the $M \times M$ matrix $\mathbf{G}^{(1)}$ and the $M \times N'$ matrix $\mathbf{G}^{(2)}$ are submatrices defined through

$$\begin{bmatrix} \mathbf{G}^{(1)} & \mathbf{G}^{(2)} \\ \mathbf{G}^{(3)} & \mathbf{G}^{(4)} \end{bmatrix} = \begin{bmatrix} \mathbf{A}_i^T\mathbf{C}_e^{-1}\mathbf{A}_i + \varsigma\mathbf{C}_x^{-1} & \mathbf{B}^T \\ \mathbf{B} & \mathbf{0} \end{bmatrix}^{-1} \tag{3.9}$$

where $\mathbf{G}^{(3)}$ and $\mathbf{G}^{(4)}$ are, of necessity, $N' \times M$ and $N' \times N'$ matrices, respectively. The resolution matrix $\mathbf{R}$ of our inversion may, therefore, be defined by virtue of (3.8):

$$\mathbf{R} \equiv \mathbf{G}^{(1)}\mathbf{A}^T\mathbf{C}_e^{-1}\mathbf{A} + \mathbf{G}^{(2)}\mathbf{B} \tag{3.10}$$

The resolution parameter $R = \mathrm{tr}\,\mathbf{R} - N'$ represents the effective number of degrees of freedom of the solution [*Gubbins and Bloxham*, 1985].

Similarly the linearized analysis yields the covariance matrix of the model sampling distribution which, according to (3.6), is given by

$$\mathbf{C} \equiv \langle \left[\frac{\partial \mathbf{x}_{i+1}}{\partial \mathbf{d}}\mathbf{e}\right] \cdot \left[\frac{\partial \mathbf{x}_{i+1}}{\partial \mathbf{d}}\mathbf{e}\right]^T \rangle = \mathbf{G}^{(1)}\mathbf{A}^T\mathbf{C}_e^{-1}\mathbf{A}\mathbf{G}^{(1)} \tag{3.11}$$

where $\langle\ \rangle$ denotes the expectation of the enclosed quantity, and we have used the fact that $\langle \mathbf{e} \cdot \mathbf{e}^T \rangle = \mathbf{C_e}$ and that $\mathbf{G}^{(1)}$ is a symmetric matrix.

In order to evaluate the matrix $\mathbf{C}$, the diagonal entries σ_e^2 of the data covariance matix $\mathbf{C}_e$ may be estimated a posteriori from the formula

$$\sigma_e^2 = \frac{(\mathbf{d} - \mathbf{f}(\mathbf{x}))^T(\mathbf{d} - \mathbf{f}(\mathbf{x}))}{N - R} \tag{3.12}$$

Taking $\mathbf{C}$ as the covariance matrix of the solution

$$\mathbf{C} = \langle \delta\mathbf{x} \cdot \delta\mathbf{x}^T \rangle = \mathbf{S}_x^2 \tag{3.13}$$

individual model parameters x_i will have standard errors:

$$\delta x_i = [S_x^2]_{ii}^{\frac{1}{2}} \tag{3.14}$$

If linear functions of the model parameters are computed, $\mathbf{z} = \mathbf{F}^T\mathbf{x}$, say, where $\mathbf{F}$ is any matrix of M rows, then the covariance matrix of $\mathbf{z}$, which we denote $\mathbf{S}_z^2$, is given by

$$\mathbf{S}_z^2 = \mathbf{F}^T \mathbf{S}_x^2 \mathbf{F} \tag{3.15}$$

In the nonlinear case $\mathbf{z} = \mathbf{z}(\mathbf{x})$ the covariance matrix S_z^2 may be approximated by using a linear approximation to $\mathbf{z}$ in the neighborhood of $\mathbf{x}$, again yielding

$$\mathbf{S}_z^2 = \mathbf{F}^T \mathbf{S}_x^2 \mathbf{F} \tag{3.16}$$

where the elements of $\mathbf{F}$ are

$$F_{ij} = F_{ij}(\mathbf{x}) = \frac{\partial z_j}{\partial x_i} \tag{3.17}$$

Note that the posteriori model covariance matrix $\mathbf{C}$ and the resolution matrix $\mathbf{R}$, and thus the error and resolution estimates, are calculated for the given a priori information ς and σ_i. The dependence of the results on such information, especially on ς, can be very strong for underdetermined inverse problems. In such a case, the error and resolution estimates become very conditional. The lack of a priori information, corresponding to imposing small ς, can lead to a large uncertainty in the solution. On the other hand, imposing strong a priori constraints (i.e., choosing ς too large) will result in unrealistically small error estimates. In an extreme case where the parameter ς is set to infinity, the solution $\mathbf{x}$ vanishes and so do the estimated errors, no matter what the data $\mathbf{d}$ is. In this case the resulting model is independent of the reality which it describes, i.e., the resolution is zero.

Chapter 4

Data Selection and Processing

In this study we consider only spheroidal modes, and our analysis is limited to modes which display little or no coupling with other modes and which can be readily identified in individual spectra. The choice of uncoupled modes implies that their splitting properties are sensitive only to the even-degree part of the Earth's lateral structure.

We retain a mode for further analysis if a window in the frequency domain can be taken such that the multiplet is the only one of significant amplitude in the window. Very long period modes are, of course, primary candidates because of their separation in the frequency domain. It is also possible to retrieve high-quality data for shorter period, high-Q overtones, either by using data from deep earthquakes, by which such modes are preferentially excited, or by discarding the first portion of the time series, so that other unwanted, low-Q modes have largely died away.

Even by combining these techniques the number of modes that can be effectively isolated is small, and we consider also frequency windows containing overlapping multiplets. The singlets of such modes interfere to produce a single pattern in the frequency domain, and thus the inverse problem for the splitting functions has to be posed simultaneously. At this stage we limit consideration to frequency windows with no more than two overlapping modes, making it easier to test for the presence of coupling and for the correct identification of the singlets.

We have also sought to choose multiplets having differential kernels which sample

the Earth in a variety of different ways. Thus we have examined all the modes with periods between 200 and 2000 s, in an effort to obtain multiplets lying on modal branches sensitive to different regions of the Earth's interior. In addition, we have included all identifiable multiplets having high sensitivity to core structure, since many of these are anomalously split and those which are not are equally valuable in attempting to identify the phenomenon responsible for anomalous splitting.

In all, we present here results for 34 spheroidal modes. They are arranged by frequency in Table 4.1, which also gives their frequencies, Q values, and the ellipticity (A) and Coriolis (B) splitting coefficients computed for the PREM model. The coefficients A and B are defined as

$$A = [\bar{\alpha}\varepsilon_h + \alpha'\Omega^2/\omega^2]/2\pi \tag{4.1}$$

$$B = \bar{\beta}\Omega/2\pi \tag{4.2}$$

where $\bar{\alpha}$, α', and $\bar{\beta}$ are the splitting parameters used throughout this thesis (see (2.8) and (2.13)) The modes span the frequency interval between 0.5 and 5 mHz, and illustrate the predominance of rotational splitting (high B) at low frequencies and ellipticity splitting (high A) at higher frequencies.

4.1 Data Selection

The analysis of long-period free oscillations requires the use of very long recordings produced by large events ($M_0 > 5 \times 10^{19}$Nm) and recorded by instruments with high sensitivity. The degree to which the goal of obtaining dense geographical coverage by stations and sources can be realized is limited by the fact that digital recordings are available only for events since 1976, and for a relatively small number of stations; also, events of the required magnitude happen, on average, only once a year.

The most abundant digital data for long-period analyses are the vertical accelerograms recorded by the International Deployment of Accelerometers (IDA) network [*Agnew et al.*, 1986], which allow the detection of free oscillations at frequencies below 1 mHz for earthquakes with $M_0 \sim 10^{21}$Nm. We have also examined digital

Table 4.1: List of the Multiplets Included in This Study

Mode	f, μHz	Q	A, μHz	B, μHz	Mode	f, μHz	Q	A, μHz	B, μHz
${}_0S_3^*$	468.564	417	0.106	2.168	${}_1S_8^*$	1799.314	379	0.960	0.771
${}_0S_4^*$	647.082	373	0.204	1.189	${}_4S_3^*$	2048.963	480	1.343	0.848
${}_0S_5^*$	840.439	356	0.320	0.710	${}_2S_8^*$	2049.206	198	1.421	0.790
${}_1S_3^*$	939.829	283	0.759	2.480	${}_5S_3^*$	2169.655	292	1.296	0.779
${}_3S_1^*$	943.944	820	0.256	1.602	${}_4S_4^*$	2279.598	290	1.434	0.538
${}_0S_6^*$	1038.233	347	0.446	0.425	${}_5S_4^*$	2379.519	489	1.531	0.671
${}_3S_2$	1106.213	367	0.682	1.620	${}_5S_5^*$	2703.354	502	1.734	0.654
${}_1S_4^*$	1172.854	271	0.924	2.287	${}_3S_8^*$	2819.644	264	1.794	0.040
${}_0S_7^*$	1231.812	342	0.585	0.227	${}_6S_3$	2821.724	426	1.528	-0.137
${}_2S_3$	1242.187	415	0.789	0.830	${}_5S_6^*$	3010.690	506	1.937	0.625
${}_1S_5^*$	1370.274	292	1.006	1.968	${}_9S_3$	3554.979	778	2.218	0.190
${}_2S_4^*$	1379.194	380	0.873	0.392	${}_{10}S_2$	4032.362	192	1.897	0.788
${}_2S_5^*$	1514.927	302	0.979	0.245	${}_6S_{10}^*$	4210.763	354	2.697	0.412
${}_1S_6^*$	1522.041	346	0.993	1.336	${}_{11}S_4$	4766.867	702	2.787	0.055
${}_0S_9^*$	1578.298	333	0.891	-0.016	${}_{13}S_2$	4845.261	879	3.188	0.145
${}_1S_7^*$	1655.516	372	0.974	0.939	${}_{11}S_5$	5074.411	665	2.958	0.019
${}_2S_6^*$	1680.839	238	1.147	0.566	${}_{13}S_3$	5193.822	909	3.156	0.128

Frequency (f), Q, ellipticity (A) and rotation (B) splitting parameters are computed for the reference model PREM. A and B are defined in (4.1) and (4.2). Modes sensitive principally to structure in the mantle are indicated by an asterisk.

data recorded by the Global Digital Seismograph Network (GDSN; *Peterson et al.* [1976]). While the currently implemented instrumental responses of these networks are not comparable to that of IDA at the longest periods, they record horizontal as well as vertical components and have the potential therefore for providing uniquely valuable information for toroidal modes. The results presented here have been obtained using only IDA data.

We use recordings collected for 10 large earthquakes that occurred from 1977 through 1985, covering all the major seismic zones, and including the events of August 19, 1977, in Sumbawa (Indonesia, $M_0 = 3.6 \times 10^{21}$Nm), June 22, 1977, in the Tonga Islands ($M_0 = 1.4 \times 10^{21}$Nm), and March 3, 1985, in Valparaiso (Chile, $M_0 = 1.0 \times 10^{21}$Nm). Very few large, deep earthquakes have been recorded since 1977; the largest was the Banda Sea event of June 22, 1982 ($M_0 = 1.8 \times 10^{20}$Nm). Table 4.2 lists the events with their locations and seismic moments. The source mechanisms of these events are shown in Figure 4.1. We have not used data for the September 19, 1985 Michoacan (Mexico) event or for any other event followed by aftershocks of moment comparable to that of the main event. Although the modal excitation of multiple sources can be easily dealt with in principle, it introduces further uncertainty in the phase equalization, and we have therefore omitted such events at this stage of the research.

In the generation of synthetic seismograms we make use of the moment tensor solutions computed with the centroid-moment tensor (CMT) method [*Dziewonski et al.*, 1981; *Dziewonski and Woodhouse*, 1983]. Seismic moments are listed in Table 4.2. A point source is assumed in computing modal excitation, and we use the CMT centroid time to account for the temporal extension of the source process of these large events. The CMT solution characterizes the source mechanism at periods between 40 and 200 s, much shorter than the periods of many of the modes under study, and comparable with the duration of the larger of the events; this is a potential source of uncertainty, and the adequacy of the CMT solutions at much longer periods requires verification. By analyzing very long period IDA data, *Riedesel* [1985] found a very close correspondence between CMT solutions and very

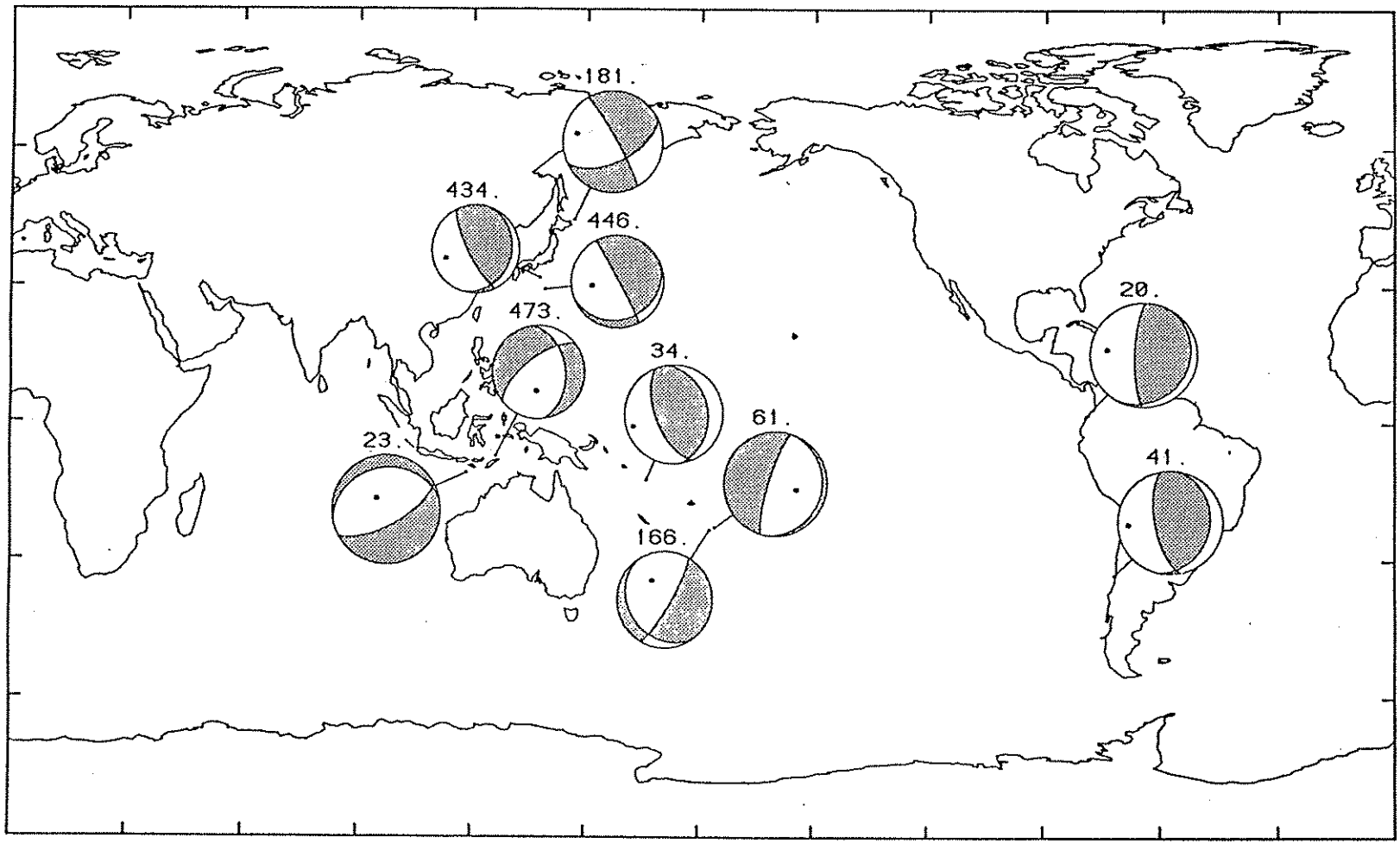

Fig. 4.1. The source mechanisms of the earthquakes used in this thesis. The depth, in kilometers, of each event is indicated. (Courtesy of Göran Ekström for the plotting program)

Table 4.2: Date and Location of Earthquakes

Date	Region	Latitude	Longitude	Depth, km	M_0, Nm	Correction
Jun 22, 1977	Tonga Is.	-22.9	-175.9	65	1.39×10^{21}	1.089
Aug 19, 1977	Sumbawa Is.	-11.1	118.5	30	3.59×10^{21}	1.009
Mar 7, 1978	South Honshu	32.0	137.6	434	5.38×10^{19}	1.003
Dec 6, 1978	Kuriles Is.	44.6	146.6	181	6.40×10^{20}	0.774
Dec 12, 1979	Ecuador	1.6	-79.4	20	1.69×10^{21}	1.265
Apr 13, 1980	Tonga Is.	-23.5	-177.3	166	2.84×10^{20}	1.017
Jul 17, 1980	Santa Cruz Is.	-12.5	165.9	34	4.84×10^{20}	1.314
Jun 22, 1982	Banda Sea	-7.3	126.0	473	1.77×10^{20}	0.906
Mar 6, 1984	South Honshu	29.4	138.9	446	1.44×10^{20}	0.907
Mar 3, 1985	Central Chile	-33.2	-72.0	41	1.03×10^{21}	0.947

The seismic moment (M_0) is that obtained using the CMT method. The multiplicative scalar correction to the seismic moment is retrieved in an earlier stage of this study based upon the data of 27 modes [*Giardini et al.*, 1988].

long period moment tensors, and we have obtained similar results by inverting our data for source parameters rather than for modal perturbations. Nonetheless, this remains a potential source of error in the computation of very long period synthetic seismograms. In *Giardini et al.* [1988], we have made an effort to invert for the corrections to the scalar moments by using most of our modal data (27 modes). It has been found that the resulting corrections prove stable and are generally almost negligible ($\sim 10\%$, smaller than the noise level). In this thesis we shall simply adopt these reported corrections, which are also listed in Table 4.2.

In general, we retain only modes for which at least 20 or more station-source pairs can be used. It will be shown later that this quantity of data is sufficient to provide passable resolution for the splitting functions.

4.2 Editing and Filtering of Seismic Traces

Our technique is based on fitting spectral peaks in the frequency domain, obtained from filtered long-period vertical recordings. For each event we view up to 6 days

of data following the earthquake, and an equal period of time before the event. The trace is band-passed to eliminate the tide signal and then purged of the presence of glitches, aftershocks, and other small events and also of clipped segments in the period immediately following the origin time of the event. The recording is discarded if more than a significant percentage of the signal is found to be unusable ($> 10\%$).

Windowing in the time domain is used to obtain higher resolution in the frequency domain. After experimenting with various windows, we elected to use a Hann window, a good compromise between visual separation of the singlets and signal-to-noise ratio degradation in the frequency domain [*Dahlen*, 1982].

Rather than selecting a fixed duration for each recording, we obtain for each mode, by trial and error, the optimal length that preserves a good signal-to-noise ratio (up to a maximum 144 hours); this sometimes exceeds, but more often is shorter than the characteristic "Q cycle" [*Dahlen*, 1982] because of the high noise content of some traces. For some high-Q, low-amplitude overtones it proved useful and sometimes necessary to discard the first portion of the time recording (up to 24 hours) in order to allow the desired signal to emerge from that of a more rapidly decaying fundamental mode. Each trace is padded with zeros up to 192 hours duration, transformed using a fast Fourier transform algorithm and divided by the instrument response to give the spectrum of ground acceleration.

To avoid any possible phase contamination introduced by the procedure, we construct the synthetic seismograms and the partial derivatives in the time domain, and we apply to them identical filtering, padding, transform, and phase equalization as we do to the data.

The inverse theory employed in this study requires that the errors associated with the data are independent samples from a normal normal distribution (see Section 3.1). However the padding and windowing described above introduce nonindependence of pointwise spectral estimates. The nonindependence caused be padding is approximately accounted for by incorporating into summations (N as used in (3.12)) over data elements a factor representing the proportion of data values which are independent; this is taken to be the ratio of the true time series length to its

padded length. This correction does not account for the effect of windowing, which requires a significantly more elaborate treatment and has been investigated only for much simpler inverse problems. Results for an ideal case (J. Park, personal communication, 1987) indicate that the effective number of independent data is likely to be further reduced by a factor approaching 2. It is likely therefore that the error estimates given in this thesis should be increased by a factor of the order of 1.5.

These corrections are also important in applying F-tests to the results of the inversion; the number of independent data is taken to be the true number of data multiplied by the same factors. The number of independent complex spectral points corresponding to each spectral segment used in inversion is, by this procedure, of the order of 4 to 10.

Figure 4.2 shows examples of spectral windows containing the multiplets ${}_{13}S_2$, ${}_3S_2$, ${}_5S_6$ and the overlapping pair ${}_0S_7$-${}_2S_3$. Each frame represents the amplitude and phase spectra in a narrow frequency band, containing only one or two modes. Data are represented by continuous lines; synthetic spectra, indicated by dashed lines, are computed for the PREM model, including the splitting due to rotation and ellipticity. Vertical dotted lines delineate the portion of the signal used in the inversion. Only traces with high signal to noise ratio are displayed in Figure 4.2, in order to clearly show the large discrepancies between data and synthetic spectra due to aspherical structure.

The amplitude and phase content of the spectrum are separated only for visual clarity; all computations are performed in terms of complex spectral values. The variance ratios shown in Figure 4.2, and throughout this thesis, refer to the complex spectrum and represent ratios of squared misfit to squared data. The frequencies and relative amplitudes of the singlets contributing to the theoretical trace are displayed as vertical bars in the bottom panel of each frame; in the case of multiple modes, the singlet amplitudes are independently normalized to the maximum amplitude for each mode.

For mode ${}_{13}S_2$ the data clearly show anomalous splitting behavior; singlets corresponding to $m = 0$ in Figure 4.2*a* and $m = \pm 2$ in Figure 4.2*b* are shifted toward

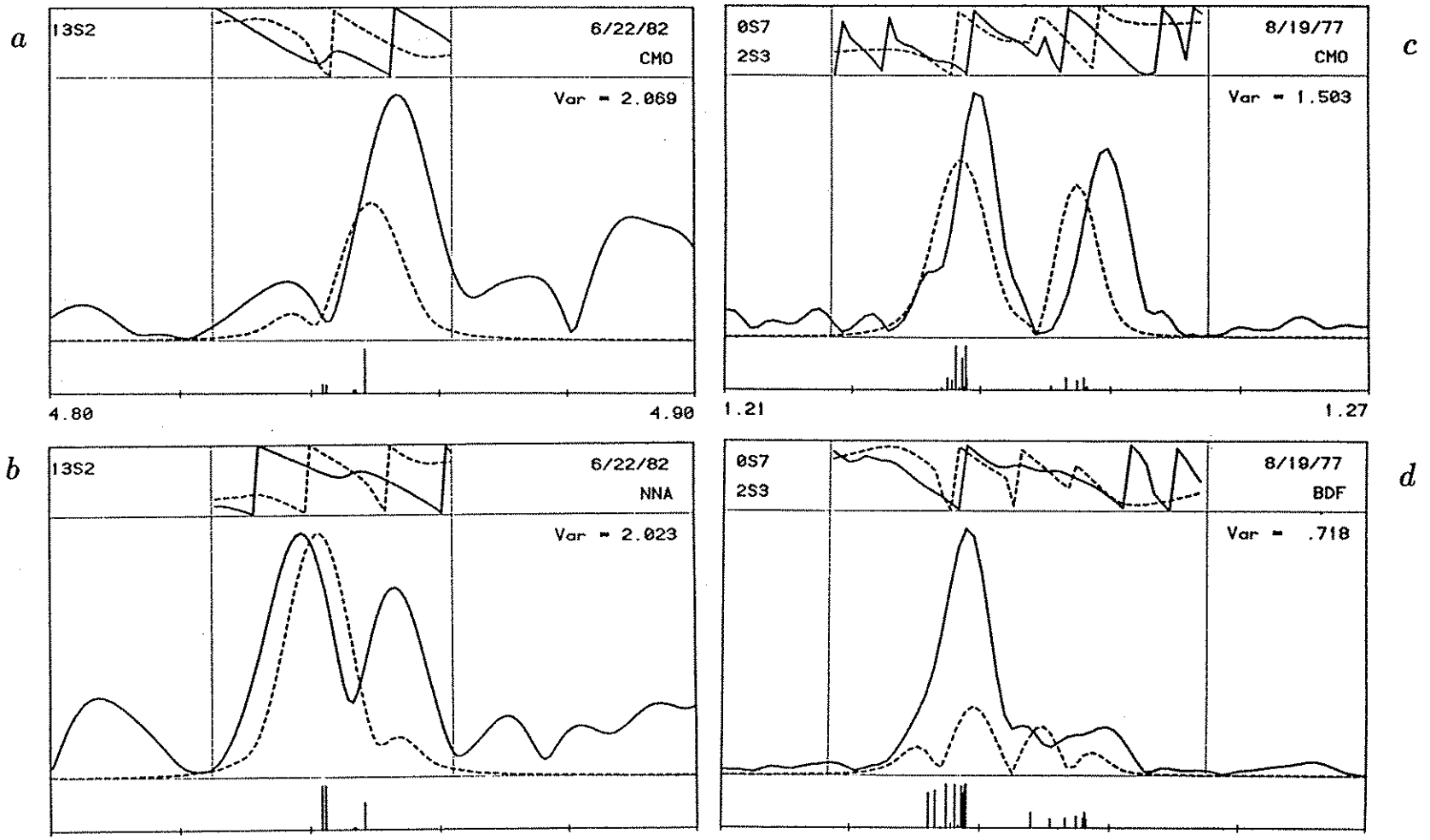

Fig. 4.2. Examples of data (solid lines) and synthetic spectra (dashed lines) in spectral windows containing one or two modes. For each window are indicated the name(s) of the multiplet(s), the range of the horizontal frequency axis (in millihertz), the earthquake date, and the recording station. The complex spectra are represented in terms of phase in the interval $(-\pi, \pi)$ (top panel of each figure), and amplitude on an arbitrary scale (middle panel). Vertical bars in the bottom panels indicate the frequencies and relative amplitudes of the singlets contributing to the theoretical spectra,

the central frequency of the mode, and the phase differs from that of the synthetics by up to half a cycle. Modes ${}_0S_7$ and ${}_2S_3$ are closely spaced, and even by using 140 hours of data, it is impossible to resolve the different singlets; the synthetics, however, are not able to reproduce the central location of the peaks in Figure 4.2*c* or match the amplitude observed in Figure 4.2*d*. For mode ${}_5S_6$, again the amplitude is very poorly reproduced in Figure 4.2*e* and a peak is completely absent in Figure 4.2*f*, whereas for mode ${}_3S_2$ the synthetics predict only one peak, and two are observed in the data in Figure 4.2*g*.

The phase agreement is very poor in all cases, which is reflected in the high variance ratios indicated for each trace, averaging well above unity. The misfit between data and predictions is attributed to the aspherical structure of the Earth, and this constitutes the information used in the inversion for the splitting functions. The data set used in this study consists of approximately 1000 spectral segments of the kind shown in Figure 4.2.

4.3 Noise

In the inverse theory presented in Chapter 3, it is assumed that the errors of all data points have the same variance σ_e^2. In order to approximate this condition, we need to weight the data of each trace by its noise level.

The noise content of the recordings varies widely among different modes, events and stations. For each mode we need to compute a reliable estimate of the noise content of each trace, in order to weight the data in the inversion procedure. Because of the presence of other modes close to the frequency window of interest, it is often impossible to evaluate directly the noise level of the trace in the frequency domain, and we use, instead, data derived from a time series recorded at the same station before the event. We select a trace of the same length as the one used as data for a specific mode, and we apply the same procedure to it as we do to the data. The noise level is then estimated by calculating average spectral power of the noise trace in the inversion window. This noise estimate is used in the inversion procedure as a weight factor for each data point in the trace.

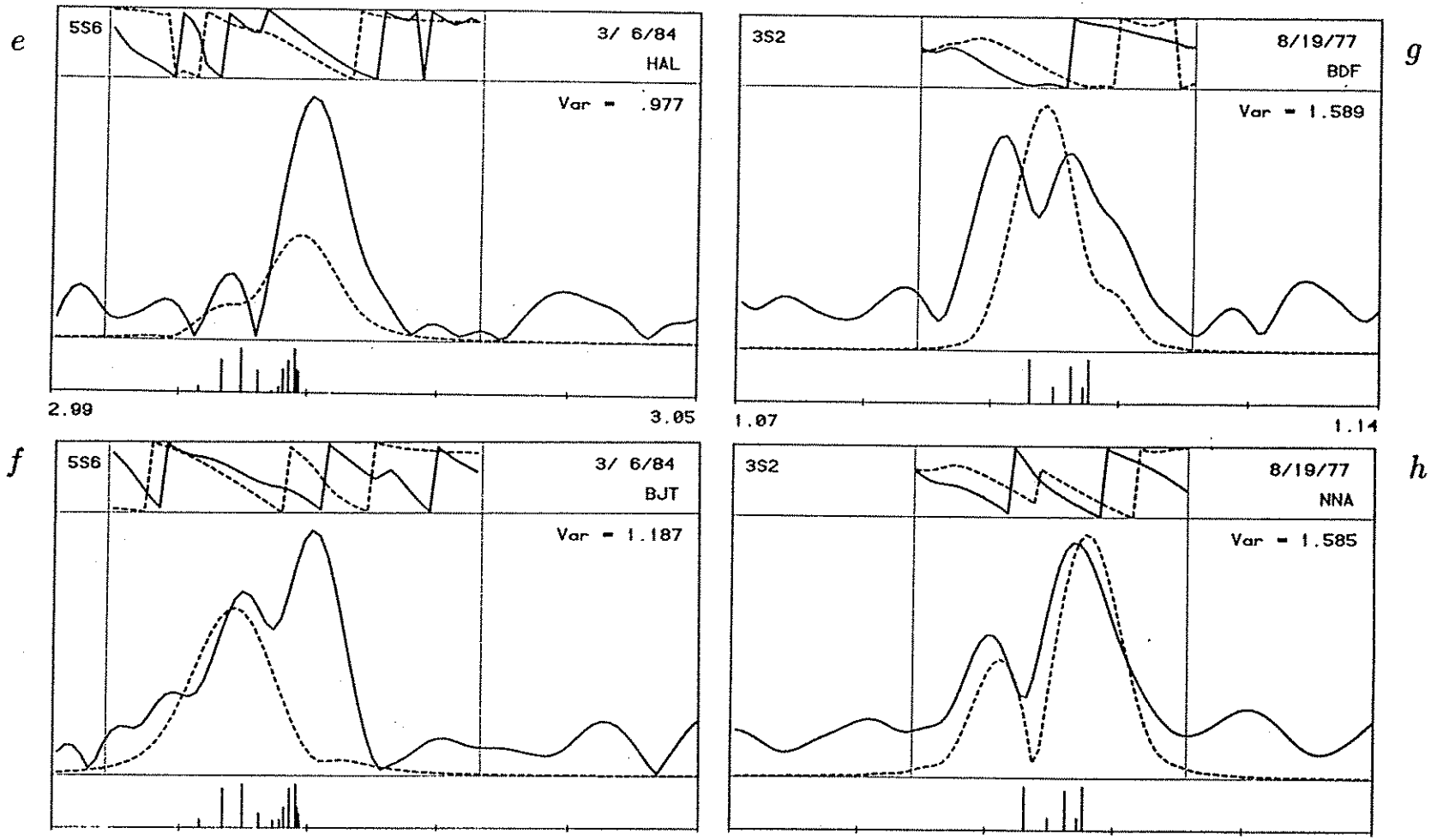

Fig. 4.2. (continued) computed for the reference model PREM, incorporating the effects of rotation and ellipticity. Vertical dotted lines delineate the portion of the signal used in the inversion. The variance ratio is a measure of the misfit between the observed and synthetic traces, computed in terms of the complex spectra. The durations and starting times (relative to event origin time) of each record are, respectively (*a*) 48, 6, (*b*) 48, 6, (*c*) 140, 5.6, (*d*) 140, 14.8, (*e*) 80, 1.4, (*f*) 80, 1.6, (*g*) 80, 15, and (*h*) 60, 7, all in hours.

Chapter 5

Inversion for the Splitting Functions

5.1 Modeling Considerations

The inversion for the lateral structure of the Earth is strictly a continuous inverse problem; as such, a complete solution is impossible. Using a finite collection of data, one is limited to solutions of finite resolution which are smoothed or filtered versions of reality. The modal splitting function, on the other hand, is represented by a finite spherical harmonic expansion, and thus the corresponding inverse problem is strictly discrete. For an isolated multiplet of angular order l there are $(l+1)(2l+1)$ complex parameters which completely characterize the splitting properties of the multiplet, its singlet eigenfrequencies and eigenfunctions. In this study, however, we limit our investigation to the low-degree, real portion of the splitting function and to the spherically symmetric imaginary part, the latter corresponding to a spherically symmetric correction to the attenuation of the multiplet.

We elect to ignore the higher-degree terms rather than solve a very underconstrained nonlinear problem. This is a matter of practicality, since as will be shown below, insufficient data are available to derive the higher-degree components of the splitting functions. This would, of course, be an unjustifiable and misleading procedure if modal splitting were caused largely by higher-degree terms; there are reasons

to believe, however, that degrees 0, 2, 4 play a major rôle. First, modes of angular order $l = 2$, which are sensitive only to these degrees, show substantial splitting anomalies and are among the modes which display the phenomenon of anomalous splitting. Second, inversion for the splitting functions of modes of angular order greater than 2 yields similar patterns (see below), and moreover, the inclusion of higher degrees in the splitting functions of these multiplets leads to only minor additional reductions in variance. Third, models of the lower mantle constructed from travel times and from waveforms [*Dziewonski*, 1984; *Morelli and Dziewonski*, 1985, 1987b; *Woodhouse and Dziewonski*, 1986] have large terms of degrees 2 and, to a lesser extent, 4.

A result of the inversion procedure is error estimates associated with the solution. These are, of course, dependent upon the parameter ς which is assigned to the "prior information". In a linear problem the analysis of resolution and error jointly should quantify the true uncertainty, assuming that the underlying statistical assumptions hold; in this nonlinear problem we attempt to further address the problem of uncertainty by performing a number of experiments devised to test the stability of the solutions with respect to the amount and quality of data, different a priori model statistics, and varying criteria used in weighting the data. We also attempt to assess the potential for aliasing from higher-degree terms, and test for instabilities between the real and complex portions of the splitting function, linearity in response to different levels of minimization, and smoothness of the iterative convergence. Because we cannot know in any objective way the spectral power distribution characterizing the Earth's heterogeneous structure, we have explored the sensitivity of our solutions to the a priori requirements of harmonic expansions with power equally distributed or decaying with increasing harmonic degree.

Experiments were also performed in which the weights assigned to the data segments to achieve uniform variance were estimated iteratively in terms of misfit between data and synthetic spectra, rather than from the spectral power in a trace preceding the earthquake. We performed inversions using only part of the data or only some of the available seismic sources, and we applied different noise thresholds

to the data. Modes that failed to show the desired stability in these tests were eliminated from the present experiment. The results of these tests are only in part presented here.

In the final solutions a weight is assigned to each of the data according to their absolute noise level. The parameter ς is chosen on the basis of an F-test of statistical significance. The convergence of the nonlinear procedure is usually very stable. Step-length damping was introduced in the iterative procedure to smooth convergence and avoid overshoot. In the more extreme nonlinear cases, in fact, we find that unless precautions of this kind are taken, the splitting function may diverge in such a manner that one or more singlet eigenfrequencies escape from the narrow frequency band used in the inversion.

The real and imaginary parts of c_{00} are of special interest, since they correspond to corrections in the eigenfrequency and attenuation of the mode in the spherically averaged Earth. Since we expect that these parameters should be among those best constrained by the data, we specify infinite prior variances (i.e., no prior information) for c_{00}. This has the desirable consequence of making these estimates essentially independent of the spherically symmetric reference model; the resulting values correspond to measurements of degenerate eigenfrequency and Q which are, as far as is possible, uncorrupted by lateral heterogeneity. The prior variances of other elements of the model are taken to be equal in the final solutions.

5.2 Results

Table 5.1 lists the relevant parameters of the final inversion. The initial variance refers to the synthetic spectra incorporating only rotation and ellipticity in the reference model (cf. Figure 4.2). The variance reductions are very substantial in most cases, both for the "anomalously" split modes such as ${}_{11}S_4$, ${}_{13}S_2$, and ${}_{13}S_3$, as well as for longer-period modes such as ${}_3S_2$, ${}_0S_7$, ${}_2S_3$, ${}_1S_7$, and ${}_1S_8$. Also listed in Table 5.1, for each mode, are the number of traces and the resolution parameter R, expressed as fraction of the total number of parameters used for each mode or mode pair.

The splitting functions for all the modes and their standard errors are tabulated in Table 5.2.

One test on the validity of the splitting functions, and thus of the earth models we will derive from them, is the degree to which they remove the large discrepancies and misfit observed in the data (Figure 4.2). Table 5.1 gives the variance reductions obtained using the tabulated splitting functions; Figure 5.1 illustrates how these variance reductions correspond to a substantially improved match between data and synthetic spectra. We display in Figure 5.1 the same spectra as those in Figure 4.2, with the synthetics computed using the splitting functions of Table 5.2.

In cases of good signal-to-noise ratio the observed and synthetic phase spectra now agree to within a few degrees and the locations and amplitudes of the peaks are also well matched. The singlet locations for the anomalously split modes ${}_{13}S_2$ and ${}_3S_2$ are well predicted in Figures 5.1*a*–5.1*b* and 5.1*g*–5.1*h*, and the amplitude and shapes of modes ${}_0S_7$ and ${}_2S_3$ are well reproduced in Figures 5.1*c*–5.1*d*. We note again that this is not due to a change in the source excitation and is only weakly dependent on the perturbed attenuation value. The most important source of improvement in the fit is the location and phase of the interacting singlets, which affects the shape and phase of the multiplets.

To illustrate the properties of the splitting functions, we concentrate here on four modes, chosen to represent characteristic mode types: ${}_3S_2$, ${}_0S_7$, ${}_5S_6$, and ${}_{13}S_2$. For these we map the splitting function and the associated error, and plot the resolution matrix; we also illustrate the dependence of the solution size (rms) on damping level (ς) and parameterization.

5.2.1 Splitting functions

The value of the splitting function at the geographic point (θ, ϕ) may be written

$$\eta(\theta, \phi) = \mathbf{c} \cdot \mathbf{y}(\theta, \phi) \tag{5.1}$$

where $\mathbf{c}$ is the vector of c_{st} coefficients and $\mathbf{y}(\theta, \phi)$ contains the spherical harmonic values at (θ, ϕ) (cf. the definition of splitting function in (2.15)). As in the case of

Table 5.1: Variance Ratios (Squared Misfit/Squared Data)

Mode	Var	Var_0	R	#
${}_0S_3$	0.169	0.206	4.3/16	22
${}_0S_4$	0.324	0.669	11.0/16	36
${}_0S_5$	0.211	0.754	12.3/16	42
${}_1S_3 - {}_3S_1$	0.299	0.436	9.1/23	37
${}_0S_6$	0.143	0.624	15.4/16	37
${}_3S_2$	0.324	1.467	11.4/16	25
${}_1S_4$	0.325	0.400	6.6/16	35
${}_0S_7 - {}_2S_3$	0.134	0.689	29.3/32	59
${}_1S_5 - {}_2S_4$	0.341	0.659	24.5/32	47
${}_2S_5 - {}_1S_6$	0.728	0.876	14.2/32	35
${}_0S_9$	0.211	0.915	15.2/16	59
${}_1S_7$	0.280	0.880	12.2/16	38
${}_2S_6$	0.449	0.787	12.3/16	34
${}_1S_8$	0.307	0.936	12.6/16	36
${}_4S_3 - {}_2S_8$	0.450	0.862	25.3/32	67
${}_5S_3$	0.376	0.554	7.0/16	11
${}_4S_4$	0.542	0.771	7.1/16	23
${}_5S_4$	0.402	0.687	13.3/16	47
${}_5S_5$	0.350	0.708	13.2/16	60
${}_3S_8 - {}_6S_3$	0.354	0.944	23.4/32	39
${}_5S_6$	0.255	0.900	12.6/16	30
${}_9S_3$	0.436	0.526	6.7/16	15
${}_{10}S_2$	0.386		14.7/16	34
${}_6S_{10}$	0.567	0.803	11.3/16	44
${}_{11}S_4$	0.403	1.406	14.9/16	22
${}_{13}S_2$	0.303	1.790	13.5/16	20
${}_{11}S_5$	0.554	1.140	15.2/16	24
${}_{13}S_3$	0.371	1.069	9.5/16	21

The variance ratios obtained using the derived splitting functions of Table 5.2 are given in the column headed by Var. Those obtained including only the effects of ellipticity and rotation for model PREM are listed in the column headed by Var_0. The resolution estimator (R) is the trace of the resolution matrix and is given as a ratio to the number of (real) unknowns in the inversion. The number of records (#) used for each spectral window is indicated.

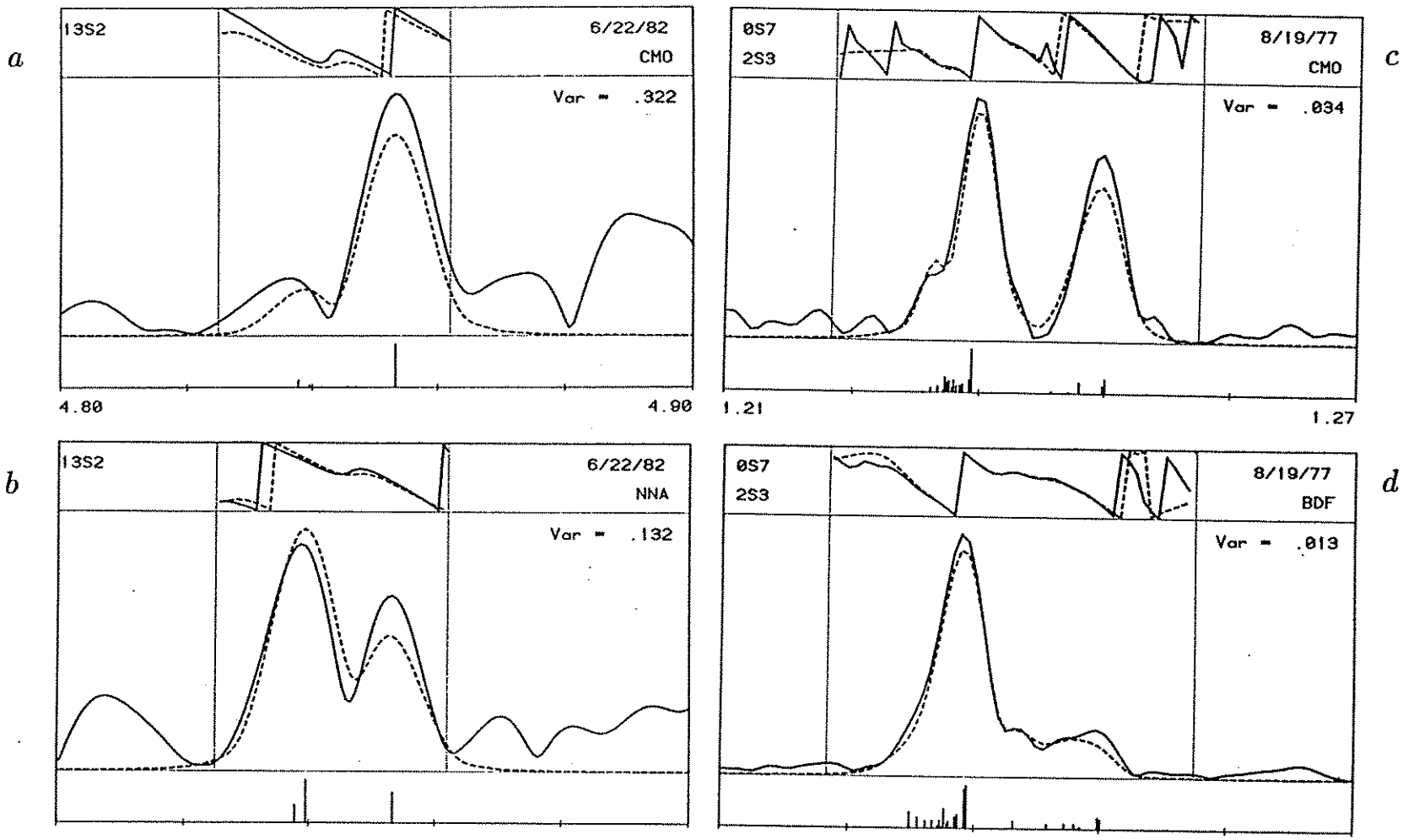

Fig. 5.1. Data (solid lines) and synthetic spectra (dashed lines), as in Figure 4.2, but with the synthetic spectra obtained using the splitting functions

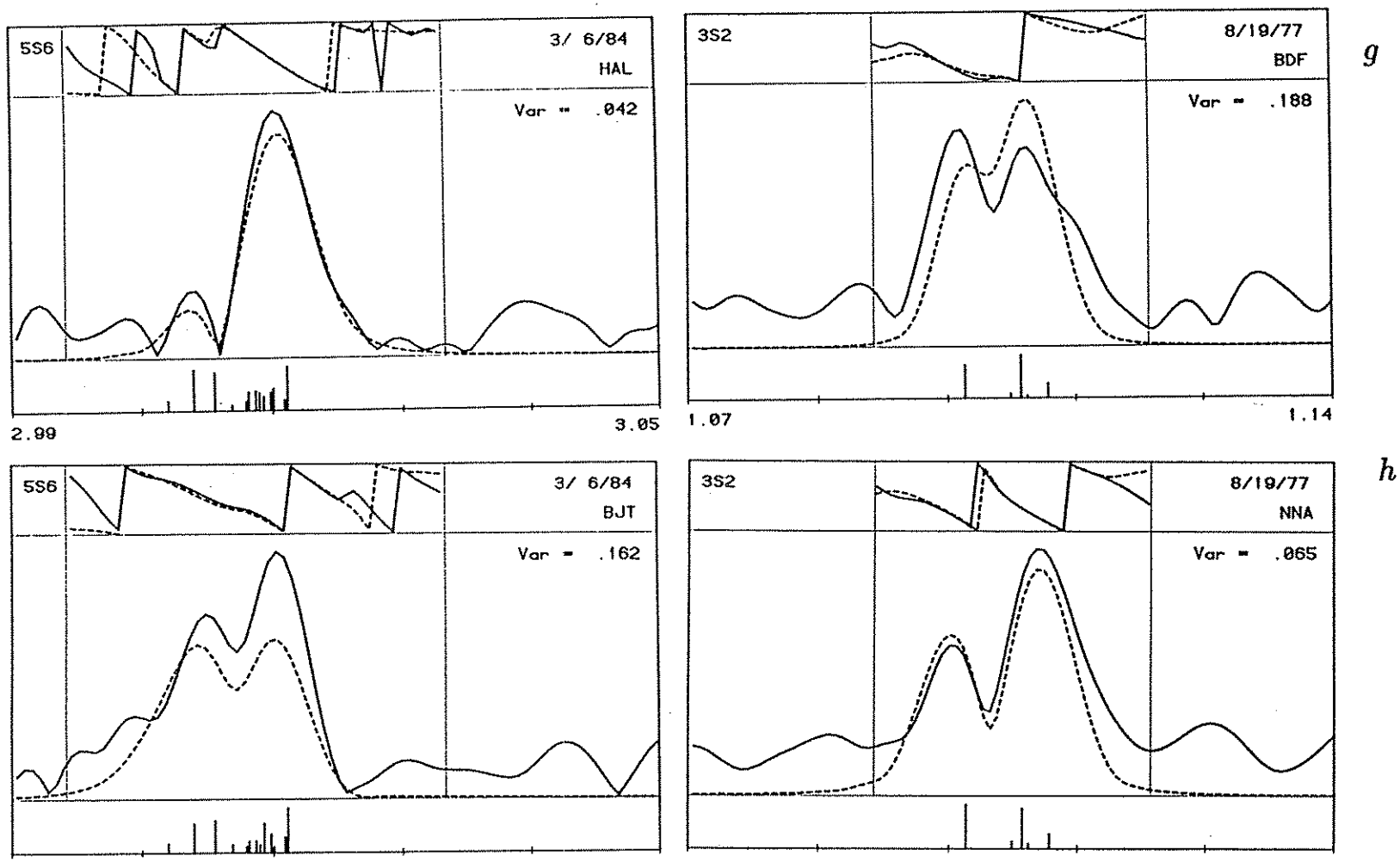

Fig. 5.1. (continued) of Table 5.2. See caption to Figure 4.2

Table 5.2: Splitting Functions and Their Error and Resolution Estimators

Mode	A_0^0	A_2^0	A_2^1	B_2^1	A_2^2	B_2^2	A_4^0	A_4^1	B_4^1	A_4^2	B_4^2	A_4^3	B_4^3	A_4^4	B_4^4	$\mathrm{Im}(A_0^0)$
	-213	226	-10	-66	18	11	13	4	-7	-7	-9	0	1	0	2	-60
${}_0S_3$	36	40	25	28	16	16	8	6	6	3	4	1	1	1	1	35
	1.00	0.49	0.11	0.15	0.04	0.04	0.04	0.03	0.03	0.01	0.01	0.00	0.00	0.00	0.00	1.00
	-479	727	-148	102	-321	-616	-101	-16	-1	85	32	-75	-43	-13	-68	-110
${}_0S_4$	27	41	48	52	63	67	39	45	43	44	43	37	41	29	27	24
	1.00	0.89	0.85	0.81	0.67	0.56	0.73	0.60	0.53	0.39	0.43	0.20	0.32	0.12	0.10	1.00
	-530	727	-289	170	-584	-760	-51	20	-61	14	-28	-74	45	92	153	-72
${}_0S_5$	21	28	23	30	38	37	26	27	29	33	32	34	32	34	32	19
	1.00	0.87	0.92	0.85	0.67	0.75	0.81	0.81	0.72	0.61	0.68	0.56	0.67	0.40	0.37	1.00
	99	14	-17	18	-1	-16	6	-7	-7	-2	0	0	0	-2	0	-248
${}_1S_3$	43	12	11	10	4	4	4	3	3	1	1	1	1	0	1	43
	1.00	0.15	0.10	0.10	0.02	0.02	0.04	0.02	0.02	0.01	0.01	0.00	0.00	0.00	0.00	1.00
	413	69	0	-12	27	-244										12
${}_3S_1$	24	35	35	33	38	38										21
	1.00	0.67	0.68	0.71	0.51	0.56										1.00
	-682	578	-190	5	-816	-932	34	-57	95	225	-214	-209	85	227	56	-78
${}_0S_6$	20	38	26	37	47	38	33	32	38	38	32	35	42	43	48	11
	1.00	0.95	0.98	0.95	0.92	0.95	0.94	0.95	0.91	0.91	0.94	0.93	0.90	0.89	0.86	1.00
	-875	1455	-31	975	169	456	-1064	399	510	-190	-100	182	-128	161	-185	139
${}_3S_2$	49	78	88	84	88	81	78	78	81	83	79	80	74	81	82	40
	1.00	0.65	0.54	0.59	0.46	0.50	0.66	0.45	0.47	0.51	0.38	0.65	0.67	0.30	0.35	1.00
	-134	33	-103	110	-160	-110	-36	48	-58	41	9	21	4	-2	8	-134
${}_1S_4$	24	28	28	28	21	20	20	18	17	12	13	7	8	4	4	23
	1.00	0.63	0.46	0.44	0.16	0.13	0.39	0.27	0.25	0.11	0.11	0.03	0.05	0.01	0.02	1.00
	-601	465	-344	117	-762	-844	7	30	41	198	-224	-325	74	45	165	-111
${}_0S_7$	19	30	23	29	35	41	30	29	34	30	32	35	34	34	37	9
	1.00	0.99	0.99	0.99	0.99	0.98	0.98	0.98	0.97	0.98	0.98	0.97	0.97	0.97	0.97	1.00

Table 5.2: continued

Mode	A_0^0	A_2^0	A_2^1	B_2^1	A_2^2	B_2^2	A_4^0	A_4^1	B_4^1	A_4^2	B_4^2	A_4^3	B_4^3	A_4^4	B_4^4	$\mathrm{Im}(A_0^0)$
	609	1511	-104	207	-685	-421	173	-105	-117	-83	-3	-30	26	-61	86	37
$_2S_3$	27	35	39	37	37	37	27	26	24	20	22	22	22	23	23	26
	1.00	0.67	0.55	0.60	0.45	0.38	0.38	0.37	0.26	0.17	0.20	0.20	0.20	0.25	0.24	1.00
	-163	283	-74	468	-597	-467	0	-70	-164	222	63	-165	-60	-46	16	-265
$_1S_5$	28	43	49	47	58	58	40	42	41	40	40	37	35	24	23	25
	1.00	0.84	0.77	0.78	0.49	0.49	0.67	0.57	0.54	0.41	0.39	0.26	0.24	0.09	0.09	1.00
	304	236	-96	124	-855	-646	-220	-112	222	87	-84	151	-121	-238	60	-22
$_2S_4$	33	45	45	50	53	54	50	51	48	55	54	54	49	52	57	29
	1.00	0.91	0.91	0.87	0.86	0.85	0.78	0.77	0.79	0.70	0.71	0.70	0.79	0.75	0.61	1.00
	468	404	78	109	58	-389	4	-82	-84	-158	-206	119	-34	-10	-58	-334
$_2S_5$	75	66	71	69	67	58	45	46	47	43	45	36	38	34	37	73
	1.00	0.42	0.51	0.41	0.31	0.22	0.22	0.23	0.27	0.19	0.22	0.12	0.16	0.11	0.15	1.00
	20	315	-171	442	-742	-343	35	0	-129	31	-13	25	87	63	-5	-127
$_1S_6$	68	77	76	83	78	85	43	44	35	37	33	35	32	21	23	62
	1.00	0.65	0.67	0.44	0.36	0.45	0.25	0.26	0.14	0.15	0.12	0.14	0.13	0.05	0.06	1.00
	-826	-28	-426	-131	-557	-788	55	-99	125	217	-36	-324	238	216	191	7
$_0S_9$	19	33	23	30	34	49	29	30	35	30	31	33	34	41	38	9
	1.00	0.94	0.97	0.96	0.94	0.85	0.93	0.93	0.90	0.93	0.91	0.91	0.91	0.84	0.88	1.00
	-642	670	-94	166	-880	-598	-75	-75	54	192	-116	-101	178	-80	181	-189
$_1S_7$	34	28	28	29	32	31	25	25	25	25	26	26	26	23	24	13
	1.00	0.82	0.84	0.78	0.65	0.74	0.61	0.61	0.52	0.49	0.56	0.47	0.43	0.29	0.32	1.00
	346	-34	-528	293	374	-1050	399	129	-49	111	301	-141	154	-54	272	-52
$_2S_6$	43	66	57	65	70	76	58	58	58	59	58	62	61	60	62	31
	1.00	0.74	0.85	0.79	0.70	0.61	0.63	0.64	0.61	0.60	0.61	0.59	0.50	0.41	0.46	1.00
	-840	745	-19	202	-977	-632	0	-120	81	278	-39	-16	42	40	185	-112
$_1S_8$	17	29	26	31	31	30	26	25	27	26	27	27	28	27	25	13
	1.00	0.82	0.86	0.78	0.72	0.79	0.61	0.66	0.50	0.56	0.56	0.45	0.46	0.41	0.40	1.00

Table 5.2: continued

Mode	A_0^0	A_2^0	A_2^1	B_2^1	A_2^2	B_2^2	A_4^0	A_4^1	B_4^1	A_4^2	B_4^2	A_4^3	B_4^3	A_4^4	B_4^4	$\mathrm{Im}(A_0^0)$
	-288	79	46	287	-177	-372	93	60	-54	-56	-14	-141	-37	196	-127	22
$_4S_3$	30	50	42	47	59	57	48	50	52	57	58	56	54	57	52	25
	1.00	0.87	0.91	0.88	0.80	0.81	0.79	0.75	0.74	0.65	0.58	0.67	0.67	0.65	0.72	1.00
	587	130	-325	33	2	-943	26	332	-166	-375	422	-31	240	-308	412	27
$_2S_8$	35	52	45	54	53	57	47	46	47	45	45	49	48	45	45	28
	1.00	0.67	0.83	0.72	0.60	0.57	0.54	0.64	0.55	0.54	0.58	0.48	0.46	0.32	0.44	1.00
	-144	248	44	19	-77	-280	34	-34	-141	-41	-16	34	18	102	42	-248
$_5S_3$	37	38	37	40	32	35	26	26	24	18	24	17	20	23	25	35
	1.00	0.57	0.49	0.39	0.27	0.32	0.32	0.30	0.20	0.13	0.21	0.11	0.13	0.20	0.22	1.00
	-147	331	75	53	166	-81	-199	-99	17	118	-6	61	72	-173	-66	-73
$_4S_4$	37	36	37	36	34	29	27	24	28	23	25	21	24	26	18	35
	1.00	0.36	0.43	0.52	0.27	0.19	0.30	0.20	0.41	0.17	0.23	0.13	0.18	0.26	0.13	1.00
	-129	-196	-58	60	-147	-728	96	-123	-301	-28	129	-60	-134	132	-23	-81
$_5S_4$	18	33	31	33	34	35	30	31	32	35	35	35	34	35	34	17
	1.00	0.84	0.85	0.83	0.83	0.81	0.75	0.71	0.70	0.59	0.56	0.57	0.62	0.55	0.63	1.00
	130	-22	-138	230	-195	-495	-88	-205	83	90	31	103	-21	-88	103	-105
$_5S_5$	13	22	21	23	25	25	21	21	21	23	23	23	23	23	23	11
	1.00	0.85	0.87	0.82	0.77	0.76	0.74	0.70	0.72	0.61	0.59	0.64	0.58	0.62	0.53	1.00
	37	1111	-156	495	-43	-284	383	-33	-270	323	-394	517	-62	-63	-149	-132
$_6S_3$	26	48	48	48	54	61	46	47	51	49	52	51	53	47	48	22
	1.00	0.84	0.84	0.83	0.73	0.67	0.75	0.67	0.53	0.39	0.44	0.39	0.41	0.72	0.69	1.00
	-41	647	-188	251	-384	-451	-16	281	63	24	115	-65	170	-53	78	-233
$_3S_8$	37	52	44	52	57	52	42	40	40	41	41	42	39	37	39	33
	1.00	0.71	0.81	0.72	0.61	0.46	0.52	0.55	0.43	0.39	0.46	0.36	0.30	0.25	0.34	1.00
	301	81	-30	216	-265	-482	-21	-190	-54	-104	31	66	10	-21	25	-171
$_5S_6$	13	20	18	19	25	23	18	18	18	19	18	20	19	19	19	10
	1.00	0.82	0.86	0.85	0.67	0.72	0.67	0.62	0.69	0.59	0.61	0.58	0.53	0.42	0.46	1.00

Table 5.2: continued

Mode	A_0^0	A_2^0	A_2^1	B_2^1	A_2^2	B_2^2	A_4^0	A_4^1	B_4^1	A_4^2	B_4^2	A_4^3	B_4^3	A_4^4	B_4^4	$\mathrm{Im}(A_0^0)$
	336	169	121	91	-93	98	-215	-13	-18	-46	1	19	15	-167	47	7
${}_9S_3$	34	35	31	37	35	32	25	19	20	15	15	14	15	27	21	33
	1.00	0.46	0.21	0.38	0.29	0.32	0.35	0.13	0.15	0.08	0.09	0.07	0.08	0.31	0.15	1.00
	-1036	1076	-94	106	-587	-757	773	330	-210	-141	-134	252	234	-190	-19	-56
${}_{10}S_2$	16	34	59	52	67	59	36	61	49	64	59	56	54	28	29	11
	1.00	0.94	0.80	0.86	0.70	0.79	0.95	0.83	0.90	0.79	0.83	0.86	0.86	0.96	0.96	1.00
	83	63	-24	234	-236	-600	-175	-155	-70	107	249	53	175	-66	7	-10
${}_6S_{10}$	27	43	34	27	43	41	34	33	31	32	32	32	33	33	32	18
	1.00	0.67	0.81	0.90	0.55	0.59	0.48	0.54	0.65	0.56	0.51	0.39	0.46	0.36	0.33	1.00
	-273	695	-31	204	-115	-56	149	-219	-123	442	-692	63	-175	-39	32	-24
${}_{11}S_4$	15	34	42	29	52	50	31	44	40	61	57	64	60	58	52	12
	1.00	0.96	0.94	0.97	0.91	0.92	0.93	0.85	0.88	0.65	0.72	0.56	0.65	0.70	0.79	1.00
	-98	965	-87	90	-116	-150	529	6	135	-69	296	-71	135	182	44	-39
${}_{13}S_2$	28	44	79	65	66	62	43	76	70	68	57	74	83	30	44	14
	1.00	0.91	0.59	0.62	0.62	0.74	0.93	0.75	0.76	0.72	0.83	0.67	0.53	0.97	0.93	1.00
	-154	711	273	209	141	-33	113	-4	-361	-199	518	238	-807	-334	-11	31
${}_{11}S_5$	25	61	41	49	76	68	54	66	60	79	71	91	78	71	75	18
	1.00	0.95	0.98	0.97	0.93	0.94	0.91	0.87	0.89	0.79	0.85	0.66	0.80	0.84	0.83	1.00
	30	863	-29	126	-55	-236	-4	-18	-167	-65	-175	25	-9	186	61	2
${}_{13}S_3$	19	28	40	40	42	39	24	22	26	13	22	22	11	25	24	16
	1.00	0.82	0.41	0.60	0.45	0.40	0.39	0.23	0.37	0.07	0.27	0.21	0.05	0.33	0.33	1.00

In order to comply with the convention used in expansions of the potential field (see, for example, *Stacey* [1977]), we express the splitting function as $\eta(\theta,\phi) = \sum_s \sum_{t=0}^{s} (A_s^t \cos t\phi + B_s^t \sin t\phi)\ p_s^t(\theta)$. The coefficients A_s^t and B_s^t are given in the first entry for each mode ($\times 10^{-6}$). In the last column, imaginary parts of A_0^0 are listed. The complex coefficients c_{st} can be derived as $c_{st} = (-1)^t (2\pi)^{\frac{1}{2}} (A_s^t - iB_s^t)$, for $t > 0$; $c_{st} = (4\pi)^{\frac{1}{2}} A_s^t$, for $t = 0$; and $c_{st} = (2\pi)^{\frac{1}{2}} (A_s^{|t|} + iB_s^{|t|})$, for $t < 0$. An estimate of the associated standard errors for the coefficients A_s^t and B_s^t is derived from the covariance matrix, and is given in the second entry for each mode (in the same units). See text for details on the reliability of the error estimates. The third entry for each mode gives the corresponding diagonal elements of the resolution matrix.

a phase velocity map, the result represents the effect of the heterogeneity integrated with depth and weighted by the corresponding differential kernels. Figures 5.2*a*–5.5*a* show the splitting function for each selected mode. We use the same maximum scale of 0.2% for all modes to highlight those requiring large aspherical perturbations; because of this, the scale can be saturated in a few extreme cases where the perturbation exceeds 0.2% of the mode frequency, as is the case for mode ${}_3S_2$ in Figure 5.4*a*.

5.2.2 Error maps

The standard errors listed in Table 5.2 are those obtained from the diagonal elements of the covariance matrix. These do not include the effects of covariances between model parameters and thus do not indicate whether model error is geographically localized or evenly distributed over the globe. Following (3.15) and (5.1), we map in Figures 5.2*b*–5.5*b*, for each selected mode, the function

$$E(\theta,\phi) = [\mathbf{y}^T(\theta,\phi)\ \mathbf{C}\ \mathbf{y}(\theta,\phi)]^{\frac{1}{2}} \tag{5.2}$$

which represents the standard error associated with the value of the splitting function at each point of the globe. We adopt a normalized scale as percentage of the maximum contour value (0.2%) of the splitting-function map in Figures 5.2*a*–5.5*a*.

Our results indicate that the errors are indeed quite uniformly distributed. The fact that uniformly distributed errors are obtained using relatively poor data coverage can be ascribed to the physical nature of these modes. Corresponding, as they do, to waves suffering numerous reflections and conversions continuing for days after the earthquake, they are sensitive to structure everywhere on the globe; in this respect they have markedly different properties than do surface wave equivalent modes at higher frequencies, which tend to have sensitivities confined to a region close to the great circle connecting source and receiver.

$_5S_6$

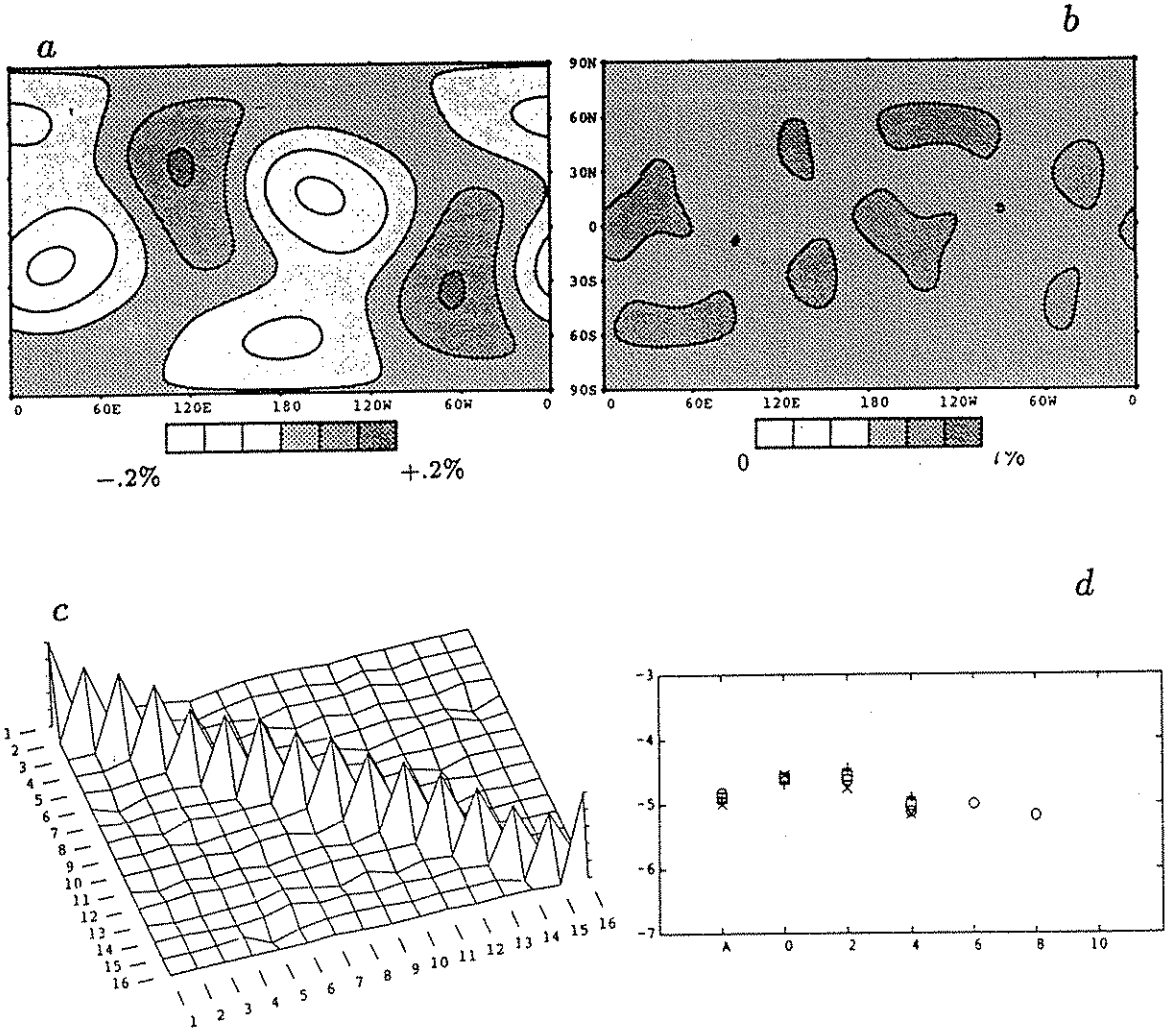

Fig. 5.2. (*a*) splitting function, (*b*) error map, (*c*) resolution matrix, and (*d*) spectral power plot for mode $_5S_6$. (*a*) the figure is normalized by mode frequency, with a maximum scale of 0.2% of mode frequency (kept constant for all modes in this thesis). (*b*) The error map is plotted in the same fashion. The maximum scale is indicated in percent of the maximum-scale value of the splitting function plot (0.2% of mode frequency). See text for details on the computation and the reliability of the error estimates. (*c*) The resolution matrix is plotted to a maximum scale of 1, a value reached only by the diagonal elements corresponding to the real and imaginary c_{s0} coefficients, left undamped in the inversion. (*d*) The spectral power plots show the average spectral power (verticle axis; logarithmic scale) in each harmonic degree ("A" indicates the results for attenuation - $\mathrm{Im}(c_{00})$) for splitting function solutions obtained at different levels of damping (ς=0.01 (plus signs), ς=0.1 (squares), and ς=0.5 (crosses)), which varies the relative weight assigned to the model norm with respect to the misfit norm; in all cases the harmonic expansion of the splitting function was truncated at degree $s = 4$. Results for the inversion extended to degree $s = 8$ (with ς=0.1) are indicated with circles.

$_0S_7$

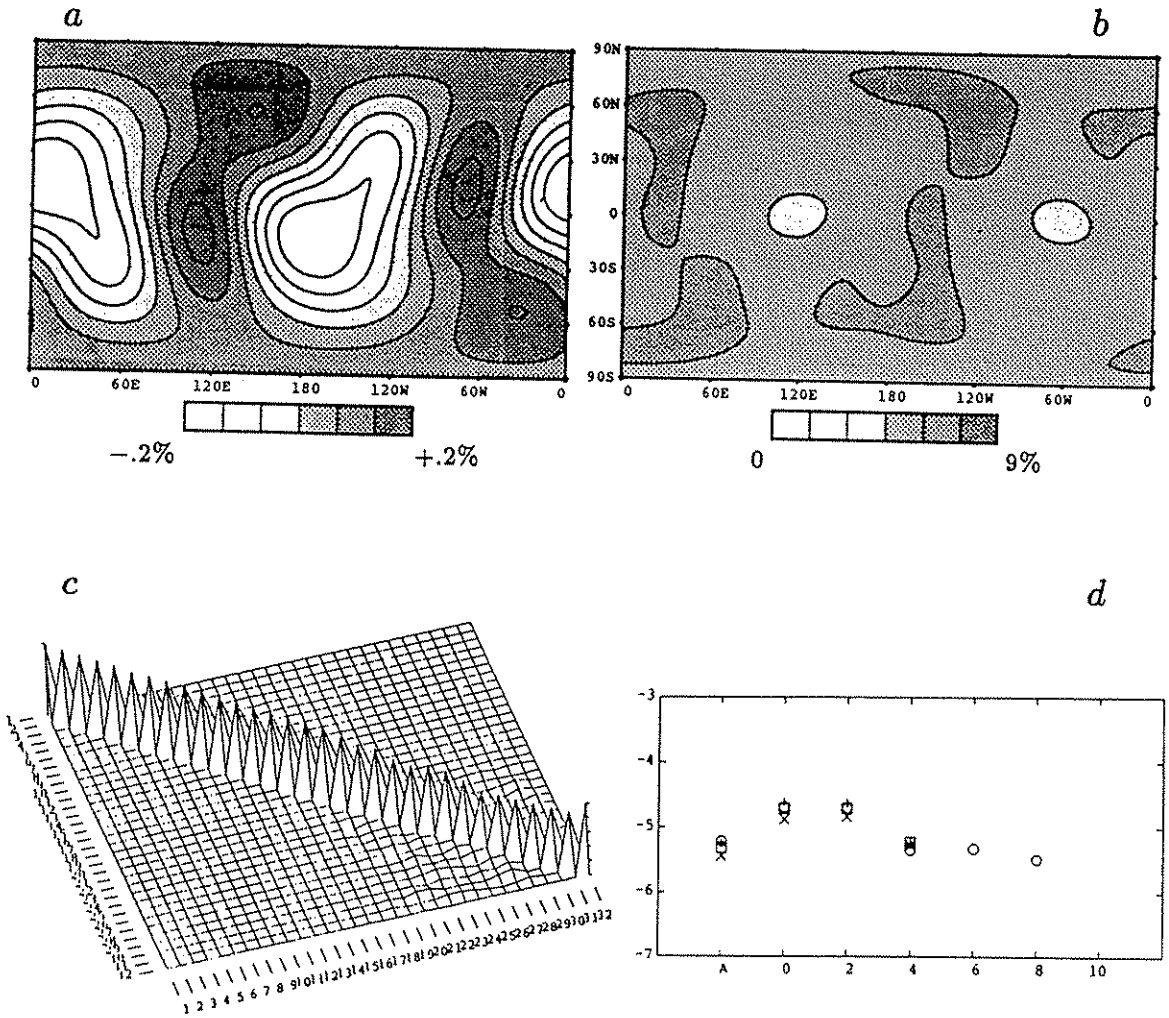

Fig. 5.3. (*a*) splitting function, (*b*) error map, (*c*) resolution matrix, (*d*) and spectral power plot for $_0S_7$. This mode is in the same spectral window of mode $_2S_3$; (*c*) the resolution matrix refers to both multiplets, with the first 16 entries belonging mode $_0S_7$. See caption to Figure 5.2 for details.

$_3S_2$

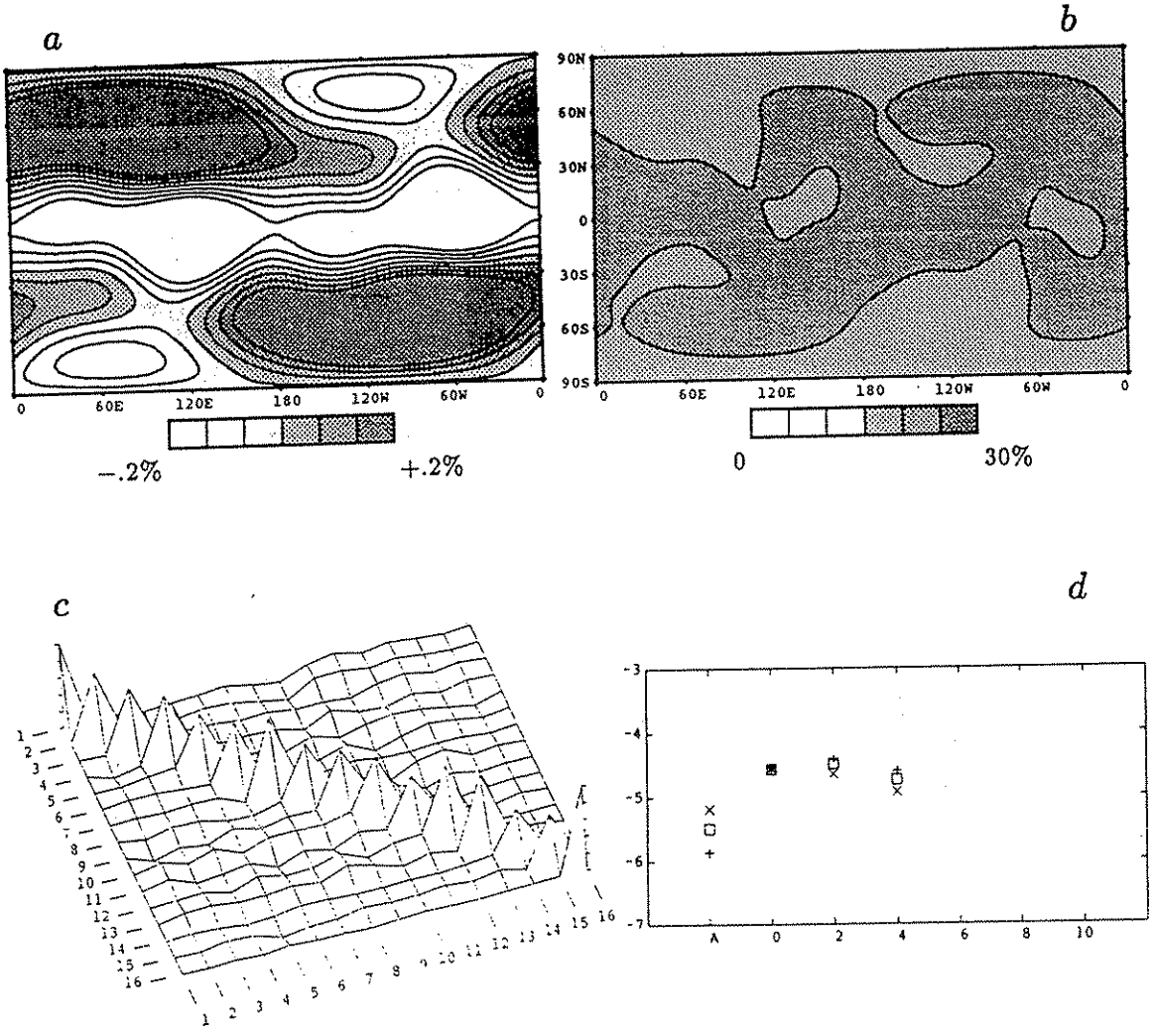

Fig. 5.4. (*a*) splitting function, (*b*) error map, (*c*) resolution matrix, and (*d*) spectral power plot for mode $_3S_2$. See caption to Figure 5.2 for details.

$_{13}S_2$

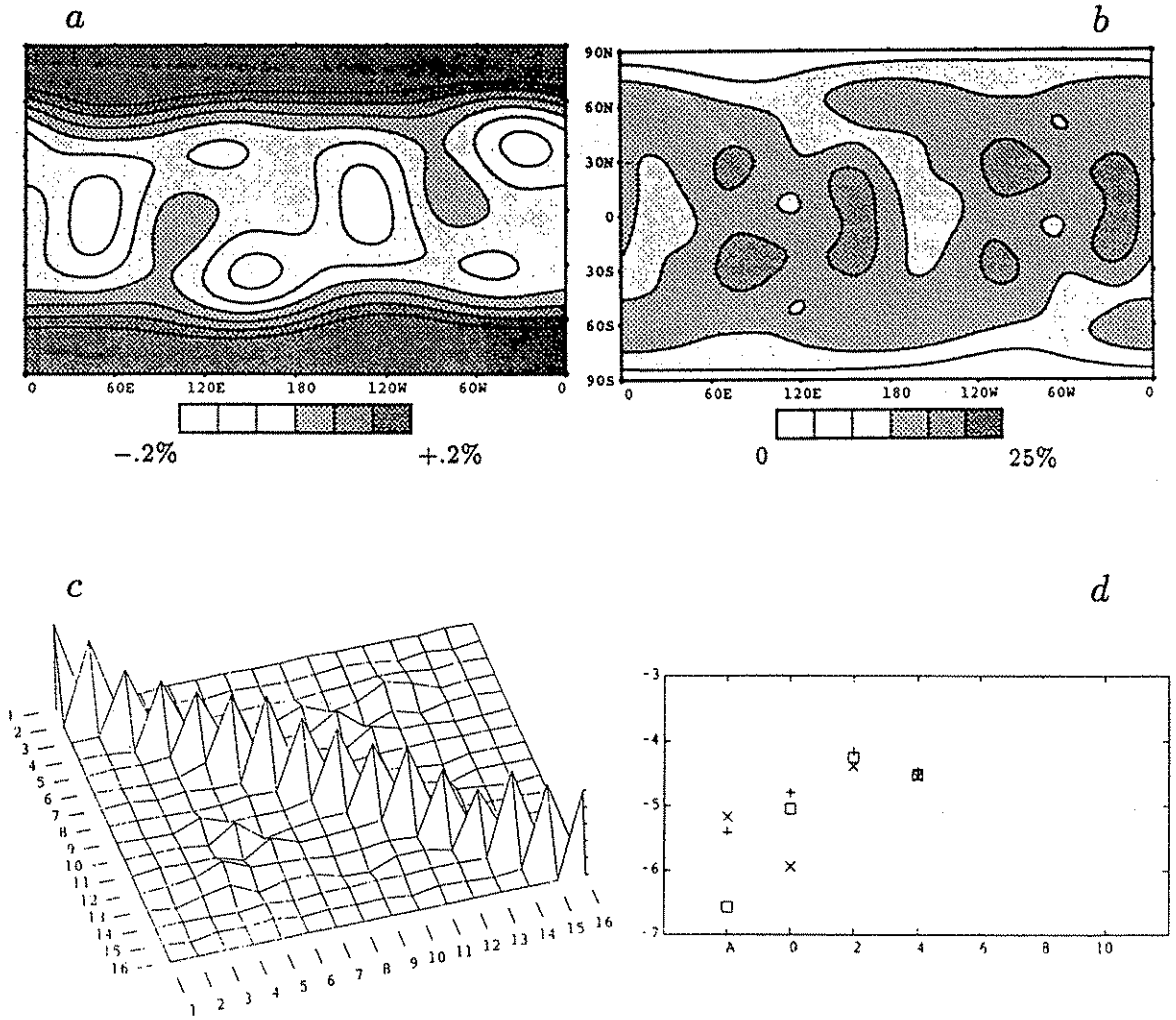

Fig. 5.5. (*a*) splitting function, (*b*) error map, (*c*) resolution matrix, and (*d*) spectral power plot for mode $_{13}S_2$. See caption to Figure 5.2 for details.

5.2.3 Resolution matrices

A successful inversion is characterized, ideally, by a small quasi-diagonal covariance matrix and by a resolution matrix close to the unit matrix. It is interesting to visually inspect the covariance and resolution matrices of the splitting functions to identify large cross-correlation terms between different singlets and model parameters insufficiently resolved. This is particularly true for the case of double modes; the joint inversion we perform, in fact, is based on the assumption that the data distribution will be sufficient to effectively separate the two modes. The elements of the resolution matrix correlating peaks of separate modes will indicate the limitations of our approach.

Figures 5.2*c*–5.5*c* display a graphic representation of the resolution matrix for the selected modes ${}_5S_6$, ${}_0S_7$-${}_2S_3$, ${}_3S_2$, and ${}_{13}S_2$. The diagonal terms of the resolution matrix of all the modes analyzed in this paper are tabulated in Table 5.2.

The resolution matrices we obtain are dominated by their diagonal elements, with many diagonal terms approaching unity, and with generally small off-diagonal terms. This is also true in the case of double modes, indicating that we are successfully separating overlapping multiplets. In some cases, the resolution of two overlapping modes can be substantially different, as it is for modes ${}_2S_4$ and ${}_1S_5$, indicating the different resolution provided by the same data for different kinds of modes.

We observe decreasing resolution with increasing harmonic degree of the splitting function coefficients. The highest resolution is achieved for both c_{00} terms, which confirms our a priori expectation.

5.2.4 Size of the splitting functions

The choice of the damping parameter ς conditions the general strength of our desire for smallness of the model with respect to the desire for smallness of the data misfit (see Section 3.1). It is clear that the total rms of the model decreases monotonically with increasing ς, and at the same time the reduction in data variance decreases with decreasing resolution of the inversion. We are interested of course

in determining the ς value providing the best compromise between model error and resolution, and in assessing the significance of the resulting solution. This value will depend on the distribution of the available data, and will be different for each mode, reflecting the physical property that the splitting function may be dominated by only one or two terms of the harmonic expansion for one mode, or by many more terms for another mode, as is illustrated by the size of the resolution parameter R in Table 5.1.

Because of the intrinsic nonlinearity of the equations, it is computationally expensive to iterate the procedure to convergence for many values of ς. We do it for three values: 0.01, 0.1, and 0.5, corresponding roughly to resolution parameters $R = 6, 9, 12$ in the case of single modes. The most "significant" ς value for each mode is determined by applying an F-test to the corresponding three hypotheses; we retain a hypothesis as statistically significant if it satisfies the F-test at a significance level higher than 75%.

Figures 5.2*d*–5.5*d* display the power content per harmonic degree for each selected mode, including the complex c_{00} term, for the different values of the damping parameter $\varsigma = 0.01, 0.1, 0.5$ (indicated with plus signs, squares, and crosses, respectively). The distance between the three curves is is related to the significance of the corresponding ς values; lower solution rms correspond to higher ς. Also, the stability of different harmonic degrees with respect to damping becomes clear; the larger variability of the degree 4 terms reflects the lower resolution shown by the resolution matrices (Table 5.2). The apparently high variability of the c_{00} terms (cf. Figure 5.4*d* for mode ${}_3S_2$ and Figure 5.5*d* for mode ${}_{13}S_2$) may be misleading; the logarithmic scale indicates that these components are usually quite small, implying a small departure of the central frequency and attenuation of the mode from the values predicted by PREM.

5.2.5 Aliasing

The splitting coefficients c_{st} constitute linear constraints on lateral heterogeneity of degree s and order t. If the results are to be so used, it is important to verify that

they are not marred by aliasing, i.e., that heterogeneity of high harmonic degree is not being misinterpreted as low-degree heterogeneity. At the same time, aliasing tests are an effective way to check the stability of the splitting function solutions. The mode ${}_5S_6$, for example, is sensitive to heterogeneity up to degree $s = 12$, and we may test if a significant variance reduction is obtained by expanding its splitting function to such degree, and if by truncating the expansion to the lower degrees we are introducing any sizable aliasing. These questions are answered by performing inversions of the splitting function to high degree and comparing the low-degree terms with those obtained in inversions for a truncated expansion. An estimate of the aliasing present in the inversion procedure can also be derived by analyzing the off-diagonal terms of the resolution and covariance matrices.

Figures 5.2*d*–5.3*d* also show the rms of the harmonic expansion coefficients, for the selected modes, up to degree 8, indicated by open circles. The damping parameter has been fixed for all the modes at $\varsigma = 0.1$, allowing a direct comparison only with the corresponding truncated values, indicated by squares in Figures 5.2*d*–5.3*d*. The comparison is satisfactory in most cases. The average power content decreases with increasing harmonic degree, suggesting a "red" spectrum in agreement with the presence of a dominant long-wavelength heterogeneity ($s = 2$) discussed previously.

We test if the available data would be sufficient to resolve the higher degrees by comparing statistically the results of the two inversions. Although a variance reduction is obtained in all cases, as is expected, it is a significant reduction for only half of the modes, as shown by the F-test. These results indicate that some multiplets possess significant sensitivity to degrees above 4, a property that will be exploited in future analysis.

We also compare the individual splitting coefficients obtained by adopting a truncated expansion with the terms of degree $s = 2, 4$ obtained using the full expansion. The results are very positive for most of the modes, producing virtually identical maps in most cases. We observe more instability precisely for the modes we expect to be more unstable: mode ${}_5S_3$, for which only 11 traces could be retrieved, and modes with significant power in higher degrees, such as ${}_{11}S_5$ and ${}_2S_5$. In these we

feel that a significant uncertainty is associated with the splitting function patterns, probably more than that indicated by the statistical errors.

5.2.6 Central frequency

Using the splitting function coefficients and their covariance matrix, we may derive, using (2.8) and (3.15), the elements of the splitting matrix and their covariance matrix. We also calculate the eigenvalues Ω_{ii} of the splitting matrix, which are the singlet eigenfrequency perturbations relative to the reference frequency, and linearized approximations to their variances and covariances using (3.16) and (3.17), together with the following result (Rayleigh's principle) for the derivatives of the eigenvalues of $\mathbf{H}$ with respect to the its individual elements:

$$\frac{\partial \Omega_{kk}}{\partial H_{ij}} = U^{-1}_{ki} U_{jk} \tag{5.3}$$

where matrix $\mathbf{U}$ has been defined as in (2.22). This calculation is needed to obtain the standard errors associated with the singlet eigenfrequencies and the splitting width. The values and covariances of Ω_{ii} may be used to calculate the central frequency and its standard error; these quantities are more simply obtained, however, from the diagonal sum rule:

$$\omega_c = \omega_0 + \frac{1}{2l+1} \sum_{i=1}^{2l+1} \mathrm{Re}(\Omega_{ii}) = \omega_0 \left(1 + \frac{c_{00}}{4\pi}\right) \tag{5.4}$$

and thus the standard error is

$$\delta\omega_c = \frac{\omega_0}{4\pi} \delta c_{00} \tag{5.5}$$

The central frequencies we obtain are very close to those predicted by PREM, their difference being of the order of a microhertz and they are invariably within the error bounds used by *Dziewonski and Anderson* [1981] in the construction of the PREM model. The standard errors obtained here, however, are much smaller; as is shown in Table 5.3, they are typically a fraction of a microhertz. Although these errors may seem exceedingly small, it should be noted that a frequency error of 10^{-7}Hz would produce a phase misalignment of $\sim 10°$ after 80 hours which approaches the level

Table 5.3: Central Frequency, Splitting Width, and Q Parameter Derived from the Splitting Functions

Mode	f	δf	Δf	W	δW	r	Q	δQ	ΔQ
${}_0S_3$	468.46	0.02	−0.10	13.01	0.03	1.00	439	27	22
${}_0S_4$	646.77	0.02	−0.31	9.54	0.04	1.00	406	15	33
${}_0S_5$	839.99	0.02	−0.45	7.31	0.03	1.03	374	11	19
${}_1S_3$	939.92	0.04	0.09	14.88	0.06	1.00	328	18	46
${}_3S_1$	944.33	0.02	0.39	3.23	0.03	1.01	802	54	−17
${}_0S_6$	1037.53	0.02	−0.71	6.14	0.04	1.20	367	6	20
${}_3S_2$	1105.24	0.05	−0.97	8.64	0.10	1.33	332	18	−34
${}_1S_4$	1172.70	0.03	−0.16	18.31	0.06	1.00	292	8	21
${}_0S_7$	1231.07	0.02	−0.74	5.41	0.04	1.70	370	5	28
${}_2S_3$	1242.94	0.03	0.757	7.36	0.06	1.48	403	17	−12
${}_1S_5$	1370.05	0.04	−0.22	19.96	0.09	1.01	345	12	54
${}_2S_4$	1379.62	0.05	0.42	5.28	0.09	1.68	386	17	6
${}_2S_5$	1515.64	0.12	0.71	5.01	0.20	1.71	378	42	76
${}_1S_6$	1522.07	0.10	0.03	16.42	0.19	1.02	379	35	34
${}_0S_9$	1576.99	0.03	−1.31	4.03	0.04	1.34	330	4	-2
${}_1S_7$	1654.45	0.03	−1.06	14.28	0.07	1.09	433	10	61
${}_2S_6$	1681.42	0.07	0.58	8.59	0.16	1.27	244	7	7
${}_1S_8$	1797.80	0.03	−1.51	14.03	0.09	1.14	414	9	35
${}_4S_3$	2048.37	0.06	−0.591	6.63	0.14	1.30	470	23	−10
${}_2S_8$	2050.41	0.07	1.21	14.96	0.16	1.18	195	4	−2
${}_5S_3$	2169.34	0.08	−0.31	6.47	0.14	1.38	342	16	50
${}_4S_4$	2279.26	0.09	−0.34	7.19	0.15	1.67	303	13	13
${}_5S_4$	2379.21	0.04	−0.31	7.29	0.11	1.36	531	19	42
${}_5S_5$	2703.71	0.04	0.35	9.18	0.08	1.40	562	15	60
${}_6S_3$	2821.83	0.08	0.11	9.04	0.19	2.36	480	20	54
${}_3S_8$	2819.53	0.11	−0.12	9.15	0.24	1.53	300	11	37
${}_5S_6$	3011.60	0.04	0.91	10.87	0.08	1.45	612	16	106

Table 5.3: continued

Mode	f	δf	Δf	W	δW	r	Q	δQ	ΔQ
${}_9S_3$	3556.18	0.09	1.20	6.33	0.15	1.14	768	55	−9
${}_{10}S_2$	4040.81	0.07		13.09	0.13	3.45	878	35	
${}_6S_{10}$	4211.12	0.12	0.35	15.22	0.32	1.64	357	9	3
${}_{11}S_4$	4765.57	0.07	−1.30	12.95	0.16	1.66	726	25	25
${}_{13}S_2$	4844.79	0.14	−0.48	15.32	0.26	2.40	943	50	65
${}_{11}S_5$	5073.63	0.13	−0.78	14.57	0.42	1.64	638	30	−27
${}_{13}S_3$	5193.98	0.10	0.16	13.75	0.20	1.74	905	54	−3

The central frequency (f), the associated errors (δf), and its distance (Δf) from the value predicted by PREM (Table 1) are in microhertz. The splitting width (W), also in microhertz, measures the difference between the largest and smallest singlet eigenfrequencies; the standard error (δW) is also indicated. The ratio of the splitting width of the multiplet to the splitting width resulting from rotation and ellipticity (r) always exceeds unity, reaching values ~ 2.5 for the anomalously split modes. The perturbed Q value, its error (δQ), and the difference (ΔQ) from the Q values of PREM are indicated. See text for details on the computation and the reliability of the error estimates.

of phase agreement obtained using the splitting functions in cases of high signal-to-noise ratio. Previous measurements of degenerate frequency have been hampered by the effects of splitting and attenuation, whereas in the present study, these effects have been explicitly accounted for; it is for this reason that much more accurate measurements of central frequency are possible.

5.2.7 Splitting width

We derive from the location of the singlets the splitting width for each mode listed in Table 5.3, together with its standard error, and the ratio of the splitting width to the theoretical splitting width due to rotation and ellipticity. These are listed primarily for comparison with the results of *Ritzwoller et al.* [1986], who adopt a different procedure, based on the retrieval of singlet frequencies through stripping techniques. Although a certain amount of damping is applied in our inversion procedure, the splitting widths recovered agree well with those recovered by singlet stripping, even for the most anomalously split modes, ${}_{13}S_2$ and ${}_6S_3$, which have a splitting width ratio of approximately 2.5.

By comparing Tables 5.1 and 5.3 we note that substantial variance reductions are obtained for modes displaying a large range of splitting width ratios.

5.2.8 Attenuation

Throughout the experiments shown here, we invert only for the c_{00} term in the harmonic expansion of the imaginary part of the splitting function. This is equivalent to inverting for a spherically symmetric correction to the Q of the multiplet or to applying the constraint that all singlets have the same Q. Inversion has been thus restricted for several reasons. First, we find the inversion for a complete c_{st} expansion frequently to be unstable, leading to large perturbations in the differential attenuation of singlets and to small shifts of the singlet eigenfrequencies; in a nonlinear problem such instability prevents a reasonable solution from being found, owing to the proliferation of local minima. Furthermore, extending the parameterization to its full complex form after convergence has been reached for the restricted inversion, leads to only a very slight additional variance reduction, statistically insignificant when account is taken of the doubled number of model parameters. A much larger body of data is needed to address the problem of lateral variations in attenuation.

The introduction of the imaginary part of c_{00}, on the other hand, is highly significant and allows us to estimate a Q value for each mode, given by

$$Q = \frac{\omega_c}{2(\alpha_0 + \mathrm{Im}(c_{00}) \cdot \omega_0 (4\pi)^{-\frac{1}{2}})} \tag{5.6}$$

where $\alpha_0 = \omega_0 / 2Q_0$ is the imaginary part of the reference frequency.

Table 5.3 lists, for each multiplet, the Q value and its standard error, which is typically of the order 1%. These values are usually within 10% of those predicted by the PREM model, listed in Table 5.3. The standard errors probably underestimate, somewhat, the true uncertainties, but we would expect that these measures of attenuation are among the most accurate ever obtained. They are the first such measurements derived from many records simultaneously and correcting, as far as is possible, for the corrupting influence of modal splitting.

5.3 Discussion

The close correspondence between the inferred splitting functions of multiplets possessing similar differential kernels provides evidence, more compelling, we believe, than the formal error estimates, that the splitting functions have been accurately retrieved and that they do, indeed, reflect the Earth's three-dimensional structure. Modes on the same branches, with comparable sensitivity in the same depth ranges, display the same degree of similarity in their splitting functions.

What emerges from our analysis of the splitting functions is a series of well-defined patterns which can be directly linked to specific regions of the Earth's interior by examining the corresponding modal differential kernels. The task of deriving an earth model that combines these patterns, satisfying all the splitting function data simultaneously, requires further use of inversion techniques and will be taken up in Chapter 7. Here we compare differential kernels and splitting functions for some of the modes analyzed, in order to illustrate these patterns and to point out similarities and differences between splitting functions of modes with similar differential kernels.

Figures 5.6–5.10 show kernels and splitting functions for five sets of modes. The splitting functions are plotted in the same fashion as those in Figures 5.2–5.5. The differential kernels for heterogeneity, which are those defined through (2.31)–(2.33), represent the sensitivity, as a function of depth, of the splitting function to the relative perturbation in P velocity (α), S velocity (β), and density (ρ). For a given mode the kernels depend upon the degree s of the perturbation, but it will be noted that for most modes, particularly those of larger angular order, the kernels are very similar for the three s values shown; in the limit $l \gg s$ they are equal, reflecting the equivalence of the splitting function to $\delta\omega_{\text{local}}$ in the asymptotic limit of large l. At the bottom of each kernel panel we also show the sensitivity to topographic perturbations (see (2.28)) of the four major surfaces of discontinuity; from top to bottom, these are the free surface (sea floor for our reference model – PREM), the 670-km discontinuity, the core-mantle boundary, and the inner-core boundary (the kernels for the inner-core boundary of many modes are so small that they vanish

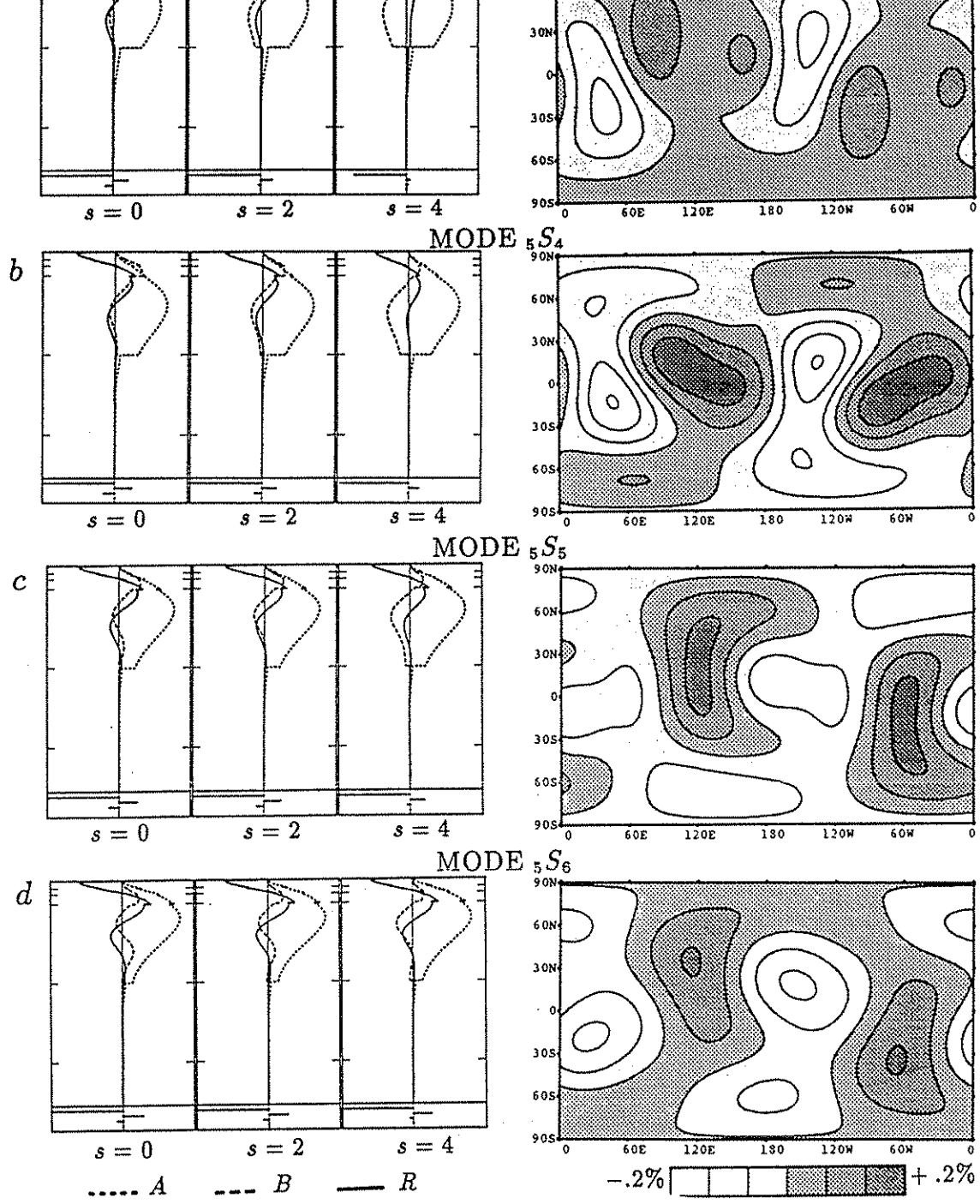

Fig. 5.6. Differential kernels (cf, (2.31), (2.32), (2.33)) and splitting functions for modes $_4S_3$, $_5S_4$, $_5S_5$, and $_5S_6$. For each degree the kernels are centered on the 0 line and the scale scans from $-4/a$ to $+4/a$, where a is the radius of the Earth. At the bottom of each panel we also show the sensitivity to topographic perturbations (cf, (2.28); scale: -1 to $+1$): from top to bottom, these are the free surface, the 670-km discontinuity, the core-mantle boundary, and the inner-core boundary. The modes shown here show predominant sensitivity to v_P structure in the lower mantle and essentially vanishing sensitivity below the core-mantle boundary.

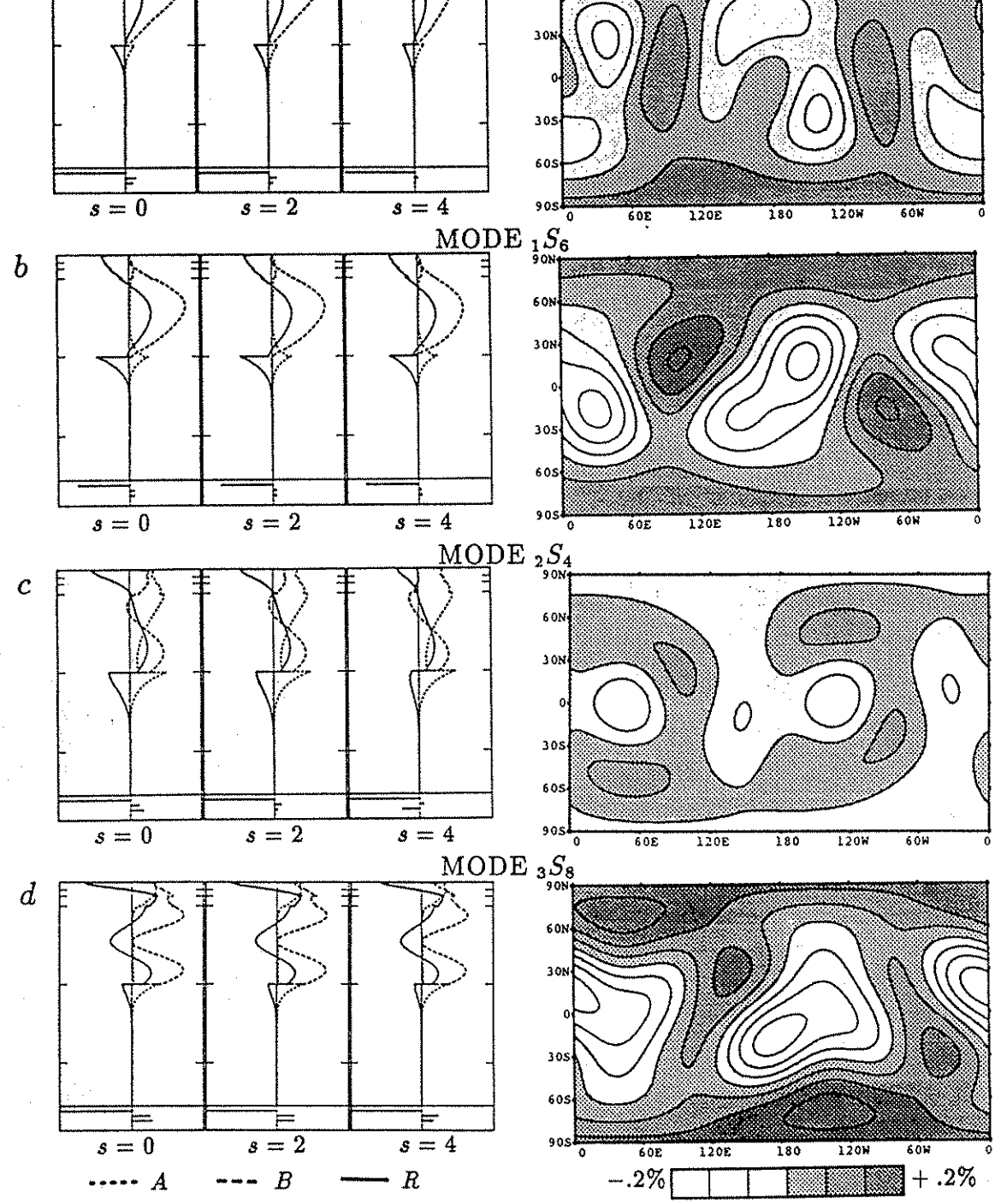

Fig. 5.7. Differential kernels and splitting functions for modes ${}_1S_5$, ${}_1S_6$, ${}_2S_4$, and ${}_3S_8$, showing large sensitivity to v_S, v_P, and ρ in the mantle and some sensitivity in the outermost core. See caption to Figure 5.6 for details.

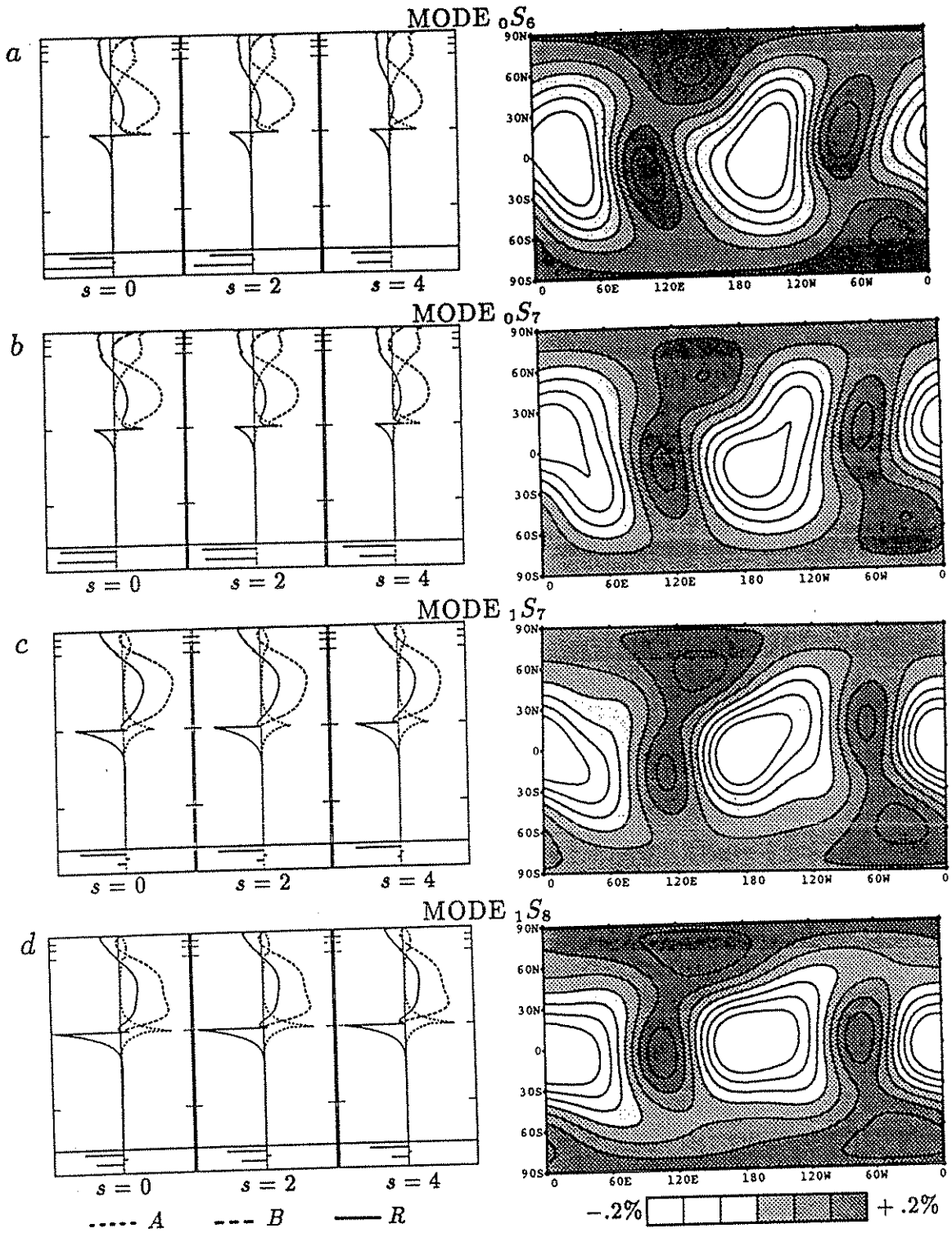

Fig. 5.8. Differential kernels and splitting functions for modes ${}_0S_6$, ${}_0S_7$, ${}_1S_7$, and ${}_1S_8$, dominated by sensitivity to v_S structure in the lower mantle and having large kernels in the outermost core and in the proximity of the core-mantle boundary. See caption to Figure 5.6 for details.

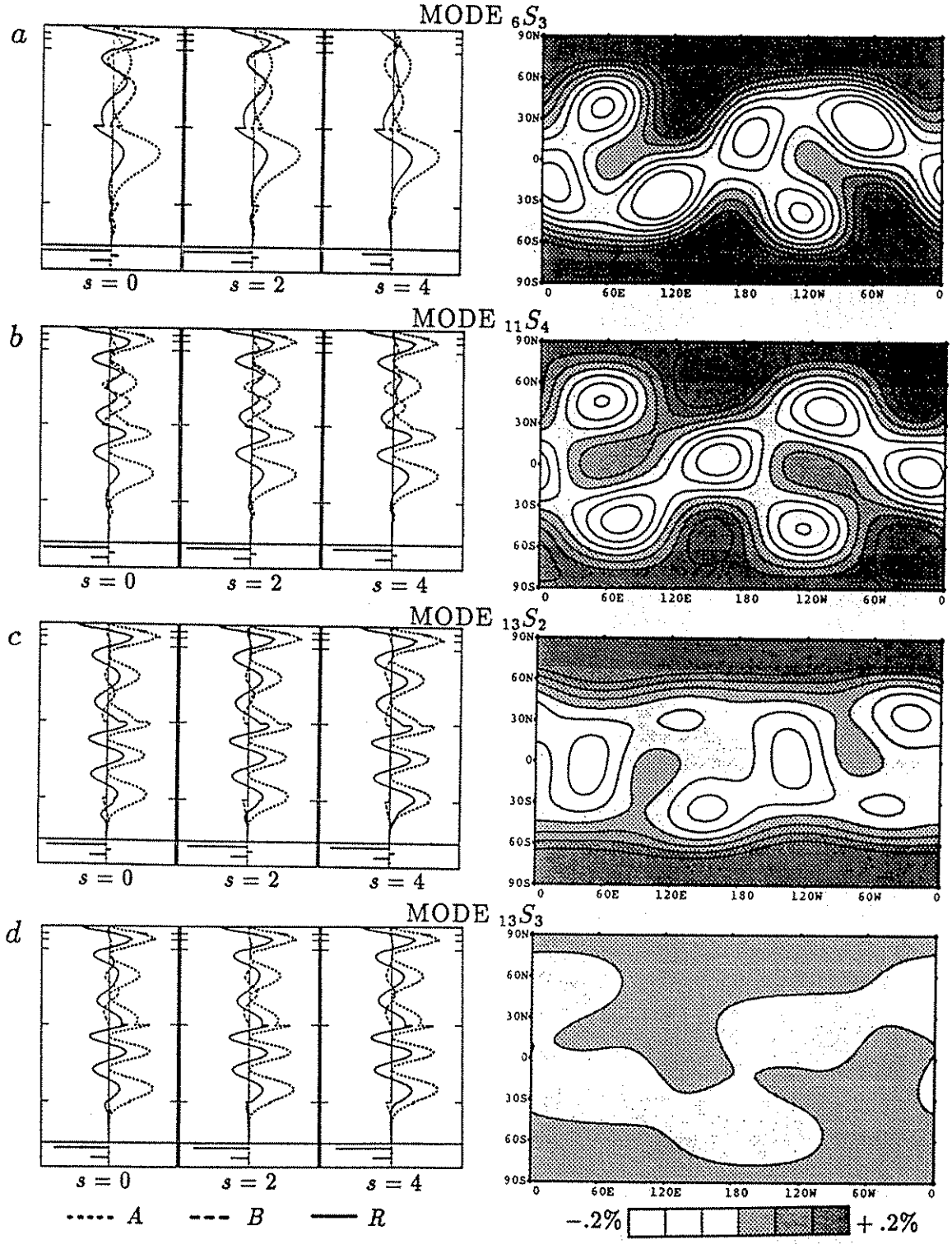

Fig. 5.9. Differential kernels and splitting functions for modes ${}_6S_3$, ${}_{11}S_4$, ${}_{13}S_2$, and ${}_{13}S_3$. These are modes of the *PKIKP* type, with generally low sensitivity to shear velocity in the mantle and kernels extending throughout the outer core into the inner core. See caption to Figure 5.6 for details.

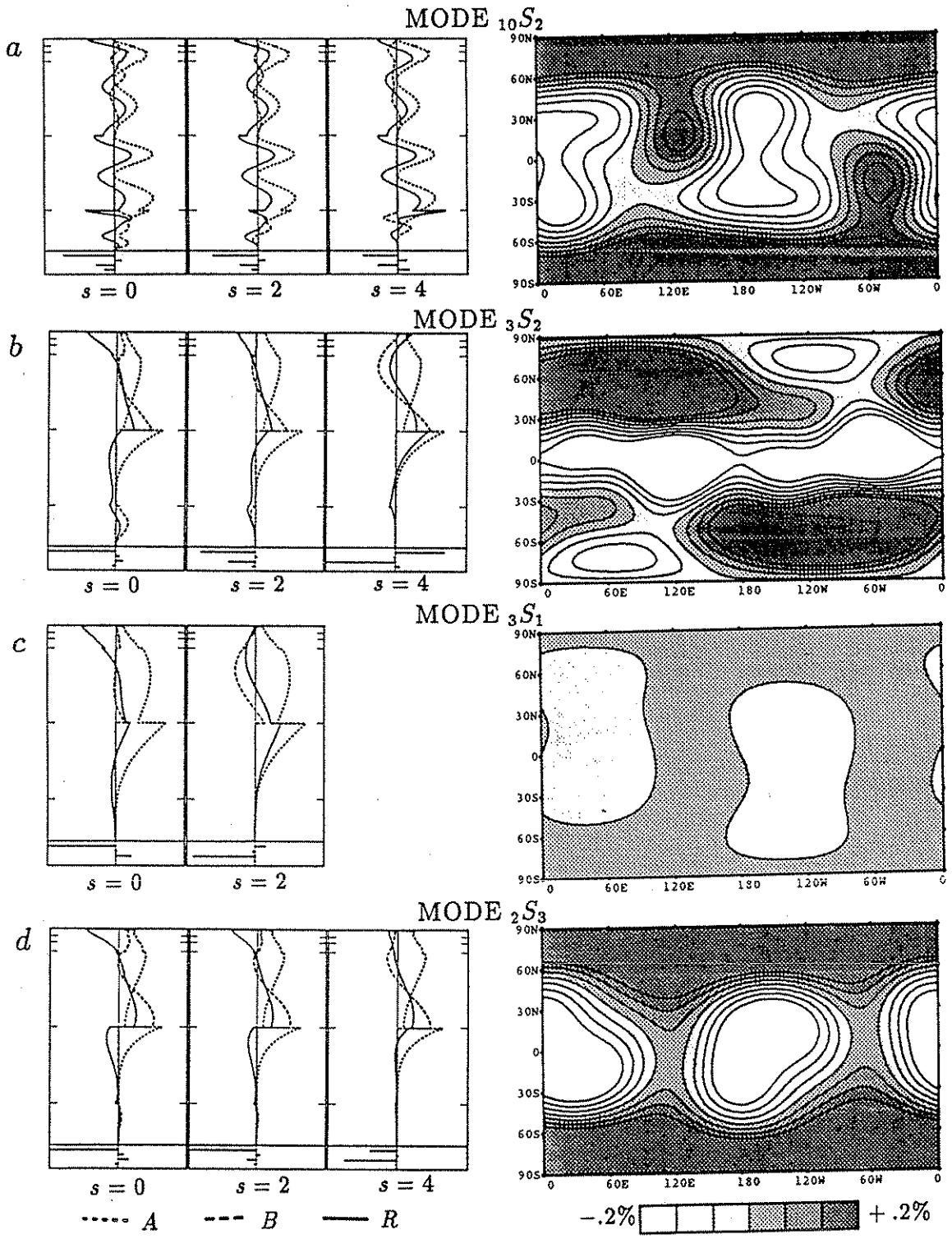

Fig. 5.10. Differential kernels and splitting functions for modes $_{10}S_2$, $_3S_1$, $_3S_2$, and $_2S_3$. The first mode, $_{10}S_2$, is again of the *PKIKP* type, with differential kernels strongly dependent on the initial reference model, at least in the inner core region, and is the subject of a detailed discussion in the text. The other modes are long-period, high-Q modes with sensitivity extending to the inner core but quite different from that of the *PKIKP* modes. See caption to Figure 5.6 for details.

from sight in these figures).

Figure 5.6 contains the results for modes ${}_4S_3$, ${}_5S_4$, ${}_5S_5$, and ${}_5S_6$, which have periods between 488s and 332s. The kernels show that these multiplets have great sensitivity to P velocity heterogeneity in the lower mantle. The splitting functions display a similar pattern, dominated by the two c_{22} terms and by the imaginary part of c_{21} (see Table 5.2, from which correlation coefficients are readily derived).

In Figure 5.7 modes ${}_1S_5$, ${}_1S_6$, ${}_2S_4$, and ${}_3S_8$ behave in similar way. The kernels are large throughout the mantle, in various combinations of α, ρ, and especially β, with some sensitivity also in the outermost core. The splitting functions, however, are dominated by c_{22} and Im c_{21} (note, for example, the patterns of modes ${}_2S_4$ in Figure 5.7*c* and mode ${}_5S_5$ in Figure 5.6*c*). The similarities among the splitting functions and the kernels of the modes shown in these two figures strongly suggest that the heterogeneity producing the splitting behavior is limited to the mantle.

This argument is reinforced by the results for the multiplets ${}_0S_6$, ${}_0S_7$, ${}_1S_7$, and ${}_1S_8$ shown in Figure 5.8. Spanning the period range 963s to 555s, the kernels are dominated by similarly large sensitivity to heterogeneity in β throughout the lower mantle and to heterogeneities in α and ρ at the top of the outer core. Again, the largest coefficients in the splitting functions are the c_{22} terms, together with significant c_{20}. The amplitude is appreciably larger than in Figures 5.6–5.7, suggesting that heterogeneity in shear velocity in the lower mantle is larger than the corresponding heterogeneity in P velocity.

A radically different set of modes is shown in Figure 5.9. with periods ranging between 354s and 192s, modes ${}_6S_3$, ${}_{11}S_4$, ${}_{13}S_2$, and ${}_{13}S_3$ are of the *PKIKP* type, with generally low sensitivity to shear velocity in the mantle and α and ρ kernels extending throughout the outer core and into the inner core. In this case they display a largely zonal pattern with a predominance of c_{20} and, to a lesser extent, c_{22} and various terms of degree 4 (see Table 5.2). This is true for modes with quite different sensitivity in the outer core (compare ${}_6S_3$ and ${}_{13}S_3$), a possible indication that the heterogeneity generating the zonal pattern may not be located in the outer core. At the same time, sensitivity to heterogeneity in the inner core is much more

pronounced for ${}_{13}S_3$ and ${}_{13}S_2$ than for ${}_6S_3$.

The splitting function and the differential kernels of mode ${}_{10}S_2$ are shown in Figure 5.10*a*.This mode holds a special position in the history of structural studies of the inner core [*Dziewonski and Gilbert*, 1973; *Masters and Gilbert*, 1981]. Because of its potential coupling with ${}_{11}S_2$, its central frequency and differential kernels are strongly model dependent. The values of ω_0 and Q predicted by PREM do not satisfy the data; a $Q \sim 800$ is observed, much higher than the value ($Q = 192$) predicted by the PREM model. The eigenfunctions and differential kernels in PREM for the modes ${}_{10}S_2$ and ${}_{11}S_2$ are of similar amplitude both in the mantle and in the inner core, making each of them a combination of a *PKIKP*-equivalent mode and an inner core oscillation. It can be shown that even a small (~2%) spherical perturbation of the elastic structure in the inner core is able to effectively decouple the two modes, in such a way that one becomes a *PKIKP*-equivalent mode and the other is almost entirely confined within the inner core. An increase in inner-core S velocity of PREM by ~2%, for example, results in ${}_{10}S_2$ becoming the observable mode at the surface, with central frequency and Q consistent with the spectral observations; ${}_{10}S_2$ becomes effectively decoupled from ${}_{11}S_2$ (this will be treated more fully in a subsequent contribution).

The modified differential kernels for ${}_{10}S_2$ (Figure 5.10*a*) are very similar to those of the *PKIKP* modes (cf. Figure 5.9); the derived splitting function is also similar and is dominated by the c_{20}, c_{40}, and c_{22} terms. The splitting properties of mode ${}_{10}S_2$ confirm its nature as a *PKIKP* mode and the likelihood that it is largely uncoupled with ${}_{11}S_2$.

Three anomalous long-period modes, ${}_3S_1$, ${}_3S_2$, and ${}_2S_3$, are displayed in Figures 5.10*b*–5.10*d*. Their periods, 1059s, 903s, and 805s, are much longer than for the *PKIKP* modes in Figure 5.9, and they provide important constraints on earth models. While the kernels here are again not totally dissimilar, unlike the modes of the groups previously illustrated, the splitting functions are profoundly different. Mode ${}_3S_1$ lacks any sensitivity to degrees higher than 2. Its α and β kernels for degree 2 are of opposite sign in the lower mantle, and kernels in the outer core decrease with

depth, and are essentially zero in the inner core. The splitting function is very small; the splitting properties of ${}_3S_1$ are very well predicted by the effects of rotation in the PREM model (cf. Figure 5.10*c*, Table 4.1). The incongruity of large differential kernels associated with a small splitting function requires an explanation; a possible solution invokes an homogeneous outer core and efficient cancellation between the effects of the heterogeneities in α and β in the mantle, provided the heterogeneity in β is larger than and proportional to that in α.

The differential kernels for mode ${}_3S_2$ are more complex in the mantle and larger for degree 2 in the inner core, and display high sensitivity to a perturbation of the core-mantle boundary at degree 4 (off scale in Figure 5.10*c*). The splitting function, dominated by the c_{40} and c_{20} terms, is very large.

Finally ${}_2S_3$ has similar kernels to those of ${}_3S_2$, and a large zonal splitting function, dominated by c_{20} and, to a lesser extent, by other degree 2 terms (Figure 5.10*d*). It should be noted that the degree 2 terms omitting c_{20} are highly correlated across most of the multiplets of Figures 7-11. For instance, for ${}_2S_3$ correlation coefficients of such terms with those of ${}_1S_7$, ${}_0S_6$, and ${}_1S_8$ are 0.96, 0.83, and 0.97 respectively, a strong indication of a common origin for these terms in the mantle. The significance levels of these correlations are 99.0%, 91.8%, and 99.4%.

Chapter 6

Forward Modeling of Splitting Functions Using Existing Mantle Models

So far we have discussed the retrieval of the splitting functions of some uncoupled, long-period modes. These can be combined in a linear inversion for an aspherical model of the Earth's mantle and core; such a procedure will be detailed in the next chapter. Here, however, we make use of existing models of the upper and lower mantle, obtained by other techniques, and seek to determine the extent to which these models are consistent with the splitting properties of the modes. We limit our investigation to modes sensitive only to heterogeneity in the mantle, and compare the splitting functions predicted from existing models with those retrieved from the modal data.

A variety of models of mantle heterogeneity has been developed in the last few years. For example, the model M84A [*Woodhouse and Dziewonski*, 1984] has been obtained by waveform inversion of mantle waves, and describes the S-velocity structure of the upper mantle. For the lower mantle, models are available from tomographic inversions of travel time data for P waves [*Dziewonski*, 1984; *Morelli and Dziewonski*, 1987b], representing the lower mantle P-velocity structure. Since the splitting properties of normal modes depend on the combined heterogeneity in α (P

velocity), β (S velocity), and ρ, both in the upper and lower mantle, we must assume proportionality laws between these aspherical perturbations in order to predict splitting functions:

$$\delta \ln \alpha = \mathcal{P} \delta \ln \beta \tag{6.1}$$

$$\delta \ln \rho = \mathcal{R} \delta \ln \alpha \tag{6.2}$$

In this chapter we shall first investigate the constraints on the factors $\mathcal{P}$ and $\mathcal{R}$ for the lower mantle provided by the splitting coefficients we have retrieved. Once the proportionality factors have been chosen, it becomes very straightforward to calculate the synthetic splitting functions from existing earth models. At the end of this chapter, we compare these synthetic splitting functions with those retrieved from the modal data (see Chapter 5).

6.1 The Relative Amplitudes of Lower-Mantle Heterogeneity in P and S Velocities

Lateral heterogeneity in seismic velocities and density in the mantle reflect variations in temperature and, possibly, in chemical composition. Thus knowledge of the relationship among the perturbations in P-velocity (α), S-velocity (β), and density (ρ), in conjunction with experimental results on rock properties at mantle conditions, has the the potential to discriminate between different mineralogies and different hypotheses concerning the cause of heterogeneity. Based upon laboratory experiments on the change in rock properties with temperature, *Anderson et al.* [1968] have concluded $d \ln \alpha / d \ln \beta = 0.8$ and $d \ln \rho / d \ln \alpha = 0.5$ and these values have been often adopted for the Earth's mantle (e.g., *Forte and Peltier* [1987]; *Ritzwoller et al.* [1988]). However, other authors have questioned the validity of these values for the lower mantle [*Anderson*, 1987; *Yeganeh-Haeri et al.*, 1989], where temperature and pressure are simultaneously high and many material properties are still unknown.

Previous attempts to estimate of $d \ln \alpha / d \ln \beta$ from seismic data have been based upon the comparison P and S station corrections (e.g., *Hales and Doyle* [1967];

Wichens and Buchbinder [1980]), which largely reflect upper mantle heterogeneity. Such studies generally concern limited areas for which S arrival times have been carefully reread for selected earthquakes. *Souriau and Woodhouse* [1985] have addressed the problem by making a worldwide comparison between the predicted S-wave delays of the upper mantle model M84C [*Woodhouse and Dziewonski*, 1984] with P station corrections [*Dziewonski and Anderson*, 1983]. These studies generaly indicate low values (0.42 – 0.75) of $d\ln\alpha/d\ln\beta$ for the upper mantle, a result which has been ascribed to the existence of partial melting in the upper mantle [*Hales and Doyle*, 1967].

In recent years, large-scale three-dimensional mantle models have been developed for both α and β. Direct comparison of these models immediately yields estimates on the value of $d\ln\alpha/d\ln\beta$. For example, *Morelli and Dziewonski* [1987b] have developed a P-velocity model V.3 for the lower mantle based on P travel time residuals (this model is very similar to the model L02.56 of *Dziewonski* [1984]); by modeling the waveforms of SH body waves, *Woodhouse and Dziewonski* [1986] have constructed a model of shear velocity heterogeneity in the lower mantle (this model will be referred to as SW).

The value of $d\ln\alpha/d\ln\beta$ in the lower mantle determined from these two models is also low (< 0.5). This is a particularly interesting result, since partial melting is a less likely explanation for the lower mantle than for the upper mantle. Two possible explanations involving the physics of mantle minerals at lower mantle conditions have been proposed by *Anderson* [1987] and by *Yeganeh-Haeri et al.* [1989]. Owing to the imperfect, and different, resolution of these two models, however, there remains the possibility that one or both of them are underestimates of the true heterogeneity of the lower mantle. It is also possible that the magnitude of heterogeneity is frequency dependent, and thus the results of comparing models based upon data at different frequencies could be biased by such an effect.

Here, we approach the problem by making use of the splitting functions we have retrieved, which are sensitive to the perturbations in α and β simultaneously and thus provide constraints on $d\ln\alpha/d\ln\beta$ from the same kind data.

Based upon the splitting of normal modes, *Giardini et al.* [1987, 1988] reported evidence that lateral variations in P-velocity are proportional to to those in S-velocity in the lower mantle. In these studies the the optimal value for $d\ln\alpha/d\ln\beta$, assumed constant in the lower mantle, was found to be approximately 0.4. This result was somewhat preliminary and potentially is open to the criticism [*Ritzwoller et al.*, 1988] that a larger value could be accommodated if a suitable model of core-mantle boundary (CMB) topography were introduced. Hence the evidence for the a small value of $d\ln\alpha/d\ln\beta$ given in *Giardini et al.* [1987] was not unequivocal.

It is our purpose here to treat the problem more completely, and to determine confidence intervals for the derived values. We make use of the splitting coefficients of 17 mantle modes. The selected modes may be partitioned into two categories: (1) modes whose sensitivity in the lower mantle is mainly to S-velocity heterogeneity and (2) modes primarily sensitive to P-velocity structure. In order to eliminate possible contamination from CMB topography, we group the CMB-sensitive modes into pairs. For each pair, a combined set of splitting coefficients is constructed by taking linear combinations of the splitting coefficients of the individual modes in such a way that the resulting coefficients have vanishing sensitivity to CMB topography. The combined splitting coefficients are then used to constrain the value of $d\ln\alpha/d\ln\beta$ with no contamination from CMB structure. Since the splitting functions currently retrieved are insufficient to yield independent heterogeneous models of α and β, from which the approach to the problem of estimating $d\ln\alpha/d\ln\beta$ would be very straightforward, we perform the analysis in the data (splitting coefficient) space with the help of preexisting heterogeneous mantle models.

One group of modes used in this study is, in the lower mantle, mainly sensitive to the heterogeneity in shear velocity. The splitting functions of these modes and the P-velocity model V.3 [*Morelli and Dziewonski*, 1987b] may be used to constrain the value of $d\ln\alpha/d\ln\beta$. Another group of modes, which is sensitive mainly to P-velocity heterogeneity in the lower mantle, can be used to determine the extent to which the the magnitude of heterogeneity in the model V.3 is consistent with modal splitting; this will be quantified in terms of a multiplying factor by which

the perturbations of V.3 need to be amplified or deamplified in order to obtain agreement with the modal results. This factor could also be interpreted as a measure of the frequency dependence of heterogeneity, since V.3 is based upon travel time anomalies of waves having periods of approximately 1s, whereas the modal periods are more the two orders of magnitudes greater. By estimating and making use of this factor, a correction can be made to eliminate the potential bias in estimating the value of $d\ln\alpha/d\ln\beta$. Parallel but independent analyses can be made by comparing the splitting data and the S-velocity model [*Woodhouse and Dziewonski*, 1986]; the characteristic period of the data used in constructing this model is of the order 60s.

In four experiments 1a, 1b, 2a, and 2b described below we seek to estimate the values of ratios which we denote by α^{TT}/β^{MD}, α^{MD}/α^{TT}, α^{MD}/β^{SW}, and β^{MD}/β^{SW}, respectively, where the symbol α^{TT}/β^{MD} indicates the ratio of the relative perturbations in α as constructed from the travel-time model (V.3) and in β as required by the modal data, β^{MD}/β^{SW} denotes the ratio of the relative perturbations in β as required by the modal data and in β as constructed from the SH-waveform model (SW), etc. These four ratios are to be used to draw our final, 'debiased', conclusion on the value of $d\ln\alpha/d\ln\beta$ in the lower mantle.

6.1.1 Experiment 1a: Value of α^{TT}/β^{MD}

Modes ${}_0S_4$, ${}_0S_5$, ${}_0S_6$, ${}_0S_7$, ${}_0S_9$, ${}_1S_5$, ${}_1S_6$, ${}_1S_7$, ${}_1S_8$, ${}_3S_8$, ${}_4S_4$, and ${}_5S_3$ are, in the lower mantle, principally sensitive to the heterogeneity in β with some minor sensitivity to the heterogeneity in ρ. The differential kernels $A_s(r)$, $B_s(r)$, and $R_s(r)$ (see (2.31)–(2.33)) of these 12 modes for $s = 2$ and 4 are plotted in Figure 6.1. At the bottom of each panel in Figure 6.1 we also show the sensitivity to topographic perturbations (kernels H_s in (2.28)) of the four major discontinuities – the surface, 670-discontinuity, the core-mantle boundary (CMB), and the inner-core boundary, (the kernels for the inner-core boundary are so small that they vanish from sight in Figure 6.1). The strong sensitivity to the CMB perturbation of most these modes is evident.

Considering the fluid outer core to be laterally homogeneous [*Stevenson*, 1987],

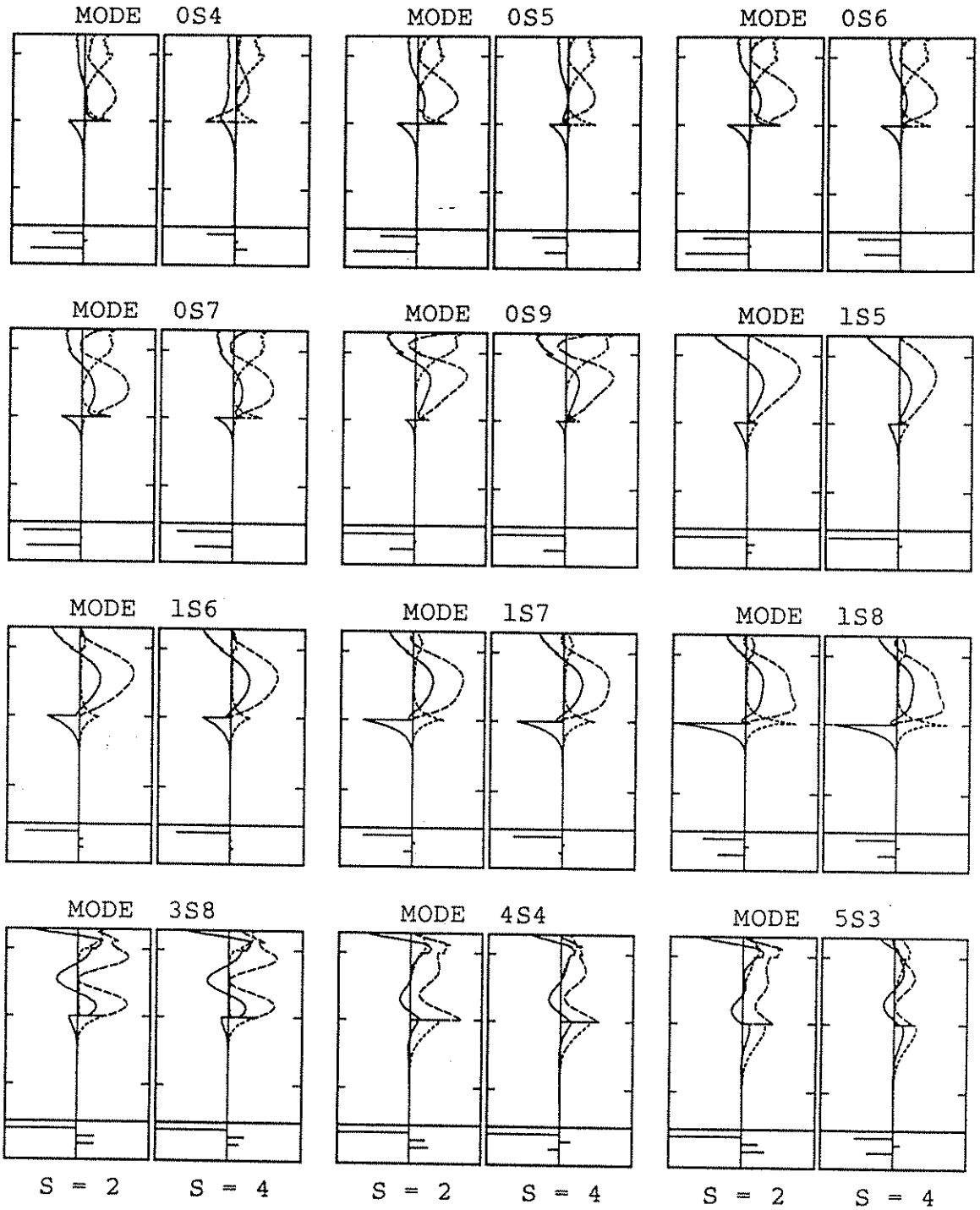

Fig. 6.1 Differential kernels (see (2.31), (2.32), and (2.33)) for spherical harmonic degrees 2 and 4 of some modes. The sensitivities of splitting functions, as a function of depth, to perturbations in v_P (dotted lines), v_S (dashed lines), and ρ (solid lines) are plotted in the upper panels. On side margins, the 670 discontinuity, the core-mantle boundary (CMB), and the inner-core boundary (ICB) are marked from the top down. The horizontal scale is $\pm 4/a$, where a is the radius of the Earth. In the lower panels, kernel coefficients H_s defined in (2.28) are plotted, from top to bottom, for the free surface, the 670 discontinuity, the CMB, and the ICB, with the scale running from -1 to $+1$. The kernels for the ICB of these modes are so small that they vanish from sight.

we may assume that the splitting of these modes is from three sources: (1) the heterogeneity in β of the lower mantle – since both the relative perturbation in ρ and its associated kernels are smaller than those in β, we may neglect the contributions from the perturbation in ρ of the lower mantle; (2) upper mantle structure; and (3) the topography of the CMB.

Since we are concerned with the relationship between perturbations in the velocities of the mantle, it is convenient to eliminate the splitting effects of CMB topography from the analysis. This can be done by grouping the 12 modes into 6 pairs and forming 6 "hybrid modes" A, B, C, D, E and F. Specifically, hybrid mode A is a combination of modes ${}_5S_3$ and ${}_0S_6$, weighted by factors .941 and .338 respectively, i.e., the splitting function coefficients and the differential kernels of mode A are the combinations of the corresponding splitting function coefficients and differential kernels of modes ${}_5S_3$ and ${}_0S_6$, with weights .941 and .338 respectively. We can write this symbolically as A= $.941_5S_3 + .338_0S_6$. In this notation the other hybrid modes are B= $.949_3S_8 + .314_0S_4$, C= $.989_1S_5 + .147_1S_8$, D= $.993_1S_7 - .116_0S_5$, E= $.943_4S_4 + .332_0S_7$ and F= $.990_1S_6 + .141_0S_9$. The differential kernels for $s = 2$ and 4 of these 6 hybrid modes are shown in Figure 6.2. The vanishing of the sensitivity to the CMB structure for $s = 2$ of these hybrid modes is evident, and for $s = 4$ the sensitivities to the CMB are very small, except for modes A and E. In this experiment we use the splitting function coefficients of $s = 2$ of all 6 hybrid modes and the coefficients of $s = 4$ of modes B, C, D, and F.

For each of the selected splitting function coefficients, we may write

$$c_{st} = c^{\beta}_{st} + \bar{c}_{st} + \varepsilon_{st} \tag{6.3}$$

where c_{st} are splitting function coefficients from modal inversion (they are combinations of coefficients listed in Table 5.2), c^{β}_{st} are the synthetic ones due to the heterogeneity in β of the lower mantle, $\bar{c}_{st}$ are the contributions from the upper mantle, and ε_{st} are error terms. Now let us assume that the relative perturbation in α and that in β are proportional to each other with a proportionality coefficient $\mathcal{P} = d\ln\alpha/d\ln\beta$. Under this assumption c^{β}_{st} can be calculated from the P-velocity model V.3 by virtue of (2.12)–(2.30)

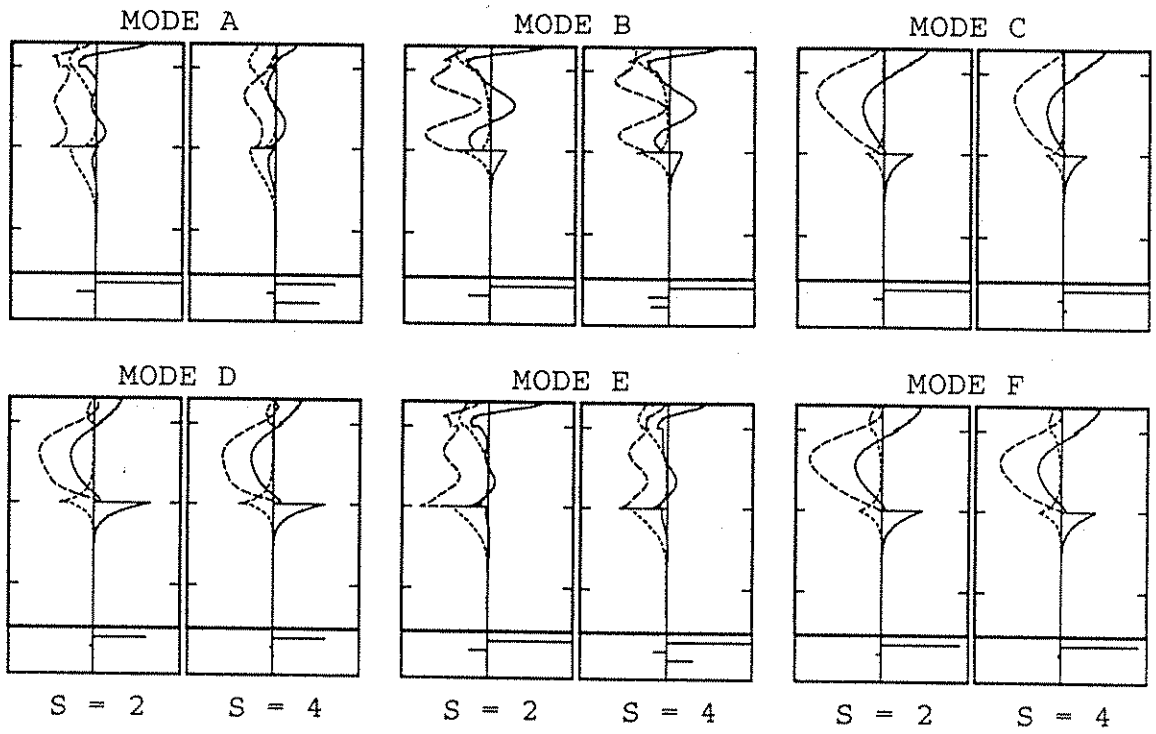

Fig. 6.2 Differential kernels for spherical harmonic degrees 2 and 4 of 6 artificial modes. Each artificial mode is a combination of two real modes, combined in such a way that it has zero sensitivity to the undulation of the core-mantle boundary for degree 2. See caption to Figure 6.1 for more details.

$$c_{st}^{\beta} = \int_{r_C}^{r_{670}} B_s(r)(\delta\beta_{st}/\beta)dr = \int_{r_C}^{r_{670}} B_s(r)(\delta\alpha_{st}/\alpha)/\mathcal{P}dr = c_{st}^{\beta\alpha}/\mathcal{P} \tag{6.4}$$

with

$$c_{st}^{\beta\alpha} = \int_{r_C}^{r_{670}} B_s(r)(\delta\alpha_{st}/\alpha)dr \tag{6.5}$$

where r_{670} and r_C are the radii of the 670-discontinuity and the core-mantle boundary respectively, the coefficients $\delta\alpha_{st}$ are those given by V.3, and the differential kernels $B_s(r)$ are given in (2.32).

In order to estimate $\mathcal{P}$ from (6.3), we need to make use of an upper mantle model to calculate $\bar{c}_{st}$. We explore two different strategies: (1) we take the S-velocity model M84A [*Woodhouse and Dziewonski*, 1984] and assume $d\ln\rho/d\ln\beta = 0.25$ and $d\ln\alpha/d\ln\beta = 0.5$; and (2) since the pattern of heterogeneity in the upper mantle is not highly correlated with that in the lower mantle (see *Dziewonski* [1984] and *Woodhouse and Dziewonski* [1984]) we simply set $\bar{c}_{st} = 0$ and consequently incorporate upper mantle contributions into the error terms, ε_{st}. The comparison of results using each of these strategies (see below) serves to quantify the influence of upper mantle structure on the results.

If we now assume that ε_{st} are independent, normal random variables with same variance, the statistical distribution of the parameter $\mathcal{P}$ in eq. (6.4) can be derived. The details of this derivation are given in the Appendix 6A.

Two solid curves in Figure 6.3*a* show the distributions of $\mathcal{P}$: the upper panel represents the result by using M84A for the upper-mantle correction, and the lower panel is for the case in which no upper-mantle correction is made. The least-squares estimators $\widehat{\mathcal{P}}$ (see Appendix 6A) for the two case are 0.37 and 0.41, respectively.

6.1.2 Experiment 1b: Correction for α^{MD}/α^{TT}

The distributions of $\mathcal{P}$ obtained in Experiment 1a could be biased due to the potential overestimate or underestimate of V.3 with respect to the modal inversion. This experiment is designed to give an estimate of the mutual overestimate or underestimate. In Figure 6.4 we plot the differential kernels of modes ${}_4S_3$, ${}_5S_4$, ${}_5S_5$,

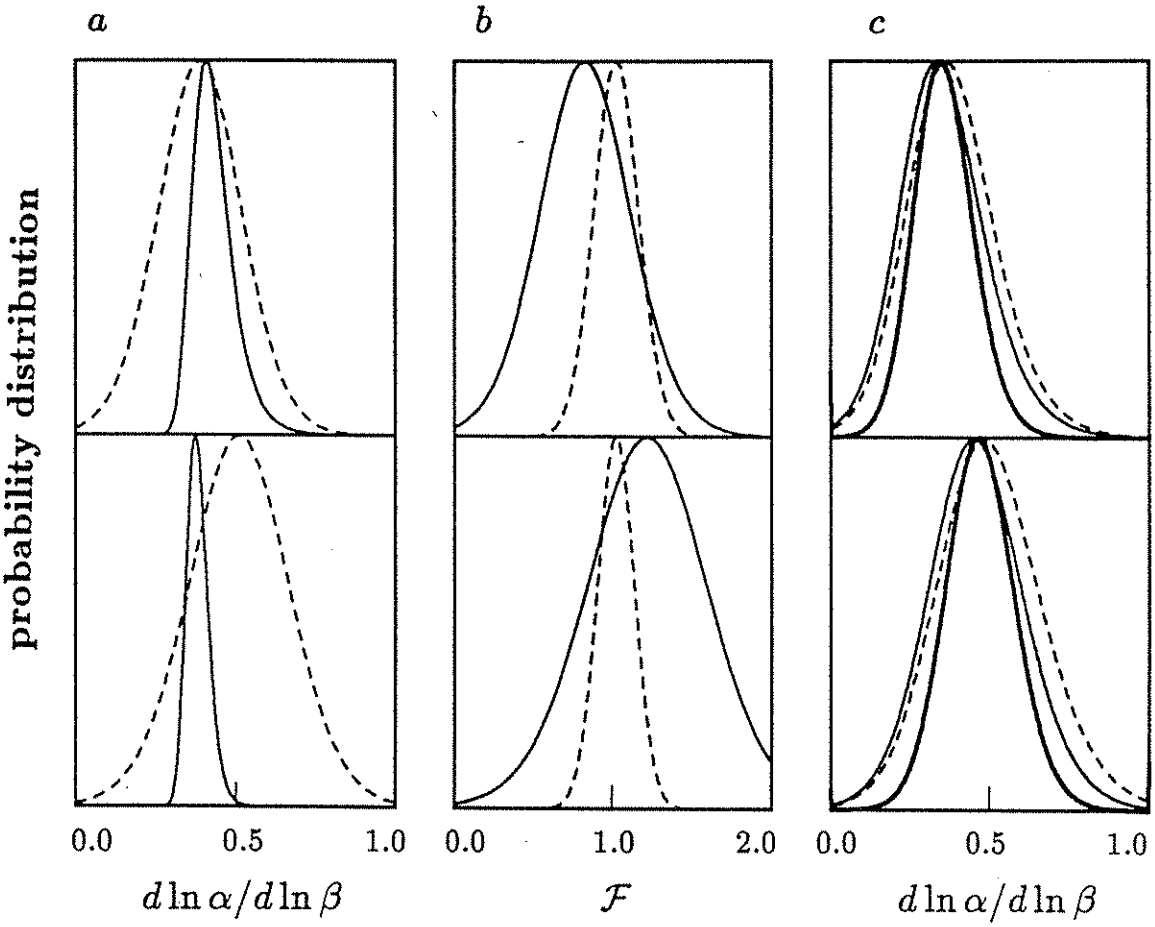

Fig. 6.3 Statistical distributions of esitimators of $d\ln\alpha/d\ln\beta$ for the lower mantle. The results in the upper panels are achieved with correction for the upper-mantle heterogeneity, while the results in the lower panels are derived without upper-mantle corrections. The distributions are constrained by the splitting functions of some mantle modes with two existing heterogeneous mantle models – the thin solid curves represent the results by using model V.3 and the dashed lines are for the results by using model SW. (*a*) Distributions of estimators of $d\ln\alpha/d\ln\beta$ are derived from observed splitting functions and synthetic splitting functions from the existing lower-mantle models. (*b*) Distributions of the estimator $\mathcal{F}$ are plotted, where $\mathcal{F}$ characterizes the potential overestimate ($\mathcal{F} < 1$) or underestimate of the existing model with respect to the effect of modal results. (*c*) The estimators of of $d\ln\alpha/d\ln\beta$ have been corrected for the biases due to the potential overestimates, with respect to the effect of modal results, of the Earth models used. The heavy solid curves are the joint distributions obtained by using V.3 and by using SW, assuming the two results are independent.

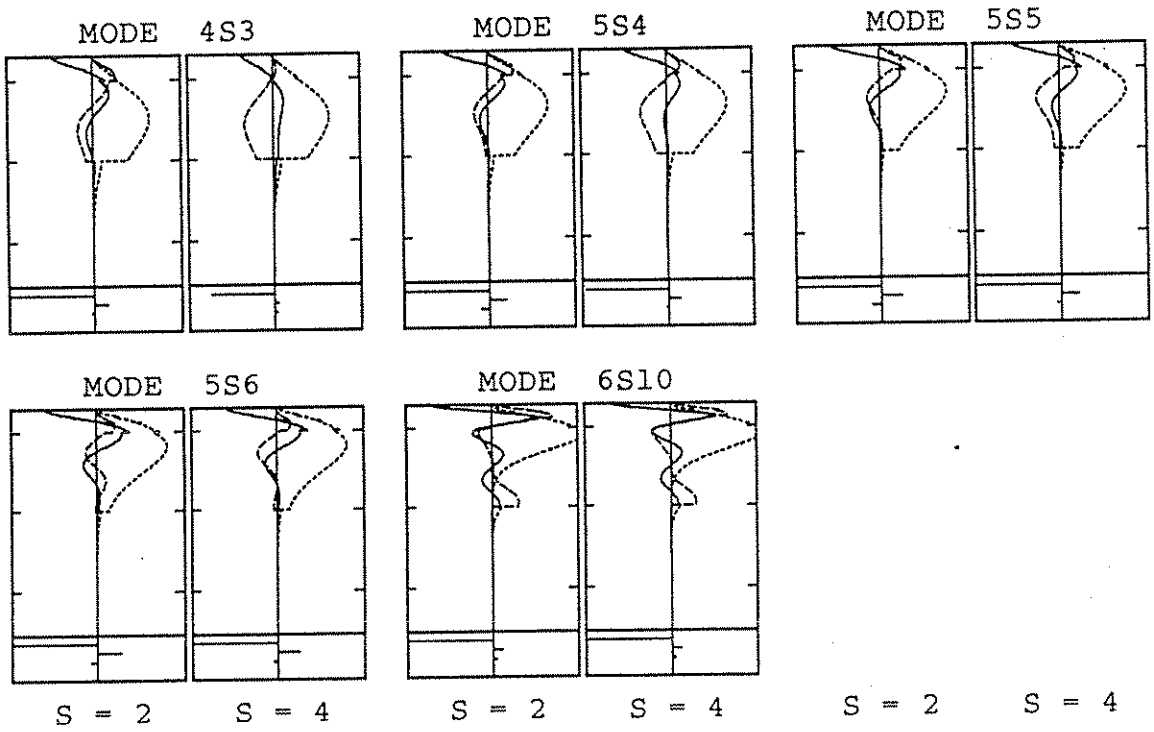

Fig. 6.4 Differential kernels for spherical harmonic degrees 2 and 4 of some modes. These 5 modes are mainly sensitive to the P velocity structure in the lower mantle. See caption to Figure 6.1 for details.

${}_5S_6$ and ${}_6S_{10}$. In this experiment we do not use mode ${}_6S_{10}$ since it is sensitive mostly to the top part of the lower mantle where the resolution of V.3 is relatively poor (A. M. Dziewonski, personal communication), however this mode is employed in Experiment 2a, below. For the spherical harmonic degree $s = 2$, these modes are, in the lower mantle, sensitive mainly to the heterogeneity in P-velocity, and their sensitivities to the CMB undulation are very small. Therefore we may write

$$c_{st} = \int_{r_C}^{r_{670}} A_s(r)(\mathcal{F}\delta\alpha_{st}/\alpha)dr + \bar{c}_{st} + \varepsilon_{st} \qquad s = 2 \tag{6.6}$$

where coefficients $\delta\alpha_{st}$ are again taken from V.3, the factor $\mathcal{F}$ characterizes the potential overestimate or underestimate of V.3 with respect to the modal inversion, and $\bar{c}_{st}$ are the contributions from the upper mantle. As previously for $\mathcal{P}$,we make use of (6.6) to find the probability distributions of $\mathcal{F}$, which are presented by the two solid curves in Figure 6.3*b*. Again the upper panel shows the result obtained using M84A for the upper-mantle correction and the lower panel is for the case in which no upper-mantle correction is made. We may regard the distributions of $\mathcal{P}$ shown in Figure 6.3*a* as conditional distributions with the condition $\mathcal{F} = 1$. The unconditional value of $d\ln\alpha/d\ln\beta$, then, is given by $\bar{\mathcal{P}} = \mathcal{P}\mathcal{F}$. Using the distributions of $\mathcal{P}$ and $\mathcal{F}$ previously found, we may calculate the distributions of $\bar{\mathcal{P}}$, the results are given by the thin solid lines in Figure 6.3*c*.

6.1.3 Experiment 2a: Value of α^{MD}/β^{SW}

The above analyses are based on comparisons of modal splitting coefficients with those calculated using the P-velocity model V.3 of *Morelli and Dziewonski* [1987b]. A parallel, but independent, analysis can be performed by comparing between observed splitting functions with those predicted using the S-velocity model SW [*Woodhouse and Dziewonski*, 1986].

Writting $d\ln\alpha/d\ln\beta = \mathcal{P}$, and using S-velocity coefficients $\delta\beta_{st}$ from SW, we have

$$c_{st} = \int_{r_C}^{r_{670}} A_s(r)(\mathcal{P}\delta\beta_{st}/\beta)dr + \bar{c}_{st} + \varepsilon_{st} \qquad s = 2 \tag{6.7}$$

for modes ${}_4S_3$, ${}_5S_4$, ${}_5S_5$, ${}_5S_6$ and ${}_6S_{10}$, using the same argument as was used in Experiment 1b. The estimated probability distributions of $\mathcal{P}$ are shown by dashed curves in Figure 6.3*a*.

6.1.4 Experiment 2b: Correction for β^{MD}/β^{SW}

To estimate the potential overestimate or underestimate of SW with respect to the modal data, we use the splitting function coefficients of hybrid modes A, B, C, D, E, and F (see Experiment 1a). The coefficients of spherical harmonic degree 4 of modes A and E are omitted as in Experiment 1a. We write, for the selected splitting coefficients:

$$c_{st} = \int_{r_C}^{r_{670}} B_s(r)(\mathcal{F}\delta\beta_{st}/\beta)dr + \bar{c}_{st} + \varepsilon_{st} \tag{6.8}$$

where $\mathcal{F}$ characterizes the potential overestimate or underestimate of SW. The distribution of $\mathcal{F}$ derived from (6.8) are shown as dashed curves in Figure 6.3*b*.

A "debiased" estimate of the ratio $d\ln\alpha/d\ln\beta$ from the comparisons between SW and splitting coefficients is $\tilde{\mathcal{P}} = \mathcal{P}/\mathcal{F}$, where $\mathcal{P}$ is that estimated in Experiment 2a. The probability distributions of $\tilde{\mathcal{P}}$ are given by the dashed lines in Figure 6.3*c*.

6.1.5 Estimate of $d\ln\alpha/d\ln\beta$ in the lower mantle

Since the estimator $\bar{\mathcal{P}}$ obtained in Experiment 1 and the estimator $\tilde{\mathcal{P}}$ obtained in Experiment 2 may be regarded as independent[1], the product of the distributions of the two distributions gives the distribution of the joint estimate of the parameter $\mathcal{P} = d\ln\alpha/d\ln\beta$. The results are represented by the thick solid lines in Figure 6.3*c* (again the upper panel shows the result obtained using M84A for the upper-mantle

[1]Strictly speaking they are not completely independent since the error terms ε_{st} in (6.3), (6.6), (6.7), and (6.8) have common sources – parts of them are from the errors in retrieved splitting functions. However, these errors influence the distributions of $\bar{\mathcal{P}}$ and $\tilde{\mathcal{P}}$ in opposite ways, so that the relationship between $\mathcal{P}$ and ε_{st} is reversed from (6.3) to (6.7); the errors from other sources (errors of V.3 and SW) are clearly independent. Therefore the independence of $\bar{\mathcal{P}}$ and $\tilde{\mathcal{P}}$ may still be assumed.

Table 6.1: Confidence Intervals for Estimating $\mathcal{P} = d\ln\alpha/d\ln\beta$

confidence level	99%	95%	90%	75%
M84A used as correction	$.12 < \mathcal{P} < .63$	$.18 < \mathcal{P} < .55$	$.21 < \mathcal{P} < .51$	$.25 < \mathcal{P} < .45$
no upper-mantle corrections	$.19 < \mathcal{P} < .78$	$.26 < \mathcal{P} < .69$	$.30 < \mathcal{P} < .65$	$.35 < \mathcal{P} < .59$

correction and the lower panel is for the case in which no upper-mantle correction is made).

Minimum length confidence intervals for $\mathcal{P} = d\ln\alpha/d\ln\beta$, derived from the distributions of Fig. 6.3, are given in Table 6.1. Again, results are given for the two cases – with and without the upper mantle correction – and for confidence levels of 99%, 95%, 90% and 75%.

The distribution of $\mathcal{P}$ obtained using the upper mantle correction (upper panel in Fig. 6.3*c*) is somewhat narrower than the case without such a correction, indicating that the upper mantle model is helpful, overall, in explaining the modal observations. Perhaps this is not surprising, since it is clearly more reasonable to assume that upper mantle heterogeneity is that of M84A than to assume that the upper mantle is homogeneous. For this reason we adopt the results with the upper mantle correction in drawing our conclusion that, with 90% confidence, the ratio $d\ln\alpha/d\ln\beta$ for the lower mantle is between 0.21 and 0.51. The value of 0.8 of *Anderson et al.* [1968] based upon laboratory experiments is ruled out with 99% confidence.

It is interesting to reexpress the above result in terms of $d\ln\kappa/d\ln\mu$, where κ is bulk modulus and μ is shear modulus. Through some straightforward algebra, we obtain

$$\frac{d\ln\kappa}{d\ln\mu} = \frac{\mathcal{P} - E}{1 - E - \mathcal{R}_\kappa(1-\mathcal{P})} \tag{6.9}$$

where $E \equiv \frac{4}{3}(\beta/\alpha)^2$ and $\mathcal{R}_\kappa = d\ln\rho/d\ln\kappa$. If we assume that $\mathcal{R}_\kappa$ is a stable parameter and it takes value 0.229 of *Anderson et al.* [1968], we can calculate the probability distribution of $d\ln\kappa/d\ln\mu$ from that of $\mathcal{P}$. Figure 6.5 gives the result using the $\mathcal{P}$-distribution shown by the heavy solid cuve in the upper panel of Figure 6.3*c*. The minimum-length interval of 90% confidence for $d\ln\kappa/d\ln\mu$ is, ac-

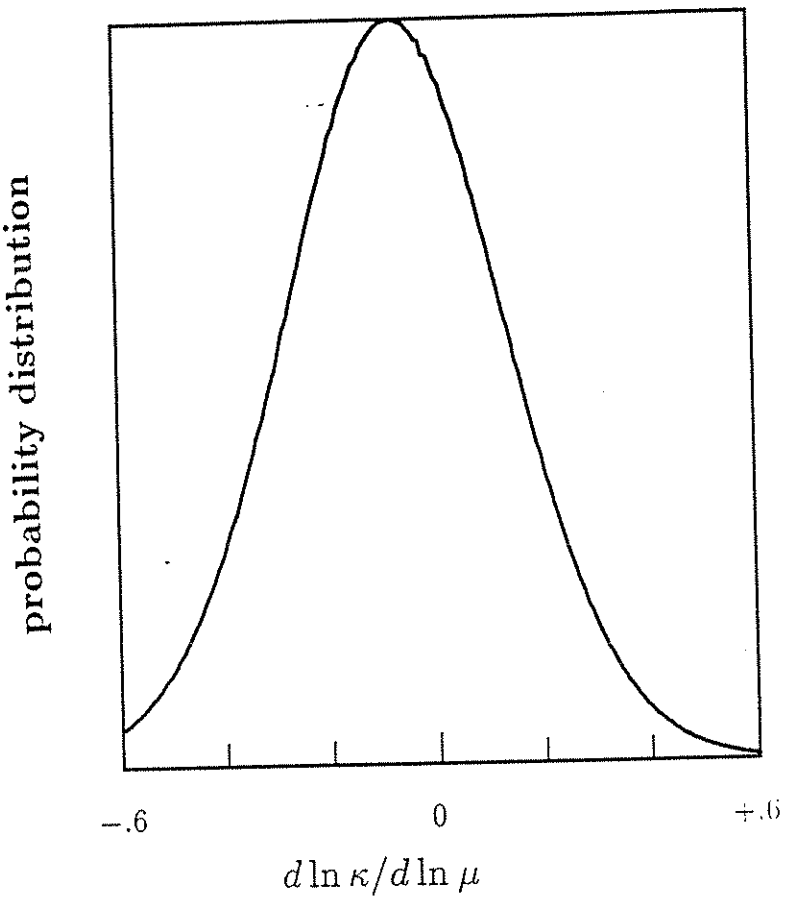

Fig. 6.5 Statistic distribution of $d \ln \kappa / d \ln \mu$. This distribution is converted from the distribution of $d \ln \alpha / d \ln \beta$ shown by the heavy solid curve in the upper panel of Figure 6.3*c*.

cording to Figure 6.5, (−0.41, 0.26). On other grounds, however, it is physically plausible to rule out negative values of $d\ln\kappa/d\ln\mu$. Correspondingly, $d\ln\alpha/d\ln\beta$ is limited to the relative narrow interval (0.39, 0.51). Comparing with the result of *Anderson et al.* ($d\ln\kappa/d\ln\mu = 0.73$), the result presented here indicates that the elastic heterogeneity in the lower mantle is mostly from the perturbation in μ, with κ being relatively homogeneous.

6.1.6 Implications of physical dispersion

The evidence presented here that the heterogeneity as seen by free oscillations is of similar magnitude to that determined using other data sets corresponding to waves of much shorter periods has interesting consequences for the possible lateral variations in attenuation. It is not unreasonable to assume, under the hypothesis that lateral heterogeneity is due to lateral variations in temperature, that there exists proportionality between variations in seismic velocity and in attenuation parameters. Let us suppose that

$$\delta q_\alpha = -\gamma_\alpha \delta\ln\alpha \tag{6.10}$$

where δq_α represents the heterogeneity in inverse quality factor ($q_\alpha = (1-E)Q_\kappa^{-1} + EQ_\mu^{-1}$, with $E = \frac{4}{3}(\beta/\alpha)^2$). Then because of physical dispersion (e.g., *Liu et al.* [1976]) $\delta\ln\alpha$ is necessarily frequency dependent. Perturbing the approximate relation [*Nowick and Berry*, 1972]:

$$\frac{d\ln\alpha}{d\ln\omega} = \frac{1}{\pi} q_\alpha, \tag{6.11}$$

where ω is frequency, we find

$$\frac{d\delta\ln\alpha}{d\ln\omega} = \frac{1}{\pi}\delta q_\alpha = -\frac{\gamma_\alpha}{\pi}\delta\ln\alpha \tag{6.12}$$

which may be regarded as a differential equation for the dependence of heterogeneity ($\delta\ln\alpha$) upon frequency. In order to solve this equation, we may, for example, assume that γ_α is independent of frequency. In this case we obtain

$$\frac{(\ln\alpha)_{\omega_1}}{(\ln\alpha)_{\omega_2}} = \left(\frac{\omega_1}{\omega_2}\right)^{-\frac{\gamma_\alpha}{\pi}} \tag{6.13}$$

or

$$\delta q_\alpha = -\pi \frac{\ln \mathcal{F}}{\ln(\omega_2/\omega_1)} \delta \ln \alpha \tag{6.14}$$

where $\mathcal{F} = (\delta \ln \alpha)_{\omega_1}/(\delta \ln \alpha)_{\omega_2}$. If we assume that the measurement of α^{MD}/α^{TT} performed in Subsection 6.1.2 gives an estimate on $\mathcal{F}$, we may take $\omega_1 \sim 2\pi/500$s, $\omega_2 \sim 2\pi/1$s, and $\mathcal{F} \leq 1.26$, this last value being the upper limit of the minimum-length 90% confidence interval for $\mathcal{F}$ (from the solid curve in the upper panel of Figure 6.3*b*). Taking $\pm 0.2\%$ to be the typical level of heterogeneity in α (in spherical harmonic degrees 2 and 4) these values give $|\delta q_\alpha| \leq 2.34 \times 10^{-4}$. A reasonable alternative assumption to solve (6.12) is that the heterogeneity δq_α is independent of frequency, since the average Q value of the Earth's mantle depends weakly upon frequency in the seismic frequency band [*Knopoff*, 1964; *Anderson*, 1967]. In this case, we obtain $|\delta q_\alpha| \leq 2.63 \times 10^{-4}$. Naturally, a similar argument can be made for β and q_β. For the comparison of SW with the modal data (Subsection 6.1.2) we may take $\omega_1 \sim 2\pi/500$s, $\omega_2 \sim 2\pi/60$s, $\mathcal{F} \leq 1.23$, and $|\delta \ln \beta| \sim 0.4\%$, yielding $|\delta q_\beta| \leq (1.23 \text{ or } 1.36) \times 10^{-3}$ if γ_β or δq_β is assumed to be independent of frequency. Assuming that attenuation is entirely in shear ($Q_\kappa^{-1} = 0$), we have, approximately, $\delta Q_\mu^{-1} = \delta q_\beta = 2.56 \delta q_\alpha$, and thus the bound derived from the comparison of V.3 with the modal data represents the more restrictive constraint, namely that heterogeneity in Q_μ^{-1} (in degrees 2 and 4) is no more than $\pm 6.7 \times 10^{-4}$, approximately 20% of the spherically symmetric lower mantle Q_μ^{-1} (from PREM). This result depends upon the assumption that there is no systematic underestimate in the inversion for the V.3 model with respect to the modal results. With more accurate information on the frequency dependence of heterogeneity, it will be possible to obtain more reliable constraints on the magnitude of the heterogeneity in attenuation. It is interesting to note that under the assumptions used here, the magnitude of heterogeneity should decrease with frequency, and thus values of the parameter $\mathcal{F}$, in Subsections 6.1.2 and 6.1.4, which are less than unity, while they are consistent with the data, are rendered implausible.

Based upon our measurements of $\mathcal{F}$, it is also possible to test whether physical dispersion can reconcile the discrepancy between the values of $d \ln \alpha / d \ln \beta$ obtained

here and those inferred from laboratory experiments. In the literature (e.g., *Liu et al.* [1976]; *Kanamori and Anderson* [1977]) band-limited constant Q models are often used. For simplicity, we may approximate such models by

$$q(\omega) = \begin{cases} \bar{q} & \omega_L < \omega < \omega_U \\ 0 & \text{elsewhere} \end{cases} \tag{6.15}$$

where $\bar{q}$ is independent of frequency, and ω_L and ω_U are the low-frequency and high-freqency cutoffs, respectively. Then in the seismic frequency band we have, according to (6.12),

$$\frac{\delta \bar{q}_\alpha}{\delta \ln \alpha} = -\frac{\pi(1-\frac{1}{\mathcal{F}})}{\ln(\omega_2/\omega_1)} \tag{6.16}$$

Equation (6.12) also yields

$$\delta \ln \alpha(\omega) - \delta \ln \alpha(\omega_U) = \frac{1}{\pi} \delta \bar{q}_\alpha \ln \frac{\omega}{\omega_U} \tag{6.17}$$

where ω is the typical frequency for free oscillations. Similarly

$$\delta \ln \beta(\omega) - \delta \ln \beta(\omega_U) = \frac{1}{\pi} \delta \bar{q}_\beta \ln \frac{\omega}{\omega_U} \tag{6.18}$$

Extrapolating the laboratory value, 0.8, of $d\ln\alpha/d\ln\beta$ [*Anderson et al.*, 1968] to the cutoff frequency ω_U, we obtain, by virtue of (6.16), (6.17), (6.18), and the relation $\bar{q}_\alpha \simeq E\bar{q}_\beta$,

$$\frac{d\ln\alpha}{d\ln\beta} = \frac{0.8(1-\Delta_2)}{1+\Delta_1-0.8\Delta_2} \tag{6.19}$$

where Δ_1 and Δ_2 are given by

$$\Delta_1 = \frac{\ln(\omega_U/\omega_1)}{\ln(\omega_2/\omega_1)}\left(\frac{0.8}{E}-1\right)\left(1-\frac{1}{\mathcal{F}}\right) \tag{6.20}$$

$$\Delta_2 = \frac{2}{\pi}\bar{q}_\mu \ln \frac{\omega_U}{\omega_1} \tag{6.21}$$

To evaluate (6.19) we require the value of the cutoff frequency ω_U, which is poorly known. *Sipkin and Jordan* [1979] have reported that when $\omega > 2\pi/10$s, Q appears to increase rapidly with frequency. If we take $2\pi/1$s as our cutoff frequency, ω_U, and make use of the result $\mathcal{F} = 1.26$, (6.19) leads to $d\ln\alpha/d\ln\beta = 0.65$ at $\omega_1 = 2\pi/500$s.

Even with a very high value ($2\pi/0.1$s) of ω_U, an $\mathcal{F}$ larger than 1.69 is required to explain $d\ln\alpha/d\ln\beta < 0.5$. Thus we conclude that other mechanisms, such as those proposed by *Anderson* [1987] and *Yeganeh-Haeri et al.* [1989], are required to reconcile the discrepancy between the $d\ln\alpha/d\ln\beta$ observed here and that obtained from laboratory experiments.

6.2 Relationship between Heterogeneities in Density and in Velocities

Another important geophysical problem is that of the relationship between heterogeneity in density and in seismic velocities. The calculation of the geoid and of plate motions using three dimensional mantle models [*Richards and Hage*, 1984; *Forte and Peltier*, 1987] clearly requires positive values of the ratios $d\ln\rho/d\ln\alpha$ and $d\ln\rho/d\ln\beta$, consistent with a thermal origin for mantle heterogeneity, but constrain these parameters only weakly owing to tradeoffs with viscosity structure and to other uncertainties. Consequently, independent estimates of these ratios would lead to more accurate estimates of mantle viscosity. The study of the Earth's free oscillations provides the sole means of placing seismological constraints on the interior distribution of density anomalies. Here, we demonstrate the possibility of estimating the value of $d\ln\rho/d\ln\alpha$ and examine the power of resolution of the current data.

For each of the mantle modes, we may assume that the splitting coefficients are composed of three parts: (1) the contribution from upper-mantle structure; (2) the contribution from lower-mantle heterogeneities in velocities (α and β); and (3) the contribution from lower-mantle density. Assuming $d\ln\rho/d\ln\alpha = \mathcal{R}$, we may write

$$c_{st} = \bar{c}_{st} + c_{st}^{vel} + \int_{r_C}^{r_{670}} R_s(r)\mathcal{R}(\delta\alpha_{st}/\alpha)dr + \varepsilon_{st} \tag{6.22}$$

where $\bar{c}_{st}$ denote the contributions from the upper mantle, which may be calculated as above, and c_{st}^{vel} are the contributions from the lower mantle velocity structure. The third term on the right side of (6.22) is the contribution from the heterogeneity in density and ε_{st} are error terms. c_{st}^{vel} and $\delta\alpha_{st}$ in (6.22) may be evaluated by using the

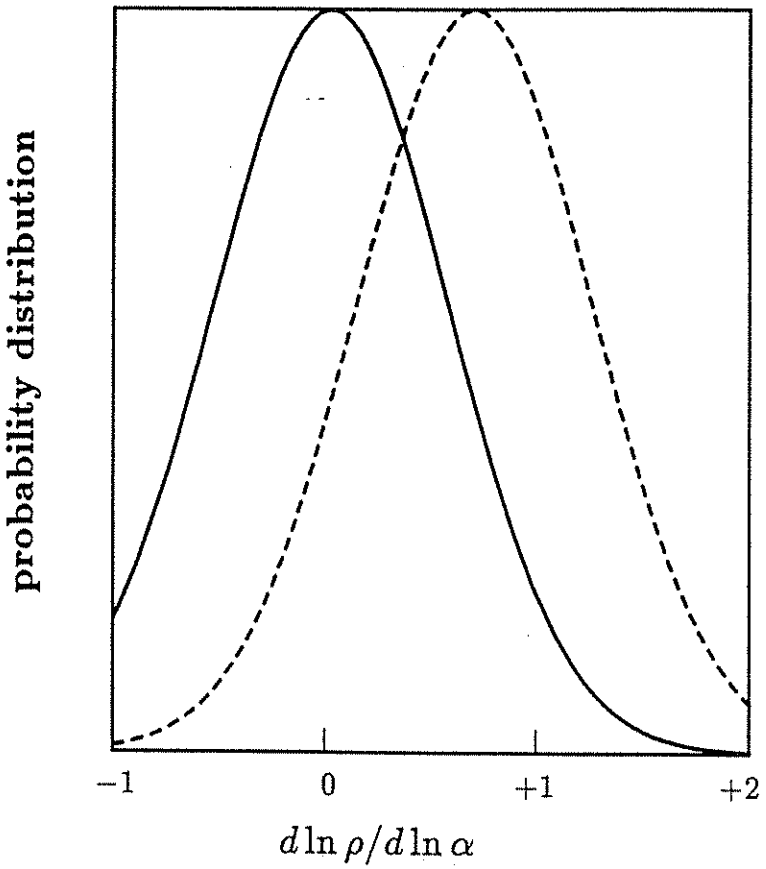

Fig. 6.6 Statistic distributions of the estimator of $d\ln\rho/d\ln\alpha$. The distributions are constrained by the splitting functions of some mantle modes and a P-velocity model V.3 of *Morelli and Dziewonski* [1987b]. The solid curve is the result by assuming $d\ln\alpha/d\ln\beta = 0.35$, and the dashed line corresponds $d\ln\alpha/d\ln\beta = 0.40$.

model V.3, together with multiplying factors determined in the preceding section; we take $\mathcal{P} = d\ln\alpha/d\ln\beta = 0.35$ (the maximum likelihood value from the heavy solid line in the upper panel of Fig. 6.3*c*). Equation (6.22) provides a constraint on the parameter $\mathcal{R} = d\ln\rho/d\ln\alpha$, which can be estimated by the method outlined in the Appendix 6A. We have calculated the probability distribution of the estimator of $\mathcal{R}$, using 25 mantle modes: ${}_0S_3$, ${}_0S_4$, ${}_0S_5$, ${}_0S_6$, ${}_0S_7$, ${}_0S_9$, ${}_1S_3$, ${}_1S_4$, ${}_1S_5$, ${}_1S_6$, ${}_1S_7$, ${}_1S_8$, ${}_2S_4$, ${}_2S_5$, ${}_2S_6$, ${}_2S_8$, ${}_3S_1$, ${}_3S_8$, ${}_4S_3$, ${}_4S_4$, ${}_5S_3$, ${}_5S_4$, ${}_5S_5$, ${}_5S_6$, and ${}_6S_{10}$. The result is given by the solid line in Fig. 6.6. In order to investigate the effect of the uncertainty in in the value taken for $\mathcal{P}$, we have repeated the experiment with the exception that we use $\mathcal{P} = 0.40$ (this value is reasonable upon our information, see Fig. 6.3*c*). The result is shown by the dashed line in Fig. 6.6.

Unfortunately, the constraint on the parameter $\mathcal{R} = d\ln\rho/d\ln\alpha$ of the current data set is not strong enough to provide a useful estimate. However, the possibility of estimating this value from seismic data has been demonstrated, the result being not contradictory to our previous information. The constraints on $\mathcal{R}$ should be improved as more high quality, very long period seismic data become available.

6.3 Prediction of Splitting Functions from Existing Mantle Models

In order to calculate synthetic splitting functions, we may use some results obtained from previous sections. We adopt 0.35 as the value for $d\ln\alpha/d\ln\beta$ in the lower mantle (the upper panel of Figure 6.3*c*). And we assume that the model V.3 [*Morelli and Dziewonski*, 1987b] needs to be multiplied by a factor 0.83 (Figure 6.3*b*, upper panel) to become consistent with the modal data; the model SW [*Woodhouse and Dziewonski*, 1986] needs a factor 1.02 (Figure 6.3*b*, upper panel). Since our modal data accept a broad range of values for the ratio $d\ln\rho/d\ln\alpha$, we simply take the conventional value (0.5) [*Anderson et al.*, 1968].

It should be noted that, because of its larger volume and of the general trend of the modal sensitivities with depth, lower-mantle structure is of greatest importance

in predicting the splitting functions. We have first compared the retrieved splitting functions (Table 5.2) with synthetic ones by using the lower-mantle models only. In Table 6.2 we list the correlation coefficients between the retrieved and predicted splitting functions, together with the corresponding significance levels, which represent the probabilities that two kinds of splitting functions are not independent. We also compare the sizes of these two kinds of splitting functions. The ratios of their r.m.s. amplitudes are given in Table 6.2 also.

To check the importance of upper-mantle structure in predicting the splitting functions, we also list in Table 6.2 the results for the case in which we have used both the lower-mantle and the upper-mantle structures. We have constructed our upper-mantle model as we did in Section 6.1 (see page 115).

First of all, the overall correlation coefficients for all modes together are very high considering that there are 341 degrees of freedom. This indicates that we have successfully retrieved reliable splitting functions for mantle modes in general. It may also be observed that the introduction of upper-mantle structure does not improve the correlation coefficients while it does increases the size of the synthetic splitting functions.

It is not surprising to observe that the best agreement is achieved for fundamental modes (mode ${}_nS_l$ with $n = 0$). We believe that the following two reasons may explain this: (1) these modes are very well excited by earthquakes, and their data, therefore, have high signal-to-noise ratios; and (2) their differential kernels are less oscillatory with depth and thus their splitting behavior is relatively insensitive to the details of the existing models.

Although the overall agreement between predicted and observed splitting functions is good, problems do exist for a few modes.

The splitting behaviors of modes ${}_0S_3$, ${}_1S_3$, and ${}_3S_1$ are well predicted by the spherical earth model PREM together with the rotation and the ellipticity of the Earth (see Table 5.1). Their retrieved splitting functions are therefore very small and comparable with the associated errors. The synthetic splitting functions of these modes are also very small – smaller, on average, than those of other modes

Table 6.2: Comparison of Predicted Splitting Functions with Retrieved Ones

Mode	V.3 alone			V.3+M84A			SW alone			SW+M84A		
	c.c.	s.l.	r	c.c.	s.l.	r	c.c.	s.l.	r	c.c.	s.l.	r
${}_0S_6$	0.89	100	0.54	0.94	100	0.53	0.83	100	0.54	0.90	100	0.52
${}_0S_7$	0.88	100	0.60	0.94	100	0.59	0.81	100	0.60	0.89	100	0.58
${}_0S_9$	0.79	100	0.60	0.93	100	0.67	0.71	100	0.66	0.92	100	0.67
${}_0S_5$	0.89	100	0.55	0.93	100	0.55	0.80	100	0.54	0.86	100	0.53
${}_1S_8$	0.93	100	0.65	0.92	100	0.66	0.87	100	0.65	0.87	100	0.66
${}_1S_7$	0.92	100	0.65	0.91	100	0.66	0.87	100	0.70	0.86	100	0.71
${}_5S_4$	0.56	98	0.22	0.80	100	0.71	0.64	99	0.22	0.85	100	0.69
${}_2S_6$	0.73	100	0.20	0.85	100	1.13	0.19	52	0.20	0.79	100	1.08
${}_1S_6$	0.82	100	0.78	0.81	100	0.83	0.79	100	0.88	0.79	100	0.92
${}_0S_4$	0.81	100	0.51	0.78	100	0.55	0.70	100	0.50	0.73	100	0.51
${}_2S_4$	0.82	100	0.54	0.77	100	0.61	0.82	100	0.49	0.77	100	0.56
${}_5S_5$	0.66	99	0.32	0.73	100	1.00	0.63	99	0.32	0.74	100	0.98
${}_6S_{10}$	0.57	98	0.40	0.69	100	1.32	0.64	99	0.35	0.72	99	1.26
${}_2S_8$	0.61	99	0.28	0.70	100	1.64	0.32	77	0.23	0.67	100	1.56
${}_5S_6$	0.62	99	0.32	0.63	99	1.08	0.74	100	0.39	0.70	100	1.11
${}_1S_5$	0.74	100	0.61	0.63	99	0.81	0.70	100	0.74	0.67	100	0.87
${}_1S_4$	0.76	100	1.65	0.57	98	3.01	0.65	99	2.02	0.60	99	2.95
${}_3S_8$	0.79	100	0.90	0.57	98	1.39	0.64	99	0.69	0.44	91	1.16
${}_1S_3$	0.61	99	10.19	0.56	98	16.51	0.24	63	11.40	0.36	83	15.77
${}_4S_3$	0.45	92	0.27	0.45	92	0.84	0.51	96	0.29	0.50	95	0.81
${}_5S_3$	0.64	99	0.88	0.46	93	2.15	0.51	96	1.03	0.45	92	2.12
${}_2S_5$	0.53	97	0.62	0.37	84	1.50	0.27	69	0.63	0.27	69	1.45
${}_3S_1$	0.14	24	0.61	0.14	24	0.54	0.20	33	0.43	0.19	32	0.43
${}_4S_4$	0.19	52	1.12	0.06	17	2.09	0.01	3	1.09	−0.04	12	1.96
${}_0S_3$	0.17	47	1.60	0.01	3	2.11	0.08	23	1.17	−0.10	29	1.53
Total	0.73	100	0.58	0.67	100	0.97	0.65	100	0.59	0.65	100	0.93

The correlation coefficients between the predicted splitting functions and the those retrieved from modal data are listed in the columns under title "c.c". The corresponding significant levels (in unit of percent) are given in the columns titled by "s.l.". Parameter r represents the ratio of the r.m.s. of the calculated splitting functions and that of the observed ones.

by a factor of 2 for the aspherical components. It is obviously a very difficult and perhaps meaningless task to match these small retrieved and synthetic splitting functions. We should be satisfied, at this stage, as long as they are small.

Modes ${}_4S_3$ and ${}_2S_5$ have been treated simultaneously with ${}_2S_8$ and ${}_1S_6$, respectively, as "overlapping modes" when the splitting functions are retrieved. This means that the number of unknowns is doubled in the inversion. Therefore they are more poorly constrainted by the data, and thus the inversion results may be less reliable.

Since only 11 traces are available for mode ${}_5S_3$ (see Table 5.1), the splitting function of this mode may be constrainted poorly by the data. The inconsistency of the retrieved and predicted splitting function of this mode is probably due to the unreliable results of the inversion.

Mode ${}_4S_4$ is a very interesting mode in terms of its differential kernel. This mode is sensitive mainly to the S-velocity perturbation in the very bottom part of the lower mantle (see Figure 6.1). Its splitting function as retrieved from the seismic data is completely different from those of most mantle modes, and is not well predicted by the existing mantle models. If the retrieved splitting function is reliable, this mode may reveal some new important features of the D'' region which are not reflected by the existing models. Unfortunately, it seems that this mode is among the poorest constrained modes in our inversion (see diagonal elements of resolution matrixes in Table 5.2). We will need more independent information to judge the disagreement between the retrieved and predicted splitting functions.

Appendix 6A

Suppose we wish to estimate $\mathcal{C}$, or $\mathcal{C}^{-1}$, from the equation:

$$y_i = \mathcal{C}x_i + \varepsilon_i\,, \qquad i = 1, 2, \ldots, N \tag{6.23}$$

where y_i and x_i are splitting function coefficients, derived from seismic spectra or calculated from existing earth models; and ε_i are errors, assumed to be independent random variables with the same (unknown) variance. The least-squares estimator $\widehat{\mathcal{C}}$ [*Kendall and Stuart*, 1977a] of $\mathcal{C}$ is given by

$$\hat{C} = \sum_{i=1}^{N} x_i y_i / \sum_{i=1}^{N} x_i^2. \tag{6.24}$$

This estimator itself is a random variable owing to the randomness of ε_i. *Kendall and Stuart* [1977a] show that the statistic

$$\tau = (\hat{C} - C)\left[\sigma^2 / \sum_{i=1}^{N} x_i^2\right]^{-\frac{1}{2}} \tag{6.25}$$

has a Student's t-distribution with $N-1$ degrees of freedom if the distributions of ε_i are normal, where

$$\sigma^2 = \sum_{i=1}^{N} (y_i - \hat{C}x_i)^2/(N-1) \tag{6.26}$$

is the estimator of the variance of ε_i. Equation (6.25) indicates that the fiducial probability distribution [*Kendall and Stuart*, 1977b] of parameter C is given by:

$$df_C \propto [\sigma^2 / \sum_{i=1}^{N} x_i^2]^{-\frac{1}{2}} \cdot t(\tau; N-1) dC \propto t(\tau; N-1) dC \tag{6.27}$$

or

$$df_{\frac{1}{C}} \propto t(\tau; N-1) C^2 d\frac{1}{C} \tag{6.28}$$

where $t(\tau; N-1)$ is the probability density of the t-distribution with argument τ and $N-1$ degrees of freedom, and $\tau = \tau(C)$ is given in eq. (6.25).

Chapter 7

Inversion for Earth Models

7.1 Introduction

In Chapter 5 we have modeled the splitting of 34 multiplets in terms of their splitting functions. These functions are linearly related to the aspherical structure of the Earth's interior through differential kernels, which can be calculated using the formulation developed in Chapter 2. In this Chapter we shall study the earth structure by using the information contained in the split seismic spectra. We employ all the modes listed in Table 4.1 except mode ${}_{10}S_2$. As we pointed out in Chapter 5, the differential kernels for mode ${}_{10}S_2$ depend strongly on the reference model we choose, due to possible coupling with ${}_{11}S_2$. We omit it here in order to avoid special treatment for this mode. We believe that the results and the conclusions of this chapter would still hold if ${}_{10}S_2$ were included, since its behavior is very similar to other *PKIKP* modes.

Using c_{st} coefficients listed in Table 5.2 as data, an inverse problem is defined by (2.12) where δh^d_{st}, $\delta \mathbf{m}_{st}$, and $\delta \bar{\mathbf{m}}_{st}$, are treated as unkowns. The problem can be solved by regular linear least-squares methods.

An alternative procedure is to find earth models to directly fit the original data from which we have retrieved our splitting function coefficients. The inverse problem is in principle posed by (2.6), (2.8), and (2.12): retrieving the earth structure δh^d_{st}, $\delta \mathbf{m}_{st}$, and $\delta \bar{\mathbf{m}}_{st}$ from data $u(t)$. This is a nonlinear problem and we solve it

iteratively.

The first procedure obviously has a great advantage. Having retrieving splitting function coefficients, c_{st}, accurately enough, the problem becomes very simple. The model parameters of spherical harmonic degree s and order t are controlled only by the splitting function coefficients of the same degree and order, as indicated by (2.12). Therefore the inverse problem is decoupled into a number of low-dimensional linear problems. This enables us to do many experiments to test the a priori constraints on the models. As more high-quality digital seismic stations are deployed and as these stations record more large events, we can continually retrieve new c_{st} coefficients for different modes and for higher degrees and improve those results which are not well-constrained.

Although following the second method is a time-consuming procedure, we think it is still valuable, at this stage, to solve the problem by directly fitting the original seismic traces. When we invert for splitting functions mode by mode, there is no guarantee that the resulting splitting function is the unique solution which represents a property of the Earth. If the splitting-function solution is not the one corresponding to reality, we are in danger of inferring erroneous earth models or of not being able to find any satisfactory model. By following the second procedure, we should overcome the possible inconsistency of the inferred splitting functions, since they are constrained by the requirement that they all be consistent with a single earth model. Models developed by such a one-step method are also expected to be statistically better constrained.

The inversion for the aspherical structure of the Earth is strictly a continuous inverse problem; as such, a complete solution is impossible. Using a finite collection of data, we are limited to solutions of finite resolution which are smoothed or filtered versions of reality. We begin by choosing a set of parameters which, we believe, can best describe the structure of the Earth which causes modal splitting.

7.2 Modeling Parameters

The splitting of normal modes depends, simultaneously, on the three-dimensional distributions of P-velocity, S-velocity, density, boundary undulations, and anisotropy of the whole Earth. To invert for all these parameters we would require a much larger data set than is now available. However the current data set can be used, together with certain assumptions and other information, to retrieve some of the major characteristics of the three-dimensional structure of the Earth. Some of the assumptions and information are based upon physical considerations, e.g., the fluid outer core is assumed to be laterally homogeneous [*Stevenson*, 1987]; some are a priori ones, for example we shall impose the requirement that heterogeneities in P-velocity and in S-velocity are proportional to one another; and some are experimental or even subjective assumptions – for example, we truncate the Legendre polynomial expansion in radius at a certain degree. With the assistance of these assumptions and information, we seek to construct earth models which are relatively simple, i.e., involving only a small number of modeling parameters. Of course, the model must be sufficient to adequately explain the data.

7.2.1 Parameterizing heterogeneity in the mantle

Since the multiplets used in this study have very long periods (the shortest period is 193 s for mode ${}_{13}S_3$), they are sensitive only to the very large scale features of earth structure. The distinction between the Earth's crust and the mantle, therefore, can be neglected. We simply treat the whole volume from the surface of the Earth (the sea floor in the PREM model) to the core-mantle boundary, as the mantle.

Although there is no definite evidence that lateral heterogeneity is continuous across the 670-discontinuity, we model the heterogeneity continuously, owing to the resolution of the data. Introducing a discontinuity in heterogeneity and parameterizing the upper mantle and the lower mantle separately is quite straightforward. However we would not expect this to allow us to retrieve more information, because the trade-off between the heterogeneities just above and just below the boundary is

severe for the current data set. Therefore we choose to avoid this complication and to model the whole mantle continuously.

We impose the constraint that the relative aspherical perturbations in α (P-velocity), β (S-velocity), and ρ (density) in the mantle be proportional to one another. It has been shown above (see Table 6.1) that the value of $d\ln\alpha/d\ln\beta$ is, with high probability (90 percent confidence), located within the interval of $(0.21, 0.51)$ based upon the modal data. If we assume that the perturbations in the bulk modulus and in the shear modulus are positively correlated, the interval can be more tightly constrained to (0.39, 0.51). We shall adopt a value of 0.5 for this ratio here. This value is at the conservative end of the interval, with respect to the experimental value, 0.8, of *Anderson et al.* [1968]. Although we have not shown this value (0.5) to be valid for the upper mantle, it is reasonable to use this value for the mantle as a whole for the following reasons: (1) some evidence has been reported that $d\ln\alpha/d\ln\beta$ for the upper mantle also takes low values, possibly due to partial melting [*Hales and Doyle*, 1967]; and (2) the value which is appropriate for the lower mantle should approximate the value for the whole mantle, since the upper mantle is much less important than the lower mantle for the splitting of most modes used in this study. For the value of $d\ln\rho/d\ln\alpha$ the current modal data allow a large range of variation (see Figure 6.6); we simply take the value (0.5) of *Anderson et al.* [1968] for the mantle. Now we can introduce a variable $\zeta(r,\theta,\phi)$ to describe the aspherical heterogeneities in the mantle

$$\zeta(r,\theta,\phi) = \frac{\delta\alpha(r,\theta,\phi)}{\alpha(r)} = 0.5\frac{\delta\beta(r,\theta,\phi)}{\beta(r)} = 2\frac{\delta\rho(r,\theta,\phi)}{\rho(r)} \tag{7.1}$$

where the denominators are evaluated in the spherical reference model.

The parameter $\zeta(r,\theta,\phi)$ may be expanded in terms of spherical harmonics for the dependences of colatitude θ and longitude ϕ, and in terms of normalized Legendre polynomials for the radial r dependence:

$$\begin{aligned}\zeta(r,\theta,\phi) &= \sum_{\substack{s=2\\ s\ \text{even}}}^{S}\sum_{t=-s}^{s}\zeta_{st}(r)Y_s^t(\theta,\phi)\\ &= \sum_{\substack{s=2\\ s\ \text{even}}}^{S}\sum_{t=-s}^{s}\sum_{k=0}^{K}\zeta_{st}^k f_k(x)Y_s^t(\theta,\phi)\end{aligned} \tag{7.2}$$

where S and K are the numbers at which the expansions are truncated, the coefficients ζ_{st}^k are unknowns to be determined by inversion, $f_k(x)$ are Legendre polynomials as used in *Dziewonski* [1984], $Y_s^t(\theta,\phi)$ are spherical harmonics as defined by *Edmonds* [1960], and x is the reduced, normalized radius running from -1 at the core-mantle boundary to $+1$ at the surface of the Earth (the sea floor).

It is not appropriate to assume a relation of the form (7.1) for the spherical part of the perturbation, and therefore for degree $s = 0$ we determine independent perturbations in P-velocity, S-velocity, and density, writing:

$$\frac{\delta\alpha_0}{\alpha} = \sum_{k=0}^{K} \alpha^{(k)} f_k(x) \tag{7.3}$$

$$\frac{\delta\beta_0}{\beta} = \sum_{k=0}^{K} \beta^{(k)} f_k(x) \tag{7.4}$$

$$\frac{\delta\rho_0}{\rho} = \sum_{k=0}^{K} \rho^{(k)} f_k(x) \tag{7.5}$$

where $\delta\alpha_0$, $\delta\beta_0$, and $\delta\rho_0$ are the spherical perturbations from the reference model and $\alpha^{(k)}$, $\beta^{(k)}$, and $\rho^{(k)}$ are unknown constants.

7.2.2 Boundary undulations

The modes used in this study are very sensitive to aspherical structure at the very top part of the mantle, including the undulations of the discontinuities. In Figures 6.1, 6.4, and 7.1, are shown the sensitivities of several modes to perturbations in the radius of the surface (the sea floor for the PREM model), together with the sensitivities to other features of the Earth. The strong sensitivities to the surface topography are evident. The sensitivities to the other main discontinuity near the surface, the Moho, are not shown, but they are comparable in magnitude with those to the sea floor. Since the wavelengths of the modes used in this study are much longer than the distance between these two discontinuities, it would give misleading results if any or both of these discontinuities were inverted for from the modal data. Trade-offs between the volumetric perturbation at the top of the mantle and the undulations of these two boundaries are also expected. Therefore we elect to

ignore perturbations of these discontinuities, and correspondingly their effects may contaminate the results of the inversion for volumetric heterogeneity at the top part of the mantle. *Ritzwoller et al.* [1988] modeled mantle structure only of spherical harmonic degree $s = 2$ by using modal data. They also found that the splitting data for mantle modes (most of the modes they used coincide with the ones used in this study) are not sufficient to infer uppermost mantle structure unambiguously, even with the assistance of the constraints provided by the frequency measurements for many fundamental surface wave equivalent modes of *Smith et al.* [1987].

The 670-discontinuity and the inner-core boundary are also not included in the inversions, owing to the poor constraints which the data set provide for these parameters. The low sensitivities to the 670-discontinuity are clear in Figures 6.1, 6.4 and 7.1, and only a small number of "core modes" are sensitive to the inner-core boundary (see Figure 7.1).

The topography of the core-mantle boundary (CMB) *is* included in the inversion. Although we do not expect to obtain unequivocal results for CMB topography, because of the low resolution of the current data, we show that some characteristics of the CMB are revealed by this experiment. A number of modes used in this study are sensitive to the perturbation of the CMB and some have very strong sensitivities; for example, see the kernels for modes ${}_0S_4$, ${}_0S_5$, and ${}_0S_6$ in Figure 6.1 and modes ${}_3S_2$ and ${}_2S_3$ in Figure 7.1.

7.2.3 Anisotropy in the inner core

As we have mentioned in Chapter 1, it is necessary to introduce inner-core anisotropy to properly explain the behavior of the anomalously split core modes. Since we do not have sufficient data (only 8 core modes are used here) to derive a unique model even for lower degrees, the result achieved by solving this underdetermined inverse problem should be regarded only as an example of a model which fits the data. The model we obtain may, however, reflect some realistic features, such as the magnitude of inner-core anisotropy.

In the discussion here we shall omit mentioning anisotropy of degree zero; such

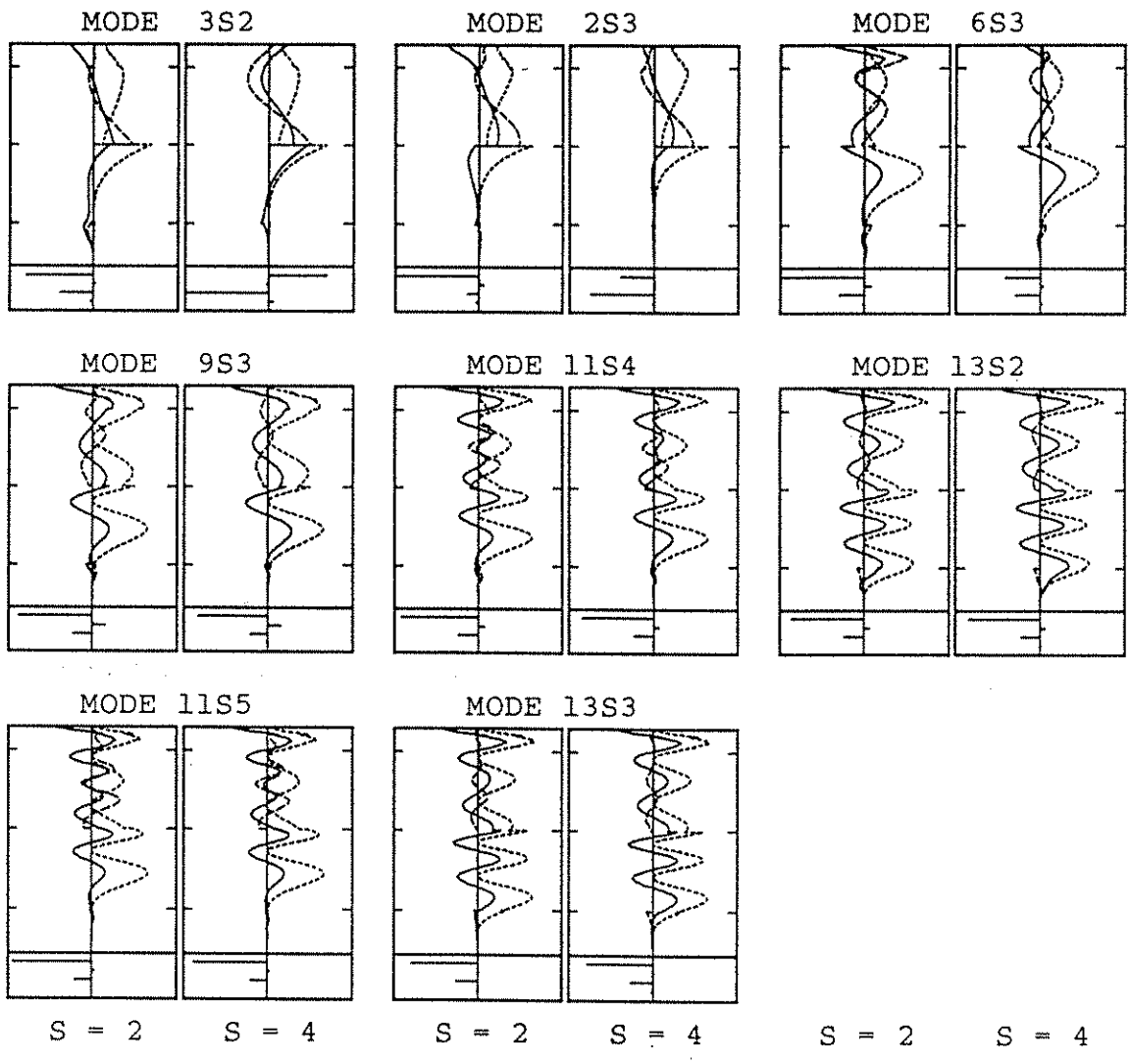

Fig. 7.1 Differential kernels for spherical harmonic degrees 2 and 4 of some core modes. The sensitivities of these mode penetrate deeply into the core. See caption to Figure 6.1 for details, with exceptions that the sensitivities to the undulation of the inner-core boundary of some modes presented here are visible now.

anisotropy corresponds to transverse isotropy about the radial vector which does not contribute to splitting, but acts only to shift the central frequency of the mode. Although there are components of degree zero in the anisotropic models to be presented, the corresponding parameters will trade off with all other spherically symmetric perturbations and thus are not well determined. Since the splitting functions of the anomalously split core modes are dominated by coefficients c_{20} and c_{40} (see Table 5.2), we invert for the cylindrically symmetric part (i.e., spherical harmonic order $t = 0$) of anisotropy only. As a result of Subsection 2.3.3, we need 24 independent parameters (11 for $s = 2$, and 13 for $s = 4$) to describe such an anisotropic tensor field $\mathbf{\Lambda}$, which is subject to the symmetry property (2.52), on the surface of a sphere. Generally speaking, these parameters are functions of radius r. Assuming that inner-core anisotropy varies smoothly with r and only terms associated with r^0, r^1, and r^2 remain in the expansion for the radial dependence, the total number of independent parameters which are needed to determine $\mathbf{\Lambda}$ would appear to number 72. However the requirement that the elastic tensor be nonsingular at the center of the Earth can help to reduce this number. It has been shown in Section 2.5 that a general analytic elastic tensor field may be expressed in terms of the basis tensors $\boldsymbol{\tau}_{kst}^{(nq)}$ given in (2.202). For the considered form of inner-core anisotropy $\mathbf{\Lambda}$, our interest is limited to $s=2,4$, $t=0$, and $\nu=n+2q \leq 2$. From Table 2.6, which gives the allowed triplets (k,n,q), the number of degree of freedom for such a tensor field $\mathbf{\Lambda}$ is found to be 17, rather than 72. Furthermore the basis tensors $\boldsymbol{\tau}_{kst}^{(nq)}$ with n odd, which correspond to the terms with odd powers of r, do not contribute to splitting (see Subsection 2.5.3). Thus only 14 independent parameters remain. In addition to the above constraints, we may also assume that there are no lateral variations in the chemical properties and in the thermal condition in the inner core, and that the zonal structure is purely due to the axi-symmetric spatial distribution of the crystal orientations. It may be demonstrated that such pure anisotropy (no lateral variations in Lamé coefficients) requires that the coefficients of $\boldsymbol{\tau}_{420}^{(20)}$ and $\boldsymbol{\tau}_{520}^{(20)}$ vanish. This working hypothesis is by no means required by the data. However since it represents a physically simpler model and is consistent with the current modal data

Table 7.1: (k,n,q) for the Inner-Core Anisotropy Model

	$p=1$	$p=2$	$p=3$	$p=4$	$p=5$	$p=6$	$p=7$
$s=0$	4,0,0	5,0,0	4,0,1	5,0,1	2,2,0	3,2,0	
$s=2$	2,0,0	3,0,0	2,0,1	3,0,1	1,2,0	2,2,0	3,2,0
$s=4$	1,0,0	1,0,1	1,2,0	2,2,0	3,2,0		

(as we show below), we shall make this assumption. And thus only 12 parameters are needed to describe the anisotropic inner-core model. If anisotropy of degree zero is included in the inversion, 6 more parameters are introduced. Specifically, we write

$$\mathbf{\Lambda} = C(r)(\sum_{p=1}^{6} \psi_0^{(p)} \boldsymbol{\lambda}_0^{(p)} + \sum_{p=1}^{7} \psi_2^{(p)} \boldsymbol{\lambda}_2^{(p)} + \sum_{p=1}^{5} \psi_4^{(p)} \boldsymbol{\lambda}_4^{(p)}) \tag{7.6}$$

where $C(r) = \kappa(r) + \frac{4}{3}\mu(r)$ is evaluated in the reference model (r is normalized such that $r=1$ at the inner-core boundary), $\psi_s^{(p)}$ are dimensionless coefficients to be determined, and $\boldsymbol{\lambda}_s^{(p)} = \boldsymbol{\tau}_{ks0}^{(nq)}$ with (k,n,q) being those listed in Table 7.1. The basis tensors $\boldsymbol{\lambda}_s^{(p)}$ may also be expressed in terms of their spherical components $\lambda_{ijkl}^{(sp)}$:

$$\boldsymbol{\lambda}_s^{(p)} = \sum_{ijkl} \lambda_{ijkl}^{(sp)} \mathbf{e}_i \mathbf{e}_j \mathbf{e}_k \mathbf{e}_l \tag{7.7}$$

where i,j,k,l take values 1,2,3 and $\mathbf{e}_1 = \hat{\boldsymbol{\theta}}, \mathbf{e}_2 = \hat{\boldsymbol{\phi}}, \mathbf{e}_3 = \hat{\mathbf{r}}$ are the unit vectors in the spherical-coordinate directions. Since we are seeking a cylindrically symmetric tensor field $\mathbf{\Lambda}$ with its symmetry axis coinciding with the Earth's rotation axis, the components $\lambda_{ijkl}^{(sp)}$ are independent of longitude ϕ. Their r and θ dependence is given by

$$\lambda_{ijkl}^{(sp)} = \sqrt{\frac{1}{4\pi}} \sum_{N=0}^{s} \lambda_{ijkl}^{(spN)}(r) P_s^{N0}(\cos\theta) \tag{7.8}$$

where $\lambda_{ijkl}^{(spN)}$ are given in Table 7.2, and P_s^{N0} are generalized Legendre functions [*Phinney and Burridge*, 1973]. In order to evaluate (7.8), we tabulate some expressions for P_s^{N0} in Table 7.3.

With the expansion of the inner-core anisotropy in the form of (7.6), the cylindrically symmetric parts of the splitting functions can be modeled by

Table 7.2: Coefficients λ_{ijkl}^{spN}

s,p,N	$\nu_{spN}(r)$	μ_{ijkl}^{spN}																					
		$\binom{1}{1}\binom{1}{1}$	$\binom{1}{1}\binom{1}{2}$	$\binom{1}{1}\binom{1}{3}$	$\binom{1}{1}\binom{2}{2}$	$\binom{1}{1}\binom{2}{3}$	$\binom{1}{1}\binom{3}{3}$	$\binom{1}{2}\binom{1}{2}$	$\binom{1}{2}\binom{1}{3}$	$\binom{1}{2}\binom{2}{2}$	$\binom{1}{2}\binom{2}{3}$	$\binom{1}{2}\binom{3}{3}$	$\binom{1}{3}\binom{1}{3}$	$\binom{1}{3}\binom{2}{2}$	$\binom{1}{3}\binom{2}{3}$	$\binom{1}{3}\binom{3}{3}$	$\binom{2}{2}\binom{2}{2}$	$\binom{2}{2}\binom{2}{3}$	$\binom{2}{2}\binom{3}{3}$	$\binom{2}{3}\binom{2}{3}$	$\binom{2}{3}\binom{3}{3}$	$\binom{3}{3}\binom{3}{3}$
0,1,0	$\sqrt{1/15}$	3			1		1	1					1					3		1	1		3
0,2,0	$\sqrt{1/12}$				2		2	-1					-1							2	-1		
0,3,0	$\sqrt{1/15}b$	3			1		1	1					1					3		1	1		3
0,4,0	$\sqrt{1/12}b$				2		2	-1					-1							2	-1		
0,5,0	$\sqrt{1/36}r^2$	6			2		-1	2					-1					6		-1	-1		-12
0,6,0	$\sqrt{7/72}r^2$				-4		2	2					-1							2	-1		
2,1,0	$\sqrt{1/84}$	6			2		-1	2					-1					6		-1	-1		-12
2,1,1	$\sqrt{1/14}$			3						1				1		3							
2,1,2	$\sqrt{1/14}$	-6					-1						-1					6		1	1		
2,2,0	$\sqrt{1/24}$				-4		2	2					-1							2	-1		
2,2,1	$\sqrt{1/4}$									1				-2									
2,2,2	$\sqrt{1/4}$						2						-1							-2	1		
2,3,0	$\sqrt{1/84}b$	6			2		-1	2					-1					6		-1	-1		-12
2,3,1	$\sqrt{1/14}b$			3						1				1		3							
2,3,2	$\sqrt{1/14}b$	-6					-1						-1					6		1	1		
2,4,0	$\sqrt{1/24}b$				-4		2	2					-1							2	-1		
2,4,1	$\sqrt{1/4}b$									1				-2									
2,4,2	$\sqrt{1/4}b$						2						-1							-2	1		

Table 7.2: continued

s,p,N	$\nu_{spN}(r)$	μ_{ijkl}^{spN}																					
		$\binom{1}{1}\binom{1}{1}$	$\binom{1}{1}\binom{1}{2}$	$\binom{1}{1}\binom{1}{3}$	$\binom{1}{1}\binom{2}{2}$	$\binom{1}{1}\binom{2}{3}$	$\binom{1}{1}\binom{3}{3}$	$\binom{1}{2}\binom{1}{2}$	$\binom{1}{2}\binom{1}{3}$	$\binom{1}{2}\binom{2}{2}$	$\binom{1}{2}\binom{2}{3}$	$\binom{1}{2}\binom{3}{3}$	$\binom{1}{3}\binom{1}{3}$	$\binom{1}{3}\binom{2}{2}$	$\binom{1}{3}\binom{2}{3}$	$\binom{1}{3}\binom{3}{3}$	$\binom{2}{2}\binom{2}{2}$	$\binom{2}{2}\binom{2}{3}$	$\binom{2}{2}\binom{3}{3}$	$\binom{2}{3}\binom{2}{3}$	$\binom{2}{3}\binom{3}{3}$	$\binom{3}{3}\binom{3}{3}$
2,5,0	$\sqrt{1/28}r^2$	3		1		-4	1						-4				3		-4	-4		8
2,5,1	$\sqrt{25/168}r^2$		3							1				1		-4							
2,5,2	$\sqrt{25/42}r^2$	-1				1							1				1		-1	-1			
2,6,0	$-\sqrt{5/126}r^2$	6		2		-1	2						-1				6		-1	-1		-12	
2,6,1	$-\sqrt{5/84}r^2$		3							1				1		3							
2,6,2	$\sqrt{5/21}r^2$	-6				-1							-1				6		1	1			
2,7,0	$-\sqrt{5/36}r^2$			-4		2	2						-1						2	-1			
2,7,1	$-\sqrt{5/24}r^2$									1				-2									
2,7,2	$\sqrt{5/6}r^2$					2							-1						-2	1			
4,1,0	$\sqrt{3/280}$	3		1		-4	1						-4				3		-4	-4		8	
4,1,1	$\sqrt{3/56}$		3							1				1		-4							
4,1,2	$\sqrt{3/7}$	-1				1							1				1		-1	-1			
4,1,3	$\sqrt{3/8}$		-1							1				1									
4,1,4	$\sqrt{3/4}$	1		-1			-1										1						
4,2,0	$\sqrt{3/280}b$	3		1		-4	1						-4				3		-4	-4		8	
4,2,1	$\sqrt{3/56}b$		3							1				1		-4							
4,2,2	$\sqrt{3/7}b$	-1				1							1				1		-1	-1			
4,2,3	$\sqrt{3/8}b$		-1							1				1									
4,2,4	$\sqrt{3/4}b$	1		-1			-1										1						

Table 7.2: continued

s,p,N	$\nu_{spN}(r)$	μ_{ijkl}^{spN}																				
		$\binom{1}{1}\binom{1}{1}$	$\binom{1}{1}\binom{1}{2}$	$\binom{1}{1}\binom{1}{3}$	$\binom{1}{1}\binom{2}{2}$	$\binom{1}{1}\binom{2}{3}$	$\binom{1}{1}\binom{3}{3}$	$\binom{1}{2}\binom{1}{2}$	$\binom{1}{2}\binom{1}{3}$	$\binom{1}{2}\binom{2}{2}$	$\binom{1}{2}\binom{2}{3}$	$\binom{1}{2}\binom{3}{3}$	$\binom{1}{3}\binom{1}{3}$	$\binom{1}{3}\binom{2}{2}$	$\binom{1}{3}\binom{2}{3}$	$\binom{1}{3}\binom{3}{3}$	$\binom{2}{2}\binom{2}{2}$	$\binom{2}{2}\binom{2}{3}$	$\binom{2}{2}\binom{3}{3}$	$\binom{2}{3}\binom{2}{3}$	$\binom{2}{3}\binom{3}{3}$	$\binom{3}{3}\binom{3}{3}$
4,3,0	$-\sqrt{5/154}r^2$	3			1		-4	1					-4					3		-4	-4		8
4,3,1	$-\frac{17}{4}\sqrt{1/154}r^2$			3							1			1		-4							
4,3,2	$-\sqrt{16/77}r^2$	-1					1						1					1		-1	-1		
4,3,3	$\frac{7}{4}\sqrt{1/22}r^2$			-1							1			1									
4,3,4	$\sqrt{49/11}r^2$	1			-1			-1										1					
4,4,0	$\sqrt{1/14}r^2$	6			2		-1	2					-1					6		-1	-1		-12
4,4,1	$\sqrt{5/14}r^2$			3							1			1		3							
4,4,2	$\sqrt{5/28}r^2$	-6					-1						-1					6		1	1		
4,4,3	0																						
4,4,4	0																						
4,5,0	$\sqrt{1/4}r^2$				-4		2	2					-1							2	-1		
4,5,1	$\sqrt{5/4}r^2$										1			-2									
4,5,2	$\sqrt{5/8}r^2$						2						-1							-2	1		
4,5,3	0																						
4,5,4	0																						

Coefficients λ_{ijkl}^{spN} are given by $\lambda_{ijkl}^{spN} = \mu_{ijkl}^{spN} \cdot \nu_{spN}(r)$, where ν_{spN} are given in the second column with $b \equiv \sqrt{7/12}(5r^2 - 3)$; μ_{ijkl}^{spN} are listed for 21 combinations of i, j, k, l, which are labeled at the top header of a column, the unlisted μ_{ijkl}^{spN} are obtained using symmetry $\mu_{ijkl}^{spN} = \mu_{klij}^{spN} = \mu_{jikl}^{spN}$.

Table 7.3: Some generalized Legendre functions $P_s^{Nt}(x)$ with $t = 0$

	$s=0$	$s=2$	$s=4$
$N=0$	1	$\frac{1}{2}(3x^2-1)$	$\frac{1}{8}(35x^4-30x^2+3)$
$N=1$		$\frac{\sqrt{6}}{2}x(1-x^2)^{\frac{1}{2}}$	$\frac{\sqrt{5}}{4}(7x^3-3x)(1-x^2)^{\frac{1}{2}}$
$N=2$		$\frac{\sqrt{6}}{4}(1-x^2)$	$\frac{\sqrt{10}}{8}(7x^2-1)(1-x^2)$
$N=3$			$\frac{\sqrt{35}}{4}x(1-x^2)^{\frac{3}{2}}$
$N=4$			$\frac{\sqrt{70}}{16}(1-x^2)^2$

$$c_{00} = \sum_{p=1}^{6} \Psi_0^{(p)} \psi_0^{(p)} \tag{7.9}$$

$$c_{20} = \sum_{p=1}^{7} \Psi_2^{(p)} \psi_2^{(p)} \tag{7.10}$$

$$c_{40} = \sum_{p=1}^{5} \Psi_4^{(p)} \psi_4^{(p)} \tag{7.11}$$

where the kernel coefficients $\Psi_s^{(p)}$ are obtainable from (2.51)

$$\Psi_s^{(p)} = \frac{r_I}{2\omega_0} \int_0^1 C(r) \sum_{\alpha\beta\gamma\delta} C_{knqs}^{\alpha\beta\gamma\delta} g_s^{\alpha\beta\gamma\delta} r^2 dr \tag{7.12}$$

where r_I is the radius of the inner-core boundary, $C_{knqs}^{\alpha\beta\gamma\delta}$ are given in (2.203), $g_s^{\alpha\beta\gamma\delta}$ are defined in (2.45), and (k, n, q), for a given (s, p), are those listed in Table 7.1.

7.2.4 Attenuation structure in the mantle

As we restricted the inversion only to the spherically symmetric components of the imaginary part of splitting function (see Chapter 5), we invert only for the spherically symmetric perturbation in the attenuation structure of the Earth. Although it is straightforward to include lateral variations in attenuation, it would lead to only insignificant additional variance reduction, as pointed out in Chapter 5.

In modeling, an assumption will be made that the imaginary part of shear modulus departs from the reference model (PREM) by $\delta\bar{\mu}(r)$ while the imaginary part of bulk modulus is fixed as in the reference model. Thus we have

$$\omega_0 \,\mathrm{Im}(c_{00}) = \int_{r_C}^{r_S} \frac{\delta\bar{\mu}(r)}{\mu(r)} \mu(r) M_0(r) r^2 dr \tag{7.13}$$

where ω_0 is the real part of reference frequency of the multiplet, $\mu(r)$ is the shear modulus evaluated in the reference model, $M_0(r)$ is the differential kernel given by equation (102) of *Woodhouse and Dahlen*, and r_S and r_C are the radii of the sea floor and the core-mantle boundary respectively. As for $\zeta_s^t(r)$ in (7.2) we expand:

$$\frac{\delta\bar{\mu}(r)}{\mu(r)} = \sum_{k=0}^{K} \bar{\mu}^{(k)} f_k(x) \tag{7.14}$$

where K is the number at which the expansion is truncated, $\bar{\mu}^{(k)}$ are the constants to be found, and $f_k(x)$ are those defined when they are introduced in (7.2).

7.3 Models to Fit Splitting Functions

Using the splitting function coefficients listed in Table 5.2 as data, we have inverted for earth models by linear least-squares methods. Here we present two aspherical earth models which are retrieved from the aspherical part ($s = 2$ and $s = 4$) of the splitting function coefficients listed in Table 5.2. The first is a heterogeneous model of the mantle and the second is an anisotropic model of the inner core.

We have not attempted to develop spherical earth models to fit the splitting function coefficients of degree 0 (A_0^0 and $\mathrm{Im}(A_0^0)$ in Table 5.2). Our reference spherical model (PREM of *Dziewonski and Anderson* [1981]) is based on a much larger data set than the one used in this study. Therefore it is expected that any significant spherical correction to PREM required by the splitting of modes probably have higher-degree components in radial dependence, which are not well constrained by our data set. To derive a more precise spherical earth model would require a much larger set of data than that involved in this study.

7.3.1 Aspherical model of the mantle

For the current experiment we use the c_{st} coefficients of the following 25 mantle modes as the vector $\mathbf{d}$ (see (3.1)): ${}_0S_3$, ${}_0S_4$, ${}_0S_5$, ${}_0S_6$, ${}_0S_7$, ${}_0S_9$, ${}_1S_3$, ${}_1S_4$, ${}_1S_5$, ${}_1S_6$,

${}_1S_7$, ${}_1S_8$, ${}_2S_4$, ${}_2S_5$, ${}_2S_6$, ${}_2S_8$, ${}_3S_1$, ${}_3S_8$, ${}_4S_3$, ${}_4S_4$, ${}_5S_3$, ${}_5S_4$, ${}_5S_5$, ${}_5S_6$, and ${}_6S_{10}$, truncate the expansion of $\zeta_{st}(r)$ at $K = 6$ in (7.2) to model the volumetric perturbation in the mantle. We invert for the topography of the CMB simultaneously. Thus the elements of vector $\mathbf{x}$ in (3.1) are ζ_{st}^0, ζ_{st}^1, $\ldots$, ζ_{st}^6, and δh_{st} (the relative perturbation in the radius of the CMB) – 8 unknowns for each s and t.

In order to approximate the assumption that the elements in the vector $\mathbf{e}$ (as defined in (3.1)) are independent samples from a normal distribution (see Chapter 3), we should divide each splitting function coefficients, c_{st}, by its associated error when it is used as an element of vector $\mathbf{d}$ in (3.1). Naturally one would consider using the error estimates listed in Table 5.2 to evaluate the error $\mathbf{e}$; however, we find that the error estimates for modes which have very small splitting effect (e.g., ${}_1S_3$) are usually unrealistically small, compared with those of the other modes, due to the damping used in the inversion for the splitting functions. This bias in the error estimates of the splitting functions forces us to select another option: we simply assume that all splitting function coefficients have the same standard errors and we let them enter into vector $\mathbf{d}$ with the same weight.

Now we turn our attention to the specification of the elements, σ_i^2, of the model covariance matrix $\mathbf{C}_x$ (see (3.6)). The orthonormality of Legendre polynomials enables us put $\sigma_i = \sigma_\zeta$ for all i corresponding to ζ_{st}^k, $k = 0, 1, \ldots, 6$. Since we can incorporate any common factor multiplying the elements σ_i into the parameter ς (see (3.6)), the remaining problem in evaluating σ_i is to choose the ratio of the element σ_h, corresponding to δh_{st}, to the other diagonal elements σ_ζ, corresponding to ζ_{st}^k ($k = 0, 1, \ldots, 6$). To seek a priori information on this issue, we have compared the size of a lower-mantle P velocity model (V.3 of *Morelli and Dziewonski* [1987b]) and the size of a CMB topography model [*Morelli and Dziewonski*, 1987a]. (The comparison has been made only for harmonic degree $s = 2$ and $s = 4$). The result corresponds to $\mathrm{rms}(\zeta_{st}^k)/\mathrm{rms}(\delta h_{st}) = 0.5$ for our case (actually we are interested only in the order of magnitude of this value, if the inverse problem is a stable one). This suggests that we set $\sigma_\zeta/\sigma_h = 0.5$ to specify the strengths of desire for the relative smallness of volumetric and boundary perturbations.

The damping parameter ς determines the general strength of our desire for the smallness of the model relative to the fit to the data. It is a trade-off parameter and is chosen so that the variance in data is reduced close to its minimum while the size of the model is kept reasonably small. This needs a subjective judgement.

The model we obtain is named SAF (*s*plitting data, *a*spherical model, from splitting *f*unctions) and it is tabulated in Table 7.4. Along with the coefficients of the model, we also list in Table 7.4 the estimates of the associated standard errors and the corresponding diagonal elements of the resolution matrix. The standard errors are derived from the covariance matrix of the model sampling distribution (see Chapter 3). The obvious tendency is that the resolution becomes poorer for coefficients of higher degree in the radial expansion. This is expected, and implies that although we could introduce higher degrees than $k = 6$ in the inversion, they would not be well resolved by the data. Therefore the truncation of the expansion of $\zeta_{st}(r)$ in (7.2) is justified.

In Table 7.5 the misfit to each mode of this model is listed. The total variance reduction is as high as 77%. However the r.m.s of the residuals in the data is larger by a factor of 3.3 than that of the error estimates listed in Table 5.2. If we believe that these error estimates are underestimated by a factor of $\sqrt{2}$ due to the effect of windowing used in the data processing (J. Park, personal communication, 1987), the residuals are still above the error level by a factor 2.3. One might argue that model SAF does not fit the splitting functions. But we rather explain it as the underestimation of the errors associated with the splitting functions, due to the damping in the inversions and due to the violation of some assumptions which are made in retrieving the splitting functions.

7.3.2 Modeling inner-core anisotropy

The splitting functions of anomalously split modes cannot be explained by mantle structure alone. Taking c_{20} and c_{40} of 8 core modes (whose differential kernels are shown in Figure 7.1) as data, the variance reduction by model SAF is only 29%. Here we shall attempt to model the residual splitting functions of these modes by

Table 7.4: Model SAF

k	${}^kA_2^0$	${}^kA_2^1$	${}^kB_2^1$	${}^kA_2^2$	${}^kB_2^2$	${}^kA_4^0$	${}^kA_4^1$	${}^kB_4^1$	${}^kA_4^2$	${}^kB_4^2$	${}^kA_4^3$	${}^kB_4^3$	${}^kA_4^4$	${}^kB_4^4$
	156	-67	66	-172	-250	-4	10	0	36	18	-32	54	-19	58
0	15	15	15	15	15	19	19	19	19	19	19	19	19	19
	.92	.92	.92	.92	.92	.91	.91	.91	.91	.91	.91	.91	.91	.91
	-157	-69	-13	197	-72	47	43	-49	-57	85	-44	42	-1	62
1	28	28	28	28	28	33	33	33	33	33	33	33	33	33
	.58	.58	.58	.58	.58	.66	.66	.66	.66	.66	.66	.66	.66	.66
	59	-14	-53	110	-36	-2	73	36	-53	37	27	22	-57	14
2	28	28	28	28	28	34	34	34	34	34	34	34	34	34
	.54	.54	.54	.54	.54	.57	.57	.57	.57	.57	.57	.57	.57	.57
	48	-55	-29	-106	-58	27	29	52	20	-67	-54	10	20	48
3	28	28	28	28	28	38	38	38	38	38	38	38	38	38
	.34	.34	.34	.34	.34	.45	.45	.45	.45	.45	.45	.45	.45	.45
	-34	-8	-50	3	83	-3	-15	7	47	-39	-51	22	49	-18
4	22	22	22	22	22	30	30	30	30	30	30	30	30	30
	.25	.25	.25	.25	.25	.29	.29	.29	.29	.29	.29	.29	.29	.29
	7	-9	4	-19	59	15	41	23	21	-13	-26	6	28	-4
5	21	21	21	21	21	27	27	27	27	27	27	27	27	27
	.15	.15	.15	.15	.15	.15	.15	.15	.15	.15	.15	.15	.15	.15
	13	-14	7	2	-12	33	25	2	-25	-16	-9	-23	3	20
6	17	17	17	17	17	24	24	24	24	24	24	24	24	24
	.08	.08	.08	.08	.08	.11	.11	.11	.11	.11	.11	.11	.11	.11
	-101	115	40	84	319	-24	35	5	-8	44	82	-1	-80	-71
c	54	54	54	54	54	70	70	70	70	70	70	70	70	70
	.67	.67	.67	.67	.67	.54	.54	.54	.54	.54	.54	.54	.54	.54

Parameter $\zeta(r,\theta,\phi)$ in (7.2) is expressed (see the legend to Table 5.2) as $\zeta(r,\theta,\phi) = \sum_s \sum_{t=0}^{s} \sum_{k=0} ({}^kA_s^t \cos t\phi + {}^kB_s^t \sin t\phi) f_k(x) p_s^t(\theta)$; and the relative perturbation in CMB radius δh is expressed in same convention $\delta h = \sum_s \sum_{t=0}^{s} ({}^cA_s^t \cos t\phi + {}^cB_s^t \sin t\phi) p_s^t(\theta)$; where $f_k(x)$ are Legendre polynomials (cf., (7.3)), $p_s^t(\theta)$ are spherical harmonics. The complex coefficients ζ_{st}^k in (7.2) can be derived from ${}^kA_s^t$ and ${}^kB_s^t$ as $\zeta_{st}^k = (-1)^t(2\pi)^{\frac{1}{2}}({}^kA_s^t - i\,{}^kB_s^t)$, for $t > 0$; $\zeta_{st}^k = (4\pi)^{\frac{1}{2}}\,{}^kA_s^t$, for $t = 0$; and $\zeta_{st}^k = (2\pi)^{\frac{1}{2}}({}^kA_s^{|t|} + i\,{}^kB_s^{|t|})$, for $t < 0$. The coefficients ${}^kA_s^t$ and ${}^kB_s^t$ are given in the first entry for each degree k in unit of 10^{-6}. An estimate of the associated error for the coefficients ${}^kA_s^t$ and ${}^kB_s^t$ is derived from the covariance matrix, and is given in the second entry (in the same unit). The third entry for each degree k gives the corresponding diagonal elements of the resolution matrix.

Table 7.5: Misfit of Model SAF to Each Mode

Mode	χ^2 Misfit*	Mode	χ^2 Misfit*
${}_0S_3$	0.20	${}_1S_7$	0.15
${}_0S_4$	0.19	${}_2S_6$	0.67
${}_0S_5$	0.10	${}_1S_8$	0.16
${}_1S_3$	0.26	${}_4S_3$	0.16
${}_3S_1$	0.09	${}_2S_8$	0.28
${}_0S_6$	0.17	${}_5S_3$	0.09
${}_1S_4$	0.19	${}_4S_4$	0.35
${}_0S_7$	0.12	${}_5S_4$	0.43
${}_1S_5$	0.16	${}_5S_5$	0.17
${}_2S_4$	0.47	${}_3S_8$	0.18
${}_2S_5$	0.36	${}_5S_6$	0.09
${}_1S_6$	0.16	${}_6S_{10}$	0.19
${}_0S_9$	0.43	average	0.23

The misfit is defined by $\chi^2 = \frac{1}{\sigma^2}[\sum_{i=1}^{N_j}(c_i - c_i^P)^2/N_j]$ where N_j is the number of coefficients used in inversion of mode j, c_i are the observed splitting function coefficients, c_i^P are the predicated splitting function coefficients from Model SAF, and $\sigma^2 \equiv \sum_{i=1}^{N} c_i^2/N$, with $N = \sum_j N_j$.

inner-core anisotropy which is assumed to take the form of (7.6). Namely, we solve (3.1), where $\mathbf{f}$ is now a linear function, for the unknown vector $\mathbf{x}$ which contains $\{\psi_2^{(p)}, p = 1, 2, \ldots, 7\}$ for $s = 2$ and $\{\psi_4^{(p)}, p = 1, 2, \ldots, 5\}$ for $s = 4$. Again, as we did during inverting for model SAF, we let splitting function coefficients enter into vector $\mathbf{d}$ with the same weight. Since the parameter set $\{\psi_s^{(p)}\}$ is associated with a set of orthonormal basis tensors, all the elements of the a priori model covariance matrix $\mathbf{C}_x$ are set to ς^{-1}.

For a given damping level, ς, we may solve the least-squares problem and check the size of the resulting model and the fit to the data. We also calculate the synthetic *PKIKP* travel times from the resulting anisotropic model. In Figure 7.2 we plot the predicted travel times of the rays which vertically penetrate the inner core, along with the associated error estimates, against the value of $\log 1/\varsigma$.

For $s = 2$, the model can essentially predict the travel times reported by *Morelli et al.* [1986] and by *Shearer et al.* [1988] for values of $\log 1/\varsigma$ greater than 6.9. For $s = 4$ the observed travel times place stricter requirements on the value of ς (or equivalently on the size of the model), and require $\log 1/\varsigma$ be between 7.4 and 8.3. Therefore the travel-time data can be easily explained if the model has an appropriate size, say, corresponding to $\log 1/\varsigma$ equal to 7.4. Meanwhile the model corresponding to this damping level can aggregately fit the data of the core modes very well – 79% variance reduction can be achieved by the inner-core anisotropy and model SAF together.

When we examine the fit of the resulting model to each individual mode, however, a serious problem appears. While the splitting function coefficients c_{20} of these core modes can be consistently explained by the model, this model is not able to explain c_{40} of mode ${}_{13}S_2$. The reason for this becomes clear if we examine the kernel coefficients $\Psi_4^{(p)}$ (see (7.11)) of this mode and mode ${}_3S_2$ (the sensitivity of the latter mode to the inner-core anisotropy is so strong that the main character of the model is determined by this mode alone to fairly large extent). For mode ${}_{13}S_2$, we have $\Psi_4^{(p)} = (12.7, -15.2, -2.0, -1.4, 3.5) \times 10^{-5}$, and for mode ${}_3S_2$, $\Psi_4^{(p)} = (11.9, -11.6, 0.0, 0.6, 3.0) \times 10^{-4}$; they are almost parallel to each other. Clearly it

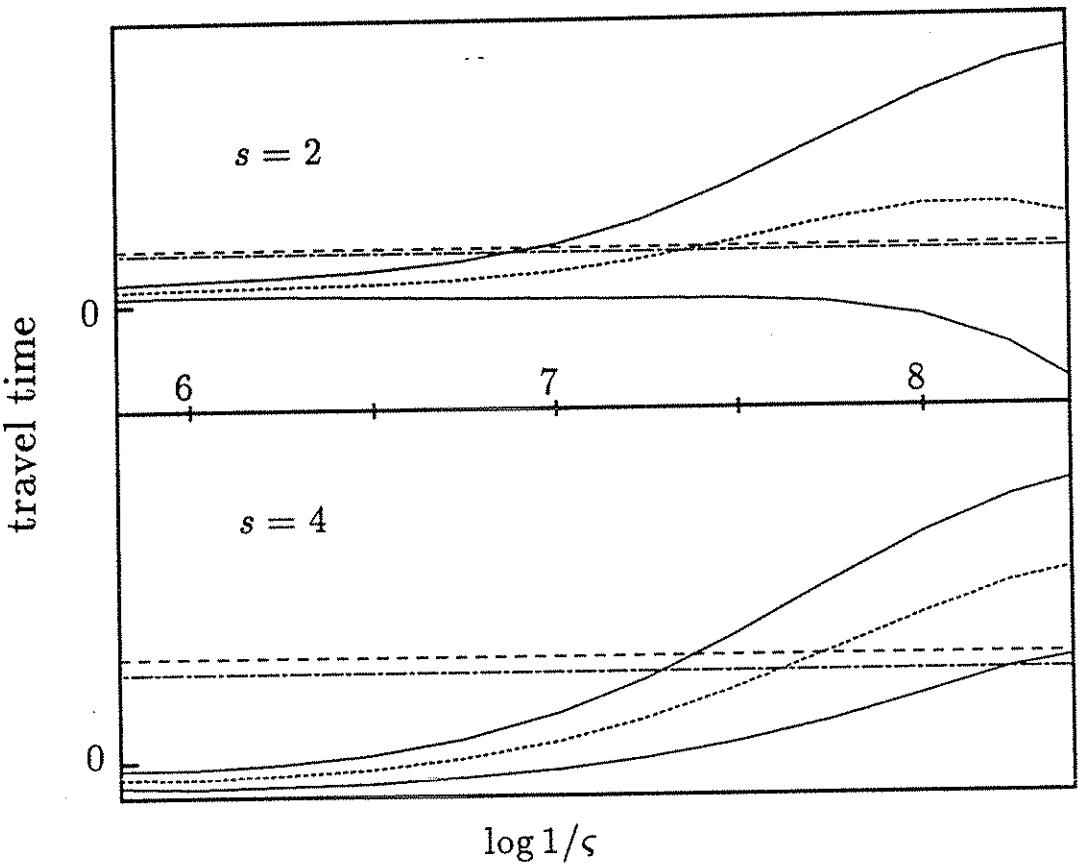

Fig. 7.2 Spherical harmonic expansion coefficients of degree $s = 2$ and 4 and order $t = 0$ of the travel-time anomalies of antipodal *PKIKP* rays. Two horizontal lines are the results estimated by *Morelli et al.* [1986] (dashed line) and by *Shearer et al.* [1988] (dashed-dotted line) from ISC data. The dotted curve is the prediction from the inner-core anisotropy model, which is inferred from the splitting functions of anomalously split core modes. The prediction is plotted as a function of the damping parameter ς, which is used in the damped least-square inversion for inner-core anisotropy. The two solid curves above and below the prediction curve indicate the standard error estimates of the prediction.

is very difficult to find a reasonable model $\psi_4^{(p)}$ which simultaneously explains the splitting function coefficients c_{40} of modes ${}_{13}S_2$ and ${}_3S_2$, which are equal to 1.2×10^{-5} and -2.4×10^{-5}, respectively.

The inconsistency of the splitting functions of these two modes could be interpreted in two ways. First, the inner-core anisotropy of the real Earth could more complicated than the form we assume here. The second possibility is that the splitting function coefficients of modes ${}_{13}S_2$, ${}_3S_2$, or both, which are retrieved by using the nonlinear least-squares method, are not the true solution corresponding to the Earth. Anticipating some results presented below, we find that the split spectra of mode ${}_3S_2$ can, indeed, be explained by a totally different splitting function from the one tabulated in Table 5.2. This will be further discussed below.

7.4 Models to Fit Split Spectra Directly

For this inverse problem, our basic equation (the first of (3.1)) has the following meanings. The vector $\mathbf{x}$ describes the earth structure, $\mathbf{d}$ is the collection of observed seismograms contributed from isolated multiplets, $\mathbf{e}$ is the error associated with the data $\mathbf{d}$, and the function $\mathbf{f}$ is nonlinear and defined by (2.6), (2.8) and (2.12).

In order to solve this problem, we evaluate the matrix of partial derivatives (3.5), using the chain rule for differentiation,

$$\mathbf{A}_i = \left[\frac{\partial \mathbf{f}(\mathbf{x})}{\partial \mathbf{x}}\right]_{\mathbf{x}=\mathbf{x}_i} = \sum_j \left[\frac{\partial \mathbf{f}(\mathbf{x})}{\partial \mathbf{c}^{(j)}(\mathbf{x})} \frac{\partial \mathbf{c}^{(j)}(\mathbf{x})}{\partial \mathbf{x}}\right]_{\mathbf{x}=\mathbf{x}_i} \tag{7.15}$$

where $\mathbf{c}^{(j)}$ represents the splitting function coefficients of mode j, and the summation is over all the modes used. In Chapter 2, we have given an efficient recipe to calculate $\partial \mathbf{f}/\partial \mathbf{c}^{(j)}$ (see (2.18) through (2.27)). $\partial \mathbf{c}^{(j)}/\partial \mathbf{x}$ is radily calculated for a particular choice of the model space since, as shown in Chapter 2, the relationship between $\mathbf{c}^{(j)}$ and $\mathbf{x}$ is linear and thus $\partial \mathbf{c}^{(j)}/\partial \mathbf{x}$ is model independent.

Again we need to discuss the conditions under which $\mathbf{e}$ in (3.1) can be treated approximately as samples from white noise so that the data covariance matrix $\mathbf{C}_e$ in (3.2) becomes proportional to identity matrix. In order to achieve this condition,

we should in principle divide each row of the both sides of the basic equation by the expected size of the associated error of the data point. Generally speaking errors in data have two sources: (1) observational noise (the noise level varies from spectrum to spectrum); (2) unmodeled effects (e.g., the contributions from higher degrees of the spherical harmonic expansion and the coupling effects between adjacent modes, etc.). The latter could be incorporated into the vector e and be regarded as "theoretical errors".

In Chapter 4 we have proposed the use of the seismogram before the earthquake as the means for estimating the noise level for a given seismic trace. Dividing each trace by the estimated noise level, an arbitrary component of the error vector e in (3.1) can be written as $e_i^{ob} + e_i^{th}$, where e_i^{ob} are observational errors which have been normalized and have unit variance, and e_i^{th} are the "theoretical errors". Assuming the variance of e_i^{th} is λ_i^2, we only need divide each row of both sides of the equation by $\sqrt{1+\lambda_i^2}$ to make the error e white. Since we do not know the precise properties of "theoretical errors", we are forced to make assumptions. We shall assume that λ_i^2 are the same, all equal to λ_j^2, for all traces i belonging to the mode j and that they are proportional to the mean of the squared data amplitude $(\sum \tilde{d}_i^{\,2}/N_j)$, where the summation is over all data points i for the mode, $\tilde{d}_i$ are the data normalized by the estimated noise level, and N_j is the number of the data points of the mode j. It is further assumed that in the limit where the "theoretical errors" are dominant ($\lambda_j^2 \gg 1$), all modes (regardless of their data dimension N_j) have the same importance in controlling the model. (This implies that the "theoretical errors" for a given mode are not independent). The idea can be formulated by assigning a multiplicative factor N_j to λ_j^2, which will be used to divide the both sides of the equation, to down-weight the modes having larger N_j. Combining the two factors, we have $\lambda_j^2 = \lambda^2 \sum \tilde{d}_i^2$, where λ^2 is a constant universal to all modes and the summation is over all data points i for the mode. λ^2 is a number related to the ratio of the variance of the "theoretical errors" and the variance of the observational errors. Due to the lack of information on these errors, we choose the number experientially. The number is chosen so that the data size of a mode (measured by $D^2 = \sum d_i^2$, where summation is over all data

points i of the mode and d_i are the data which have been fully weighted) varies by a factor 5 from its minimum to maximum. For the relative data size of each mode, see Table 7.6.

Now let us describe what the model vector $\mathbf{x}$, introduced in (3.1), contains. Of course the heterogeneity parameters ζ_{st}^k defined by (7.2) should be given the first consideration. As above, we truncate the spherical harmonic expansion at $s = 4$ and the radial expansion at $k = 6$. For the spherical correction to mantle structure we use the parameters $\alpha^{(k)}$, $\beta^{(k)}$, and $\rho^{(k)}$, introduced in (7.3), (7.4), and (7.5). We truncate the corresponding radial expansion at $k = 3$ The topography of the CMB, represented by the spherical harmonic components of relative perturbation in the radius of the CMB (δh_{st}, $s = 0, 2, 4$), are retrieved simultaneously. The anomalously split modes are modeled by inner-core anisotropy – we include, in the vector $\mathbf{x}$, the parameters $\psi_s^{(p)}$ ($s = 0, 2, 4$), introduced in (7.6). Finally parameters $\bar{\mu}^{(k)}$ ($k = 0, 1, \ldots, 6$) (see (7.14)) are also included in the vector $\mathbf{x}$ to incorporate a spherical perturbation in mantle attenuation structure. The total dimension of the vector $\mathbf{x}$ is 150.

Having chosen the model space, we are now able to consider the specification of the model covariance matrix $\mathbf{C}_x$, which has been introduced in Chapter 3. Since the parameter sets $\{\zeta_{st}^k\}$ in (7.2), $\{\delta h_{st}\}$ (spherical harmonic expansion coefficients of the relative perturbation in the radius of the CMB), and $\{\psi_s^{(p)}\}$ (see (7.6)) are associated with orthonormal bases, we may set all σ_i corresponding to $\{\zeta_{st}^k\}$ be σ_ζ, set all σ_i corresponding to $\{\delta h_{st}\}$ be σ_h, and set all σ_i corresponding to $\{\psi_s^{(p)}\}$ be σ_ψ. In evaluating the covariance matrix $\mathbf{C}_x$ for the linear inversion (see Subsection 7.3.1), we describe a strategy for choosing the value of σ_ζ/σ_h, which we also employ in the present case. In modeling the splitting functions of core modes, we were unable to find an inner-core model of the form (7.6), which could fit all modes. However the experiments that have been performed enable us gain some knowledge on the intensity of inner-core anisotropy. Relying upon this kind of knowledge and the r.m.s. value of $\{\zeta_{st}^k\}$ of model SAF, we may choose a value of σ_ζ/σ_ψ for the current problem, which gives $\sigma_\zeta/\sigma_\psi = 0.01$. Although the parameters for spherical perturbations, $\alpha^{(k)}$,

Table 7.6: Misfit to Each Mode of Model SAT and Splitting Functions

Mode	D^2	Var	Var′
${}_0S_3$	1.21	0.20	0.17
${}_0S_4$	0.74	0.40	0.32
${}_0S_5$	0.83	0.26	0.21
${}_1S_3 - {}_3S_1$	0.96	0.36	0.30
${}_0S_6$	1.26	0.18	0.14
${}_3S_2$	0.91	0.38	0.32
${}_1S_4$	1.03	0.36	0.33
${}_0S_7 - {}_2S_3$	1.63	0.25	0.13
${}_1S_5 - {}_2S_4$	1.25	0.49	0.34
${}_2S_5 - {}_1S_6$	1.21	0.84	0.73
${}_0S_9$	1.65	0.38	0.21
${}_1S_7$	1.00	0.41	0.28
${}_2S_6$	0.56	0.58	0.45
${}_1S_8$	1.07	0.46	0.31
${}_4S_3 - {}_2S_8$	1.22	0.68	0.45
${}_5S_3$	0.33	0.49	0.38
${}_4S_4$	0.42	0.68	0.54
${}_5S_4$	1.01	0.64	0.40
${}_5S_5$	1.13	0.44	0.35
${}_6S_3 - {}_3S_8$	0.85	0.59	0.35
${}_5S_6$	1.14	0.48	0.26
${}_9S_3$	0.82	0.70	0.44
${}_6S_{10}$	0.71	0.67	0.57
${}_{11}S_4$	0.97	0.68	0.40
${}_{13}S_2$	1.12	0.36	0.30
${}_{11}S_5$	1.02	0.81	0.55
${}_{13}S_3$	0.95	0.46	0.37
average	1.00	0.47	0.34

Squared data D^2 for each mode have been calculated from the weighted data (see text for details) and have been normalized so that their average is unity. Variance ratios (squared misfit/squared data) are listed for model SAT (Var), see Table 7.7a–c; and for splitting function coefficients (Var′), see Table 5.2. The average of Var and Var′ is weighted average with D^2 as the weight.

$\beta^{(k)}$, $\rho^{(k)}$ and $\bar{\mu}^{(k)}$ (see (7.3), (7.4), (7.5), and (7.14), respectively) have been included in the model vector $\mathbf{x}$, the main interest of this study is in the aspherical structure of the Earth. For this reason we allow the parameters for the spherical perturbations move to wherever the data prefer, within the limits required by the stability of the inversion. Namely we set elements σ_i corresponding to the parameters for the spherical perturbations to very large values relative to the other elements of $\mathbf{C}_x$.

In our inversion we also use the results derived from antipodal *PKIKP* travel-time data [*Morelli et al.*, 1986] as constraints on the inner-core anisotropy $\psi_s^{(p)}$ (see (7.6)). We use the spherical harmonic coefficients of the travel-time anomalies as the constraints $\mathbf{g}$ in (3.1). The reported travel-time residuals have a cylindrically symmetric distribution with the symmetry axis coinciding with the Earth's rotation axis. Thus they provide 2 (for $s=2,4$ and $t=0$) constraints on the model parameters $\psi_s^{(p)}$.

The result of the inversion is called SAT (*s*plitting data, *a*spherical, from seismic *t*races), and it is tabulated in Tables 7.7a–7.7c. The coefficients for the heterogeneity parameter $\zeta(r,\theta,\phi)$, see (7.2), and the CMB topography δh are listed in Table 7.7a. Table 7.7b tabulates the parameters, $\psi_s^{(p)}$, for the inner-core anisotropy, see (7.6). In Table 7.7c we list the coefficients for the spherical perturbations in P velocity (α), S velocity (β), density (ρ), and the imaginary part of the shear modulus in the mantle.

In Tables 7.7a–7.7c the associated standard errors of all of the model parameters and the corresponding diagonal elements of the resolution matrix are given. For the derivation and the reliability of these quantities, see Chapter 3. One may immediately see that these error estimates are far too small. We ascribe the underestimate mainly to the damping of the model. The general deviation of the diagonal elements of the resolution matrix from unity (see Table 7.7a–7.7c) indicates that the model is heavily damped. In such a case, the formal error analysis described above is very likely to lose meaning.

The misfit of this model for each mode is listed in Table 7.6. The misfit of a mode is defined by $\mathrm{Var} = \sum(d_i - d_i^P)^2/\bar{d}^2$, where d_i^P are the predicted values by SAT, and

Table 7.7a: Model SAT, Part 1: Mantle Heterogeneity and CMB Topography

	${}^kA_0^0$	${}^kA_2^0$	${}^kA_2^1$	${}^kB_2^1$	${}^kA_2^2$	${}^kB_2^2$	${}^kA_4^0$	${}^kA_4^1$	${}^kB_4^1$	${}^kA_4^2$	${}^kB_4^2$	${}^kA_4^3$	${}^kB_4^3$	${}^kA_4^4$	${}^kB_4^4$
	–	170	−69	68	−216	−262	23	−10	−17	64	39	−43	76	−51	63
$k=0$	–	2	2	3	3	2	3	4	5	5	4	5	5	5	4
	–	0.73	0.79	0.76	0.66	0.66	0.64	0.64	0.60	0.58	0.60	0.52	0.53	0.48	0.48
	–	−109	−11	−15	101	−4	17	−5	−31	−37	71	23	0	−6	−21
$k=1$	–	3	5	4	0	2	4	4	4	4	4	4	3	3	3
	–	0.26	0.32	0.27	0.20	0.20	0.20	0.21	0.17	0.16	0.16	0.13	0.13	0.10	0.11
	–	16	5	−11	45	−12	−18	13	−8	−57	6	49	−35	−15	17
$k=2$	–	3	5	5	2	2	3	4	4	4	3	4	3	3	3
	–	0.24	0.27	0.24	0.17	0.16	0.15	0.16	0.14	0.13	0.14	0.11	0.12	0.08	0.09
	–	60	−33	−37	−37	15	5	12	39	17	−34	−31	−1	35	0
$k=3$	–	2	3	4	3	3	3	3	4	3	3	3	3	3	3
	–	0.16	0.18	0.17	0.11	0.12	0.13	0.11	0.12	0.09	0.09	0.07	0.07	0.08	0.07
	–	−18	−33	−69	10	87	13	16	45	32	−13	−46	26	41	−37
$k=4$	–	4	4	4	3	1	3	4	3	3	3	3	3	3	2
	–	0.16	0.19	0.15	0.12	0.12	0.11	0.12	0.10	0.08	0.09	0.07	0.07	0.07	0.07
	–	−47	−26	−30	22	52	−26	20	21	20	−13	−13	16	3	−18
$k=5$	–	2	3	3	2	3	3	3	3	2	2	2	2	3	2
	–	0.10	0.10	0.10	0.06	0.08	0.12	0.07	0.07	0.05	0.06	0.03	0.03	0.06	0.07
	–	−38	−7	6	2	−12	−27	3	−5	−7	−11	5	−10	−5	5
$k=6$	–	1	2	3	1	2	1	2	2	2	2	1	1	2	1
	–	0.04	0.05	0.07	0.02	0.03	0.05	0.03	0.04	0.03	0.03	0.02	0.02	0.02	0.03
	379	−135	54	13	175	148	1	11	−1	16	68	16	21	45	−69
$k=c$	17	11	12	12	10	10	8	10	9	9	9	11	11	8	8
	0.99	0.37	0.41	0.38	0.27	0.27	0.14	0.19	0.17	0.16	0.16	0.26	0.25	0.15	0.15

For convention see the legend to Table 7.4. Note: the spherical components of parameter $\zeta(r,\theta,\phi)$ are not defined due to the failure of (7.1) for the spherical perturbations; for the spherical corrections in α, β, and ρ see Table 7.7c.

Table 7.7b: Model SAT, Part 2: Inner-Core Anisotropy

	$\psi_s^{(1)}$	$\psi_s^{(2)}$	$\psi_s^{(3)}$	$\psi_s^{(4)}$	$\psi_s^{(5)}$	$\psi_s^{(6)}$	$\psi_s^{(7)}$
	2.1	−2.9	0.9	−2.5	0.7	0.7	
$s=0$	0.2	0.1	0.1	0.2	0.2	0.2	
	0.86	0.79	0.80	0.76	0.70	0.50	
	−3.4	−1.7	1.8	4.3	0.1	−4.1	0.6
$s=2$	0.1	0.1	0.1	0.2	0.2	0.2	0.2
	0.75	0.84	0.55	0.84	0.23	0.62	0.32
	0.1	−3.7	0.0	−0.3	1.2		
$s=4$	0.1	0.1	0.2	0.0	0.2		
	0.61	0.63	0.47	0.76	0.61		

Parameters $\psi_s^{(p)}$ (see (7.6)) are listed in the first entry for each spherical harmonic degree s in units of 10^{-2}. The estimates of standard errors are derived from the covariance matrix, and are given in the second entry for each s (in the same units). The third entry gives the corresponding diagonal elements of the resolution matrix. See Chapter 3 for details on the computation and the reliability of the error estimates.

Table 7.7c: Model SAT, Part 3: Spherical Mantle Perturbations in α, β, ρ, and Imaginary Part of Shear Modulus

	$k=0$	$k=1$	$k=2$	$k=3$	$k=4$	$k=5$	$k=6$
	−62	−198	−403	−433			
$\alpha^{(k)}$	17	28	23	26			
	0.82	0.59	0.39	0.30			
	−415	356	749	−25			
$\beta^{(k)}$	20	29	28	23			
	0.78	0.53	0.56	0.23			
	217	−844	545	−565			
$\rho^{(k)}$	17	30	20	22			
	0.10	0.41	0.22	0.24			
	132	417	268	368	−166	−170	−447
$\bar{\mu}^{(k)}$	25	61	68	69	67	66	54
	0.96	0.73	0.63	0.47	0.46	0.35	0.18

Use (7.3), (7.4), (7.5), and (7.14) to calculate the spherical perturbations in α, β, ρ, and the imaginary part of shear modulus, respectively. The coefficients are listed in the first entry for each parameter, $\alpha^{(k)}$, $\beta^{(k)}$, $\rho^{(k)}$, and $\bar{\mu}^{(k)}$, in unit of 10^{-6}. The associated standard errors estimated from the covariance matrix are listed in the second entry for each parameter in the same units. In the third entry are listed the corresponding diagonal elements of the resolution matrix. See Chapter 3 for details on the computation and the reliability of the error estimates.

$\overline{d}$ is the r.m.s. of the data d_i of the mode. We also list in Table 7.6 the misfits corresponding to the splitting functions tabulated in Table 5.2 using the same data. These misfits could be regarded as the minimum values which earth models could achieve.

7.5 Discussion

7.5.1 Heterogeneity in the mantle

In Figures 7.3–7.9, four different mantle models are shown at depths of 300, 500, 700, 1200, 1700, 2200, and 2700 km: (*a*) model SAT, modal model retrieved directly from seismic traces; (*b*) model SAF, modal model retrieved from splitting functions; (*c*) model SW, based on waveform studies on SH body waves [*Woodhouse and Dziewonski*, 1986]; and (*d*) model M84A (for the upper mantle) [*Woodhouse and Dziewonski*, 1984] or model V.3 (for the lower mantle) [*Morelli and Dziewonski*, 1987b]. To be comparable with the other models, P-velocity model V.3 has be multiplied by a factor 2 when it is presented in Figures 7.5*d*–7.9*d*.

First of all, great similarities between models SAT and SAF are evident at all depths. This verifies that the inversion results for the splitting functions of the mantle modes, as given in Chapter 5, are mutually consistent. This consistency provides evidence (which we believe is more compelling than the formal error estimates) that the splitting functions have been successfully retrieved and that they do, indeed, reflect the Earth's three-dimensional structure.

Upper-mantle heterogeneity, as revealed by waveform studies [*Woodhouse and Dziewonski*, 1984; 1986], varies with depth relatively rapidly. For example, both models SW and M84A exhibit a dramatic change in the depth range 300 km to 500 km (Figures 7.3 and 7.4). Naturally the splitting of low-frequency normal modes are sensitive to larger-scale structures. Thus it may not be appropriate to expect that the modal models, retrieved from the current data set, could recover the rapid radial variation in the upper mantle. We should be satisfied if the models can represent

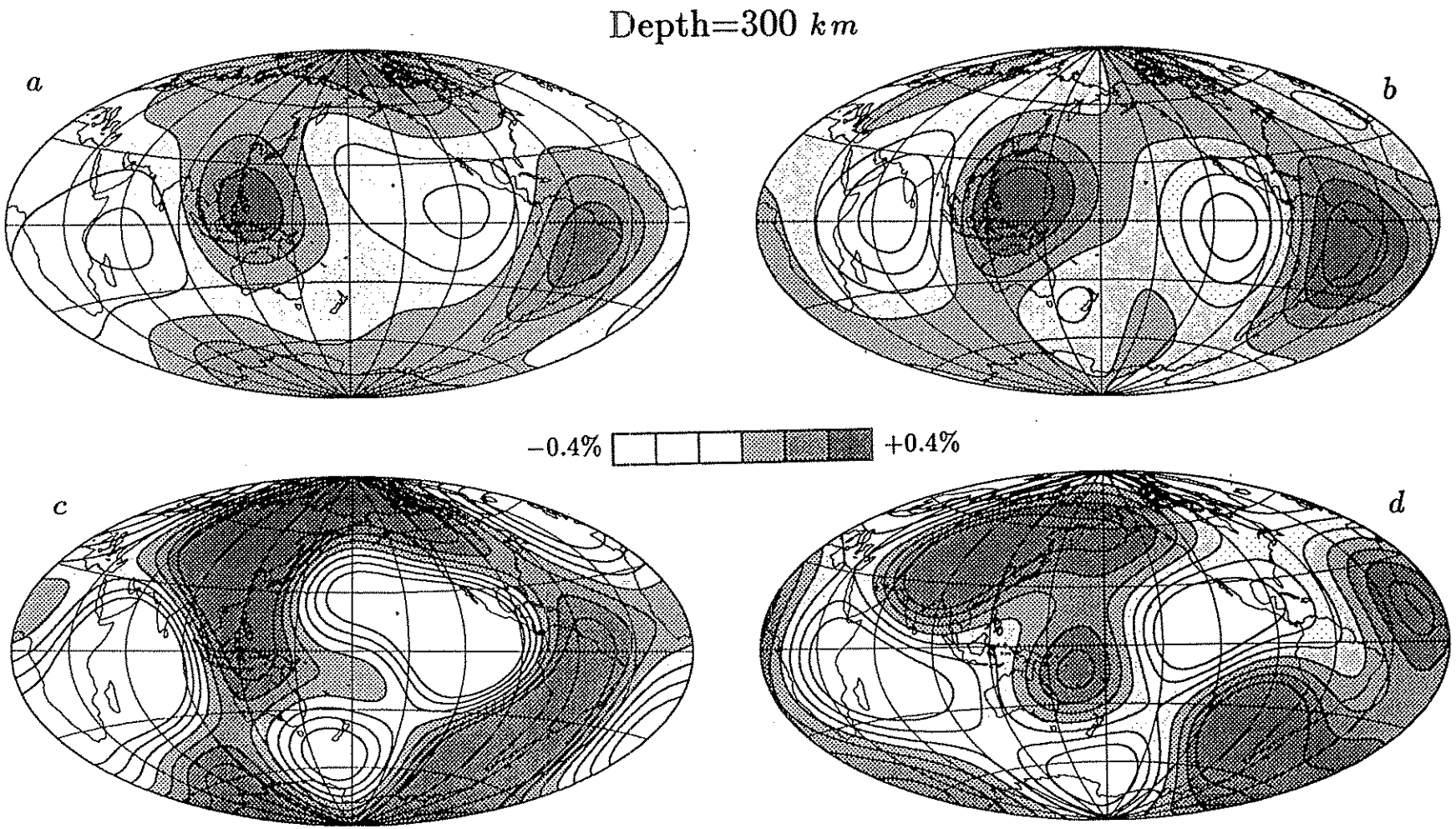

Fig. 7.3 Maps of heterogeneity in the mantle of spherical harmonic degree $s = 2$ and 4 only. (*a*) v_S heterogeneity of model SAT, retrieved directly from the split spectra of free oscillations from which splitting functions of some modes have been inferred; (*b*) v_S heterogeneity of model SAF, retrieved from splitting functions; (*c*) model SW, a v_S model based on waveform study of *SH* body waves by *Woodhouse and Dziewonski* [1986]; (*d*) model M84A, a *S*-velocity model based on waveform study of mantle waves by *Woodhouse and Dziewonski* [1984].

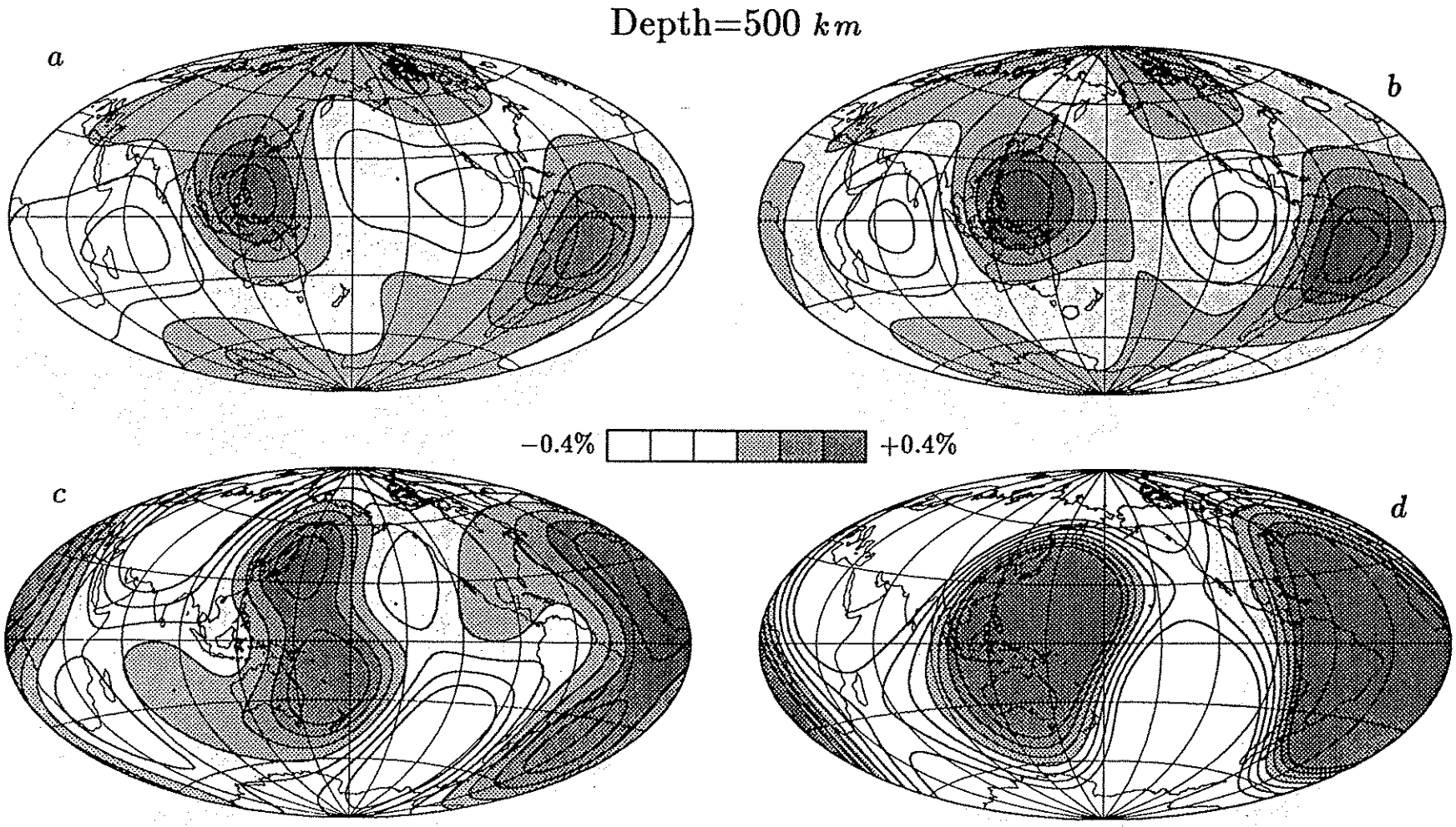

Fig. 7.4 Maps of heterogeneity in the mantle of spherical harmonic degree $s = 2$ and 4 only. See caption to Figure 7.3.

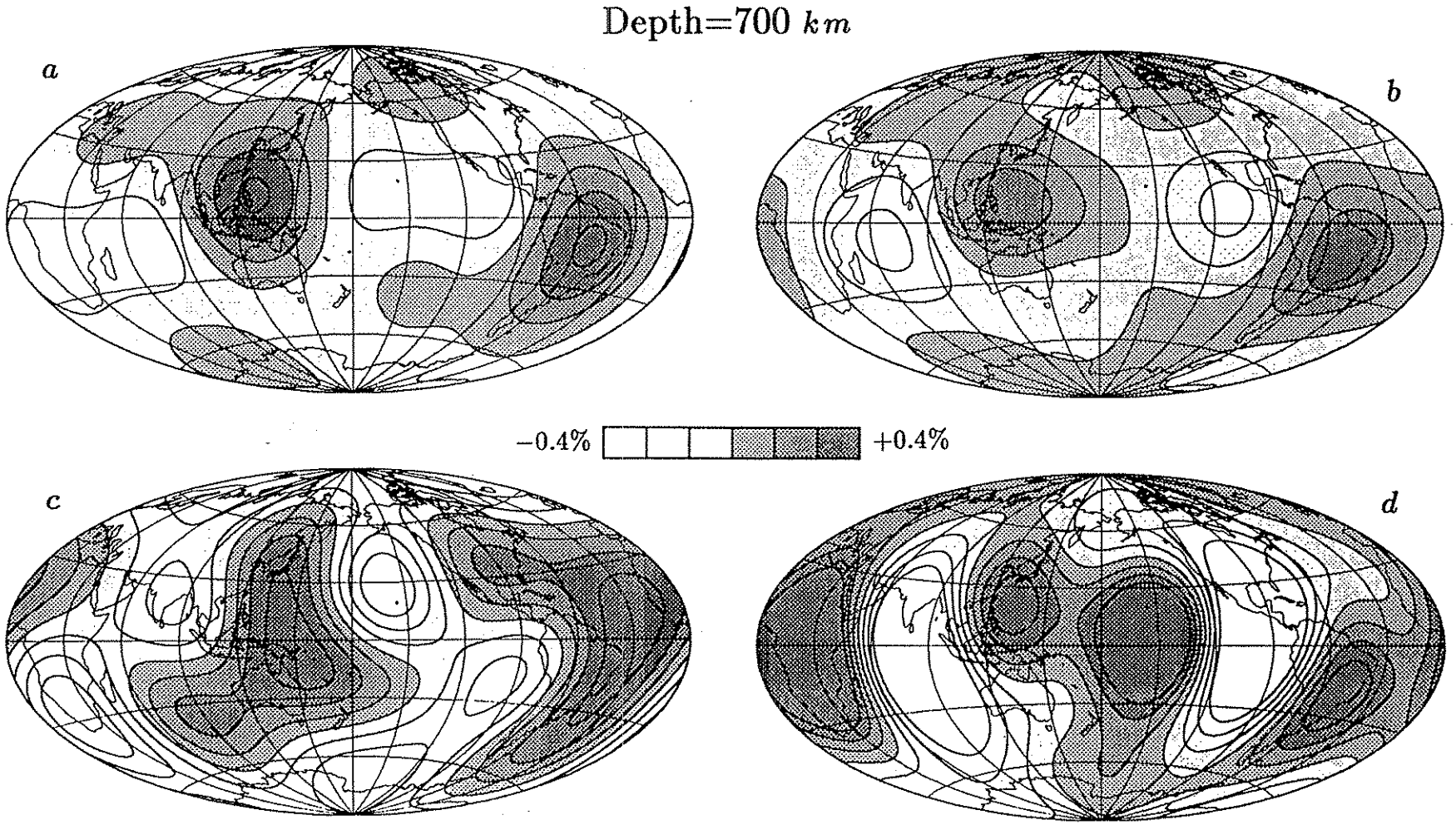

Fig. 7.5 Maps of heterogeneity in the mantle of spherical harmonic degree $s = 2$ and 4 only. See caption to Figure 7.3 with exceptions that (d) is replaced by $2\times$ v_P perturbation of model V.3, a model based P travel-time residuals by *Morelli and Dziewonski* [1987*b*].

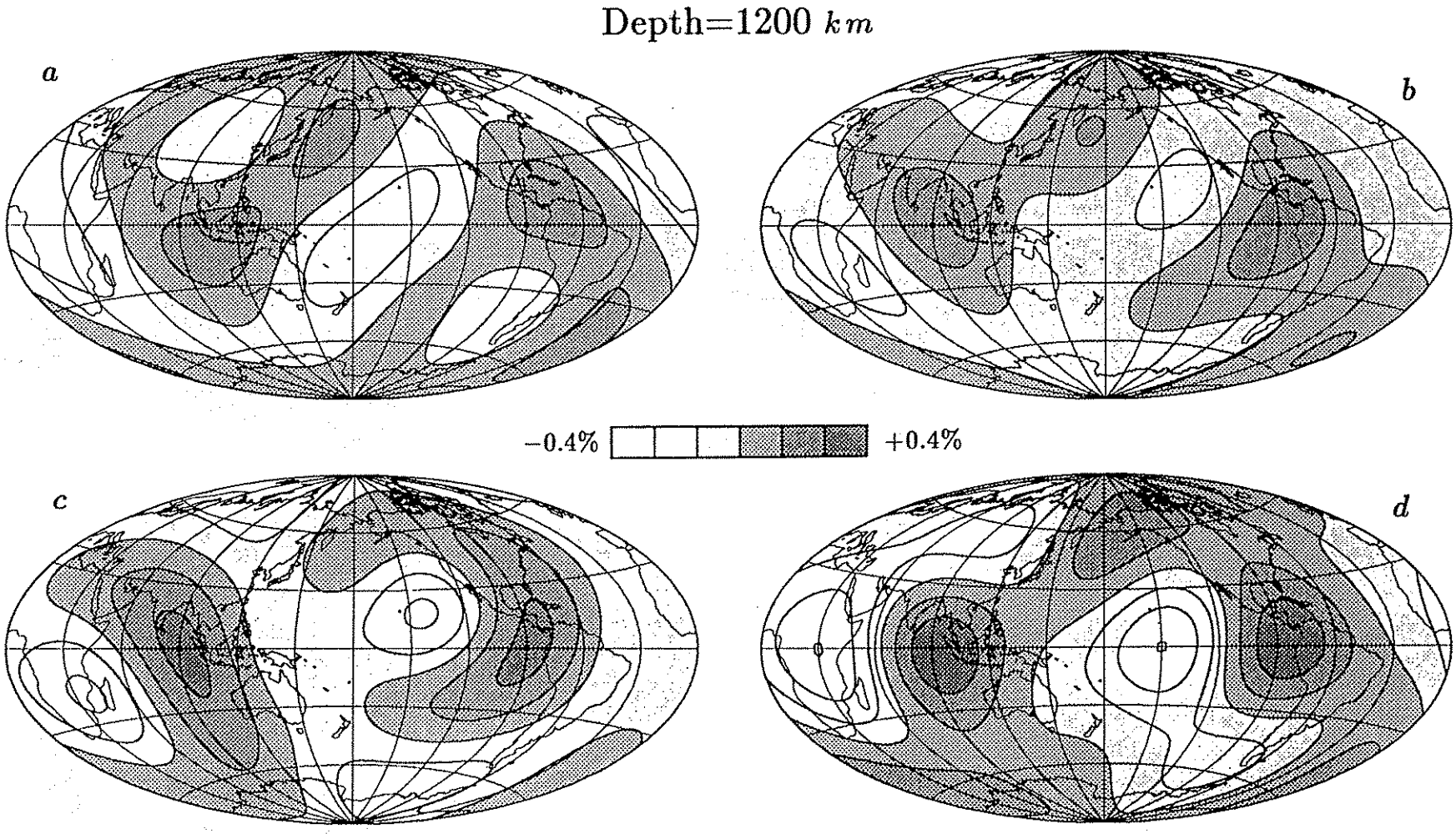

Fig. 7.6 Maps of heterogeneity in the mantle of spherical harmonic degree $s = 2$ and 4 only. See caption to Figure 7.5.

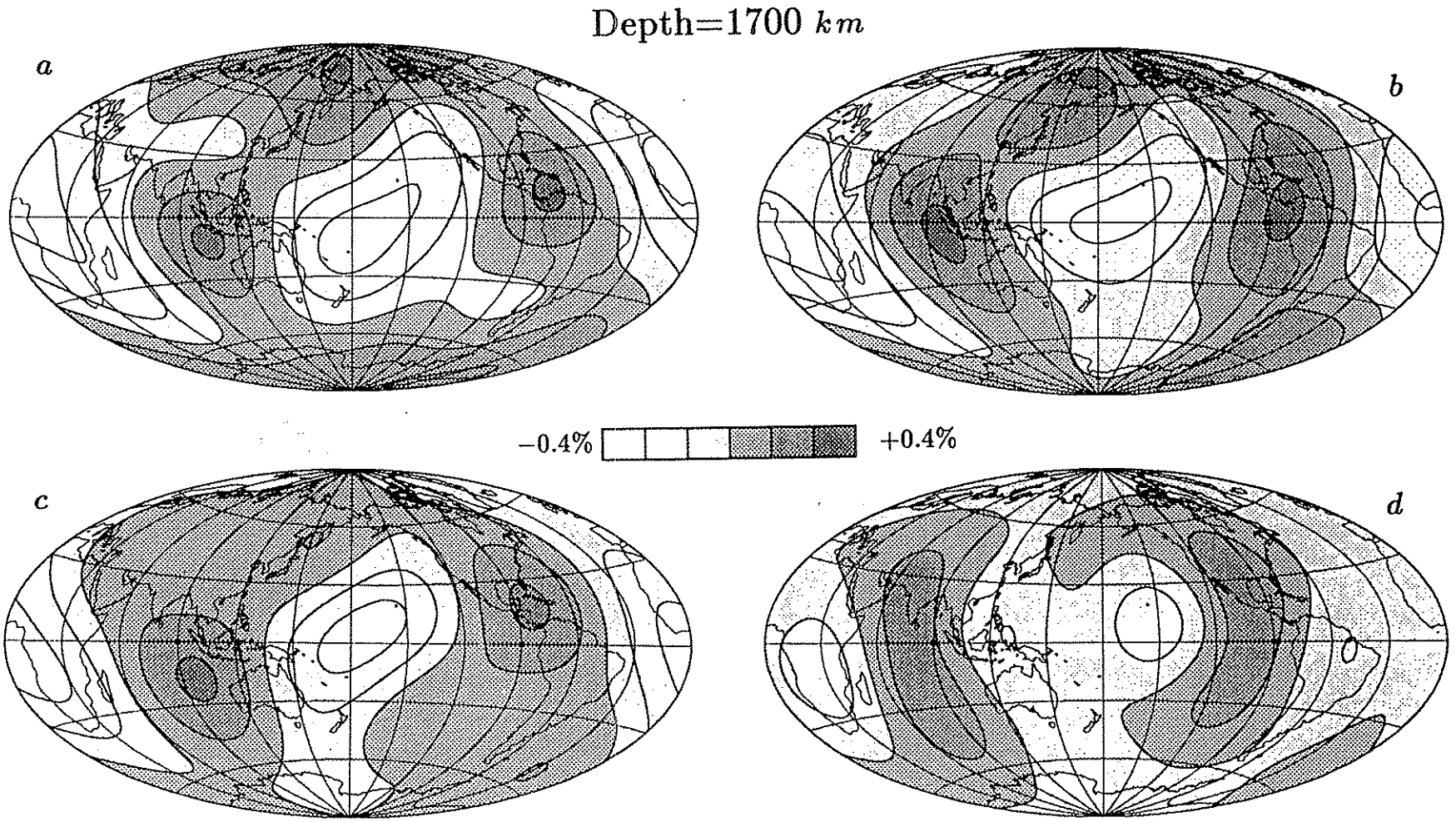

Fig. 7.7 Maps of heterogeneity in the mantle of spherical harmonic degree $s = 2$ and 4 only. See caption to Figure 7.5.

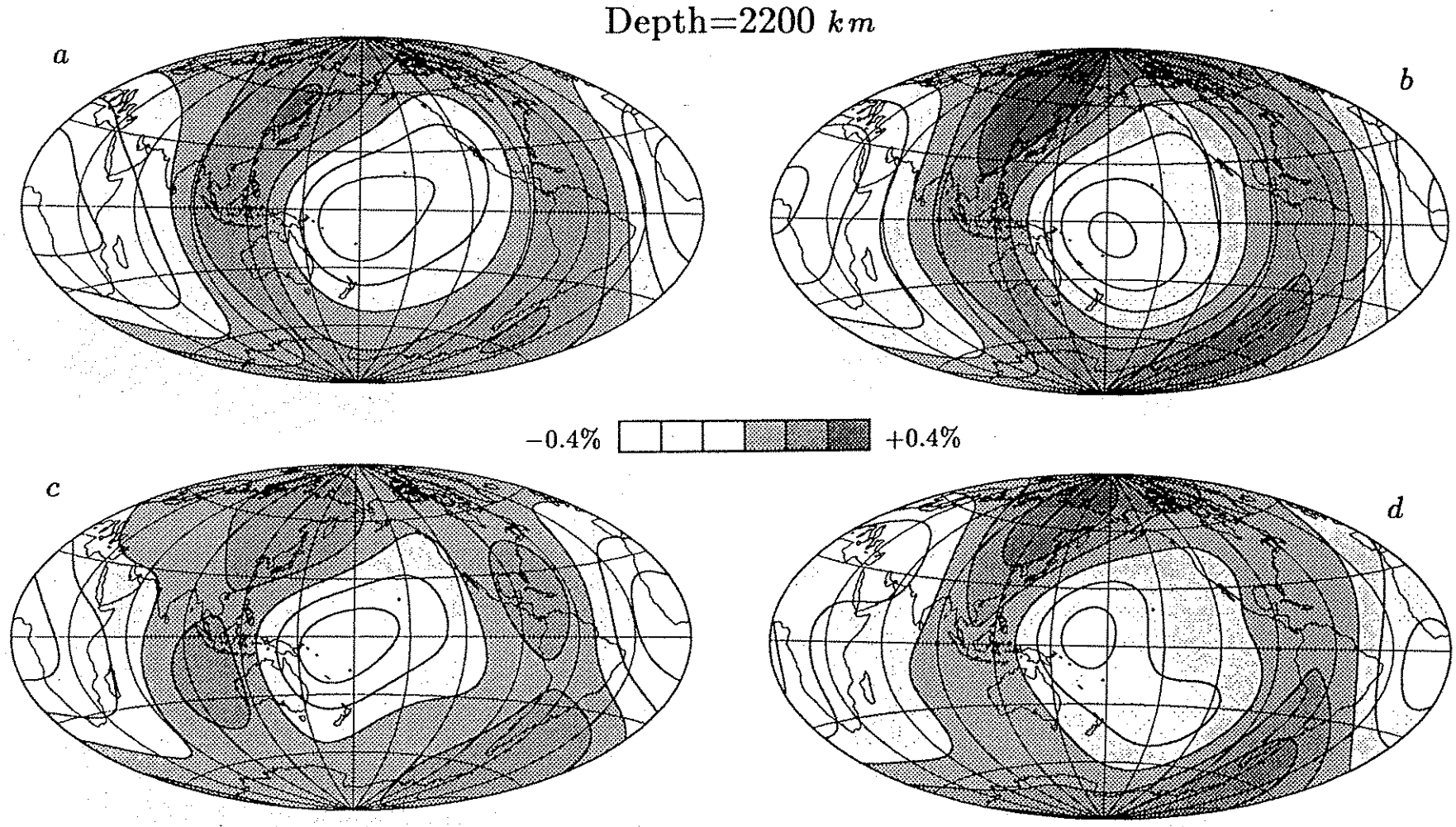

Fig. 7.8 Maps of heterogeneity in the mantle of spherical harmonic degree $s = 2$ and 4 only. See caption to Figure 7.5.

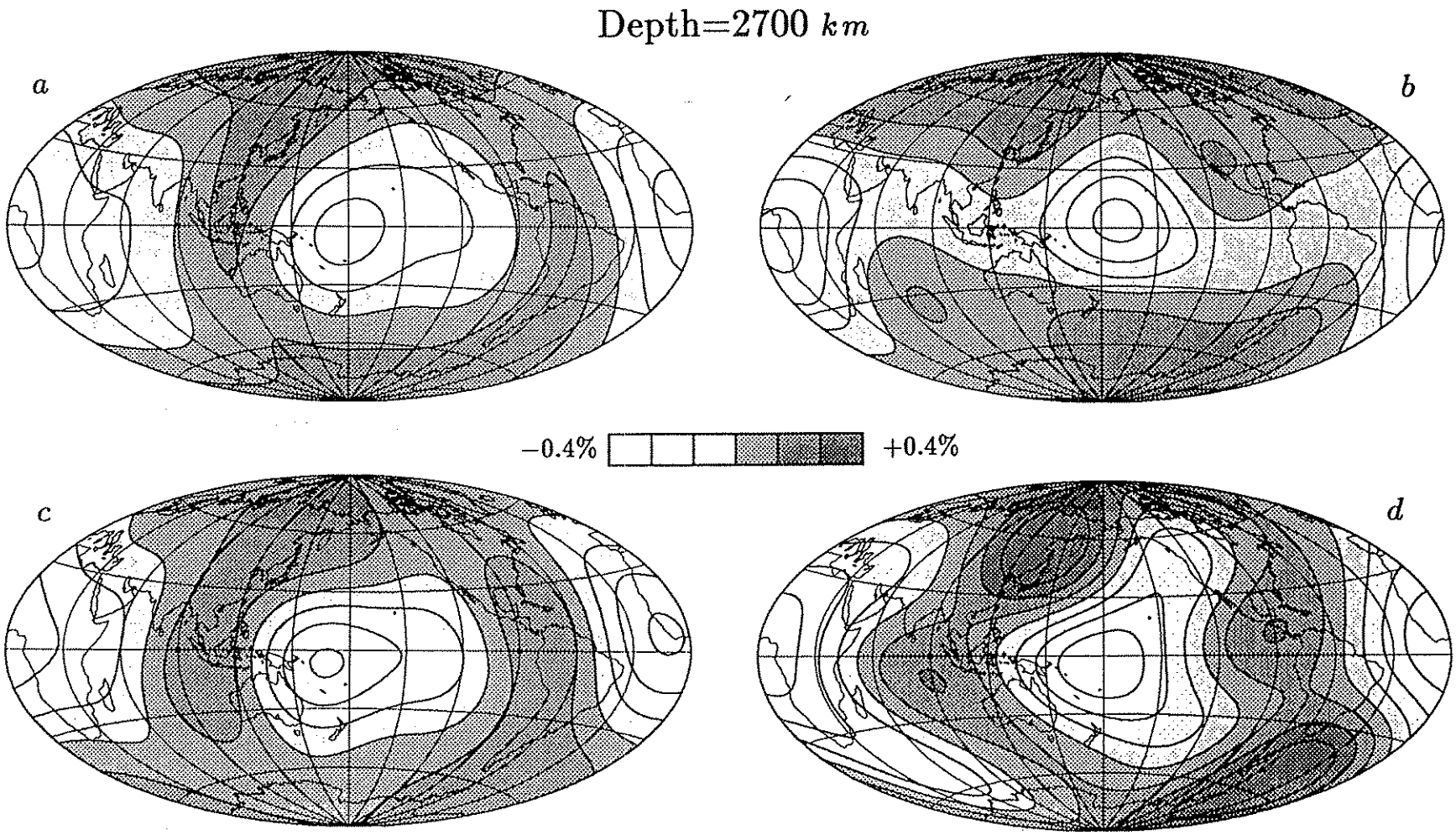

Fig. 7.9. Maps of heterogeneity in the mantle of spherical harmonic degree $s = 2$ and 4 only. See caption to Figure 7.5.

the very-large-scale features of the upper mantle. Our resulting models, SAF and SAT, are, indeed, correlated with the models based on the waveform studies. The correlation coefficients between, for example, the modal model SAF and the *SH* waveform model SW is above 0.5 (corresponding to 95% significance level) for most of the upper mantle, except in the region near depth of 500 km where the correlation coefficient is still positive. The strong similarity in pattern between SAT and SW at 300 km depth (Figures 7.3*a* and *c*) further confirms that the modal models do bear important signals from the upper mantle. We have pointed out in Chapter 6 that our data are sensitive mostly to the lower-mantle structure. This is also verified by the inversion results. While the damping level we used makes the modal models too small for the upper mantle, as compared with waveform models, the results for the lower mantle are in agreement with our knowledge based other existing models, e.g., model SW and travel-time model V.3 of *Morelli and Dziewonski* [1987b].

The agreement in the lower mantle among modal models SAT and SAF, *SH*-waveform model SW, and *P* travel-time model V.3 is remarkable. At the depth interval between 2000 km to 2700 km, the agreement is almost perfect: correlation coefficients are around 0.9 – corresponding to 100% significant level. The excellent agreement extends up to the depth of 1300 km between the modal models and the waveform model. The travel-time model V.3 is highly consistent in pattern with the other models between depths of 1000 km and 2000 km, but it has a very small amplitude from the depth of 1600 km to 1900 km, relative to the other models (cf., Figure 7.7). The discrepancy of these models at the top of the lower mantle (for example, see Figure 7.5) may be largely attributed to the following facts. The aliasing from the strong heterogeneity in the upper mantle is expected for all models, especially the modal models (e.g., comparing Figures 7.3*a* – 7.5*a*). The horizontal resolution of the travel-time model V.3 may also be poor in this region (A. M. Dziewonski, personal communication).

7.5.2 Core-mantle boundary

In Figure 7.10 we plot four topography models for the core-mantle boundary:

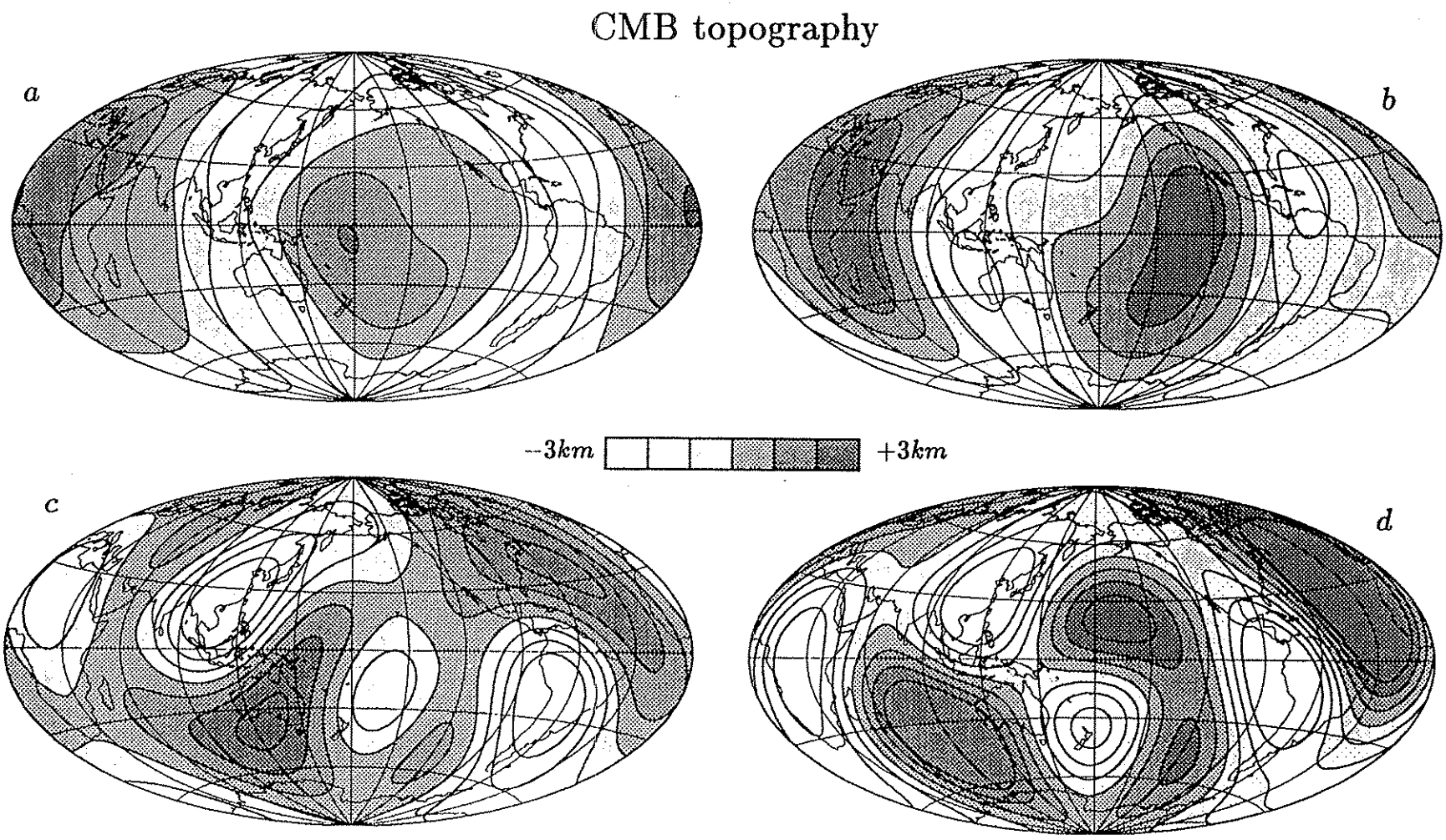

Fig. 7.10 Maps of topography models of the core-mantle boundary. (*a*) model SAT, retrieved directly from the split spectra of free oscillations from which splitting functions of some modes have been inferred; (*b*) model SAF, retrieved from splitting functions; (*c*) the even-degree portion of the model by *Morelli and Dziewonski* [1987a]; (*d*) the full model (with both even and odd degrees) of *Morelli and Dziewonski* [1987a] constrained by *PcP* and PKP_{BC} travel times.

(a) the modal model SAT, and (b) the modal model SAF; for comparison the CMB model X222 of *Morelli and Dziewonski* [1987a] is also plotted in Figure 7.10: (c) the filtered version of X222 with only even degrees and (d) the original model with both even and odd degrees. Model X222 is inferred from PcP and PKP_{BC} travel times. This model has very large odd-degree components, which can be observed from Figure 7.10. Since the data distribution of travel times is uneven (see Figures 3 and 5 of *Morelli and Dziewonski* [1987a]), it is possible that aliasing between even- and odd-degrees terms may occur. Therefore it is a safer strategy to compare the modal models with the unfiltered travel-time model, which has to be done region by region instead of term by term in harmonic expansion. Some similarities between the modal models and the unfiltered X222 model in Figure 7.10 are evident, especially if we ignore the Africa–Indian-Ocean–Australia region, where the travel-time sampling is relatively poor (see Figures 3 and 5 of *Morelli and Dziewonski* [1987a]). The modal models are smaller than the travel time model by a factor of the order of 2. This could be attributed to the trade-off between the CMB structure and the lower-mantle perturbation for the modal models.

It is an encouraging result that the patterns of the CMB-topography models from the modal data are consistent with geodynamic predictions [*Richards and Hager*, 1984; *Hager et al.*, 1985; *Horte and Peltier*, 1989]. Under the Pacific ocean, for example, the arising of the CMB is associated with slow velocities (corresponding to hot material) in the lower mantle (compare Figure 7.10a with Figures 7.7a– 7.9a, for instance).

Although the trade-off between the CMB undulation and the lower-mantle structure (including the value of the ratio of the relative perturbations in P-velocity and in S-velocity) prevent us from making a stronger statement in favor of our result, the results presented here demonstrate the ability that the splitting of normal modes can provide independent constraints on the problem.

7.5.3 Spherical corrections in the mantle

Our main interest in this study is focused on the aspherical structure of the Earth.

In order to investigate the contamination to our results due to the potential spherical deviation from the reference starting model, however, we have simultaneously included spherical corrections (for velocities, density, and attenuation) in our inversion. The correction results are list in Table 7.7c. The sizes of these corrections are very small, though no damping is applied on these parameters (as a strategy we have not damped the spherical-correction parameters so that they can absorb the data residuals as much as possible). This indicates that our reference model (PREM of *Dziewonski and Anderson* [1981]) is a very precise spherical model for this study. Although the corrections obtained here may contain some information on the Earth's spherical structure, we expect that a much larger data set is needed to make reliable spherical corrections to PREM.

7.5.4 Core modes and inner-core anisotropy

Since the inversion for the inner-core anisotropy is an underconstrained inverse problem, we do not expect to find the unique solution from our data set (8 core modes only). Instead, we seek to demonstrate that inner-core anisotropy can provide an explanation for the behavior of the anomalously split core modes, which have not been successfully modeled using other hypotheses. Here we shall address two questions: (1) how well does model SAT, which includes the inner-core anisotropy, fit the data for core modes? and (2) can the model predict the *PKIKP* travel-time anomalies?

In attempting to explain the zonal part of splitting function of the core modes, we were unable to derive a relatively simple model of inner-core anisotropy to fit the splitting function coefficients listed in Table 5.2 (see Subsection 7.3.2). The anisotropic inner-core model of SAT, however, is required to optimally fit the original seismic trace from which the splitting functions have been retrieved. It is interesting, therefore, to see to what extent the predicted zonal parts of the splitting functions of the core modes agree with those retrieved for individual mode. In Table 7.8 the predicted c_{20} and c_{40} of 8 core modes are tabulated together with those retrieved from the split spectra.

Table 7.8: Comparison of Predicted and Retrieved c_{20} and c_{40} of Core Modes

	c_{20}		c_{40}	
Mode	pred.	retr.	pred.	retr.
${}_3S_2$	205	52	99	−38
${}_{13}S_2$	39	34	14	19
${}_6S_3$	40	39	7	14
${}_2S_3$	40	54	4	6
${}_{13}S_3$	32	31	0	0
${}_9S_3$	25	5	−5	−12
${}_{11}S_4$	24	25	1	5
${}_{11}S_5$	15	25	0	4

Splitting function coefficients c_{20} and c_{40} predicted from model SAT are listed in the columns titled "pred."; and those retrieved from the seismograms are listed in the columns titled "retr.". All are in units of 10^{-4}.

We can see immediately that the predicted c_{20} and c_{40} of mode ${}_3S_2$ by model SAT do not agree with those retrieved from the seismograms at all. However model SAT does explain fairly well the original split spectra from which the splitting function has been derived – as indicated by ratio Var/Var′, where Var and Var′ are listed in Table 7.6. The ratio for mode ${}_3S_2$ is 1.19, better than the average value for all the modes together. Therefore we are convinced that there is more than one splitting functions, possibly a sequence of them, which can explain the spectral splitting of mode ${}_3S_2$ essentially equally well for the current data. The predicted splitting function by model SAT is favored over the one listed in Table 5.2, owing to its consistency with splitting functions of other modes.

The retrieved c_{20} and c_{40} of the other core modes can be explained very well by the anisotropic inner-core model – an overall 90% variance reduction is achieved if mode ${}_3S_2$ is excluded. Therefore we may conclude that the anisotropic inner-core model, part of model SAT, is a model which can explain the anomalous splitting of core modes.

Now let us turn our attention to the predicted *PKIKP* travel times of model SAT.

In Table 7.9 we compare the anisotropic inner-core model with the models of *Morelli et al.* [1986] and *Shearer et al.* [1988], which are based upon *PKIKP* travel-time studies. Although these models represents very different anisotropic fields, they predict practically same antipodal *PKIKP* travel times. In an attempt to reduce the discrepancy between the results derived from travel-time anomalies and those derived from modal splitting, *Morelli et al.* [1986] introduced a radial dependence proportional to r^2 in the inner-core anisotropic parameters. This model is still not successful in modeling modal results and, furthermore, *Shearer et al.* [1988] point out that this model predicts overly large travel-time anomalies for rays which turn at shallow depths in the inner core. In Figures 5, 6, and 7 of *Shearer et al.* [1988], they show the average travel-time anomalies, observed and predicted by some models, as a function of the depth of the turning point and of the ray angle from the Earth's rotation axis. Such averages are sensitive to inner-core anisotropy. In order to make a comparison with these results, we plot the predictions of the model SAT in Figure 7.11. Clearly the problem of overly large travel-time anomalies, shown in Figure 6 of *Shearer et al.* [1988], is overcome by the model SAT.

In summary, the inner-core anisotropy of model SAT successfully explains the splitting of anomalously split modes, and simultaneously predicts *PKIKP* travel-time anomalies fairly well.

Table 7.9: Comparison of Inner-Core Anisotropic Models

		$\psi_s^{(1)}$	$\psi_s^{(2)}$	$\psi_s^{(3)}$	$\psi_s^{(4)}$	$\psi_s^{(5)}$	$\psi_s^{(6)}$	$\psi_s^{(7)}$	travel-time coefficients t_s
$s=0$	SAT	2.1	-2.9	0.9	-2.5	0.7	0.7		$-.387\psi_0^{(1)}+.394\psi_0^{(3)}+.333\psi_0^{(5)}$
	MDW	1.17		0.51					
	STO	.77							
$s=2$	SAT	-3.4	-1.7	1.8	4.3	0.1	-4.1	0.6	$.293\psi_0^{(1)}-.298\psi_0^{(3)}$ $-.113\psi_0^{(5)}-.178\psi_0^{(6)}$
	MDW	-4.95		-2.16					
	STO	-2.58							
$s=4$	SAT	0.1	-3.7	0.0	-0.3	1.2			$-.138\psi_0^{(1)}+.141\psi_0^{(2)}$ $+.080\psi_0^{(3)}+.178\psi_0^{(4)}$
	MDW	7.51	3.28						
	STO	3.52							

In order to compare our inner-core anisotropic model with the models of *Morelli et al.* [1986] (*MDW*) and of *Shearer et al.* [1988] (*STO*), we here express these two models in terms of the parameters $\psi_s^{(k)}$ (see (7.6)), in units of 10^{-2}. The antipodal *PKIKP* travel-time residuals, δt, can be calculated from $\delta t = T(t_0 Y_0^0 + t_2 Y_2^0 + t_4 Y_4^0)$, where T is the travel time predicted by the spherical reference model (PREM of *Dziewonski and Anderson* [1981]), and $Y_s^t = Y_s^t(\theta,\phi)$ are completely normalized spherical harmonics as defined by *Edmonds* [1960] with θ and ϕ being the polar coordinates of the point where the ray intersects with the inner-core boundary.

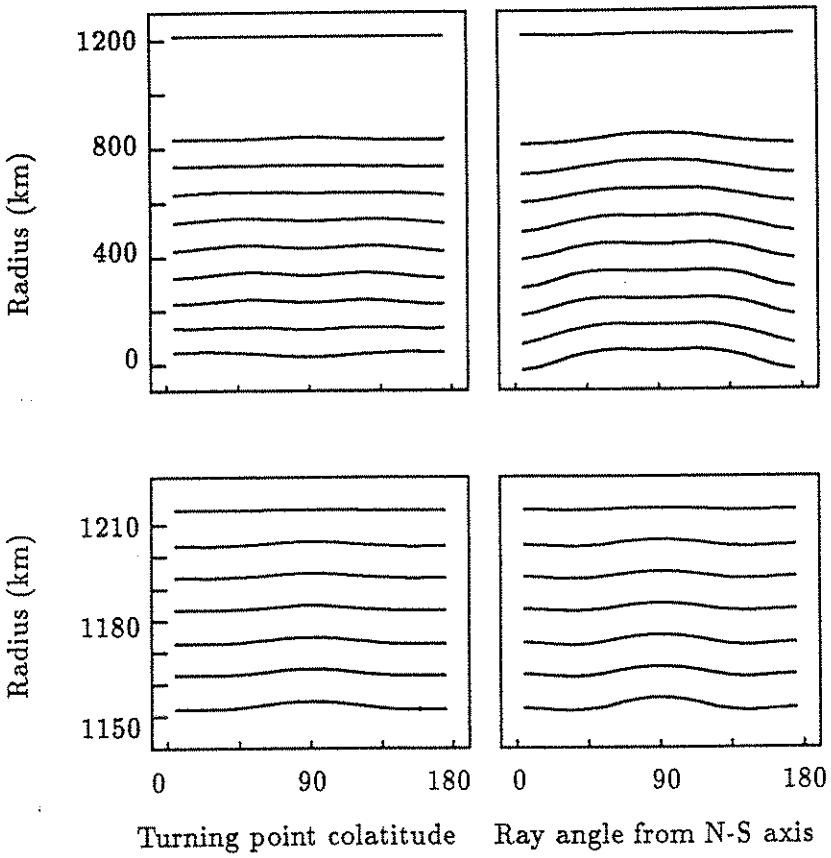

Fig. 7.11 Predictions from model SAT of the averaged *PKIKP* travel-time anomalies, as a function of the turning point of the ray, which is characterized by its depth and colatitude (left panels) or the ray angle from the rotation axis (right panels). This figure should be compared with Figures 5 and 6 in *Shearer et al.* [1988], which show too large predicted anomalies by a particular model of inner-core anisotropy of [*Morelli et al.*, 1986]. For the observed anomalies see Figures 3, 6 and 7 in *Shearer et al* [1988]. Scaling is the same as in *Shearer et al.* [1988]: 3 s is equivalent to 100 km in the upper panels and 1 s is equivalent to 6 km in the lower panels.

Chapter 8

Conclusions

We have derived large-scale, three-dimensional Earth models from the information contained in split spectra of free oscillations. The results are essentially consistent with existing heterogeneous Earth models, based upon independent data and techniques, indicating that heterogeneity in the seismic velocities is, at most, weakly dependent on frequency. This consistency is very encouraging and demonstrates the ability to obtain models of Earth structure spanning three orders of magnitude in frequency.

A very important concept used in this study is the splitting functions of normal modes. The splitting functions fully describe the splitting properties of the modes and provide linear constraints on three-dimensional Earth models which are essentially model independent. It has been shown that we may invert for these splitting functions, as an intermediate step in retrieving the structure of the Earth, mode by mode, from very long period seismic data. With the current data, approximately 30 trace for each mode, we are able to retrieve the low-degree terms (spherical harmonic degrees $s = 2$ and 4) in the splitting functions of isolated, low-frequency multiplets. The reliability of these splitting functions has been examined by comparison with the predictions of existing models, and by retrieving the Earth structure from these functions; we have found that most splitting functions retrieved can be consistently explained by relatively simple three-dimensional models of the mantle, together with a zonally anisotropic inner core. Modeling has revealed that the split spectra of a

few multiplets ($_3S_2$ is the most serious case) can be fit by very different splitting functions. This nonuniqueness should be overcome, we believe, when more data are available.

In addition to confirming existing models of mantle heterogeneity, our results present two new major features of the Earth's interior. The ratio of relative aspherical perturbations in P-velocity and in S-velocity is (with 90% confidence) smaller than 0.5 for the mantle, much lower than the value (0.8) conventionally used, which is based on the laboratory experiments [*Anderson et al.*, 1968]. In order to explain the anomalous splitting behavior of the core modes, we are forced to introduce anisotropy in the inner core. We have developed a formulation to expand a general analytic tensor field in the inner core and have shown that out of 21 independent components of an elastic tensor field only 13 independent combinations of them are responsible for the splitting of the normal modes. Using these theoretical constraints, we have developed a relatively simple model of inner-core anisotropy, which can explain both the anomalous splitting of the core modes and the *PKIKP* travel-time data.

The technique presented in this study provides a very encouraging prospect for the study of normal modes. It is straightforward to generalize the technique to include the coupling of different multiplets. This will make it possible to employ much more data and to study the splitting and the coupling of many new modes. The new networks currently under development [Romanowicz et al., 1984; Nolet et al., 1985; Smith, 1986; Romanowicz and Dziewonski, 1986] will make it possible to study splitting function coefficients of higher degrees and will provide better-constrained results. Some very important geophysical problems which cannot be solved today, such as that of constraining the lateral heterogeneity in density of the mantle, will eventually have reliable solutions.

References

Abramowitz, M., and I. A. Stegun, *Handbook of mathematical functions, with formulas, graphs, and mathematical tables*, Dover Publications, New York, 1965.

Agnew, D. A., J. Berger, W. E. Farrell, F. Gilbert, G. Masters, and D. Miller, Project IDA: a decade in review, *Eos Trans. AGU, 67*, 203–212, 1986.

Alsop, L. E., G. H. Sutton, and M. Ewing, Free Oscillation of the Earth Observed on Strain and Pendulum Seismographs, *J. Geophys. Res., 66*, 631–641, 1961.

Anderson, D. L., The anelasticity of the mantle, *Geophys. J. R. Astron. Soc., 14*, 135–164, 1967.

Anderson, D. L., A seismic equation of state II. Shear properties and thermodynamics of the lower mantle, *Phys. Earth Planet. Int., 45*, 307-323, 1987.

Anderson, O. L., E. Schreiber, R. C. Liebermann, and M. Soga, Some elastic constant data on minerals relevant to geophysics, *Rev. Geophys., 6*, 491–524, 1968.

Backus, G. E., Converting vector and tensor equations to scalar equations in spherical coordinates, *Geophys J. R. Astron. Soc., 13*, 71–101, 1967.

Backus, G. E., A geometrical picture of anisotropic tensors, *Rev. Geophys. Space Phys., 8*, 633–671, 1970.

Benioff, H., F. Press, and S. Smith, Excitation of the free oscillations of the Earth by earthquakes, *J. Geophys. Res., 66*, 605–619, 1961.

Bogert, B. P., An observatoin of free oscillations of the Earth *J. Geophys. Res., 66*, 643–646, 1961.

Clayton, R. W., and R. P. Comer, A tomographic analysis of mantle heterogeneities from body wave travel times, *Eos Trans. AGU, 64*, 776, 1983.

Creager, K. C., and T. H. Jordan, Aspherical structure of the core-mantle boundary from PKP travel times, *Geophys. Res. Lett., 13*, 1497–1500, 1986.

Dahlen, F. A., The normal modes of a rotating, elliptical earth, *Geophys J. R. Astron. Soc., 16*, 329–367, 1968.

Dahlen, F. A., The normal modes of a rotating, elliptical earth, II, Near resonant multiplet coupling, *Geophys. J. R. Astron. Soc., 18*, 397–436, 1969.

Dahlen, F. A., Inference of the lateral heterogeneity of the Earth from the eigenfrequency spectrum: à linear problem, *Geophys. J. R. Astron. Soc., 38*, 143–167, 1974.

Dahlen, F. A., Reply, *J. Geophys. Res., 81*, 491, 1976.

Dahlen, F. A., The effect of data windows on the estimation of free oscillation parameters, *Geophys. J. R. Astron. Soc., 69*, 537–549, 1982.

Davies, J. P., Local eigenfrequency and its uncertainty inferred from fundamental spheroidal mode frequency shifts, *Geophys. J. R. Astron. Soc., 88*, 693–722, 1987.

Dziewonski, A. M., Mapping the lower mantle: Determination of lateral heterogeneity in P velocity up to degree and order 6, *J. Geophys. Res., 89*, 5929–5952, 1984.

Dziewonski, A. M., and D. L. Anderson, Preliminary reference earth model (PREM), *Phys. Earth Planet. Inter., 25*, 297–356, 1981.

Dziewonski, A. M. and D. L. Anderson, Travel times and station corrections for P-waves at teleseismic distances, *J. Geophys. Res., 88*, 3295–3314, 1983.

Dziewonski, A. M., and F. Gilbert, Observations of normal modes from 84 recordings of the Alaskan earthquake of 1964 March 28, II., Further remarks based on new spheroidal overtone data, *Geophys. J. R. Astron. Soc., 35*, 401–437, 1973.

Dziewonski, A. M., and J. H. Woodhouse, An experiment in systematic study of global seismicity: Centroid-moment tensor solutions for 201 moderate and large earthquakes of 1981, *J. Geophys. Res., 88*, 3247–3271, 1983.

Dziewonski, A. M., and J. H. Woodhouse, Global images of the Earth's interior, *Science, 236*, 37–48, 1987.

Dziewonski, A. M., B. H. Hager and R. J. O'Connell, Large scale heterogeneity in the lower mantle, *J. Geophys. Res., 82*, 239-255, 1977.

Dziewonski, A. M., T.-A. Chou, and J. H. Woodhouse, Determination of the earthquake source parameters from waveform data for studies of global and regional seismicity, *J. Geophys. Res., 86*, 2825–2853, 1981.

Edmonds, A. R., *Angular Momentum and Quantum Mechanics*, Princeton University Press, Princeton, N. J., 1960.

Forte, A. M., and W. R. Peltier, Plate tectonics and aspherical Earth structure: the importance of poloidal-toroidal coupling, *J. Geophys. Res., 92*, 3645–3679, 1987.

Forte, A. M., and W. R. Peltier, Mantle convection and core-mantle boundary topography: Explanations and implications, *Tectonophysics*, in press, 1989

Giardini, D., X.-D. Li, and J. H. Woodhouse, Three-dimensional structure of the Earth from splitting in free oscillations spectra, *Nature, 325*, 405–411, 1987.

Giardini, D., X.-D. Li, and J. H. Woodhouse, Splitting functions of long-period normal modes of the Earth, *J. Geophys. Res., 93*, 13,716–13,742, 1988.

Gilbert, F., Excitation of the normal modes of the Earth by earthquakes sources, *Geophys. J. R. Astron. Soc., 22*, 223–226, 1971a.

Gilbert, F., The diagonal sum rule and averaged eigenfrequencies, *Geophys. J. R. Astron. Soc., 23*, 125–128, 1971b.

Gilbert, F., and A. M. Dziewonski, An application of normal mode theory to the retrieval of structure parameters and source mechanisms from seismic spectra, *Phil. Trans. R. Soc., A278*, 187–269, 1975.

Gubbins, D., and J. Bloxham, Geomagnetic field analysis, III, Magnetic fields on the core-mantle boundary, *Geophys. J. R. Astron. Soc., 80*, 695–713, 1985.

Gwinn, C. R., T. A. Herring, and I. I. Shapiro, Geodesy by radio interferometry: studies of the forced nutations of the earth, Part II: interpretation, *J. Geophys. Res., 91*, 4755–4765, 1986.

Hales, A. L., and H. A. Doyle, P and S travel time anomalies and their interpretation, *Geophys. J. R. Astron. Soc., 13*, 403–415, 1967.

Hager, B., R. Clayton, M. Richards, R. Comer, and A. Dziewonski, Lower mantle heterogeneity, dynamic topography and the geoid, *Nature, 313*, 541–545, 1985.

Jackson, D. D., The use of "a priori" data to resolve non-uniqueness in linear inversion, *Geophys. J. R. Astron. Soc., 57*, 137–157, 1979.

Jeanloz, R., and H.-R. Wenk, Convection and anisotropy of the inner core, *Geophys. Res. Lett., 15*, 72–75, 1988.

Jordan, T. H., A procedure for estimating lateral variations from low-frequency eigenspectra data, *Geophys. J. R. Astron. Soc., 52*, 441–455, 1978.

Kanamori, H., and D. L. Anderson, Importance of Physical Dispersion in Surface Wave and Free Oscillation Problems: Review, *Rev. Geophys. Space Phys., 15*, 105–112, 1977.

Kendall, M., and A. Stuart, *The Advanced Theory of Statistics, vol 2*, 4th ed., pp. 377–386, Charles Griffin & Company Limited, London & High Wycombe, 1977a.

Kendall, M., and A. Stuart, *The Advanced Theory of Statistics, vol 2*, 4th ed., pp. 147–152, Charles Griffin & Company Limited, London & High Wycombe, 1977b.

Knopoff, L., *Q*, *Rev. Geophys. Space Phys., 2*, 625–660, 1964.

Lay, T., Structure of the Earth: mantle and core, (U.S. National report to IUGG 1983–1986), *Rev. Geophys., 85*, 1161–1167, 1987.

Lerner-Lam, A. L., and T. H. Jordan, Earth structure from fundamental and higher-mode waveform analysis, *Geophys. J. R. Astron. Soc., 75*, 759–797, 1983.

Liu, H.-P., D. L. Anderson, and H. Kanamori, Velocity dispersion due to anelasticity; implications for seismology and mantle composition, *Geophys. J. R. astr. Soc., 47*, 41–58, 1976.

Luh, P. C., Free oscillations of the laterally inhomogeneous Earth: Quasi-degenerate multiplet coupling, *Geophys. J. R. Astron. Soc., 32*, 187–202, 1973.

Luh, P. C., Normal modes of a rotating, self-gravitating, inhomogeneous Earth, *Geophys. J. R. Astron. Soc., 38*, 187–224, 1974.

Masters, G., and F. Gilbert, Structure of the inner core inferred from observations of its spheroidal shear modes, *Geophys. Res. Lett., 8*, 569–571, 1981.

Masters, G., T. H. Jordan, P. G. Silver, and F. Gilbert, Aspherical earth structure from fundamental spheroidal-mode data, *Nature, 298*, 609–613, 1982.

Mochizuki, E., Spherical harmonic decomposition of an elastic tensor, *Geophys. J. R. Astron. Soc., 93*, 521–526, 1988.

Morelli, A., and A. M. Dziewonski, Stability of aspherical models of the lower mantle, *Eos Trans. AGU, 66*, 975, 1985.

Morelli, A., and A. M. Dziewonski, Topography of the core-mantle boundary and lateral homogeneity of the liquid core, *Nature, 325*, 678–683, 1987a.

Morelli, A., and A. M. Dziewonski, The harmonic expansion approach to the retrieval of deep earth structure, in *Seismic Tomography*, (edited by G. Nolet, pp. 251–274), D. Reidel, Hingham Mass., 1987b.

Morelli, A., A. M. Dziewonski and J. H. Woodhouse, Anisotropy of the inner core inferred from *PKIKP* travel times, *Geophys. Res. Lett., 13*, 1545–1548, 1986.

Nakanishi, I. and D. L. Anderson, Measurement of mantle wave velocities and inversion for lateral heterogeneity and anisotropy 1. Analysis of great circle phase velocities, *J. Geophys. Res., 88*, 10,267–10,283, 1983.

Nakanishi, I. and D. L. Anderson, Measurement of mantle wave velocities and inversion for lateral heterogeneity and anisotropy 2. Analysis by the single-station method, *Geophys. J. R. Astron. Soc., 78*, 573–617, 1984.

Nataf, H.-C., I. Nakanishi, and D. L. Anderson, Measurement of mantle wave velocities and inversion for lateral heterogeneity and anisotropy 3. Inversion, *J. Geophys. Res., 91*, 7261–7307, 1986.

Ness, N. F., J. C. Harrison, and L. B. Slichter, Observations of the free oscillations of the Earth, *J. Geophys. Res., 66*, 621–629, 1961.

Nolet, G., B. Romanowicz, R. Kind, and E. Wielandt, ORFEUS science plan, Report, Observ. and Res. Facil. for Eur. Seismol. (ORFEUS), Luxembourg, 1985.

Nowick, A. S. and B. S. Berry, *Anelastic Relaxation in Crystalline Solids*, Academic Press, New York, 1972.

Park, J., Asymptotic coupled-mode expressions for multiplet amplitude anomalies and frequency shifts on an aspherical Earth, *Geophys. J. R. Astron. Soc., 90*, 129–169, 1987.

Peterson, J., H. M. Butler, L. G. Holcomb, and C. R. Hutt, The Seismic Research Observatory, *Bull. Seismol. Soc. Am., 66*, 2049–2068, 1976.

Phinney, R. A. and R. Burridge, Representation of the elastic-gravitational excitation of a spherical earth model by generalized spherical harmonics, *Geophys. J. R. Astron. Soc., 34*, 451–487, 1973.

Poupinet, G., R. Pillet, and A. Souriau, Possible heterogeneity of the Earth's core deduced from *PKIKP* travel times, *Nature, 305*, 204–206, 1983.

Richards, M. A. and B. H. Hager, Geoid anomalies in a dynamic Earth, *J. Geophys. Res., 89*, 5987–6002, 1984.

Riedesel, M., Seismic moment tensor recovery at long frequency, Ph.D. thesis, Univ. of Calif., San Diego, 1985.

Ritzwoller, M., G. Masters, and F. Gilbert, Observations of anomalous splitting and their interpretation in terms of aspherical structure, *J. Geophys. Res., 91*, 10,203–10,228, 1986.

Ritzwoller, M., G. Masters, and F. Gilbert, Constraining aspherical structure with low-degree interaction coefficients: application to uncoupled multiplets, *J. Geophys. Res., 93*, 6369–6396, 1988.

Romanowicz, B., and A. M. Dziewonski, Towards a federation of broadband seismic networks, *Eos Trans. AGU, 67*, 541–542, 1986.

Romanowicz, B., M. Cara, J. Fels, and D. Rouland, GEOSCOPE: A French initiative in long-period three-component global seismic networks, *Eos Trans. AGU, 65*, 753, 1984.

Shearer, P. M., K. M. Toy and J. A. Orcutt, Axi-symmetric Earth models and inner-core anisotropy, *Nature, 333*, 228–232, 1988.

Sipkin, S. A., and T. H. Jordan, Frequency dependence of Q_{ScS}, *Bull. Seism. Soc. Am., 69*, 1055–1079, 1979.

Smith, M., G. Masters, and M. Ritzwoller, Constraining aspherical structure with normal mode frequency and attenuation measurements, *Eos Trans. AGU, 68*, 358, 1987.

Smith, S. N., IRIS: a program for the next decade, *Eos Trans. AGU, 67*, 213–219, 1986.

Souriau, A., and M. Souriau, Ellipticity and density at the inner core boundary from subcritical PKiKP and PcP data, Geophys. J. Int., 98, 39–54, 1989.

A worldwide comparison of predicted S-wave delays from a three-dimensional upper mantle model with P-wave station corrections, *Phys. Earth Planet. Inter., 39*, 75–88, 1985.

Souriau, A., and J. H. Woodhouse, A worldwide comparison of predicted S-wave delays from a three-dimensional upper mantle model with P-wave station corrections, *Phys. Earth Planet. Inter., 39*, 75–88, 1985.

Stacey, F. D., *Physics of the Earth*, 2nd ed., pp. 319–323, John Wiley, New York, 1977.

Stevenson, D. J., Limits on lateral density and velocity variations in the Earth's outer core, *Geophys. J. R. Astron. Soc., 88*, 311–319, 1987.

Sumino, Y., and O. L. Anderson, Elastic constants of minerals. In *Handbook of Physical Properties of Rocks, v.III* (R. S. Carmichael, ed.), pp. 39–138, CRC Press, Boca Raton, Florida, 1984.

Tanimoto, T., The Backus-Gilbert approach to the three-dimensional structure in the upper mantle –I. Lateral variation of surface wave phase velocity with its error and resolution, *Geophys. J. R. Astron. Soc., 82*, 1105–1124, 1985.

Tanimoto, T., The Backus-Gilbert approach to the 3-D structure in the upper-mantle – II. *SH* and *SV* velocity, *Geophys. J. R. Astron. Soc., 84*, 49–69, 1986.

Tanimoto, T., The three-dimensional shear wave structure in the mantle by overtone waveform inversion – I. Radial seismogram inversion, *Geophys. J. R. Astron. Soc., 89*, 713-740, 1987.

Tanimoto, T., The 3-D shear wave structure in the mantle by overtone waveform inversion – II. Inversion of X-waves R-waves and G-waves, *Geophysical Journal, 93*, 321-334, 1988.

Tarantola, A., and B. Valette, Generalized nonlinear inverse problems solved using the least squares criterion, *Rev. Geophys., 20(2)*, 219–232, 1982.

Wichens, A. J. and G. G. R. Buchbinder, S-wave residuals in Canada, *Bull. Seismol. Soc. Am., 70*, 809–822, 1980.

Wong, Y. K., Upper mantle heterogeneity from phase and amplitude of mantle waves, Ph.D. thesis, Harvard University, Cambridge, 1989.

Woodhouse, J. H., The coupling and attenuation of nearly resonant multiplets in the earth's free oscillation spectrum, *Geophys. J. R. Astron. Soc., 61*, 261–283, 1980.

Woodhouse, J. H., and F. Dahlen, The effect of a general aspherical perturbation on the free oscillations of the earth, *Geophys. J. R. Astron. Soc., 53*, 335–354, 1978.

Woodhouse, J. H., and A. M. Dziewonski, Mapping the upper mantle: Three-dimensional modeling of Earth structure by inversion of seismic waveforms, *J. Geophys. Res., 89*, 5953–5986, 1984.

Woodhouse, J. H., and A. M. Dziewonski, Three dimensional mantle models based on mantle wave and long period body wave data, *Eos Trans. AGU, 67*, 307, 1986.

Woodhouse, J. H., and A. M. Dziewonski, Seismic modelling of the Earth's large-scale three-dimensional structure, *Phil. Trans. R. Soc. Lond. A, 328*, 291–308, 1989.

Woodhouse, J. H., and D. Giardini, Inversion for the splitting function of isolated low order normal mode multiplets, *Eos Trans. AGU, 66*, 300, 1985.

Woodhouse, J. H., and T. P. Girnius, Surface waves and free oscillations in a regionalized earth model, *Geophys. J. R. Astron. Soc., 68*, 653–673, 1982.

Woodhouse, J. H., and Y. K. Wong, Amplitude, phase and path anomalies of mantle waves, *Geophys. J. R. Astron. Soc., 87*, 753–773, 1986.

Woodhouse, J. H., D. Giardini, and X.-D. Li, Evidence for inner core anisotropy from splitting in free oscillations data, *Geophys. Res. Lett., 13*, 1549–1552, 1986.

Yeganeh-Haeri, A., Weidner, D. J., and Ito, E., Elasticity of $MgSiO_3$ in the perovskite structure, *Science, 243*, 787–789, 1989